Spectromicroscopy of Plasmonic Multipoles

Electron Spectromicroscopy of Multipole Moments in Plasmonic Nanostructures

Isobel Claire Bicket, B.A.Sc.

A Thesis Submitted to the School of Graduate Studies in Partial Fulfillment of the Requirements for the Degree of Doctor of Philosophy

McMaster University

May 2020

McMaster University — Hamilton, Ontario, Canada
Doctor of Philosophy (2020) — Materials Science and Engineering

TITLE: Electron Spectromicroscopy of Multipole Moments in Plasmonic Nanostructures
AUTHOR: Isobel Claire Bicket, B.A.Sc. (University of Waterloo)
SUPERVISOR: Prof. Gianluigi A. Botton
NUMBER OF PAGES: xxv, 176

Lay Abstract

Certain types of metallic particles are capable of trapping light on a scale far below that which we can see; their light-trapping properties depend on their material and on their geometry. Using these tiny particles, we can manipulate the behaviour of light with greater freedom than is otherwise possible. In this thesis, we study how we can engineer the geometry of these particles to give predictable responses that can then be targeted towards specific applications. We study a fractal structure with predictable self-similar responses useful for high sensitivity detection of disease or hormone biomarkers; a resonating structure emulating a magnetic response which can be used in the design of unique new materials capable of bending light backwards and cloaking objects from sight; and a combination of these resonators in an array to demonstrate exotic electromagnetic behaviour still on the limit of our understanding.

Abstract

The geometry of a plasmonic nanostructure determines the charge-current distributions of its localized surface plasmon resonances (LSPR), thereby determining the device's interactions with external electromagnetic fields. To target specific applications, we manipulate the nanostructure geometry to create different electromagnetic multipole moments, from basic electric and magnetic dipoles to more exotic higher order and toroidal multipoles. The nanoscale nature of the resonance phenomena makes electron beam spectromicroscopy techniques uniquely suited to probe LSPRs over a wide spectral range, with nanoscale spatial resolution. We use electron energy loss spectroscopy (EELS) in a monochromated scanning transmission electron microscope and cathodoluminescence spectroscopy (CL) in a scanning electron microscope to probe the near-field and far-field properties of LSPR.

Electric dipoles within triangular prisms and apertures in Sierpiński fractals couple as the generation number is advanced, creating predictable spectral bands from hybridized dipole modes of parent generations with hierarchical patterns of high field intensity, as visualized in EELS. A magnetic dipole moment is engineered using a vertical split ring resonator (VSRR), pushing the limits of nanofabrication techniques. On this nanostructure we demonstrate the calculation of spatially resolved Stokes parameters on the emission of the magnetic dipole mode and a series of coupled rim modes. Coupling of the magnetic dipole mode of four VSRRs in a circular array creates an LSPR mode supporting the lesser-known toroidal dipole moment. We further probe the near-field configuration of this 3D array through tilting under the electron beam in EELS, and the far-field emission through CL of higher order rim modes. We also propose further configurations of five and six VSRRs to strengthen the toroidal dipole moment.

All of the data presented herein was analyzed using custom Python code, which provides a unique graphical interface to 3D spectromicroscopy datasets, and a parallelized implementation of the Richardson-Lucy deconvolution algorithm.

Acknowledgements

I have spent my PhD years at McMaster in the presence of many fine people (many of whom I don't know half as well as I should like!), at school and at home, in Canada and in foreign lands, in the lab and in the office. Thank you first to my supervisor, Gianluigi Botton, for your belief in the abilities of a young student to do things she didn't even know she could. You have given me all the opportunity I could ask for to pursue my interests and the room I needed to stretch my metaphorical wings and fly on my own power. Thanks also to my other committee members, for the yearly support and occasionally more frequent consults. François, thank you for your tireless advice on the fractal papers, and Harold, for your interest in the (still not working, alas) laser project. I am also grateful to Profs. Spencer Smith and Adam Hitchcock: your classes are among those I remember best and you taught me far more than the syllabus promised. I thankfully acknowledge OGS, NSERC, the CMSC, and McMaster University, EGS, and the Department of Materials Science and Engineering for the funding necessary to support myself throughout the PhD, and to attend conferences in far distant lands.

I remember with much appreciation the many post-docs who have passed through our lab during my time here, particularly Matthieu Bugnet, David Rossouw, and Stefan Löffler. To Matthieu, for his patience in dealing with first year students who don't quite know what they're doing, but need help doing it, I still remember you taking the time on a weekend right before my first conference to help me acquire *something* to present. David, you left us with a strong foundation in plasmon EELS and I hope I have carried on your inheritance and added my two cents to the group's knowledge. Stefan, you brought with you an amazing new perspective on the microscope and on physics and a willingness to try out new experiments and teach me so many new things and I am forever grateful for not only your friendship, but for introducing me to your then-fiancée Veronika and starting two valuable friendships. Thank you also to Maureen Lagos, for the exciting prospects and new research opportunities that your presence at McMaster brings, and sharing your knowledge on new topics.

By sharing an office with so many students, I cannot help but be indebted to them for the good times and discussions we shared together and for the progress in my research and worldly experience. Thanks to Steffi, Alex, Amin, Shayan, Viktor, Eric, Alfredo, Tyler, Andrew, Sam, Sagar, Edson, Hanshuo, Nafiseh, our newer members Milenka and Jingyi, and our visiting students, Catalina, Ramon, Natalia, and Wen.

You each brought something special and unique to my time here and to my life hereon out. Thanks to Viktor and Shayan (and to my summer students!), for trusting me with your samples and teaching me I could inspire and teach others, to Eric for the cheery attitude and lithography discussions, and Alfredo for not abandoning the office when everyone else did. Especial thanks to Alex, for showing up right when I started my PhD, travelling this path with me, and for giving me the confidence to achieve a new degree of freedom on the microscope (free lens mode!), and for your willingness to discuss difficult questions of both a technical or philosophical nature. Very importantly, thank you to Edson, my mentor since first year, you always have enthusiastic help and a smile to offer. You were always willing to help me and teach me *everything* I needed to know to start my experiments, not to mention your genuine interest in my results and in science in general, above and beyond the call of duty.

Particular thanks go to Prof. Albert Polman and his group of post-docs and students for hosting my research stay in Amsterdam for three months; you make your visitors feel very welcome and integrated in your group. Special thanks to Sophie for your guidance (and the loan of your bicycle!), and Benjamin, Philip, and Toon for lending me your CL expertise during a busy time for all of you, and to Verena, Magda, and the other group members for your friendship and hearty welcome. Additional thanks go to my other collaborators, who enabled new techniques to take part in my research.

Thanks must go to all of the staff at the CCEM and the CEDT, for teaching me to use the instruments and treat them with respect, especially to Doris Stevanovic, Glynis de Sylveira, Chris Butcher, Andreas Korinek, and Andy Duft. Thank you especially, Andy, for sharing your knowledge with me and for the countless on-the-spot sample coatings that enable my plasmons to live. Going back further in time, I gratefully recall my co-op supervisor, Don Steele, who first showed me that boring old 3 mm aluminium disks hold within them a startling beauty, revealed by the electron microscope, and who trusted a second-year student with his fancy equipment, igniting my love of microscopy (and even introducing me to my future-supervisor!).

Outside of my academic life, thank you to the Dundas Badminton Club (particularly Sandy and Daniel) for the weekly opportunity to release some frustration on the poor birdies, and to Alan Hansell, for organizing such a fulfilling volunteering opportunity that lets me get good and dirty every week, for the sake of the environment. Many thanks also go to my long-time friends, Adriana, Alison, Alison, and Jennifer, for the constant good cheer and friendship throughout my years in high school and university, and for participating in mutually-enabled shenanigans with me. Endless thanks go to my parents, who first encouraged me in my love of science and pointed me towards engineering, and have been there throughout the long process.

Most importantly of all, thank you to my then-fiancé, now-husband, Will, for his never-ending support, unwavering backing, and unconditional love. You taught me to appreciate life as more than work or school, and picked me up and took me outside when I became too much like a Morlock to be healthy.

The Road goes ever on and on,
Down from the door where it began.
Now far ahead the Road has gone,
And I must follow, if I can,
Pursuing it with eager feet,
Until it joins some larger way
Where many paths and errands meet.
And whither then? I cannot say.
-J.R.R Tolkien, through the mouth of Bilbo Baggins, a Hobbit

Contents

List of Figures

List of Tables

List of Acronyms

1D	One-dimensional
2D	Two-dimensional
3D	Three-dimensional
AC	Alternating current
ADF	Annular dark-field
AM	Amplitude modulation
AR	Angular-resolved
BEM	Boundary element method
BP	Bulk plasmon
BPF	Band-pass filter
BSD	Berkeley Software Distribution
BSE	Back-scattered electron
C1	First condenser lens
C2	Second condenser lens
C3	Third condenser lens
$\mathbf{C}_3$	Three-fold rotational symmetry
$\mathbf{C}_\infty$	Infinite rotational symmetry (rotationally invariant)
CAD	Computer-aided design
CCD	Charge-coupled device
CE	Common Era
CFEG	Cold field emission gun
CL	Cathodoluminescence
CPU	Central processing unit
CSV	Comma-separated value
DM	Digital Micrograph
DQE	Detector quantum efficiency
EBL	Electron beam lithography
EDXS	Energy-dispersive x-ray spectroscopy
EELS	Electron energy loss spectroscopy

EFTEM	Energy-filtered transmission electron microscope/microscopy
EM	Electromagnetic
EMLDOS	Electromagnetic local density-of-states
FDTD	Finite-difference time domain
FEG	Field emission gun
FEM	Finite-element method
FM	Frequency modulation
FWHM	Full width at half maximum
G0	Generation 0 Sierpiński fractal
G0.5	Intermediate structure halfway between G0 and G1 Sierpiński fractals
G1	Generation 1 Sierpiński fractal
G1.5	Intermediate structure halfway between G1 and G2 Sierpiński fractals
G2	Generation 2 Sierpiński fractal
G3	Generation 3 Sierpiński fractal
GIF	Gatan imaging filter
GIL	Global interpreter lock
GL	Gun lens
GUI	Graphical user interface
HAADF	High-angle annular dark-field
IDE	Independent development environment
IEEE	Institute of Electrical and Electronics Engineers
iG0	Inverse G0 Sierpiński fractal (a triangular aperture)
iG2	A series of triangular apertures arranged in the same way as inside a G2 Sierpiński fractal
IPA	Isopropyl alcohol
IR	Infrared
LAB	Longitudinal anti-bonding
LB	Longitudinal bonding
LC	Inductor-capacitor
LED	Light-emitting diode
LHC	Left-handed circular
LP	Linear polarizer
LSPR	Localized surface plasmon resonance
MIBK	Methyl isobutyl ketone
ML	Maximum likelihood
MNPBEM	Metallic Nanoparticle Boundary Element Method
NA	Numerical aperture
NASA	National Aeronautics and Space Administration

NPGS	Nanometer Pattern Generation System
OOL	Object-oriented language
P1	First projector lens
P2	Second projector lens
PI	Princeton Instruments
PML	Perfectly matched layer
PMMA	Poly methyl(methacrylate)
PSF	Point spread function
QWP	Quarter waveplate
RAM	Random access memory
RHC	Right-handed circular
RLC	Resistor-inductor-capacitor
RLD	Richardson-Lucy deconvolution
RPM	Rotations per minute
SE	Secondary electron
SEA	Spectrometer entrance aperture
SEM	Scanning electron microscope/microscopy
SERS	Surface-enhanced Raman scattering
SFEG	Schottky field emission gun
SHG	Second harmonic generation
SI	Spectrum image
SIAn	Spectrum Image Analysis
SNOM	Scanning near-field optical microscopy
SNR	Signal-to-noise ratio
SP	Surface plasmon
SPP	Surface plasmon polariton
SRR	Split ring resonator
STEM	Scanning transmission electron microscope/microscopy
STS	Scanning tunnelling spectroscopy
T4	Toroidal array of four vertical split ring resonators
T5	Toroidal array of five vertical split ring resonators
T6	Toroidal array of six vertical split ring resonators
TAB	Transverse anti-bonding
TB	Transverse bonding
TEM	Transmission electron microscope/microscopy
UV	Ultraviolet
VSRR	Vertical split ring resonator

VSRR-h	Vertical split ring resonator, oriented horizontally with respect to the CL mirror (top-down view)
VSRR-v	Vertical split ring resonator, oriented vertically with respect to the CL mirror (top-down view)
WD	Working distance
WDXS	Wavelength-dispersive x-ray spectroscopy
ZLP	Zero loss peak

List of Symbols

α	One stage tilt direction on the FEI stage
β	One stage tilt direction (orthogonal to α) on the FEI stage
χ	Fraction of a piece of code which can be parallelized
δ	Phase delay between two waves
ϵ	Complex dielectric function $= \epsilon_0\epsilon_\mathrm{r} = \epsilon_1 + i\epsilon_2$
ϵ_1	Real part of the complex dielectric function
ϵ_2	Imaginary part of the complex dielectric function
ϵ_0	Vacuum permittivity
ϵ_r	Relative (to vacuum permittivity) dielectric function
$\boldsymbol{\varepsilon}$	Electric field vector
ε	Electric field vector component (subscript indicates direction)
$\boldsymbol{\varepsilon}^\mathrm{ind}$	Induced electric field
$\boldsymbol{\varepsilon}_\mathrm{amp}$	Amplitude of the far-field radiation electric field
$\boldsymbol{\varepsilon}_\mathrm{ff}$	Far-field radiation electric field
η	Detector and signal noise
η_0	Combination of vacuum permittivity and permeability $= \sqrt{\epsilon_0\mu_0}$
γ	Damping factor
Γ_EELS	Electron energy loss probability
κ	Imaginary part of the complex refractive index (extinction coefficient)
λ	Wavelength
μ	Magnetic permeability $= \mu_0\mu_\mathrm{r}$
μ_0	Vacuum permeability
μ_r	Relative (to vacuum permeability) magnetic permeability
ω	Frequency
ω_0	Resonance frequency
ω_P	(Bulk) plasma frequency
ω_SP	Surface plasmon frequency
ϕ	Azimuthal angle in spherical coordinate systems
$\hat{\boldsymbol{\phi}}$	Azimuthal direction vector in spherical coordinates
Φ	Scalar potential
Ψ_UN	Wave pattern of light if no screen exists $= \Psi_\mathrm{S} + \Psi_\mathrm{CS}$
Ψ_S	Wave pattern after light passes through a screen

Ψ_{CS}	Wave pattern after light passes through a complementary screen
σ	Charge density
$\dot{\sigma}$	Time derivative of the charge density
ς	Fraction of a piece of code which must be run serially
τ	Performance measure of a code
θ	Polar angle in spherical coordinate system
$\hat{\boldsymbol{\theta}}$	Polar direction vector in spherical coordinates
ξ	Point spread function
$\tilde{\xi}$	Discretized point spread function
ζ	Number of electrons detected per pixel
A	Area
$\boldsymbol{A}$	Vector potential
b	Background intensity
$\boldsymbol{B}$	Magnetic induction
c	Speed of light in vacuum
D	Largest dimension of an antenna
DoP	Degree of polarization
DoLP	Degree of linear polarization
DoCP	Degree of circular polarization
e	Elementary charge
E	Energy
E_{p}	Plasma energy
f	(Original) electron image function
$\tilde{f}$	Discretized (original) electron image function
g	Gain coefficient
G	Axial toroidal moment
G	Green's function
$\hbar$	Reduced Planck constant
$\boldsymbol{H}$	Magnetic field vector
i	Imaginary number $= \sqrt{-1}$
I	Intensity
I_{obs}	Intensity of the observed (measured) spectrum
I_{pol}	Intensity of polarized light

I_{theory}	Intensity of the theoretical spectrum
I_{true}	Intensity of the 'true' spectrum (as emitted from the sample)
I_{H}	Intensity of horizontally polarized light
I_{V}	Intensity of vertically polarized light
I_{135}	Intensity of light linearly polarized at 135°
I_{45}	Intensity of light linearly polarizad at 45°
I_{LHC}	Intensity of left-handed circularly polarized light
I_{RHC}	Intensity of right-handed circularly polarized light
$\hat{\text{I}}$	Spatial inversion operation
$\boldsymbol{j}$	Current density vector
j	Component of the current density (subscript indicates direction)
k	Wavevector
k_0	Free-space wavevector
k_{p}	Free-space wavevector of a wave at the plasma frequency
l	An index (a counting integer)
$\boldsymbol{m}$	Magnetic dipole moment (subscript indicates orientation)
M_l	Magnetic multipole form factors (order l has 2^l poles)
$\boldsymbol{M}$	Mueller matrix of the object indicated by the subscript in the text
$\tilde{n}$	Complex refractive index $= n + i\kappa$
n	Real part of the complex refractive index
N	Dataset size on each spatial axis
N_{proc}	Number of processing units (threads) used in parallel processing
N_{it}	Number of iterations
$\boldsymbol{p}$	Electric dipole moment (subscript indicates orientation)
$\boldsymbol{p_0}$	Static component of the electric dipole moment
P_l	Electric multipole form factors (order l has 2^l poles)
Q	Quality factor
r	Distance from the source or centre
$\boldsymbol{r}$	Vector from the source or centre to the observer
$\hat{\boldsymbol{r}}$	Radial unit vector in spherical coordinates
$\boldsymbol{r}_{\text{e}}$	Position of the electron beam
R	Magnitude of the distance between two location coordinates
$\hat{\text{R}}$	Time reversal operation

$\boldsymbol{s}$	A point in 2D space (*e.g.*, on an interface or on a plane)
$\tilde{\boldsymbol{s}}$	A point in discretized 2D space (*e.g.*, on a detector or array)
$\boldsymbol{S}$	Stokes vector
S_0	Zeroth Stokes parameter: total light intensity
S_1	First Stokes parameter: horizontal and vertical linearly polarized light
S_2	Second Stokes parameter: 45° and 135° linearly polarized light
S_3	Third Stokes parameter: circularly polarized light
t	Time
$\boldsymbol{T}$	Toroidal dipole moment
$\boldsymbol{T_0}$	Static component of the toroidal dipole moment
T_l	Toroidal multipole form factors (order l has 2^l poles)
T_{corr}	CL detector correction function
$\boldsymbol{v_e}$	Electron velocity
x	Cartesian coordinate system axis
$\hat{\boldsymbol{x}}$	Direction unit vector along x in Cartesian coordinates
$\boldsymbol{x}$	Position vector in Cartesian coordinates
y	Cartesian coordinate system axis
$\hat{\boldsymbol{y}}$	Direction unit vector along y in Cartesian coordinates
z	Cartesian coordinate system axis

Declaration of Academic Achievement

This thesis has been written solely by me, Isobel Claire Bicket. The research work is my own, with the exception of the contributions listed below.

Danielle M. McRae, under the supervision of Prof. François Lagugné-Labarthet at the University of Western Ontario, performed the FDTD calculations on the Sierpiński fractal structures presented in Chapter 3 and Appendix C. Most of the EELS data presented on the split ring resonators (Chapter 4) and the toroidal structures (Chapter 5) was acquired with the help of Dr. Edson P. Bellido. The FEM simulations of the toroidal array presented in Chapter 5 were performed by Dr. Ahmed Elsharabasy under the supervision of Prof. Mohamed Bakr at McMaster University.

Portions of this thesis work have been published and are under the copyright of the publishing society, as indicated in the text in Chapters 3 and 4. Permissions from these journals, printed in Appendix D, have been obtained for re-use of the copyrighted material.

Chapter 1

Introduction

1.1 Photonics

Light plays an important role in our society, where so much of our knowledge of the world comes through vision. Starting in ancient societies, we have used light to highlight leadership by dressing them in shiny reflective silver or gold surfaces. Reflective surfaces are relatively simple to create, with a smooth metal or even the surface of calm water, and give us the ability to bend light and send it in different directions (Figure 1.1). Academically, the study of light has been of interest since ancient Egypt and ancient Greece, where philosophers worked to understand light as it relates to vision [1]. The ability to focus light came through the mathematical concept of the parabolic or ellipsoidal mirror (reflective focusing of light) and the lens (refractive focusing of light) [1].

The concept of the refractive lens dates back to at least the tenth century in a treatise by Ibn Sahl, which described the concept of using 'burning mirrors' to focus light enough to create fire at the focal point [2]. Manipulation of light to magnify an image came from observations through droplets of water or glass [3], and Alhazen's work on the bending and focusing properties through reflection and refraction provided the mathematics necessary for the design of lenses and mirrors [1].

Lenses were first used in refractive telescopes and later, reflecting telescopes in the 17th century to study astronomical phenomena [1]. Glassmaking opened up the manufacture of lenses for magnifying to make, for instance, spectacles [3]. The use of basic microscopes to magnify things that were too small to see with the naked eye goes back to at least the end of the 16th century [3]. Introducing lenses of short focal length was done by Hooke, and van Leeuwenhoek's skill in grinding and mounting high quality glass lenses extended the resolution of the optical microscope [3], opening up the study of the microscopic world beyond our everyday sight.

The concept of light as a wave was introduced by Huygens, debated by Newton, strengthened by Young and Maxwell, and finally unified with the particle nature of light (photons) by Dirac [1]. Maxwell's work [7], confirmed by Hertz [8], revealed light

Figure 1.1: Reflective surfaces in history. Reflective surface of still water (top) [4]; Giulio Parigi's painting (c. 1600) of Archimedes using a parabolic mirror to focus light to burn enemy ships (bottom) (retrieved from [5]); reflective silver headdresses (right) [6].

to be composed of transverse waves with alternating electric and magnetic fields [1]. These electromagnetic (EM) waves are not limited to visible light, but extend from low energy, long wavelength radio waves to extremely energetic, short wavelength gamma rays (Figure 1.2). This is the EM spectrum, of which visible light actually makes up a very small portion; our vision and the popular appreciation of light is fairly limited compared to the whole spectrum. The transverse EM waves which make up the EM spectrum behave both as particles, carrying quanta of energy, and as waves with a specific frequency and wavelength, travelling through space and subject to diffraction phenomena.

Advancing through the development and history of technology, we use more and more of the EM spectrum in our everyday lives. We use low frequency light, with its long wavelength and long propagation distance, to widely transmit information through radio- and microwaves: *e.g.* AM and FM radio, WiFi, and cell phone signals. In this region, we interact with light through specifically engineered antennas, often of dimensions comparable to some fraction of the wavelength of light, designed to emit and absorb long wavelength radiation. We also use microwaves to heat food, as in this energy regime radiation interacts with and excites water molecules, which then release energy as heat.

At higher frequencies, infrared (IR) radiation finds uses in the release and absorption of heat, as many molecules and materials possess vibrational modes which can absorb or emit quanta of IR light. IR radiation is also used to transmit information, providing the developed world with global communications and allowing us to send digital messages across the world through undersea fibre optic cables.

At higher frequency/energy than IR is the most familiar region, the visible region of the spectrum, though it takes up a minuscule fraction of the whole EM spectrum. With visible light, we image, see, and understand the world. This regime (and the IR) contains the transition energies of many common semiconductors, which allows us to

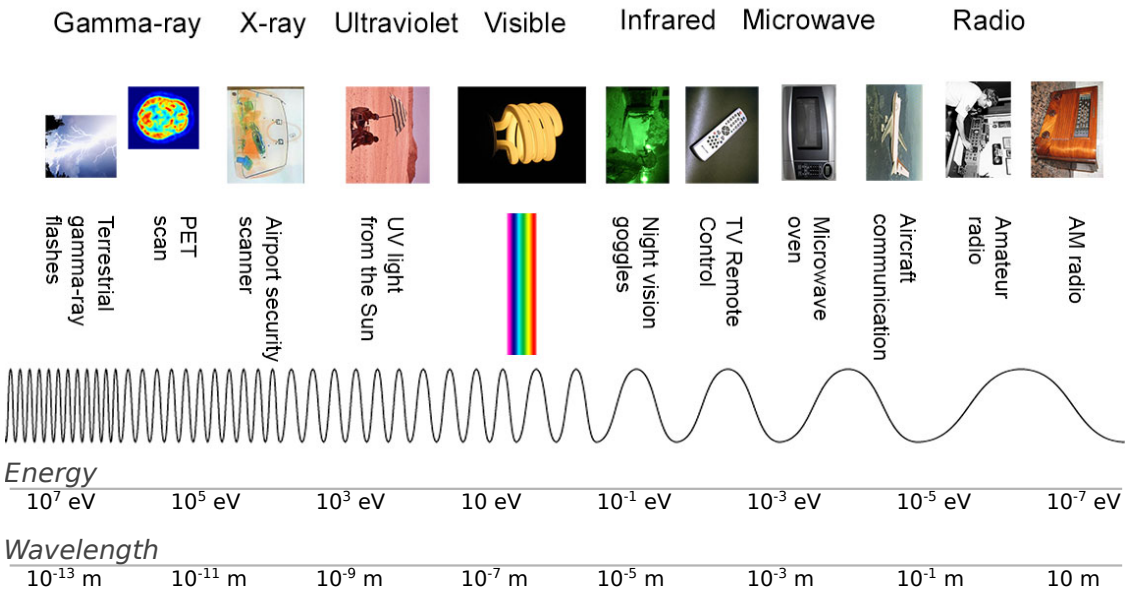

Figure 1.2: The electromagnetic spectrum (adapted from NASA's Imagine the Universe [9]).

use semiconductor technology to absorb or emit visible light and create, for example, LEDs, lasers, microscopes, and cameras. There are many electronic or vibrational transitions which can take place under light within this energy region, particularly in biological materials, making visible light a natural choice for imaging and studying the world around us.

At even higher frequencies, ultraviolet light has a high enough energy to damage organic molecules. Ultraviolet (UV) light excites higher energy transitions in organic molecules or insulating materials and can be used to study these materials. The short wavelength of UV light allows us to use it for nanoscale photolithography methods. Beyond UV lie the x-ray and gamma ray spectral regimes, which are used for medical imaging, security, and for materials characterization methods using the diffraction or absorption of light. We also use this regime to reach beyond our planet to study the far reaches of the universe.

For imaging, the wavelength of light is an important parameter. The smallest distinguishable feature is determined by the diffraction limit of light, which is approximately the wavelength of light which is being used to look at the feature: visible light, perhaps the most natural candidate for imaging, is limited to features on the order of hundreds of nanometers. Continued development in the manipulation of light is focused on the ability to shrink the energy contained in light to much smaller scales, beating the diffraction limit for denser packing of information-carrying conduits or for the ability to use light to see and manipulate ever smaller objects [10–12]. This field is generically known as nanophotonics.

1.2 Nanophotonics

Nanophotonics covers the field of manipulating light below the diffraction limit and the study of light's interactions with sub-wavelength objects, including efforts to beat the resolution limit of light and to study the behaviour of light on the nanoscale [12]. Applications in this area include optoelectronics, the combining of optical signals with electronic signals, which are generally on the micro- to nanoscale [13]; sub-wavelength imaging [14]; optimization of light capture and conversion in the solar cell industry [15]; enhancement of spectroscopic signal, such as surface-enhanced Raman spectroscopy, where sub-wavelength field enhancements boost the response signal of small amounts of analytes [16–19]; and manipulation of the optical properties of materials to achieve unique cloaking or superlens behaviour [20].

To achieve these goals, researchers have turned to near-field optics, making use of evanescent fields which often accompany the emission or absorption of far-field radiation, but extend only a limited distance from the emitter (Figure 1.3) [11]. Near-field optics are used in scanning probe microscopy, which can achieve a spatial resolution down to tens of nanometers [14]. A major player in the creation of evanescent waves is the surface plasmon (SP), an evanescent EM wave propagating along metal or metal-like surfaces. SPs are able to concentrate EM energy into a much smaller space than the diffraction limit of light otherwise allows [10].

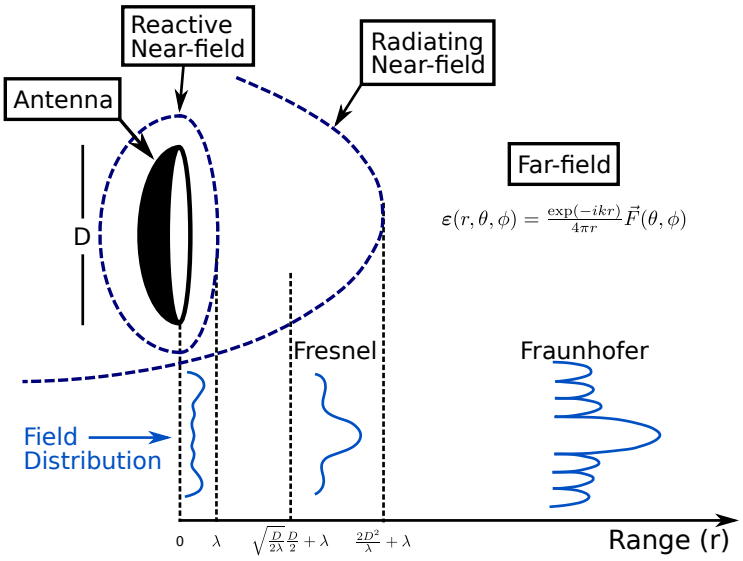

Figure 1.3: Field distributions in the near-field and far-field regions of a radiating antenna. Adapted from [21] (©1995 IEEE).

1.3 Plasmonics

One of the earliest and most well-known examples of the use of plasmonic nanoparticles to manipulate light is the Lycurgus cup from the 4th century CE, in ancient Rome [22]. The cup has the unique optical property of appearing green under reflected light and red under transmitted light, which has been linked to the presence of minute traces of colloidal gold-silver alloy nanoparticles within the glass [23]. An empirical understanding that coating glass with metallic paint and then annealing it at high temperatures in the right chemical environment creates different colours, depending on the metal composition and annealing parameters, led to the use of colloidal gold, silver, and copper nanoparticles in stained glass windows for wealthy churches [24,25].

Despite their long use for decorative glassware, a physical understanding of the phenomenon which caused these interesting optical properties only began in the 19th and 20th centuries. In the mid-19th century, Faraday observed a bright red colour produced by a solution of gold particles [26], and in the early 1900s, Wood and Rayleigh observed strong optical phenomena on metallized diffraction gratings [27,28]. Academic studies continued sporadically on these strange optical phenomena [29–31], and picked up pace in the 1950s when the theory of collective oscillations of the electron gas was developed in parallel with experimental evidence found using electron energy loss spectroscopy in a transmission electron microscope [32–39]. The description of these collective oscillations of the electron gas, or electron plasma, as a quasiparticle, combined with the tendency of physicists to add the suffix '-on' to define new particles led to the word 'plasmon' being used to describe this quasiparticle [35, 40]. Although it is possible to study surface plasmons using optical methods, the early work in electron microscopes and the unmatched spatial resolution in the electron microscope have made it a favourite for discovering new behaviour of the surface plasmon.

Since the original observations of plasmons in the 1950s, electron microscopy has advanced greatly, and now boasts spatial resolution below 1 Å and energy resolution below 10 meV [41, 42]. The development of monochromators and focused scanning electron probes has allowed the study of plasmons in many different materials. The plasmon exists both within the volume of a material, where it is a longitudinal oscillation known as the bulk plasmon (BP), and on interfaces, where it is a transverse oscillation know as the surface plasmon. The BP suffers heavy losses due to scattering within the material and has a short lifetime and short propagation distance. The energy of the BP is dependent on the density of free electrons within a material and is usually within the range of a few eV for metals to a few tens of eV for insulators.

The SP, on the other hand, has a longer lifetime and propagation distance, and, given the right experimental conditions, can interact with external light. To support an SP, there must be free electrons on one side of the interface. Most commonly, the interface consists of a metal on one side, which has a negative dielectric function in the frequency region that supports plasmons, and a dielectric material or air on the other

side, with a positive dielectric function at the same frequency. Mathematically, the SP is a wave which exists at a pole in Maxwell's equations, where an oscillating function can be used to describe the EM response of matter. The SP energy is typically below 10 eV and responses related to SPs are typically found in the IR to UV range of the spectrum (0.1 eV to 7 eV), depending on the material and structural parameters.

Aluminium was an early candidate for surface plasmon studies in the electron microscope [43] because of its high surface plasmon frequency, and thereby more spectroscopically accessible energy, which did not require high energy resolution to detect. As technology advanced and monochromation improved the energy resolution of electron energy loss spectroscopy, the detectable energy range was reduced to below 1 eV [44], and lower energy plasmon excitations can be detected in, for example, gold and silver. More detail on SPs and the use of electron microscopes to study them can be found in Chapter 2.

Much of what makes plasmonics an interesting field comes from the similarity of plasmonic devices to macroscale radio antennas, scaled down to the nanoscale and interacting with IR, visible, and UV light [45]. These spectral regimes are much more relevant to our sense of vision and to vibrational and electronic properties of matter. The ability to absorb and emit light and to concentrate EM energy into a length scale relevant to the nano-world brings many interesting applications and opportunities for plasmonic devices as we learn to manipulate and understand the world below our sight.

1.3.1 Applications

Applications of plasmonic structures come from their ability to concentrate EM energy into very small regions well below the diffraction limit, and to interact with light in interesting and unique ways, including dying glass red. Applications beyond decorative glassware are beginning to appear in the commercial domain, including the fabrication of biosensors, enhancement of spectroscopic signals, manipulation of the optical properties of materials through the creation of metamaterials, and as carriers of information in nano-electronic circuits. Both the propagating surface plasmon, the surface plasmon polariton (SPP); and the localized surface plasmon resonance (LSPR), a standing wave confined within a nanostructure, find uses in different fields.

Sensors

The SP is sensitive to the local environment; if the local environment changes by, for instance, binding an analyte such as a biomolecular marker to the surface, the properties of the SP will change [46]. This provides a spectroscopic signature which can be used to detect the presence of the analyte with high sensitivity. The concentrated electric field accompanying the plasmon is also capable of enhancing spectroscopic signals, as is done in surface-enhanced Raman spectroscopy (SERS) [47]. The SP boosts the Raman signal of molecules within its electric field, thereby improving the

detection limit and increasing the sensitivity of the test [46,48]. The high electric field around a plasmonic nanoparticle polarizes the organic molecule, and when two plasmonic nanoparticles are in close proximity, the coupling of the EM fields can enhance the spectroscopic signal by a factor of over 10^4 [47,48], which allows the use of smaller sample sizes and improves early detection of, for example, low concentrations of disease markers or pregnancy hormones. Currently, the field of biosensors and enhanced spectroscopies may be one of the biggest commercial applications of the SP [49,50].

The enhancement of Raman signal that the SP provides is also beneficial in detecting very small concentrations of analytes, or even studying single molecules [19,51], and SERS is found in many labs, both industrial and academic, around the world. There are many labs working towards building better SERS platforms; studying plasmon modes and their behaviour in different geometries provides the toolkit for intelligent design of sensing platforms. Particularly, the high spatial resolution and detection capabilities of electron energy loss spectroscopy performed in an electron microscope is highly advantageous when engineering new plasmonic structures. Of all the myriad different structures which can be used for biosensing, fractal structures offer multi-band and multi-scale responses, with localized hotspots on different length scales at different energies according to the construction parameters of the fractal. Chapter 3 contains a study of the surface plasmon resonance behaviour in Sierpiński fractal nanostructures.

Metamaterials

Metamaterials are materials which are artificially structured to have properties which would be difficult or impossible to find in natural materials. Radio and IR metamaterials are constructed using sub-wavelength metamolecules shaped specifically to produce different optical properties in the metamaterial, such as a negative refractive index, through the introduction of artificial magnetic dipoles or other EM multipole moments. The possibility to arbitrarily manipulate optical properties brings with it the hope for a superlens, in which near-field components are projected into the far-field in order to image objects below the diffraction limit [11,52], and for invisibility cloaking devices, such as used for military stealth applications [53].

The split ring resonator (SRR) is a popular candidate for metamaterials because of its ability to support an induced magnetic dipole moment under resonance conditions [54,55], granting the metamaterial a negative refractive index. Using the SRR, an invisibility cloak in the microwave regime of the spectrum has been demonstrated [56]. Reducing the wavelength at which the metamaterial is active requires that the metamolecules be likewise scaled down in size.

The ability of plasmonic nanostructures to act as miniaturized optical components with strong electric and magnetic responses [12] means that metamaterial design in the IR, visible, or UV regimes is turning to plasmonic devices for their construction. Plasmonic nanoantennas provide a way to engineer different combinations of EM multipole moments for use in metamaterials. Chapter 4 presents a study of the

plasmonic response of vertically oriented split ring resonators (VSRR) in the IR and visible regions of the spectrum. The VSRR is also used to construct more exotic multipole moments, such as the toroidal dipole moment, in Chapter 5.

Nanoelectronics

Photonic circuits are fast and in common usage to transfer information over long distances at the speed of light, but cannot be scaled down below the micrometer scale without encountering the diffraction limit of the photons used to carry information. Electronic circuits, on the other hand, can be scaled down to the nanoscale, to the limit of quantum tunnelling and thermal fluctuations [57], but as the size of circuit components is decreased and the packing density is increased, information transfer is limited by the speed of electrons in increasingly resistive wires, and challenges in heat dissipation.

Plasmonic circuits offer an intermediate solution to these problems; plasmonic signals travel at a significant portion of the speed of light and components can be scaled down much further than is possible in photonic circuits, to enable denser packing of components on a chip [13]. Plasmonic circuits are suggested as an intermediate solution to transfer information from microscale photonic circuits across chips or between chips to nanoscale electronic circuits, or as a way to increase the information density of optical circuits by using smaller components packed more closely together without the problems encountered in nanoscale electronic circuits [12].

Currently plasmonic circuits have not yet made it into large scale commercial production due to a design trade-off between achieving small field confinement, which determines the size and spacing of circuit components on a chip, and the propagation distance of the plasmon, which determines the distance information can be carried before it is lost. However, plasmonic components may find their niche in intra- or inter-chip connections, carrying signal between different electronic components at a faster speed, with less heat generation, than is achievable with electronic interconnects, and taking up less space than the equivalent photonic interconnects would require. One solution to enhancing the distance that a plasmon can travel between electronic components uses concepts from fibre optic technology; that of regularly spaced signal enhancers to amplify signal before it decays, thereby extending its propagation distance. This is used in fibre optic technology to, for instance, transmit internet signals across the oceans, and can be applied to boost plasmonic signals and extend their reach across an electronic chip when combined with a gain medium and an energy source. It has been suggested that the toroidal dipole moment, presented in Chapter 5, would prove to be a good candidate for such an application [58].

1.4 Layout of the thesis

The field of plasmonics is beginning to emerge on the commercial stage, but much remains to be learned in order to fully exploit this phenomena and fulfill the potential of this branch of science. In this thesis, I use high resolution electron beam spectromicroscopy techniques and electromagnetic simulations to study the EM multipole moments that can be produced by using different nanostructure geometries. Specifically, I use electron energy loss spectroscopy in a transmission electron microscope to study the near-field localization of surface plasmon modes, and cathodoluminescence in a scanning electron microscope to study the far-field emission properties of the surface plasmon resonances.

The thesis contains the following chapters, presented graphically in Figure 1.4. Chapter 2 is an overview of the theoretical background and experimental and analytical methods used to acquire and understand the data presented in this thesis. Presentation of experimental results begins in Chapter 3, with a discussion of the interaction of complicated combinations of dipoles within the first three generations of the Sierpiński fractal structure. In Chapter 4, the near-field electric field localization and the far-field emission properties of the vertical split ring resonator are presented. Chapter 5 expands these results by using the VSRR to construct more complex structures capable of producing the toroidal dipole moment. Data processing should be considered to be an equally important part of the experiment as the acquisition of data, and in Chapter 6, the custom Python code written over the course of this thesis work is presented. The final chapter, Chapter 7, presents a general summary and conclusion of the thesis work, and as well as some interesting questions which arose over the course of the thesis, for future pursuit of knowledge.

Appendix A contains more background on the concept of plasmonic devices as nanoantennas, the calculated emission properties of electric and magnetic dipoles, and simulations of the emission from simple plasmonic devices. Appendix B contains a description of the microscope hardware to supplement the information contained in Chapter 2, with a particular focus on the monochromated scanning transmission electron microscope. Additional calculations on the electric and magnetic field distributions of the LSPR modes in the Sierpiński fractal can be found in Appendix C. Appendix D contains copies of the copyright permissions for the reproduction of some of the published work presented in this thesis.

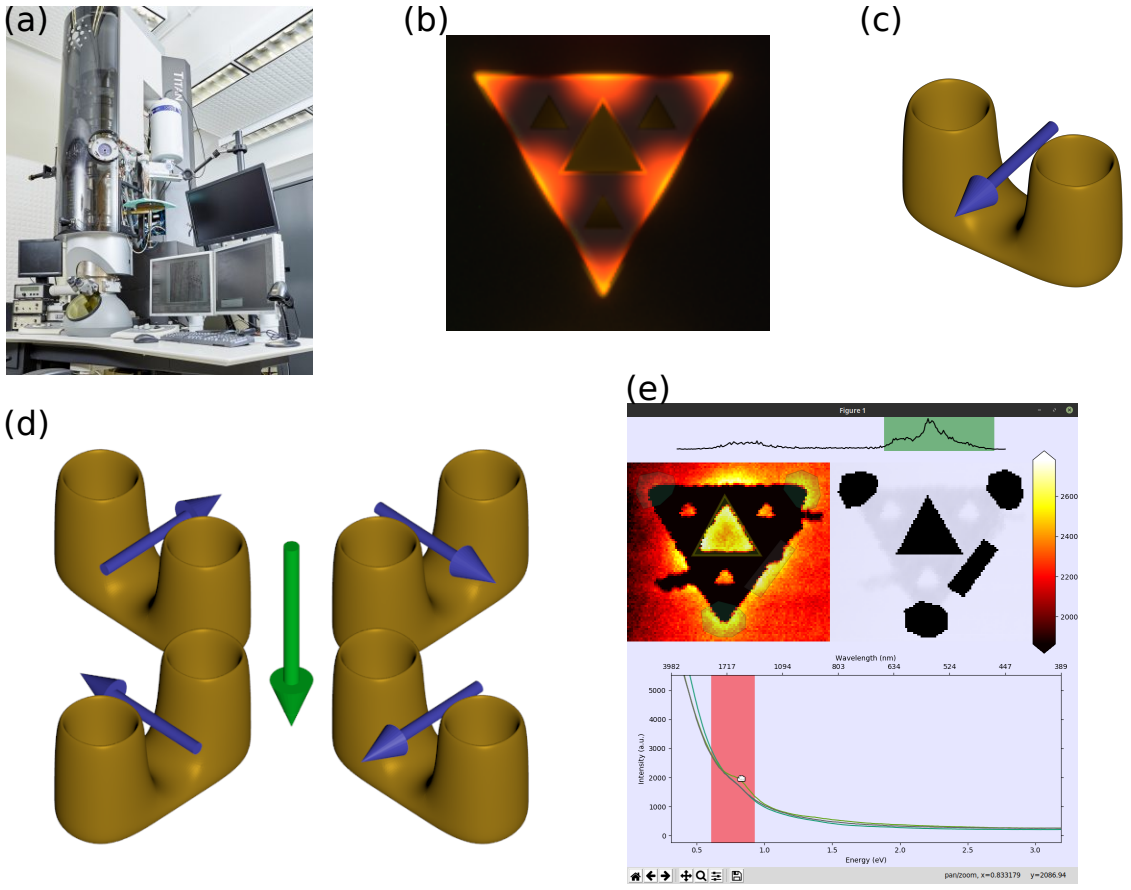

Figure 1.4: Graphical summary of the thesis. (a) Chapter 2: Background and Methods (Image: [59]); (b) Chapter 3: Sierpiński Fractals; (c) Chapter 4: Split Ring Resonators; (d) Chapter 5: Toroidal Array; (e) Chapter 6: Data Analysis with SIAn.

Chapter 2

Background and Methods

This chapter contains background on surface plasmons and the techniques used in this thesis to fabricate, characterize, and analyze localized surface plasmon resonances (LSPR) in metallic nanostructures. Specific details of the simulations, fabrication, and experimental conditions are given towards the end of the chapter (Section 2.8). The samples studied include planar structures (Chapter 3: Sierpiński fractals) and three-dimensional (3D) nanostructures (Chapter 4: vertical split ring resonators (VSRR) and Chapter 5: a toroidal array of four VSRRs, 'T4').

Samples were fabricated using electron beam lithography (EBL), then characterized with a combination of electron energy loss spectroscopy (EELS) in a scanning transmission electron microscope (STEM) and cathodoluminescence (CL) in a scanning electron microscope (SEM). Data processing of EELS data relies heavily on the Richardson-Lucy deconvolution (RLD) algorithm implemented in custom Python code, which itself is described in Chapter 6. Modelling of the LSPR discussed in this thesis was performed in part by collaborators and in part by me, and a brief overview of the modelling techniques used will be given here.

2.1 Optical Response of Metallic Nanoparticles

The ability of a nanostructure to support an LSPR depends on the material that it is made of, specifically on the dielectric function of the material. The focus of this thesis is not on the properties of the material, but on how the geometry of the nanostructure affects the LSPR behaviour. As such, the materials chosen are those which support plasmon resonances and are relatively easy to work with.

2.1.1 Dielectric Function

The property that determines how electromagnetic (EM) radiation (specifically the electric component) interacts with a material is the dielectric function, or permittivity. The material's response to applied magnetic fields is described by its magnetic

permeability, relative to vacuum. For most materials, barring magnetic materials, and for all the materials considered in this thesis, the relative permeability is one ($\mu = 1$) and does not have a significant effect on the interaction of the material with the EM fields of light. The dielectric function ($\epsilon(\omega)$), a function of frequency, is closely linked to the more commonly known refractive index (Equation 2.1, in which $\tilde{n} = n + i\kappa$ makes up the complex refractive index, with the real part n and the imaginary part or extinction coefficient κ).

$$\epsilon = \epsilon_1 + i\epsilon_2 \tag{2.1a}$$
$$\epsilon_1 = (n^2 - \kappa^2)/\mu \tag{2.1b}$$
$$\epsilon_2 = 2n\kappa/\mu \tag{2.1c}$$

The dielectric function is a complex function, with real (ϵ_1) and imaginary (ϵ_2) components. The real component is correlated with the polarizability of the medium, while the imaginary component represents the damping or losses of the electric field inside the material. A peak in the imaginary component of the dielectric function is associated with an absorption band in the material. Permanent dipoles within the material respond to microwave frequencies. At higher frequencies in the IR, the response of atomic nuclei dominates, taking the form of vibrational responses such as phonons [60]. As the frequency is increased beyond the IR, the electric field is oscillating too fast for the heavy nuclei to respond and the phonon response decays.

Instead, in the near-IR to UV regimes, the dielectric function is often dominated by the electronic response [60, 61]. The electron response comes from inter- or intra-band transitions through excitation of valence electrons or, at higher energies, core shell electrons to higher energy empty states. A given transition may have a resonant response, which appears as a pole in the dielectric function and a peak in the imaginary component (see Figure 2.1(a)). The full dielectric function is a tensor property which can possess different values along different crystal axes in response to longitudinal or transverse waves, but with cubic or isotropic materials it is simplified to a single value [61, 62]. In this context, longitudinal waves are EM waves in which the electric field vectors are parallel to the wavevector and are decoupled from the magnetic field vectors. Transverse waves, such as photons, have coupled electric and magnetic field vectors which are perpendicular to the wavevector. Longitudinal waves are produced by charge density and will induce longitudinal current; transverse waves are produced by current density and induce transverse current [61].

Classical models used to describe the dielectric function are the Drude model and the Lorentz model (Figure 2.1). The Lorentz model applies best to electrons which are bound to the atomic nuclei of the material. It treats the system as a set of springs with a small mass electron attached to a larger mass nucleus by a spring, and includes a damping term, a restorative force between the electron and nucleus, and the driving force of an applied electric field [60]. It is used, for example, to model interband transitions [60].

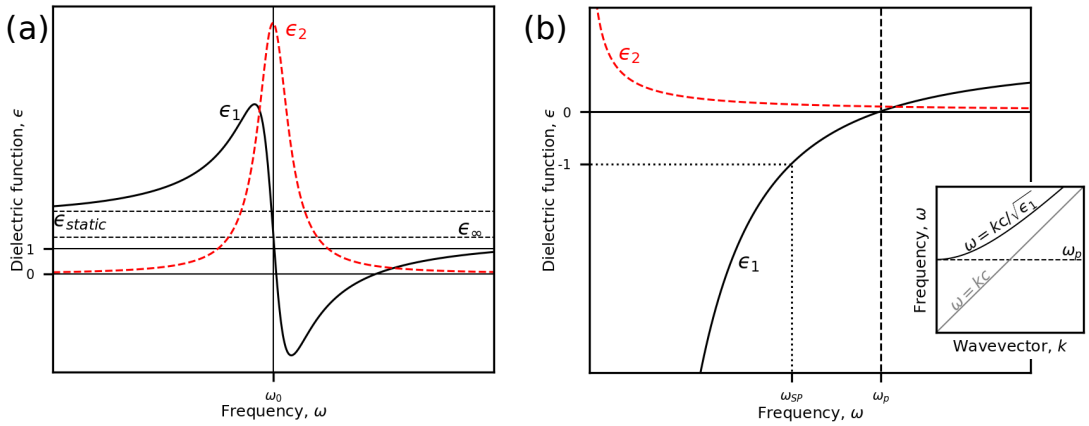

Figure 2.1: Classical models of the complex dielectric function. (a) Lorentz model with a resonance at ω_0; (b) Drude model with the plasma frequency (ω_P) and surface plasmon frequency (ω_{SP}) indicated, inset shows the dispersion relation for free space (gray) and for a Drude metal with negligible damping (black).

The Drude model is similar, but best describes free electrons which are not bound to nuclei, so does not have a restoring force, only a damping term from Ohmic scattering of free electrons in the metal [60]. The Drude model, given in Equation 2.2, is typically used to model free-electron metals [60]. In this equation, ω_P is the plasma frequency of the material and γ is the damping factor.

$$\epsilon = 1 - \frac{{\omega_P}^2}{\omega^2 + \gamma^2} + i\frac{{\omega_P}^2\gamma}{\omega({\omega_P}^2 + \gamma^2)} \tag{2.2}$$

Below the plasma frequency, the reflectivity of an ideal Drude metal is almost perfectly 1 and the propagation of longitudinal or transverse EM waves inside the medium is mathematically forbidden [60]. However, in the early 1900s, it was found that creating grating structures on the surfaces of such metals causes anomalous reflection and absorption of light [27,31] which could not be explained for many years and became known as 'Wood's anomalies'. Later these anomalies were linked to the excitation of surface waves dependent on the grating geometry and the metal it was made of [63–65].

At the plasma frequency ($\epsilon(\omega_P) = 0$) longitudinal waves can propagate in the material [60,66]. When free electrons in an undamped Drude metal are subjected to an electric field at the plasma frequency, they are pushed in one direction, creating an electric restoring force in the opposite direction between free electrons and positive ion cores, to which they respond, oscillating back in the other direction. At ω_P, this oscillation has a wavelength which tends towards infinity (wavevector, $k \to 0$, inset in Figure 2.1(b)), meaning that all free electrons participating in the oscillation are in phase with each other [60,67]. This longitudinal wave is the bulk plasmon: collective quantized longitudinal oscillations of free or nearly-free electrons within the bulk of a

material, possessing a quantized unit of energy [40,66], for which Coulomb interactions between electrons dominate over single electron behaviour [40]. When damping is high in a more realistic material, the bulk plasmon is identified by a peak in the electron energy loss function ($\mathrm{Im}(1/\epsilon)$) where both ϵ_1 and ϵ_2 are small [68]. Since the bulk plasmon is longitudinal, it cannot couple to the transverse EM waves of photons and can only be excited by, for example, a beam of swift electrons. In low-loss EELS, the bulk plasmon peak is used as an indicator of the electronic structure of the valence and conduction bands of the material, but otherwise the bulk plasmon is subject to high damping and short propagation distances and its applications are limited.

At higher frequencies, there are more quantized longitudinal oscillations with finite wavevectors (Figure 2.1(b) inset, dark line) [67]. Transverse waves may also propagate through the medium, so above the plasma frequency, an ideal Drude metal is transparent [60, 67]. However, interband transitions within a realistic material may contribute to absorption of the propagating transverse wave.

Below the bulk plasmon frequency, conductive materials support surface plasmon waves along interfaces with dielectric materials.

2.1.2 Surface Plasmons

The surface plasmon (SP) is a collective oscillation of the electron 'plasma', which is confined to an interface [69]. Unlike the bulk plasmon, the SP is a transverse oscillation with an electric field vector that is perpendicular to the direction of propagation and normal to the interface [70, 71]. Without special excitation conditions, such as the presence of a grating on the surface, SPs cannot be excited by incident light due to a lack of momentum conservation [70–72].

For the surface plasmon to exist, the sum of the real parts of the dielectric functions of the materials on either side of the interface (materials A and B) must be less than 0 ($\mathrm{Re}(\epsilon_A) + \mathrm{Re}(\epsilon_B) < 0$), and the real part of the dielectric function should change sign across the interface ($\mathrm{Re}(\epsilon_A)\,\mathrm{Re}(\epsilon_B) < 0$) [71]. These conditions define a maximum SP frequency (ω_{SP}) in a Drude metal when the sum of the real parts of the dielectric function is equal to 0 [71]. In a common metal/air interface, the real part of the dielectric function of the metal is equal to -1 at ω_{SP} (Figure 2.1(b)). The real part of the dielectric function of the metal must also be larger in magnitude than the imaginary part of the metal dielectric function for the surface plasmon to exist, otherwise the attenuation is high and the SP cannot propagate [71].

Many of the properties of the plasmon response can be understood by looking at its dispersion relation (Equation 2.3, Figure 2.2(a)) [71]. The dispersion relation describes how the frequency (ω) of a wave is related to its wavevector (k) and wavelength (through $k = 2\pi/\lambda$). The simplest dispersion relation is that of light in a medium with a constant dielectric function, such as air. The dispersion relation of photons in air increases linearly with the wavevector, with the slope giving the speed of light in the medium (Figure 2.2(a), gray line). Assuming the dielectric function of the metal

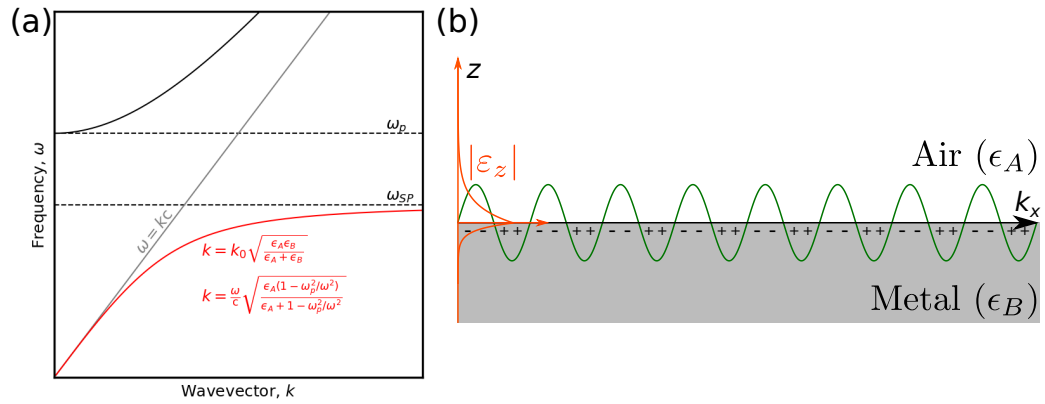

Figure 2.2: Surface plasmon dispersion curve for an ideal Drude metal and air interface (red). The dispersion relation of light in air is shown by the gray line. Bulk plasmon (ω_{P}) and surface plasmon frequencies (ω_{SP}) are shown by dotted lines; (b) schematic of the propagating surface plasmon polariton on an air/metal interface, orange indicates the evanescent decay of ε_z.

is described by the Drude model and its damping is small, the dispersion relation of the surface plasmon polariton (SPP) is shown by the red curve in Figure 2.2(a), in which k_0 is the free-space wavevector at a given frequency and the other variables are as defined in Figure 2.2(b).

$$k_x = k_0 \sqrt{\frac{\epsilon_A \epsilon_B}{\epsilon_A + \epsilon_B}} \tag{2.3}$$

The SPP is an oscillating EM wave tightly bound to the interface, with a larger wavevector than light of an equivalent frequency [70], directed along the interface (Figure 2.2(b)) [71]. It is a propagating transverse surface wave created by collective oscillations of conduction electrons in the metal and is characterized by evanescent fields normal to the interface, decaying exponentially into the media on either side [70, 71]. A surface plasmon is classified as a surface plasmon polariton when retardation effects are important and the bound wave exchanges energy between collective electron motion and propagating EM fields [69].

The SPP possesses electric fields which are both transverse to the wavevector and parallel to the direction of the wavevector, but is considered a transverse wave because the divergence of its electric field is 0 ($\nabla \cdot \boldsymbol{\varepsilon} = 0$) [69]. The lifetime of the SPP is finite, primarily due to energy losses occurring within the metal and associated with the electron motion. The SPP may undergo radiative decay, if conditions for momentum matching with radiation are present; Landau damping, in which the collective oscillation decays by exciting electron hole pairs; or other scattering mechanisms off the lattice or other electrons [69].

As the SPP frequency approaches ω_{SP}, its wavevector goes to infinity and its group velocity asymptotically goes to zero (Figure 2.2(a)) [70]. The evanescent field is proportional to $\exp\{-kz\}$, so with increasing wavevector, the confinement of the fields

is stronger and more energy is bound closer to the metal surface [67], with a higher proportion of the SP energy in the kinetic energy of the oscillating electrons [70, 71]. This also means that the SPP decay is faster and its propagation length shorter as the wavevector increases [70, 71]. Highly localized SPPs occur only near the surface plasmon frequency, usually in the near-IR to UV range of the spectrum [70, 73]. The oscillation at large wavevector begins to take on more of a longitudinal, electrostatic character in the non-retarded regime and, in the limit approaching ω_{SP}, it becomes the surface plasmon, which has a very large momentum and wavevector [67, 69].

At the other end of the dispersion curve, as the wavevector and frequency both decrease and approach zero and the wavelength of the SPP approaches infinity, the wavevector and velocity of the SPP become very close to that of light in free space [70, 71]. The SPP behaves less like oscillating electron density and takes on more characteristics similar to those of a photon at grazing incidence travelling along and bound to the surface [70, 71]. More of the SPP's energy is in the external fields, which are less confined and may extend several wavelengths into the dielectric medium [70, 71]. As this happens and the strong sub-wavelength field confinement associated with the SPP is lost, classification of the wave changes and it is called a Sommerfeld-Zenneck wave [67]. At low frequencies, the metal behaves more like a perfect conductor than as a medium for oscillating plasma; to maintain the field confinement, artificial surface structures can be engineered to create spoof SPPs [70].

The SPP dispersion curve is to the right of the light line, implying that for the same energy, the SPP has a higher momentum and cannot couple to light without a means of compensating the momentum mismatch [70]. Examples of coupling schemes used include prism coupling through the evanescent fields created by frustrated total internal reflection [74, 75] or the use of a grating or surface roughness to supply the difference in momentum and allow excitation of an SPP [72, 76]. This momentum mismatch does not hold for excitation by fast electrons, which can otherwise be considered as broadband white-light sources [69].

In real metals, the SPP wavevector is complex, so the SPP decays from free-electron scattering or interband transitions as it propagates. When damping is included, the SPPs approach a finite wavevector at the surface plasmon frequency, instead of the idealized asymptotic approach to ω_{SP}, limiting the shortest possible SPP wavelength and the amount of confinement possible [67].

The SPP is a propagating wave, and if the propagation length is long enough, the SPP can be used for carrying information in a plasmonic waveguide.

2.1.3 Localized Surface Plasmon Resonance

Another way of solving the momentum mismatch between surface plasmons and light is to use a sub-wavelength nanoparticle to provide the difference in momentum. The LSPR is a non-propagating surface plasmon trapped in a nanoparticle (Figure 2.3). LSPRs are collective oscillations of surface charges that form various orders of standing

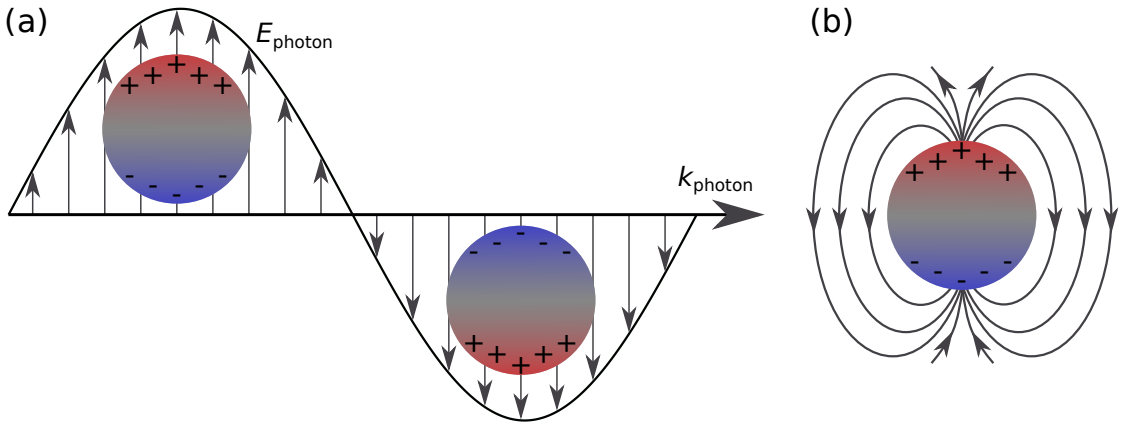

Figure 2.3: Localized surface plasmon resonance of a spherical nanoparticle under photon excitation. (a) Movement of surface charges under photon excitation; (b) electric field of the LSPR dipolar response.

wave patterns, according to the geometry of the nanoparticle, and provide resonant local enhancement of EM fields below the diffraction limit of the equivalent photon energy. It is the LSPR which gives gold and silver nanoparticles their striking, intense colours, such as those of the Lycurgus Cup [23] or in stained glass windows [25,77]. The response of plasmonic nanoparticles is broken up into discrete resonances corresponding to different standing wave patterns across the nanoparticle surface. The factors affecting the nature of the LSPR in plasmonic nanoparticles include the nanoparticle material and environment, and the specific size and shape of the nanoparticle.

This dependence on geometry opens up a wealth of research opportunities to explore two- and three-dimensional nanostructures. The geometry determines the charge distributions and locations of hotspots, or localized field enhancements, and the use of geometry to manipulate LSPR behaviour is currently a very active research field. Plasmonic nanoparticles can also act as nanoscale antennas, similarly to radio antennas, but interacting with light in the IR, visible, or UV regions of the EM spectrum through radiative damping [69].

With the ability to manipulate the geometry, there is a lot of freedom to engineer specific charge-current configurations that are required to create different multipole moments, some of which cannot be found or are difficult to find in nature. The classic example is an electric dipolar mode, in which opposite charges are concentrated at opposite ends of a nanostructure, but there also exist quadrupolar and higher order multipole modes [78, 79]. This thesis is concerned with the behaviour of LSPR in engineered nanostructures and their use in artificially creating EM multipole moments.

Plasmon Coupling

If two plasmon-sustaining surfaces are brought close enough together, the SPs couple to each other. In general, spectral and spatial overlap of the fields of the SP is required

for coupling [80]. Coupling across a thin metal film occurs when the film is thinner than the penetration depth of the electric fields of one SPP in the metal. Then the SPP fields extend through the metal thickness to interfere with the electric fields of the wave on the other surface [38, 81], splitting the resonance into two modes of different energy with different dispersion relations [35, 82].

On the lower energy mode, the two surface waves are π out of phase with each other and the charge distributions are anti-symmetric; on the higher energy mode, the charge distributions are symmetric and the SPP waves are in phase with each other. The anti-symmetric mode produces a dipole moment normal to the plane of the thin film and can radiate into free space [81]. The symmetric mode can propagate long distances, since it excludes electric fields from the metal [69], making this mode a good candidate for long range SPP waveguides.

A similar phenomenon happens when two or more nanoparticles are brought close enough together such that the EM fields of their LSPR modes interfere with each other. The distance they must be from each other to achieve coupling varies depending on the wavevector of the plasmon mode, which determines the field confinement and how far the evanescent fields extend into vacuum. Coupling between nanoparticles causes peak splitting and spectral shifts, as well as changes in the spatial distribution of the field intensity [43, 83].

For example, on a pair of identical nanospheres, the dipolar mode is split into two modes at a lower and higher energy than the original dipolar mode [83]. Analogously to molecular orbital hybridization theory, these two modes are known as bonding and anti-bonding modes and have anti-symmetrical and symmetrical charge configurations [47, 84, 85]. Depending on the symmetry of the nanoparticles, bonding and anti-bonding modes may be formed along the longitudinal axis of the dimer or along the transverse axis, giving a total of four possible hybridization combinations of two dipolar modes (Figure 2.4).

When the two dipoles are oscillating in phase with each other along the long axis of the dimer, there is a net dipole moment with a strong optical signal and the mode is classified as the longitudinal bonding (LB) mode [85]. In the longitudinal anti-bonding (LAB) mode, the dipole moments on each of the particles move in anti-phase and if the dipole moments are identical, there is no net dipole moment [85]. If retardation does not play a significant role, the LAB mode is a dark mode [85]. Retardation occurs when the size of the particles are comparable to the wavelength of light and accounts for the finite time that it takes EM radiation to propagate across the particle, such that at an instant in time one side of the particle may feel a different field from the other side [86]. Retardation effects can cause normally dark modes to become radiative [87–89] or cause redshifts to the LSPR energy relative to the assumptions of the non-retarded approximation [69].

When the dipole moments in the particles are oriented perpendicularly to the long axis of the dimer, the anti-bonding mode is a higher energy symmetric mode with both dipoles oscillating in phase, while the bonding mode has anti-symmetric

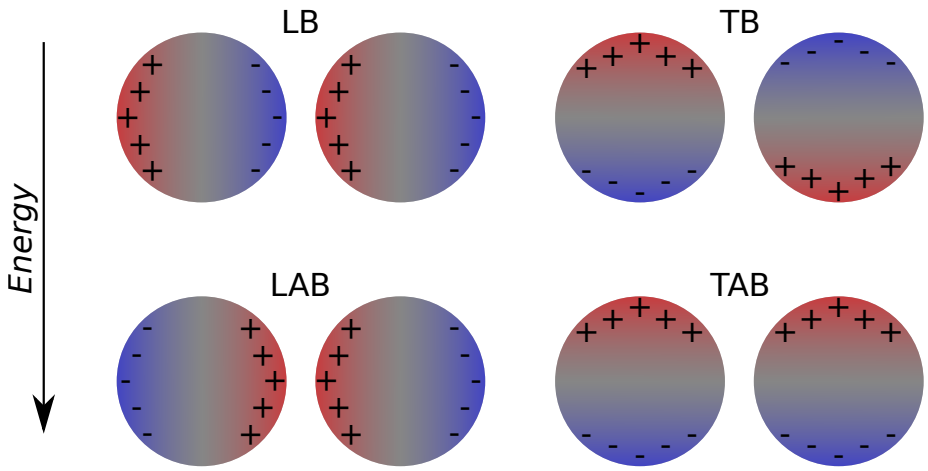

Figure 2.4: Charge configurations for the coupled dipolar modes on a pair of plasmonic nanospheres: longitudinal bonding (LB); longitudinal anti-bonding (LAB); transverse bonding (TB); and transverse anti-bonding (TAB) modes.

dipole moments and a lower energy [85]; these are transverse anti-bonding (TAB) and transverse bonding modes (TB), respectively. As the nanoparticles are brought closer together, the interaction strength and energy splitting between modes increases. The symmetric plasmon redshifts faster than the anti-symmetric mode blueshifts, producing overall a lower energy response than the individual particle [85]. The same concepts of bonding and anti-bonding modes from coupling of electric fields also apply to EM modes in dielectric or semiconductor nanoparticles [90].

Coupled dimers show a much stronger local field enhancement in the void between nanoparticles than a single nanoparticle [47, 48], allowing even single molecule detection in SERS [19]. In a nanosphere dimer, coupling enhances the EM fields of incident laser light by a factor which can be over 10^4, much larger than the simple sum of the fields from each individual sphere [47, 48]. The enhancement between nanoparticles is higher at the low frequency LB mode [48].

When the two nanoparticles are brought into conductive contact with each other, there is an abrupt blueshift in the energy of the primary plasmon modes, changing the phenomenon from plasmon coupling to charge transfer plasmons [91–96]. Since surface charge is able to flow freely, a dipolar mode over the whole structure can be formed. As the junction width is increased, the dipolar peaks blueshift and Wen *et al.* found a relationship between the junction conductance and the energy of the primary dipolar mode in a connected nanoparticle dimer structure [92].

Coupling and hybridization phenomena are important to the work done in this thesis. In Chapter 3, the modes of triangular cavities couple to the modes of the triangular prisms in which they are embedded; in Chapter 4, dipolar modes within substructure features of a VSRR couple to form LB, LAB, TB, and TAB modes; and in Chapter 5, coupling between separate VSRRs creates an LSPR mode with a

toroidal dipole moment.

2.2 Plasmonic Nanoantennas

A structure which either transmits or receives EM waves is considered an antenna [97, 98]. Antennas are commonly used to send and receive signals in the radio and microwave regimes of the EM spectrum and they find application in many parts of modern everyday life [97]. To produce an EM field, either a charge density or current density can be used [86]. For the EM field to be radiative, the charge or current density must vary in time: there must be accelerating charges [97, 99]. In radio and plasmonic antennas the charges are the conduction electrons, which behave as nearly-free charges within the structure and respond to applied EM fields. Intuitively, applying an oscillating EM field to a collection of free charges causes these charges to move in an equally oscillatory manner in response. Applying an oscillating EM field to a radio antenna produces alternating current which is then fed to a read-out circuit, demonstrating the concept of a receiving antenna. Likewise, if an alternating current is used to drive an antenna, the oscillating free charges radiate energy into free space according to the periodicity of the applied current. Modulating the applied current in a known pattern allows the user to transmit signals, receive them on another antenna, and decode the original signal [97].

Although the frequency range and applications involved are slightly different, the concepts behind the coupling of radiation to plasmonic nanoantennas are similar. Applying an oscillating EM field to a plasmonic nanostructure can excite LSPR modes; likewise, an excited LSPR mode can emit radiation through radiative decay.

2.2.1 From Radio Antennas to UV Antennas

Maxwell [7] provided the fundamentals for today's antenna theory when he unified the theories of electricity and magnetism and produced the theory that light is an oscillating EM wave, not limited to the visible spectrum [100]. The first demonstration of the propagation of long wavelength EM radiation, radio waves with a wavelength of approximately 4 m, is attributed to Heinrich Hertz [8]; Hertz' work was followed by the experiments of Marconi, who transformed the communications industry by using long wavelength radiation to send messages from Cornwall, England to Newfoundland, Canada [100] in 1901, making up for inefficiencies and radiation losses with brute power. Following this transmission, antennas and antenna design became a popular topic of research and industrial application [100]. The coming of World War II pushed development down to the microwave and radar regimes [100], with wavelengths down to approximately 1 cm. In the 1960s, the computational power and numerical methods needed to model the behaviour of antenna designs were developed [97] and today antennas are used in a wide variety of applications considered necessary to the functioning of modern society.

The wavelength of EM radiation with which an antenna can most efficiently couple depends on its physical size. Typically the antenna size is much smaller than the wavelength it couples to ($\lambda/2$ or $\lambda/4$, for example); progress to smaller and smaller wavelengths in the IR or below requires more specialized fabrication techniques capable of fabricating precise antennas on the micrometer or nanometer scale [98]. In the IR, tungsten 'cat-whisker' antennas were developed in the 1960s and 70s, but were limited to wavelengths longer than approximately 2 µm [98, 101]. As antennas are scaled further down to couple to shorter wavelengths, the typical scaling laws used for antenna design begin to break down because the penetration depth of the EM waves into the metal structures is no longer negligible relative to the small size of the antennas, and because of increased losses in the metals [98].

In the IR to UV range of the spectrum, the surface plasmon response has become the dominant technology for transmitting or receiving antenna signal, outside of semiconductor technology [98]. Although the mechanism is different from that of the more classic radio antennas, the ability of a plasmonic nanoparticle to transduce light fulfills the basic function of an antenna. The first proposed use of a plasmonic nanoparticle as an applied antenna comes from Wessel in 1985 [102], who proposed the use of a silver nanoparticle mounted on a scanning tip to enhance Raman spectroscopy signal of a surface under laser excitation, with nanometer imaging capabilities. This concept, taking advantage of the ability of the plasmonic nanoparticle to couple to far-field radiation and concentrate the energy into a space much smaller than the diffraction limit, leads to arguably the most widely used application of plasmonics: surface-enhanced Raman spectroscopy.

Of primary importance in designing plasmonic nanoantennas is the ability to model and characterize the plasmonic response, which, similarly to the response of larger antennas, depends strongly on the geometry of the antenna and on the local environment.

2.2.2 Radiative Antenna Fields

The regions around an antenna are separated into the near-field and far-field regions (Figure 2.5) [103]. The near-field region itself can be further separated into the reactive near-field, in which fields reactive to the charge and current distribution dominate; and the radiating near-field, or Fresnel region, in which radiation fields dominate but have not settled into their final pattern yet, the angular distribution is still evolving with respect to the distance from the antenna, and there may be a significant contribution from radial fields [86, 103].

In the propagating far-field, or Fraunhofer, region, the angular distribution of EM fields is independent of the distance from the antenna structure and the radiation pattern is well formed with dominantly transverse components [86, 103]. The radial components of the EM fields are usually very small in comparison with the other components. The far-field region is, in practice, defined in relation to the size of the

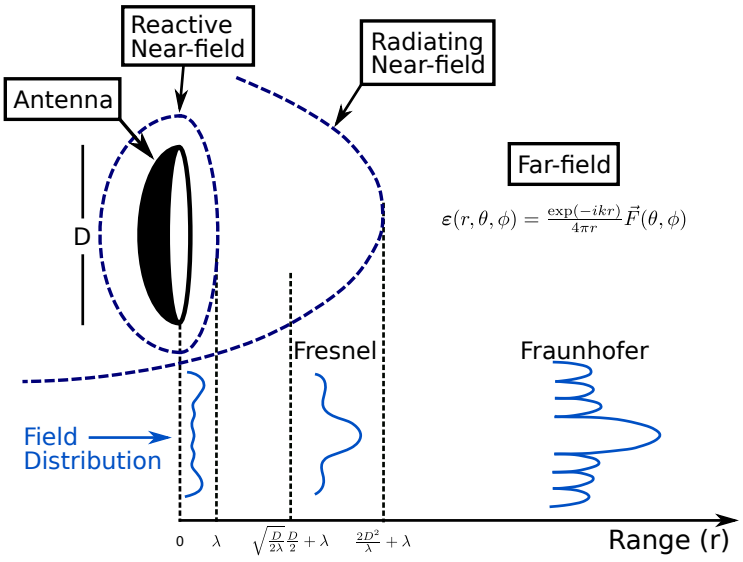

Figure 2.5: Field distributions in the near-field and far-field regions of a radiating antenna (repeated from Chapter 1, Figure 1.3) as a function of wavelength (λ), antenna size (D), and distance from the antenna (r). Adapted from [21] (©1995 IEEE).

antenna and the wavelength of the emitted radiation based on Equation 2.4, in which r is the distance from the antenna, D is the largest dimension of the antenna, and λ is the wavelength of emitted radiation [104]. In the far-field, the antenna can generally can be considered as a point source of EM radiation and spherical coordinates are used, making the electric field a function of the spherical coordinate vectors, $\boldsymbol{\varepsilon} = \boldsymbol{\varepsilon}(r, \theta, \phi)$, in which ε_r is very small [86,103]. Unless the size of the antenna is very small compared to the wavelength, retardation effects must be taken into account when calculating the potentials and EM fields radiated by an antenna.

$$r >> \frac{2D^2}{\lambda} \tag{2.4}$$

In this thesis, both the near-field and far-field responses of plasmonic nanoantennas are probed: electron energy loss spectroscopy uses a nanometer-sized probe to interact with the near-field of the LSPR; cathodoluminescence uses a small probe to excite the LSPR through its near-field, but collects the far-field from LSPR radiative decay. Both EELS and CL data are complemented with simulations. Appendix A describes the polarization properties of some basic dipole configurations and of simulated CL radiation.

2.2.3 Multipole Expansion of Electromagnetic Fields

The radiation fields of any arbitrary system of charges and currents can be modelled using the multipole expansion formalism [105, 106]. The most well-known results of

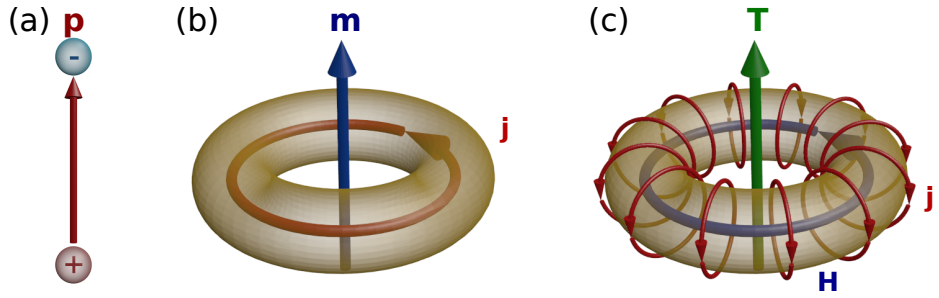

Figure 2.6: Schematics of the dipole moments of three multipole families: (a) the electric dipole ($\boldsymbol{p}$); (b) the magnetic dipole ($\boldsymbol{m}$), created by the current density ($\boldsymbol{j}$); (c) and the toroidal dipole ($\boldsymbol{T}$), created by poloidal current ($\boldsymbol{j}$) and circulating magnetic field ($\boldsymbol{H}$). Inspired by [107].

the multipole expansion of charge-current configurations are the electric and magnetic dipoles, though the expansion also provides for the existence of higher order multipole moments of order 2^l, such as quadrupole moments and octupole moments. The multipole expansion breaks down radiation fields and interactions with external EM fields into the responses from charge and current density within the system [105]. The charges and currents in a system are described by four quantities: σ, the charge density; and $\boldsymbol{j} = (j_x, j_y, j_z)$, the three-component vector current density. The four quantities are not wholly independent of each other, as they must obey the conservation relation $\nabla \cdot \boldsymbol{j} = \dot{\sigma}$, leaving three independent quantities. From these, three independent multipole contributions can be derived [105].

The electric (P_l) and magnetic (M_l) multipole form factors are the well-known quantities which describe electric and magnetic dipoles ($l = 1$), quadrupoles ($l = 2$), *etc.* The electric multipole family describes the response of charge density or longitudinal current components; the simplest member of this family is the charge density, which can be used to generate the rest of the family members [106], followed by the electric charge dipole (Figure 2.6(a)) [105]. The electric multipole form factors are invariant under time reversal operations (in which $t \rightarrow -t$), but their sign is reversed with spatial coordinates ($(x, y, z) \rightarrow (-x, -y, -z)$), preserving spatial parity (Table 2.1) [106]. The discussion of LSPR behaviour in Chapter 3 deals primarily with electric multipoles.

The magnetic multipole form factors are described in terms of their simplest

Table 2.1: Summary of the symmetry operations of the multipole families under spatial inversion ($\hat{\mathrm{I}}$) and time reversal ($\hat{\mathrm{R}}$).

	$\hat{\mathrm{I}}$	$\hat{\mathrm{R}}$
P_l	-	+
M_l	+	-
T_l	-	-
G	+	+

constituent: a magnetic dipole, geometrically represented by a current loop (Figure 2.6(b)) [105]. The magnetic dipole can be used to generate the rest of the family of magnetic multipoles [106]. The magnetic multipoles behave in the opposite way to the electric multipoles when it comes to time and spatial parity. Under spatial inversion, the magnetic multipoles retain their sign, whereas under time reversal they switch their sign (Table 2.1) [106]. The magnetic dipole can be created by the lowest energy LSPR of a split ring resonator (SRR) structure, as discussed in Chapter 4.

The transverse current density has two independent components, one of which is accounted for by the magnetic multipole family [105]. The other is accounted for by the third family, the transverse-electric moments, which are the sum of the time derivative of the charge dipole and the toroidal moments (T_l) [105]. The transverse-electric is often, in the long-wavelength limit, taken simply to be proportional to the time derivative of the electric multipole family, but this neither makes it an independent multipole family nor does it complete the multipole description of all possible charge-current configurations [105]. Instead, the transverse-electric multipole form factors can be considered to be the toroidal multipole form factors [106].

The simplest member of the toroidal family is the toroidal dipole moment, which is generated geometrically by a wire solenoid wrapped around a torus shape (Figure 2.6(c)), the response of which is not described by either electric or magnetic moments [105, 106, 108]. The poloidal current (indicated by $\boldsymbol{j}$ in Figure 2.6(c)) running through the wire creates magnetic moments which are completely confined within the torus, there is no charge density, and there are no fields created outside the torus when the current is constant; the toroidal dipole is characterized by circulating magnetic field vectors [105, 108, 109]. Higher order toroidal multipoles can be created by making each winding on the dipole torus into a wound torus itself [109]. Under both spatial inversion and time reversal, the toroidal multipoles are inverted: these multipoles break both time and space parity, unlike either the electric or magnetic families (Table 2.1) [106]. The toroidal dipole moment is created by an LSPR resonance from a particular arrangement of SRRs, described in Chapter 5, showing that antenna geometries can be engineered to produce EM multipole moments which are otherwise difficult to create or detect.

The fourth moment (G) in Table 2.1 fills out the final combination of time and space symmetries: maintaining the same sign under spatial inversion and time reversal [106]. This moment is not required by the multipole expansion, nor does it exist in classical electrodynamics, as it is the equivalent of the toroidal moment for magnetic charges [106]. However, it is possible to create this moment, named an axial toroidal moment (as opposed to T_l, the polar toroidal moments), when averaging over the microscopic properties of macroscopic media (such as in pyroelectric media or phase transitions in liquid crystals), using a ring of elementary electric dipole moments, whereas the polar toroidal dipole moment is created by a ring of magnetic dipole moments [106, 108].

2.3 Materials for Plasmonics

To create a plasmonic nanoantenna, the material must support LSPR. A good indication that a material will support well-defined collective resonances is when ϵ_1 crosses zero with a positive slope [62]. For conductive metals, the plasma frequency is usually in the UV and below this energy, the real part of the dielectric function is negative [71] and there is hope for sustaining plasmon resonances. Alkali metals, aluminium, and, at low frequencies, conductive noble metals (copper, silver, gold, classified by their fully occupied d-band) provide a good approximation to a Drude metal [81]. Alkali metals are highly reactive and difficult to work with, but aluminium and some of the noble metals, in particular gold and silver, are among the most popular plasmonic materials.

Aluminium is a popular choice for plasmonic applications and has a high plasma frequency in the UV region (around 15 eV), which allowed some of the early electron spectroscopy experiments to be performed on aluminium foils or nanoparticles without the need for a monochromator [38, 43, 82]. It presents a low cost alternative plasmonic material with a high-energy response and the possibility of UV plasmonics, though optical experiments are challenging at these energies [81]. However, aluminium forms a self-limiting surface oxide layer in air which may damp or absorb radiation from plasmons [81], and causes changes to the theoretically predicted surface plasmon frequency, playing an important role in the SP response [38, 82].

Noble metals have a high conductivity and a plasma frequency around 10^{15} Hz (visible or UV spectrum) [60], although the presence of the d-band in these metals causes screening of the conduction electrons, and interband transitions from the d-band dominate the optical response at higher energies [68, 81]. The noble metals have one free s-electron in the conduction band and a full d-band in their ground state. At low frequencies, only intraband transitions inside the half-empty s-band are possible and noble metals exhibit free-electron-like behaviour with a good approximation to the Drude model [68, 110]. Conductivity is made possible through these intraband transitions, in which an electron below the Fermi energy is excited to another state in the same band above the Fermi energy [60]. The d-band lies a few eV below the Fermi level and interband transitions from d-band electrons to empty s-band states above the Fermi level dominate the optical response at higher energies, in the visible to UV regime [110]. The d-band electrons are strongly localized [111] and the presence of the d-band screens the free electrons from the atomic cores, causing a redshift of the free-electron plasma frequency [60, 68].

In copper, the d-band is approximately 2.2 eV below the Fermi level [112], and interband transitions dominate the optical losses in the spectrum before the plasma frequency is reached, while ϵ_1 is still negative [68]. Interband contributions cause high spectral absorption (high ϵ_2) where ϵ_1 crosses 0 and copper does not exhibit good conditions to support a bulk plasmon [110]. Copper, therefore, despite being a noble metal, does not make a good plasmonic material.

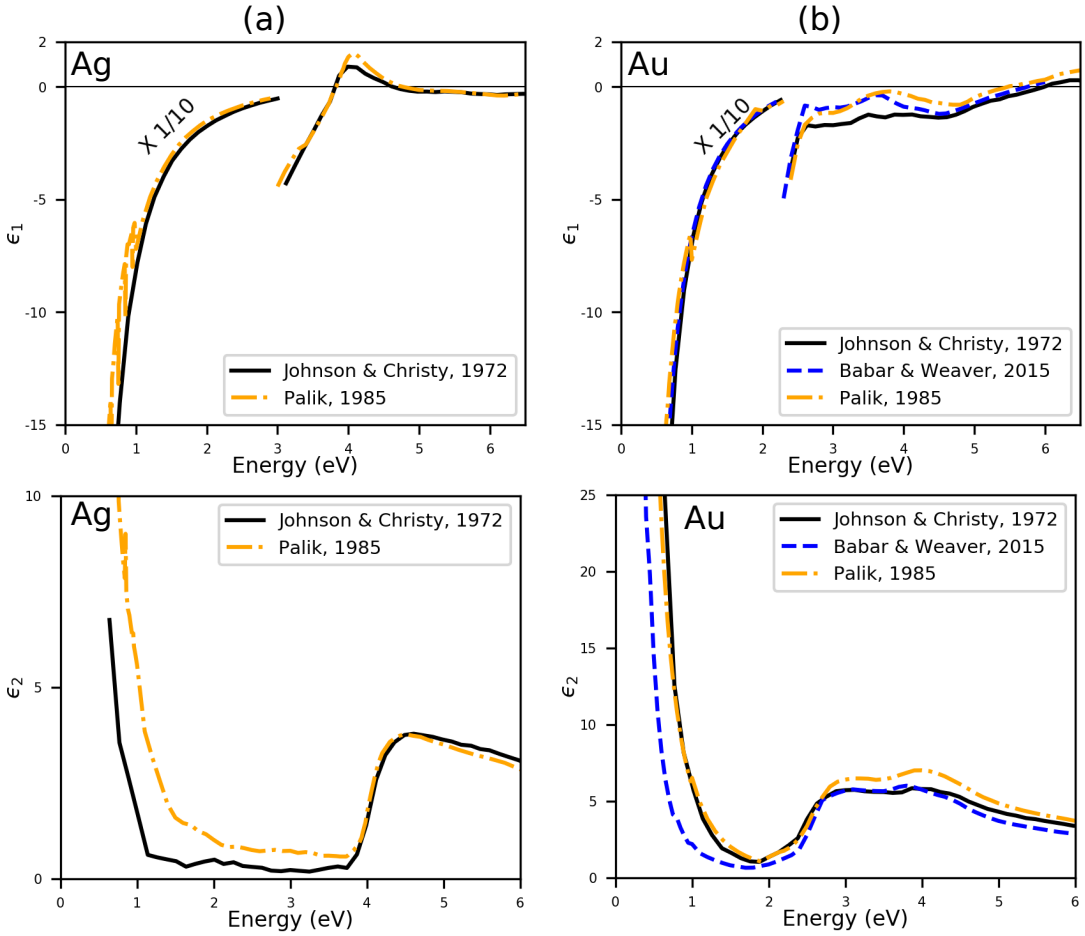

Figure 2.7: Complex dielectric functions of silver and gold. (a) Silver, measured by Johnson and Christy [110] and Palik [113]; (b) Gold, measured by Johnson and Christy [110], Babar and Weaver [114], and Palik [113].

The undamped plasma energy of silver is at 9.2 eV, but the presence of *d*-band states below the Fermi level redshifts this to 3.9 eV [68] and the plasma oscillation in silver can be thought of as a combined oscillation of *s*-band conduction electrons screened by *d*-band electrons [60, 68, 110]. *d*-band electrons undergo interband transitions at around 4 eV in silver, increasing both ϵ_1 and ϵ_2 and causing ϵ_1 to cross 0 at a lower energy than expected without damping (Figure 2.7(a)). ϵ_2 remains small at this value, so the plasma frequency and bulk plasmon are still observed [68, 110]. Silver shows smaller damping and a sharper plasma resonance than other metals because of the close proximity of this interband transition [81], which sets in about 0.1 eV above the plasma frequency and steepens the ϵ_1 curve [68]. Because of this, silver is a popular choice for strong plasmon resonance, but a bare silver surface has a limited lifetime because of its reactivity with oxygen or sulphur in the air.

The optical response of gold, another popular choice for plasmonics with higher

chemical stability than silver, approximates the Drude model (Figure 2.7(b)) and has similar behaviour to copper [115]. The d-band of gold is broader than that of silver [111], so the onset of interband transitions is more gradual than that in silver, beginning at around 2.4 eV with a long tail down to approximately 1.5 eV [111, 115]. The surface plasmon energy is at approximately 2.7 eV, where interband transitions dominate the optical response.

Both gold and silver are used in this thesis work: silver for its strong and sharp plasmonic resonances with low damping is used for the fractal structures presented in Chapter 3. Gold, for its longer shelf life and better chemical stability while still maintaining a strong detectable plasmonic response is used for the VSRRs and T4 arrays presented in Chapter 4 and 5.

2.4 Fabrication

Methods of producing plasmonic nanoparticles include bottom-up wet chemistry synthesis in solution [116] or on a substrate [17], or top-down lithography methods such as nanosphere lithography [117], soft imprint nanolithography [118], optical or electron beam lithography, and focused ion beam milling [17].

Bottom-up methods are more scaleable than top-down methods: large batches of nanoparticles can be synthesized together, but these methods are limited in the shapes that they can produce. Nevertheless, chemically synthesized plasmonic nanoparticles are typically high quality single or twinned crystals with strong plasmonic responses.

Top-down methods allow more freedom in the choice of nanostructure geometry, but are slower and are usually performed serially. Optical lithography exposes a large area with radiation through a pattern mask, but its resolution is limited by the wavelength of light used. Focused ion beam technology can mill out arbitrary structures of two or three dimensions, but is a serial technique and quite slow. It may also leave ion beam damage and sputtered ions scattered around the nanostructure.

Electron beam lithography (EBL) is a serial batch-processing technique with a strong foothold in academic research for prototyping and manufacturing small scale systems, though there is work towards making EBL more industry-compatible through parallelizing the exposure process with multiple electron beams [119, 120]. EBL provides the freedom to define pattern features of arbitrary complexity based on CAD (Computer-Aided Design) drawings [121–123] with higher resolution than optical lithography, down to approximately 1 nm feature size for state-of-the-art EBL systems [124]. EBL often produces nanostructures with smaller grain sizes and more plasmon damping than chemically grown particles, but makes up for this with the freedom in defining the nanostructure geometry. EBL is usually used for 2D planar shapes, but can also be used to produce limited 3D structures.

The work in this thesis relies on the ability to manipulate the precise geometrical features of plasmonic nanostructures in order to achieve certain charge configurations and study how the geometry affects the LSPR modes, making EBL a good choice for

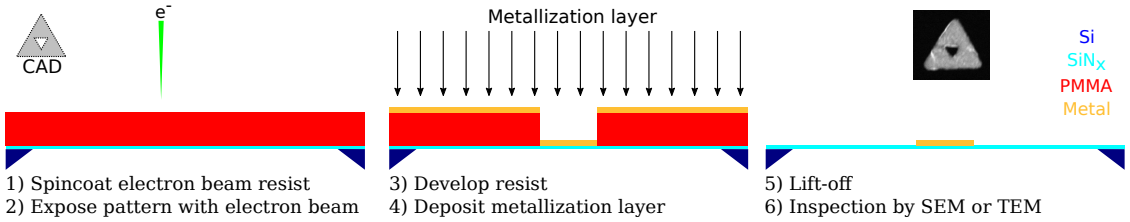

Figure 2.8: Electron beam lithography process flow. An electron beam resist is spincoated onto the sample and exposed under the electron beam according to a CAD pattern; the resist is developed and a metal layer is deposited; the remaining resist is dissolved during lift-off and the result is inspected.

the fabrication of nanostructures.

To allow EELS measurements to be performed the sample must be electron-transparent, imposing limitations on the sample substrates that can be used. The samples used in this thesis were fabricated on silicon TEM grids with nine windows of suspended 50 nm thick silicon nitride membranes, providing a flat, smooth platform capable of surviving the lithography processing steps. A thinner membrane reduces back-scattering during EBL and reduces the effect that the presence of the substrate has on the LSPR behaviour, but is prone to breakage during handling [125]. Using a slightly thicker membrane adds background signal to the EELS spectrum and slightly increases back-scattering during EBL, but reduces the change of breakage during the lithography steps.

2.4.1 Electron Beam Lithography

Typically done in an SEM or dedicated electron beam lithography machine, EBL relies on the ability to scan a focused electron probe over an arbitrary pattern area. The EBL process is outlined in Figure 2.8 for a positive resist, starting with the design of a CAD pattern giving the features to be patterned by the electron beam [126].

The substrate to be patterned is spincoated with an electron beam resist, such as poly(methyl methacrylate) (PMMA). A post-bake on a hotplate smooths the resist layer surface and evaporates any remaining solvent. The sample is then loaded into an EBL system equipped with a beam blanker, where a focused electron beam is scanned according to the CAD pattern. After exposure, the sample is exposed to a development solution for a strictly limited time period to remove either the exposed regions (in a positive resist) or the unexposed regions (in a negative resist).

In a positive resist, a layer of the desired material is then deposited; in a negative resist the layer may have been deposited before the resist, which now acts as a mask during an etching process. Lift-off is done to remove the remaining photoresist, revealing the pattern features on the substrate below.

Electron Beam Resist

PMMA is one of the most commonly used electron beam resists, and can be used as a positive resist at low doses or a negative resist at higher doses [127]. At low electron beam doses, the electron beam causes chain scission in PMMA, breaking up the long polymer chains into smaller, more soluble fragments which can be dissolved more easily in the developer [127, 128]. At higher doses, the electron beam induces crosslinking between polymer chains, creating a harder, more insoluble material [127].

A higher molecular weight PMMA layer requires a higher exposure dose for equivalent development conditions, providing the possibility to engineer the resist profile using multiple layers of different molecular weights [128]. A lower molecular weight has a higher solubility in the developer solution [128].

Electron Beam Lithography Resolution

The achievable pattern resolution of EBL is typically not limited by the electron beam diameter, but by contributions to the exposure from forward and back-scattered electrons, as well as secondary electrons [125, 128, 129]. When the electron beam enters the resist, elastic scattering causes lateral beam broadening as the electrons travel, thereby exposing a much larger spot than expected from the electron beam diameter [129].

Electrons entering the substrate underneath the resist layer may be back-scattered by the substrate to areas within a few microns of the electron beam location, though this mechanism of increased dosage is not a severe factor for sparse patterns, but mostly for dense pattern features [125]. Performing EBL on a thin electron-transparent membrane has the added advantage of reducing back-scattering off the substrate [125, 128], although the silicon nitride membranes are fragile and prone to breaking during handling and processing. Nearby EBL patterns or large patterns increase the effective dose in a given location through the proximity effect from lateral scattering of the beam within the resist and back-scattering off the substrate; distributing patterns more sparsely across the substrate helps to reduce this, but the resolution of small features within a larger pattern may still be degraded [128].

The dominant mechanism affecting EBL resolution may be exposure through secondary electrons. Inelastic scattering of the primary beam deposits energy into the resist, causing chain scission and emission of SEs [125, 128, 129]; the low energy SE travels through the resist and, with a higher scattering cross-section than the primary beam, causes chain scission further away [128, 129]. The primary beam may also excite bulk plasmons within the resist, which then propagate away from the primary beam and expose the resist or decay into SEs, which themselves expose the resist and broaden the resolution [129].

2.5 Characterization of Surface Plasmons

LSPRs respond to both light and swift electrons and are studied using both excitation methods. The spatial resolution of far-field optical methods is limited by the diffraction limit of light [69]. Absorption and scattering optical spectroscopies obtain spectral information on the ensemble average of nanoparticles or on individual nanoparticles in dark field microscopy, but these techniques do not have the spatial resolution to obtain details on the field distributions of individual modes [69]. To achieve nanometer spatial resolution, very high energy photons can be used, such as UV or x-ray photons, but optical components for such high energies are difficult to manufacture and these energies are on the upper limit of typical LSPR signal [69]. Near-field optics provide an alternate route to circumvent the far-field diffraction limit.

Near-field techniques include scanning near-field optical microscopy (SNOM), or scanning tunnelling spectroscopy (STS) and can achieve higher resolution than the far-field diffraction limit allows, but are still limited to approximately 10 nm [69,130]. STS signal is dominated by single electron interactions with the tip [69], so it is hard to gain information on the collective response of the surface plasmon with this technique. In SNOM, a nanoscale tip is scanned over the sample and evanescent waves are detected through optical tunnelling between the sample and tip [131]. At the apex of the scanning tip, light is confined to a region much smaller than the diffraction limit would allow and the SNOM tip acts as a point source of surface plasmons [132], perturbing the sample near-field and causing non-radiative components to become radiative [69,131]. The near-field components hold sub-wavelength information about the sample and by scanning the tip, a high resolution image of the sample can be obtained [131]. The tip acts to couple external light to surface plasmons or vice versa, allowing the surface plasmon to be studied at higher spatial resolution, though the interference of the tip with roughness in the sample can cause interference effects in the scattered images [132].

In an electron microscope a beam of swift electrons, travelling at a significant fraction of the speed of light, probes the near-field of plasmonic nanostructures with unmatched spatial resolution [69]. The signal from the electron microscope is surface-sensitive, but information can also be obtained from the bulk using the transmitted electron beam [69]. Although the spectral resolution of optical measurements is typically higher, optical measurements are limited to a small range of photon energies compared to electron beam spectroscopies, which can measure a wide spectral range in a single measurement [82]. Although photons are transverse waves and fast electrons are a source of longitudinal fields to the sample, the transverse and longitudinal dielectric functions are approximately the same in most samples and comparable information can be gained from both optical and electron-based experiments [62].

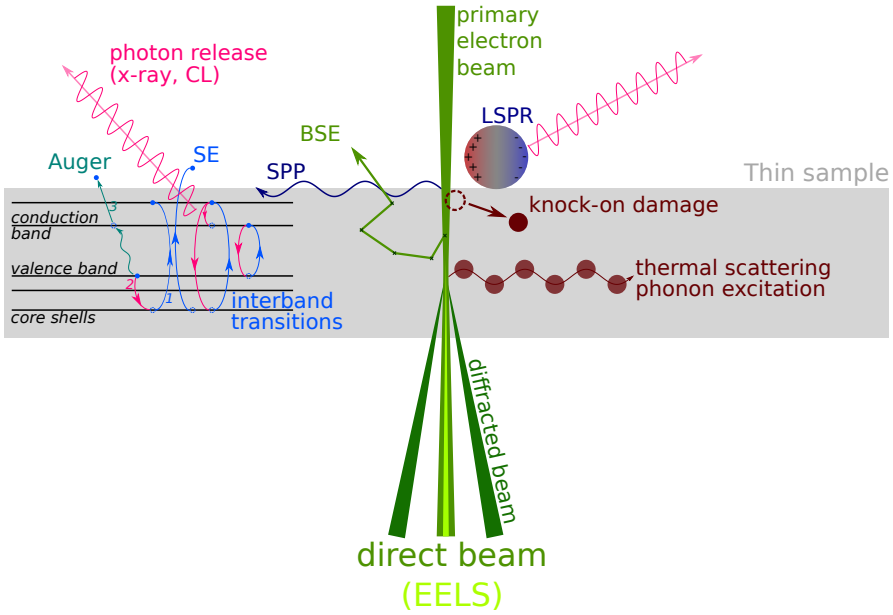

Figure 2.9: An overview of different excitations in matter caused by an incident electron beam. Inspired by [69].

2.5.1 Interaction of Swift Electrons with Matter

Electrons in the primary beam affect the specimen through electrostatic Coulomb interactions between the electron beam and either the nucleus or electron cloud of the sample's atoms [80, 133]. Interactions with the nucleus are usually classified as elastic scattering or Rutherford scattering, while interactions with the electron cloud of the sample typically result in an exchange of energy through inelastic interactions [133]. A graphical summary of the scattering interactions is shown in Figure 2.9.

Elastic Scattering

Elastic scattering events typically result in no detectable energy loss to the primary electron beam at small scattering angles, but can cause knock-on damage through the transfer of a large amount of momentum to a sample nucleus, displacing it and damaging the sample [62, 133]. Other elastic scattering processes include thermal scattering and diffraction [62]. Thermal scattering from interaction with phonons in the sample causes low-energy losses (less than 0.1 eV) that are difficult to detect in all but the most advanced monochromated systems [62, 134]. Diffraction provides a fully-fledged characterization method for crystalline and amorphous samples in the TEM or SEM, giving information on the atomic spacing and crystal orientation of a sample and enabling dark-field imaging in the TEM (see, for example, [135]).

Interaction with the sample nucleus may cause strong deviation of the electron beam, with a chance to scatter the primary beam electron backwards at an angle

greater than 90 degrees [133]. In bulk samples, the primary beam electron may undergo many scattering events until it emerges back out of the surface through which it entered, after which it is considered a back-scattered electron (BSE) [136, 137]. BSE signals are often collected in an SEM and give information on the chemical composition of the sample, since the BSE scattering probability of an atom increases with the atomic number [136], or on the relative crystallographic orientations within the sample through channelling contrast [137]. While elastic scattering does not contribute to spectroscopic signal, it does contribute to imaging contrast mechanisms in SEM and TEM/STEM [138].

Inelastic Scattering

Most of the primary beam electrons travel further away from the sample nucleus and either pass through thin samples with no interaction at all or interact with the atomic electrons in the sample through inelastic scattering. Inelastic scattering implies that some energy is lost from the beam electron and includes the excitation of a single core shell electron from a low-lying orbital to a higher energy level or band [133]; scattering from electrostatic interactions with the outer shell electrons (*e.g.* in the valence or conduction bands); or interactions with collections of atomic electrons [62]. The sample experiences the beam electron's electric field for a very short time as it passes by, translating to a broad band of excitation frequencies, and the beam acts effectively like an evanescent source of white light [69, 80]. The electron beam can excite a variety of transitions in the sample over a huge spectral range.

A primary beam electron can promote a single core shell or valence electron to a higher energy state within the sample or above its vacuum level [133,138]. Transitions to states above the Fermi level include interband excitations across the bandgap or intraband excitations of electrons just below the Fermi level [133]. If the higher energy state is above the sample's vacuum level, the excited atomic electron is released as a secondary electron (SE) [133].

SEs are by definition low energy electrons emitted from the sample and are usually reabsorbed if they are more than a few nanometers from the surface of the specimen [136]. Within a few nanometers of the surface, SEs can escape and are used for one of the most common imaging methods in SEM, giving highly surface sensitive topographic information about the sample [136, 137].

The primary electron beam can also excite collective modes of valence or conduction electrons in the sample via transitions from the valence band or conduction band to energy states just above the Fermi level [138]. These collective modes may be bulk plasmons, SPPs, or LSPR in metals or metal-like samples. The electron beam couples efficiently to the longitudinal bulk plasmon [69]. When the electron beam passes through a conductive sample, it trails behind it a plasmon wake which propagates laterally outwards, oscillating at the bulk plasmon frequency [62]. In an insulator, the energy excites a single valence electron to a higher energy delocalized state, but over time this energy is distributed between many atoms and the energy loss peak is

still referred to as the bulk plasmon [133]. The decay of a bulk plasmon may produce heat or transfer energy to a single electron excitation, emitting an SE or promoting a higher energy interband transition [62, 133]. In some samples, surface plasmons (SPPs or LSPRs) may be excited as the electron beam passes through or nearby to the specimen surface [133].

All of these excitation processes result in an energy loss from the beam, with the probability given by Equation 2.5 [69]. This energy loss is detected in electron energy loss spectroscopy. As it approaches, the electron induces a field in the sample, which acts back on the electron, slowing it down and causing energy loss [69]. When the sample has a resonant response at a particular frequency/energy, there is a high loss probability for the electron beam to excite a transition at that energy and the beam donates a quantum of energy to exciting that resonance, resulting in a peak in the EELS spectrum [69]. The energy lost by the primary electron is related to the optical extinction properties of the sample, described by the sample's dielectric function [62], and the projection of the sample's electric field along the beam direction [80]. The energy loss probability (Γ_{EELS}) is a function of frequency (ω), the electron velocity ($\boldsymbol{v}_{\mathbf{e}}$), the sample's response ($\boldsymbol{\varepsilon}^{\mathrm{ind}}(\boldsymbol{r}_{\mathrm{e}}(t),\omega)$), and the position of the electron beam ($\boldsymbol{r}_{\mathrm{e}}(t)$) [69].

$$\Gamma_{\mathrm{EELS}}(\omega) = \frac{\mathrm{e}}{\pi\hbar\omega}\int \mathrm{d}t\,\mathrm{Re}(\exp(-i\omega t)\boldsymbol{v}_{\mathbf{e}}\cdot\boldsymbol{\varepsilon}^{\mathrm{ind}}(\boldsymbol{r}_{\mathrm{e}}(t),\omega)) \tag{2.5}$$

Secondary Processes

Excitation of an electron within the specimen leaves behind an empty low-energy electronic state, into which the excited electron or another specimen electron can return, releasing the transition energy either into the surrounding sample or as radiation [138]. The energy difference between the top and bottom levels of this transition determines the energy of the photon released. For big energy gaps, the photon may be an x-ray with an energy characteristic of a particular transition in a specific atom, enabling chemical identification using energy-dispersive x-ray spectroscopy (EDXS) or wavelength-dispersive x-ray spectroscopy (WDXS) [133,138]. If the excited atomic electron drops to an empty state in the outer shell or valence band, the decay emits a lower energy photon in the IR, visible, or UV regions of the spectrum, which can be detected using CL equipment [80,133]. The decay of collective oscillations such as LSPRs may also be radiative, contributing to CL signal.

The emitted radiation may also excite another electron in the atom to an energy state above the vacuum state, releasing an Auger electron, which can be detected in Auger spectroscopy [133, 138]. The energy can also be released as heat or phonons, causing local heating of the sample [133]. Radiolysis or ionization damage may occur if the electron configuration of the sample is changed after the interaction [133]. In exciting electronic transitions in a sample, the electron energy loss gives an indication of the joint density of states: the convolution between occupied states where the

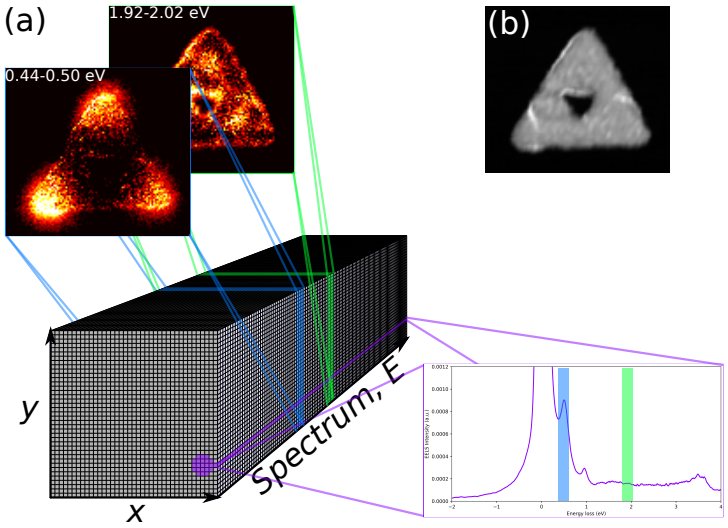

Figure 2.10: Spectrum imaging data cube. (a) The data cube has two spatial dimensions, from which spectra can be extracted (purple) and the spectral dimension, from which energy-filtered images can be selected (blue, green); (b) ADF image acquired simultaneously with the spectrum image.

transition starts and the unoccupied states in which the transition finishes [69].

2.5.2 Electron Spectromicroscopy

The term 'spectromicroscopy' is used to encompass characterization techniques which provide both spatial (microscopy) and spectral information (spectroscopy) simultaneously. Electron spectromicroscopy techniques can be done in either an SEM or a STEM or TEM. These techniques provide information with spatial resolution that is unmatched by any other technique. In a STEM instrument, the spatial resolution is often less than 1 nm, and can even be down to sub-Ångström with the right equipment, while still maintaining energy resolutions of a few tens of meV [69, 80]. In the SEM, the spatial resolution is usually below 10 nm and the spectral resolution is comparable to optical techniques [69]. Spectromicroscopy techniques rely on the concept of a spectrum image (SI) dataset.

Spectrum Image

Most of the EELS and CL data presented in this thesis was acquired in the form of a SI, a concept introduced to EELS in the 1980s [139]. An SI is a 3D ($x \times y \times E$) dataset, containing two spatial axes (x and y), and one energy or spectral axis (E) (Figure 2.10). In the case of EELS, the spectral axis corresponds to the energy loss spectrum; in the case of CL, the spectral axis is the wavelength spectrum of the light emitted from the sample.

To acquire a spectrum image, a STEM or SEM is used. The electron beam is raster scanned over the specimen and at each pixel in the scan a spectrum is acquired, building up the 3D dataset. Often there is simultaneous acquisition of an annular dark-field (ADF) image (STEM) or SE image (SEM) to correlate the features of the sample with the spectral features observed in the SI [80]. Acquisition of the SI necessarily takes longer than single spectrum acquisition, but provides more complete spatially-resolved information about the sample. Acquisition of an EELS SI can also be done by acquiring energy-filtered images (EFTEM), in which image stacks filtered around specific energy ranges are collected [80, 140]. Acquisition of the SI may be slow, depending on the integration time and number of pixels chosen. If the sample is drifting, drift correction through cross-correlation routines can be applied and a sufficiently fast spectrum acquisition can take advantage of the presence of the zero loss peak to calibrate and re-align each spectrum to correct energy drift [141].

The 3D dataset is more complicated to navigate and visualize on a 2D computer screen and requires some additional data processing steps, but brings the freedom of summing spectra over arbitrary areas post-acquisition or of extracting energy windows or slices and projecting the spatial distribution of the spectral intensity within those slices [139]. In order to take advantage of the possibilities of the 3D SI, a Python software dedicated to SI visualization and analysis was written over the course of this thesis (Chapter 6).

2.5.3 STEM-EELS

An EELS experiment gives a spectrum of the number of electron counts as a function of the kinetic energy they have lost from inelastic scattering events on passing through the sample [133]. In this thesis, EELS was acquired using a monochromated FEI Titan STEM instrument. A brief schematic of the instrument is shown in Figure 2.11; more details are given in Appendix B. A typical STEM instrument is operated between 80 and 300 kV and the energy losses detected in a plasmon experiment are on the order of a few hundred meV to a few eV.

The spatial resolution of an EELS SI can be similar to that of STEM, particularly in the core-loss region, allowing atomic-resolution core-loss EELS maps to be made [141–143]. However, the nature of the transition under study and its spatial extent also affects the spatial resolution of EELS [69, 141]. The electric field of the fast electrons has a finite field extending into space, causing Coulomb delocalization of the signal obtained, with increased delocalization as the wavevector of the energy loss is reduced [69]. For low-energy excitations, the delocalization of the signal can be macroscopic in nature, extending several microns into vacuum, while for core-losses, the signal can be localized within an Ångström or so [69]. EELS can be used to study phonon excitations, surface plasmon modes [43, 144], bandgap transitions, excitons, defect states, bulk plasmon excitations, and the chemical composition and electronic configuration of the specimen, giving a wealth of information over an unmatched

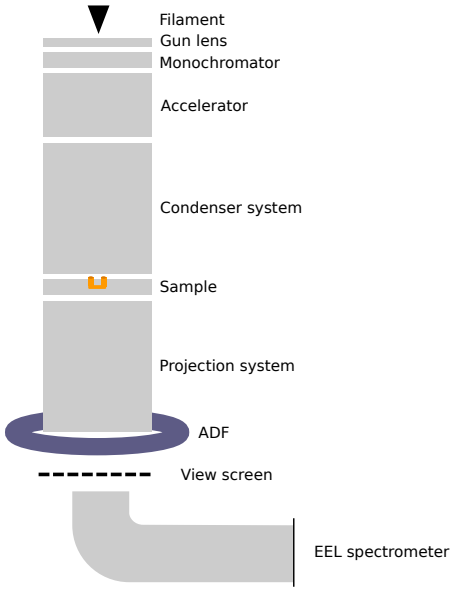

Figure 2.11: Schematic of the FEI Titan column. Electrons are emitted from the filament and are focused by the gun lens, energy-filtered by the monochromator, accelerated, and formed into a focused probe by the condenser system before hitting the sample; the projection system passes the electron beam to the annular dark-field detector and the EELS spectrometer.

energy range.

EELS Spectrum

The EELS spectrum is usually dominated by the zero loss peak (ZLP), which contains electrons that have been transmitted without any detectable energy loss [133]. This can include unscattered, elastically scattered, or inelastically scattered electrons which have lost so little energy that they cannot be distinguished from unscattered electrons because of the limited spectral resolution of the system [133]. The detection limit of advanced monochromated systems is in the mid-IR [41]. The energy resolution of a spectrum is defined by the full-width at half-maximum (FWHM) of the ZLP [80]. The shape of the ZLP is determined by the shape of the emission spectrum from the electron gun, or by the monochromator and aberrations in the spectrometer. The extent of the ZLP tails is also a parameter of interest for systems being used to study extremely low-energy losses [145], as the ZLP tail can be significant compared to energy losses in the first few eV of the spectrum, leading to the need for monochromatization, increased system stability, or deconvolution techniques [80]. For example, Figure 2.12 shows the extent of the ZLP tail overlap with the low-loss peaks in a monochromated system (purple), compared to the same spectrum (green) after deconvolution has reduced the effect of the tails.

Apart from the ZLP, bulk plasmon excitations have the largest scattering cross-section and thereby the largest signal in the spectrum [69, 141]. The bulk plasmon

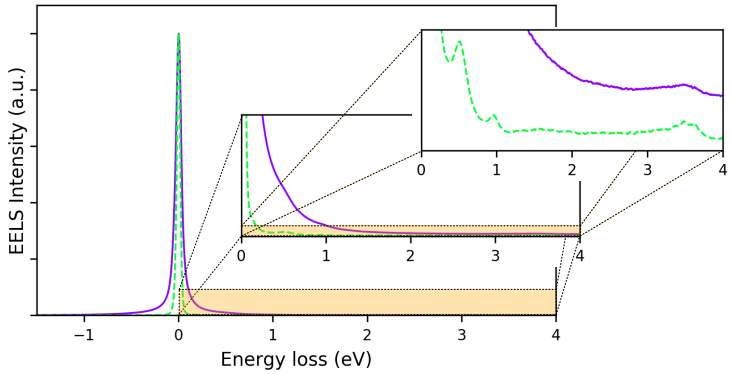

Figure 2.12: A low-loss EELS spectrum. Purple curve shows a raw, monochromated EELS spectrum dominated by the zero loss peak. Green dashed curve shows the same spectrum after deconvolution with the Richardson-Lucy algorithm. Insets show zoomed in views of the LSPR peaks of a silver nanostructure.

excitation dominates the low-loss region ($<$ 50 eV of energy loss) and can be used to estimate sample thickness [62, 69, 141]. Other outer shell electron excitation peaks are also present in the low-loss region of the spectrum, including electron-hole pair excitations across the bandgap, valence electron transitions into the conduction band, exciton creation, and phonon or surface plasmon excitation (smaller peaks in Figure 2.12) [133,138]. Electron screening of excitations is more significant at low energies and the loss function includes the polarizability and absorption from the dielectric response [138]. The delocalized nature of the signal can make interpretation of low-loss images complicated [69].

Optical excitations in the near-IR, visible, and UV regions of the spectrum, such as phonon and plasmon excitations, are now routinely available in monochromated instruments. When the electron beam passes through a plasmonic nanoparticle, it can excite both bulk and surface losses, but in aloof configuration (*i.e.* when the electron beam passes directly adjacent to the sample without impacting it), only surface modes are excited [69]. Low-energy transfers with an exponential decay dependent on the wavelength of the excitation are favoured when the electron beam does not intersect the specimen. An aloof electron can excite SPPs with a momentum component parallel to the electron beam velocity vector [69].

At higher energy losses is the core-loss region of the EELS spectrum, where primary beam electrons have lost energy to excite core-shell electrons in the sample. Core-loss edges give the characteristic binding energy of the excited electron or ionization threshold of the atom [133,138,146]. The intensity in this region decreases rapidly with increasing energy loss [133] and acquisition times must be long to obtain good signal-to-noise ratio (SNR) at high energy losses. The core-loss edge rises rapidly at the binding energy of that orbital, followed by a long slow tail with increasing energy loss [133]. Integration under these edges allows quantification of the atomic composition of the sample and near-edge fine structure gives information on the electronic structure

and bonding state of the atoms [133, 138]. At high energy losses, the real part of the sample's dielectric function is usually low and the energy loss function is dominated by the imaginary component [138], which relates directly to transitions within the sample.

Annular Dark-Field Imaging

Dark-field signal in the STEM reveals mass-thickness contrast from incoherent elastic scattering off the sample's atomic nuclei, and crystallographic contrast from diffraction [147]. The scattering probability for mass-thickness contrast increases with the atomic number of the atoms in the specimen and the thickness of the material through which the electron beam passes [147]. At higher collection angles, diffraction contrast dominates, but low intensity mass-thickness contrast can also be detected and the signal is sensitive to atomic number [141, 147], making compositional contrast clear in ADF images [141].

Many detailed studies have gone into the contrast mechanisms of STEM imaging, but in this thesis the STEM-ADF image is used simply to interpret the structure and geometry of the nanostructure under study, in parallel with the spectroscopic information from EELS. The samples are metal on a thin silicon nitride membrane and show up clearly as bright features (the metal) on a dark background (the silicon nitride). The metallic nanostructures diffract much more strongly than the amorphous substrate and have a much higher atomic number than the silicon nitride substrate; both factors contribute to making the metallic nanostructures bright in the STEM-ADF image. A very rough estimate of thickness can be inferred from the relative brightness of the image of the metallic structures, which, for instance, helps to identify the pillars on the VSRRs in Chapters 4, and 5.

2.5.4 SEM-CL

Cathodoluminescence (CL) is a technique which concerns the collection of radiation that is emitted from a sample under the impact of an electron beam. It was first discovered over a century ago when cathode rays (electrons) struck a phosphorescent material, which gave off light, now used to give light in cathode ray tubes. Collecting CL in an electron microscope allows analysis of the spectral signal that is emitted when a nanoscale electron beam is focused at a chosen location. The technique uses an SEM or STEM with the addition of a reflective mirror near the sample to collect radiated light. Depending on the configuration of the system, the mirror may be flat, ellipsoidal, or paraboloid in shape [80]. Under the electron beam, the sample radiates in any direction; some of this radiation is collected by the mirror and directed out of the microscope chamber to an optical analysis system which can give information on the angular distribution of emission [148, 149], the polarization of the emitted light [148, 150], time-resolved spectroscopy [151, 152], and the distribution of spectral features in space through spectrum imaging.

Ideally, the mirror used should collect as much radiation as possible from the sample and direct it out of the microscope, so it should have a high numerical aperture (NA). However, for a high spectral resolution the CL spectrometer should have a low NA, to make the beam coming into the spectrometer as small as possible. This is in direct conflict with the high NA desired for the collection system and often a lot of CL intensity is cut before reaching the spectrometer in order to use a spectrometer with a small NA [80].

CL can be done in either SEM or STEM machines. In a STEM instrument there are more restrictions on the size of the mirror, since it must fit in between the narrow polepiece gap, and usually there is a sacrifice to the optimal spatial resolution of the system [80]. In an SEM system, the space restrictions are eased and a larger mirror can be used. The larger mirror in the SEM has a higher collection efficiency and angular resolution. Examples of different mirror configurations include a single mirror either on top of or underneath the sample in a STEM instrument, a double mirror covering a hemisphere from top to bottom [148], or a single mirror in an SEM [153]. SEM-CL can be used for the study of bulk samples which need not be electron-transparent, but even electron-transparent samples benefit from the increased collection efficiency of the larger mirror in the SEM and reduced signal from the substrate.

The mirror in the SEM chamber is located above the sample and imposes a minimum working distance (WD) on the SEM, which is typically larger than the optimal WD and results in a sacrifice of spatial resolution. The mirror is opaque to electrons and a small hole must be drilled in the mirror to allow the electron beam to pass through. Care must also be taken as to the relative orientation of the mirror and the SEM SE or BSE detectors. A schematic of an SEM column with a parabolic mirror is given in Figure 2.13. Further description is given in Appendix B.

It is difficult to define the spatial resolution of CL, because in a CL SI, the light collected at each pixel corresponds to the photon count emitted from anywhere in the sample when the electron beam is located at that pixel location. There is no direct information on where the light was emitted from, though sometimes it is possible to derive where the light came from with knowledge of the sample. The spectral resolution is comparable to optical techniques.

Emission of light within the electron microscope can come from many sources, including radiation from the primary beam interacting with the dielectric environment, or from secondary processes within the sample [69, 80].

Emission from the Primary Beam

Emission from the primary beam can come from transition radiation, Cherenkov radiation, diffraction radiation, or Bremsstrahlung radiation.

Transition radiation occurs when a fast electron impinges on a metal surface. The charge of the approaching electron is mirrored in the free electrons within the metal and when the electron enters the metal, the effective induced dipole is eliminated and

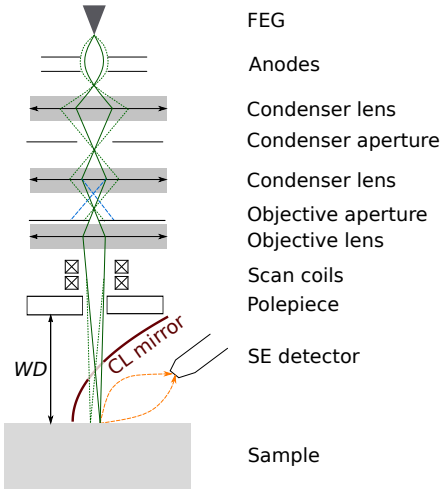

Figure 2.13: Schematic of an SEM column with a CL mirror. Green lines show the electron beam path down the column, blue indicates the spreading of the beam over the objective aperture when the spot size is changed. Orange lines indicate SE emission from the sample. The CL mirror imposes a minimum working distance (WD). Inspired by [154].

radiation is emitted [69]. The emitted radiation is p-polarized and is similar to the radiation from an oscillating dipole oriented perpendicularly to the surface [69].

Cherenkov radiation is emitted by the primary electron beam when the electron is travelling faster than the speed of light in the medium. The photon dispersion relation overlaps with allowed transfers from moving electrons and the moving electron can radiate [69]. The fast electron sets up far-field electric field oscillations which then propagate outwards as radiation. Cherenkov radiation occurs when the real part of the dielectric function is large and the speed of light in the medium is slow ($v = \mathrm{c}/\tilde{n}$), which happens often in insulating materials [62].

Diffraction radiation can occur when an electron beam passes near a periodically structured surface, such as a grating or series of metallic slits, and is seen in the Smith-Purcell effect [69, 155]. When the electron beam is decelerated by close interactions with heavy atoms within the sample, Bremsstrahlung radiation is emitted [69]. This type of radiation is often seen as background in the x-ray spectrum collected by EDXS. It is even possible sometimes to see the glow of the heated electron gun when all other signals in the CL acquisition are low, and care must be taken to disable the light source for the chamber camera that SEMs are often equipped with when doing CL experiments.

Emission from the Sample

Sources of CL signal within a sample include electron-hole pair recombination, exciton decay, or the decay of bulk delocalized excitations such as plasmons [69, 80]. Unlike EELS, CL is limited in its spectral range and is most efficient for visible light. Ex-

periments in the IR or UV regimes are possible, but challenging due to inefficiencies in the collection and detection optics.

When electron-hole pairs or excitons created by the electron beam recombine they can emit a photon with an energy close to the bandgap or interband transition energy within the material. Electron-hole pairs may travel through the sample before recombining, which can make it difficult to locate the source of light [80]. CL is a popular technique for exploring the radiation properties of photovoltaic materials, particularly in semiconductor heterostructures using quantum confinement, when the high spatial resolution of the electron microscope is particularly beneficial [69, 80]. CL can also occur from secondary excitations within the sample. For instance, SEs excited in the sample may travel through the sample and emit radiation or excite radiative transfers further away from the primary beam [69].

For many years it was not possible to detect plasmon radiation with CL due to struggles with collection efficiency, SNR, and the relatively low radiative efficiency of plasmon modes. Advances in high brightness electron guns; in the quality of the detection equipment through better mirror machining, design, and alignment and improved intermediate optical lens quality; and in the SNR of CCD (charge-coupled device) cameras allowed plasmons to finally be detected [78, 80].

Nevertheless, SNR remains a persistent problem in CL. A high beam current or a long acquisition time must be used to obtain sufficient CL signal from plasmonic nanostructures; for example, 2 nA of beam current was used with a dwell time of 1 s to obtain sufficient signal from silver nanoparticles, with a CL mirror covering a solid angle of 2π sr [148].

Not all plasmon modes are radiative, but the presence of dark LSPR modes with no net dipole moment is only prohibitive to CL when the particle size is very small compared to the wavelength of light [69, 89]. When nanoparticles are sufficiently large and retardation affects the LSPR properties, not only dipole, but quadrupole, hexapole, and even higher order multipole modes can be detected [78, 89]. Radiative damping of LSPR modes becomes more efficient as the particle size increases [69, 89, 156], but the energy also redshifts and can move into the IR out of CL detection range. Larger particles have broader dipole moments due to the increased dipole strength with particle size, and thereby increased radiative coupling and shorter lifetime [69].

In metals, CL radiation comes primarily from the skin-depth surface layer due to strong dynamical screening from the free-electron response of the metal, which eliminates effects from the propagation of the electron probe into the deeper regions of the sample [69]. Increasing the accelerating voltage of the electron microscope can also enhance the spectral signal from surface excitations while suppressing those of bulk excitations [157]. Aloof excitation can also be used for providing information on LSPR, due to the interaction of the LSPR evanescent fields with the electron beam [69].

SEM Imaging

Like STEM, SEM is a scanning beam technique using a focused electron probe to raster across a grid pattern over the sample. Acquired signals include SEs, BSEs, x-rays, electron diffraction, or CL signal, according to the specifications of the instrument. The vacuum requirements and strict sample preparation requirements for TEM work are relaxed for SEM samples, and bulk samples can be used. SEM detectors are usually located above and to the side of the sample surface [137].

To produce an SE image, the SE intensity is integrated for each pixel in the raster scan. The magnification of the SEM image is set by the magnitude of beam deflection applied by the scan coils [137]. SEs emitted from interactions with the primary beam are a high resolution signal, since they are low energy and can only escape the sample surface if they are excited within a few nm, but the lateral resolution is degraded by BSEs or SEs excited by other means than the primary beam [136]. SEs are relatively insensitive to atomic number, but hold information on the surface topology of the sample.

2.5.5 EELS and CL for Plasmonics

Both EELS and CL have been used to map LSPR behaviour, showing similar responses for the plasmon modes of a nanowire [44, 157]. The main difference is that EELS detects the excitation of an LSPR mode and CL collects the radiative decay. There are several examples in literature showing good complements between the data acquired from EELS and CL studies [158–161].

Early EELS studies of plasmons were done on aluminium because of its high energy free-electron-like behaviour in the visible and UV regimes, which did not require monochromated systems to study. Surface plasmons were mapped in energy-filtered imaging mode [43] and later in STEM mode [144]. The introduction of commercial monochromators extended the accessible energy range of EELS to below 1 eV and even below 0.5 eV [44]. Further advances in system stability and instrumentation technology has allowed probing of collective phonon modes and vibrational excitations below 0.1 eV [134, 162, 163].

Although EELS is not directly related to the local density of states of optical excitations in the sample [164], some efforts have been made to link it to the electromagnetic local density of states (EMLDOS) [159, 165] and the optical extinction properties of the sample [80]. EELS maps compare well with the near-field enhancements expected under optical illumination and include information on higher order multipole modes, which optical methods struggle to access [69, 79], although EELS can be blind to strong LSPR hotspots if the fields are perpendicular to the beam [164].

CL is limited to the detection of radiative modes, while EELS can detect both bright and dark modes, although in large particles retardation effects can make dark modes radiative and thereby detectable in CL as well [69, 89]. On the other hand, conventional EELS is polarization-insensitive and it is not easy to differentiate dif-

ferent LSPR modes with the same symmetry without beam-shaping techniques [166], whereas CL can also detect the polarization state and emission angles of the emitted light and from this the combination of multipole moments present in the sample can be derived [167]. Momentum-resolved EELS also allows direct mapping of the dispersion relation of the surface plasmon [82].

Both techniques are well-suited to the study of localized fields in sub-wavelength objects, benefiting from the high spatial resolution of the electron microscope, which is particularly advantageous when studying complicated or asymmetrical shapes which are difficult to study optically or by applying analytical equations [80]. The spectromicroscopy techniques allow spectral features to be related to specific topological features on the sample [80].

2.6 Data Analysis

The spectrum image poses an interesting challenge for navigation and visualization, which is usually solved by representing the dataset as spatially-resolved energy slices at chosen peak energies and as spectra extracted from specific locations on the sample. This can be done using the Python software described in Chapter 6.

The raw datasets from both EELS and CL contain contributions from the instrumentation used to acquire the data. This includes contributions from noise in the beam or camera, the different sensitivities of the camera at different pixels or to different wavelengths, and beam broadening from the point spread function (PSF) of the microscope system or the camera. Both the EELS spectrometer and the visible spectrometer and angle-resolved cameras in the CL system use CCD cameras to detect signal.

2.6.1 CCD Response

A CCD is separated into an array of discrete pixels, each of which can be located by the coordinate vector $\tilde{\boldsymbol{s}} = (l_1, l_2)$. The intensity ($I(\tilde{\boldsymbol{s}})$) readout at each pixel can be described mathematically by Equation 2.6. The electrons detected at each pixel ($\zeta(\tilde{\boldsymbol{s}})$) are multiplied by the gain coefficient of each pixel ($g(\tilde{\boldsymbol{s}})$), which represents the relationship between the number of counts read from a pixel and the number of electrons which created signal in that pixel [168].

In the EELS camera, the gain coefficient is affected by the conversion efficiency of the electron scintillator (how many photons are emitted per incoming electron), the optical coupling efficiency through the fibre optic array, and the sensitivity of the CCD array [168]. The gain may also be affected by dirt on the camera, the accelerating voltage used, or fluctuations in the response of individual pixels coming from sensitivity differences in the CCD diodes, non-uniformity in the optical coupling system, or variations in the scintillator sensitivity, which add a fixed pattern of noise to the spectrum [138, 168]. To handle differences in gain across the CCD camera, the

spectral readout is divided by a saved reference image representing the response of the array to broad, flat, undispersed illumination [138]. In the CL camera, the gain response of each pixel must also account for variances in CCD efficiency as a function of the incoming wavelength and is taken into account with the system response function.

$$I(\tilde{\boldsymbol{s}}) = g(\tilde{\boldsymbol{s}})\zeta(\tilde{\boldsymbol{s}}) + b(\tilde{\boldsymbol{s}}) + \eta(\tilde{\boldsymbol{s}}, \zeta) \tag{2.6}$$

The other two terms in Equation 2.6 represent the background intensity, $b(\tilde{\boldsymbol{s}})$, and a noise term, $\eta(\tilde{\boldsymbol{s}}, \zeta)$ [168]. The background intensity primarily comes from the dark current of the CCD array. Thermal excitation of electron-hole pairs within each pixel creates background thermal noise [138, 168], even when no light is hitting the camera, thus 'dark' noise. The dark noise is corrected for after acquisition on the microscope; after every SI, a dark reference is acquired with the beam blanked and the same acquisition parameters, then subtracted from the acquired gain-corrected spectrum.

The noise term comes from a combination of sources. There is Poisson shot noise in the electron beam [122, 138, 168, 169], Poisson noise in the conversion processes from electrons to photons and back and in the bias applied on the CCD, as well as Gaussian readout noise [138,168,169]. The effects of noise are minimized by increasing the amount of signal acquired, if the experiment allows, through increasing the beam current or acquisition time.

Point Spread Function

An electron from an EELS experiment hitting one pixel on the camera, $\tilde{\boldsymbol{s}}'$ may contribute to the signal obtained at another pixel, $\tilde{\boldsymbol{s}}$; the signal read out of each pixel is the sum of the signal from electrons hitting that pixel and signal leaking over from nearby pixels [168]. The probability of this happening is the PSF of the camera, which affects the energy resolution by blurring the acquired spectrum [168]. The PSF causes information from one location in the original image or spectrum to be redistributed to other locations in the measured image [170]. Lateral scattering of the electron beam within the scintillator blurs the collected readout, back-scattered electrons off other components in the spectrometer or off the scintillator add background signal away from the primary beam location, and mixing between neighbouring channels in the camera all contribute to the spectrometer's PSF [143]. Signal mixing can come from light spreading within the scintillator, as light emitted near one location may propagate to a neighbouring pixel before being collected in the fibre optic array, or from cross-talk and inter-channel coupling in the fibre optic or diode array itself [138, 168].

Given a detector PSF, $\xi(\boldsymbol{s}, \boldsymbol{s}')$, in which $\boldsymbol{s}$ indicates a location in the 2D detector plane and $\boldsymbol{s}'$ indicates a different location, the signal collected by each pixel can be described using Equation 2.7a in continuous space, where it is integrated over the area of a pixel, or by Equation 2.7b once the space has been discretized into pixels [168]. Here, $f(\boldsymbol{s}')$ is the incoming electron image at location $\boldsymbol{s}'$, $\tilde{f}(\tilde{\boldsymbol{s}}')$ is the discretized

version of the incoming electron image hitting pixel $\tilde{\boldsymbol{s}}'$, and ξ and $\tilde{\xi}$ are the PSF of the detector in continuous and discrete space, respectively, representing the probability of an electron hitting pixel $\tilde{\boldsymbol{s}}'$ contributing to the signal at pixel $\tilde{\boldsymbol{s}}$ [168].

$$\zeta(\boldsymbol{s}) = \int_{pixel} \mathrm{d}\boldsymbol{s}(\int f(\boldsymbol{s}')\xi(\boldsymbol{s},\boldsymbol{s}')\mathrm{d}\boldsymbol{s}') \tag{2.7a}$$

$$\zeta(\tilde{\boldsymbol{s}}) = \sum_{\tilde{\boldsymbol{s}}'} \tilde{f}(\tilde{\boldsymbol{s}}')\tilde{\xi}(\tilde{\boldsymbol{s}},\tilde{\boldsymbol{s}}') \tag{2.7b}$$

When the assumption that the PSF is uniform over the area of the CCD is made, Equation 2.7a and 2.7b become a convolution product (Equation 2.8) [168–170]. The measured image or spectrum, ζ, is given by the convolution of the true image, f, with the PSF of the acquisition system, ξ^{Acq} [170]. In an EELS experiment, the measured PSF includes not only the PSF of the CCD camera ($\tilde{\xi}$), but also contributions from the intrinsic energy spread of the electron beam and aberrations from the spectrometer [169].

$$\zeta = f \otimes \xi^{\mathrm{Acq}} \tag{2.8}$$

Having corrected the measured signal for the gain coefficient and background addition, the most intuitive way to recover the original image would seem to be to reverse the integral given in Equation 2.7a [171]. Unfortunately, performing this reversal often results in large oscillations in the solution, because any errors or noise in the measured signal are amplified [171].

Instead, statistical estimation methods must be used to estimate the original image. Considering the image as a probability distribution function requires the conditions that the values be non-negative and the integral over the whole image (or spectrum) must be normalized to 1 [171]. The unique solution to the integral equation is eliminated because it takes into account all of the high frequency noise components in the measured image and attributes them to the 'true' image [168, 171, 172]. Any other calculated solution with a reasonable error, given the experimental parameters, is acceptable as a solution, allowing for statistical fluctuations in the data without needing the original image to also possess these fluctuations [171, 172]. In fact, the unique solution will have a residual error of 0, which is not a realistic expectation for any experiment, and so the unique solution is not be considered as an acceptable answer [172]. The Richardson-Lucy deconvolution (RLD) algorithm is one method to try and reconstruct the original image through iterative deconvolutions [170, 172]. Compared to Fourier-based methods, the RLD is less sensitive to noise, but is computationally more expensive [170].

2.6.2 Richardson-Lucy Deconvolution

The RLD algorithm was first developed to help remove the effect of the PSF of the Hubble space telescope's reflection mirrors [170] and has been used in astronomical applications and more recently, in electron microscopy and spectroscopy [122, 168, 169]. The algorithm is used to sharpen images [168] and increase the effective energy resolution of EELS spectra [122, 169].

Given the value at ζ_l, an arbitrary pixel in the degraded image, the probability of there having been $\tilde{f}_l$, a pixel value in the original undegraded image, is given by Bayes' Theorem in Equation 2.9, normalized by the sum over the image pixels $\tilde{\boldsymbol{s}}$ [170].

$$\mathrm{P}(\tilde{f}_l|\zeta_l) = \frac{\mathrm{P}(\zeta_l|\tilde{f}_l)\mathrm{P}(\tilde{f}_l)}{\sum_{\tilde{\boldsymbol{s}}} \mathrm{P}(\zeta_l|\tilde{f}_{\tilde{\boldsymbol{s}}})\mathrm{P}(\tilde{f}_{\tilde{\boldsymbol{s}}})} \tag{2.9}$$

This equation is reformulated into an iterative equation (over N_{it} iterations) in terms of the probabilities of signal being detected at each pixel (Equation 2.10) [170].

$$\mathrm{P}_{N_{\mathrm{it}}+1}(\tilde{f}_l) = \mathrm{P}_{N_{\mathrm{it}}}(\tilde{f}_l) \sum_l \frac{P(\zeta_l|\tilde{f}_l)P(\zeta_l)}{\sum_{\tilde{\boldsymbol{s}}} P(\zeta_l|\tilde{f}_{\tilde{\boldsymbol{s}}})\mathrm{P}_{N_{\mathrm{it}}}(\tilde{f}_{\tilde{\boldsymbol{s}}})} \tag{2.10}$$

Simplifying this equation by the substitution of equivalent forms of the probabilities ($\mathrm{P}(\tilde{f}_l) = \tilde{f}_l/\tilde{f}$, and $\mathrm{P}(\zeta_l|\tilde{f}_l) = \mathrm{P}(\xi_l^{\mathrm{Acq}}) = \xi_l^{\mathrm{Acq}}/\xi^{\mathrm{Acq}}$) gives Equation 2.11 [170]. An initial guess must be made for $\tilde{f}_{l,N_{\mathrm{it}}=0}$ (the values at pixel l in the original image) if the undegraded image is unknown, as is usually the case in experiments. $\xi_{\boldsymbol{s}}^{\mathrm{Acq}}$ is the PSF and ζ_l is the degraded image. Equation 2.11 is iterated over N_{it} to improve the approximation to the original image ($\tilde{f}_{l,N_{\mathrm{it}}+1}$) [170]. A typical initial guess might be the measured image or spectrum, then the estimate is updated with the result of the iteration and the algorithm continues [122, 169, 172].

$$\tilde{f}_{l,N_{\mathrm{it}}+1} = \tilde{f}_{l,N_{\mathrm{it}}} \sum_l \frac{\xi_l^{\mathrm{Acq}}\zeta_l}{\sum_{\tilde{\boldsymbol{s}}} \xi_l^{\mathrm{Acq}} \tilde{f}_{\tilde{\boldsymbol{s}},N_{\mathrm{it}}}} \tag{2.11}$$

As the number of iterations increases, the solution converges to the maximum likelihood (ML) solution for the ideal image [169]. However, it must be noted that the ML solution is dependent on the measured image, which contains noise, and so the ML solution will include this noise [171, 172]. Therefore, it is not necessarily desirable to reach the ML solution. After a small number of iterations, the calculated image will start appearing worse because of the noise, and the number of iterations must be limited to find the optimum result [170–172]. The algorithm assumes that the noise in the degraded image is Poisson noise, which is mostly true in the case of inelastic electron scattering statistics [143], except for the Gaussian readout noise, which is neglected [122, 168].

If the estimate of the ideal image is incorrect or has large-scale differences from the measured image, the division in the equation, with the previous estimate in both

the numerator and denominator, allows the algorithm to correct it quickly [170, 172]. Small-scale differences between the estimate and the measured image tend to get averaged out in the convolution sum and are corrected much more slowly, which is beneficial because these fluctuations are typically more representative of noise [172].

The first few iterations fit the large scale structure of the data, providing a good estimate of the ideal image, but continued iterations begin to fit the smaller scale, high frequency components of the measured data (Figure 2.14), introducing additional noise components into the estimated ideal image or spectrum [171]. After many iterations, the data becomes overfitted and the algorithm starts to fit the noise (Figure 2.14, yellow spectrum); the algorithm should be halted when the statistical uncertainty between the estimate and the ideal solution is less than the experimental error [171,172]. The challenge for the user is to know when this transition from fitting the low frequency, large-scale components to fitting high frequency, small-scale components occurs, and to stop the iterations before amplifying the noise; this transition is not always evident, but means that there is an optimum number of iterations for this algorithm [171]. After the optimum number of iterations is exceeded, the calculated image begins to emphasize high frequency noise, exhibiting wavy or speckled features and hindering the interpretation of the data [122,168–172]. Small noise spikes in the data may become large spikes in the reconstruction, with lower values next to the spike to maintain the flux/normalization condition.

If the normalization condition and non-negative condition are fulfilled, the algorithm will converge to the ML solution [172], maintaining the non-negativity and flux (normalization) conditions [169]. The algorithm does not feel the effect of small errors in the PSF, which allows the use of an experimental PSF [122,169] acquired over vacuum, but even this representative PSF may be different from that in the acquired data because of differences in inelastic scattering or instabilities in the microscope [169]. It is possible to use a smoothing function to reduce the effect of high frequency noise in the solution, as has been done to some benefit by Bellido *et al.* [122], but convolving the image or spectrum with a smoothing function means that this smoothing function must be taken into account during the deconvolution, making the process more complex [172].

In electron spectroscopy, the PSF includes the effect of the energy spread in the primary beam, which blurs the spectrum, and the effect of optical aberrations of the spectrometer lenses, which can cause electrons of one energy to hit pixels in the camera representing electron counts of a different energy, as well as the PSF of the EELS CCD itself [122,169]. Spectrometer aberrations can cause a point source in the entrance plane to appear as a non-point image on the detector plane by scattering electrons away from this point [169]. The PSF takes into account spectrum blurring because of both the camera PSF and because of other components in the microscope.

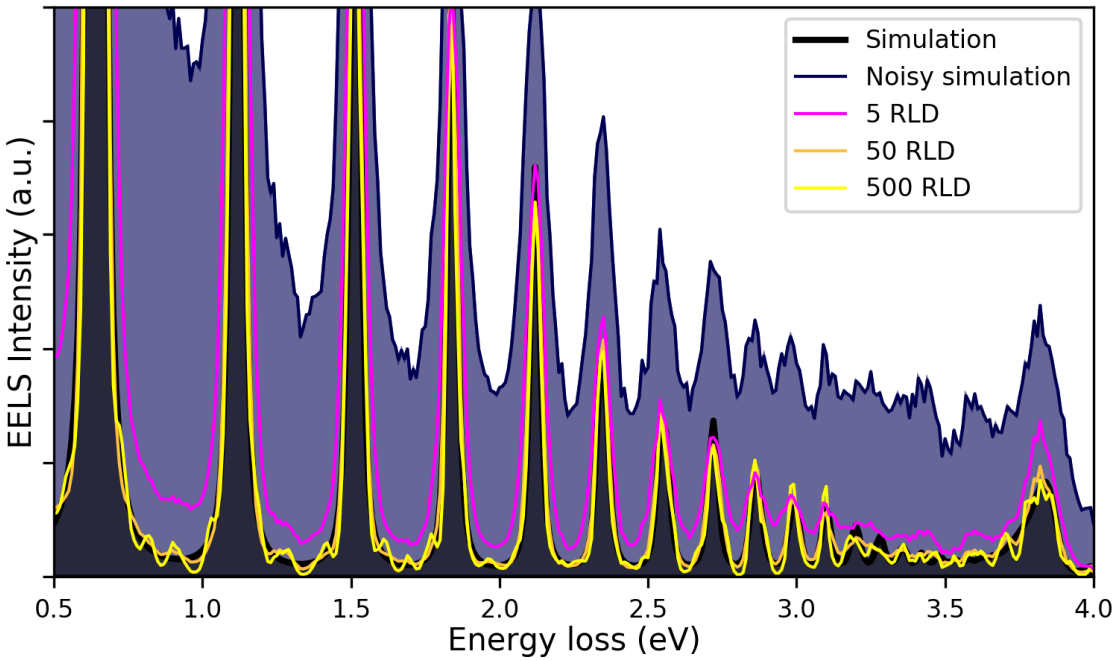

Figure 2.14: Overfitting of the Richardson-Lucy deconvolution algorithm. A simulated spectrum from a plasmonic nanorod convolved with a point spread function (black) with added Poisson noise (dark blue). Pink, orange, and yellow spectra show the noisy spectrum after the number of RLD iterations indicated in the legend.

2.6.3 CL System Response

The CL radiation emitted from the sample must bounce off the paraboloid mirror, pass through the SEM chamber window and a focusing lens, and travel through an optical fibre after reflecting off a mirror, before it is dispersed by the spectrometer grating and imaged using the CCD or a photodiode array. Each of these components has different efficiencies at different wavelengths, particularly the grating and camera [148]. The spectral dependence of the optical component efficiencies can alter the shape of the CL spectrum and must be corrected for to obtain the true spectrum as emitted from the sample [148]; to do this, a reference spectrum is used. Transition radiation from aluminium or silver is used for calibration; it has a simple spectral shape between the IR to the UV regions, is easily excited by electrons, and the spectral yield can be quantitatively calculated after measuring the electron beam current [148, 153]. The theoretical spectrum ($I_{\text{theory}}(\lambda)$) for transition radiation is calculated analytically and compared to the collected spectrum ($I_{\text{obs}}(\lambda)$) to obtain the correction function ($T_{\text{corr}}(\lambda)$) (Equation 2.12) [148].

$$T_{\text{corr}}(\lambda) = \frac{I_{\text{theory}}(\lambda)}{I_{\text{obs}}(\lambda)} \tag{2.12}$$

An experimental correction function is acquired using a flat metal film for all desired grating positions and acquisition conditions. The correction function is then used as a reference ($T_{\text{corr}}(\lambda_l)$) for future measured spectra ($I_{\text{obs}}(\lambda_l)$) to obtain the true spectrum as emitted from the sample ($I_{\text{true}}(\lambda_l)$) by applying Equation 2.13 to the measured spectrum.

$$I_{\text{true}}(\lambda_l) = T_{\text{corr}}(\lambda_l) I_{\text{obs}}(\lambda_l) \tag{2.13}$$

To display the CL emission as a function of energy instead of a function of wavelength, the unequal translation between the wavelength and energy must be accounted for in the binning. Each channel in the spectrometer represents a range of wavelengths ($\Delta\lambda$) binned into one pixel: to change the central channel value into the equivalent energy, the energy range (ΔE) for each channel is also needed in Equation 2.14 [148].

$$I_{\text{true}}(E_l) = I_{\text{obs}}(\lambda_l) T_{\text{corr}}(\lambda_l) \frac{\lambda_l}{E_l} \frac{\Delta E}{\Delta \lambda} \tag{2.14}$$

2.7 Modelling the Plasmonic Response

Modelling of the plasmonic response is used to confirm and explain experimental results by accessing parameters not retrievable experimentally, such as the surface charge or EM field distribution of an LSPR. Simulations for LSPR responses typically involve defining a nanoparticle or nanostructure and solving Maxwell's equations under an incident EM excitation source.

Simple geometries such as planes, spheres, or ellipsoids allow analytical solutions [69], but more complicated geometries require numerical methods to solve Maxwell's equations [173]. The geometry of a plasmonic nanostructure is discretized by dividing it into, for instance, a collection of discrete dipoles (the discrete dipole approximation), or a series of connected nodes (finite element method: FEM). The discretization may define either the volume and surrounding space (FEM) or only the surface of the nanostructure (boundary element method: BEM). Maxwell's equations are solved at each node using information from neighbouring nodes, so the computational resources required increase quickly with the number of nodes in the mesh. Simulating the response of large nanostructures with fine features requires a high density mesh to accurately model the geometry, which makes the computation very expensive. Defining a surface mesh reduces the computational resources required by only defining interfaces between features and not defining the volume of each material.

2.7.1 FDTD

In finite difference time domain (FDTD) calculations, both time and space are discretized and finite difference equations are used to solve Maxwell's equations [174,175]. Solutions for the electric and magnetic fields are calculated half a time and space step

off from each other, so that the full set of equations does not need to be solved simultaneously for both time and space [175]. The spatial grid defined must be small enough to resolve the smallest features of the structure and response under study, but finer meshes increase the computational resources required [174–176]. Demands for a fine mesh can be mitigated by using a variable mesh size over the structure and environment, increasing the mesh density near fine features [175]. Nevertheless, the method may still require heavy computational resources [175, 177]. The time-dependent response can be converted to a spectrum through a Fourier transform to put the solutions into frequency space. FDTD modelling (Lumerical Inc.) was used to model the spectral response of the Sierpiński fractals presented in Chapter 3; specific details of the modelling parameters are given in Section 2.8.6.

2.7.2 FEM

Finite element methods involve discretization of space around user-defined meshes, allowing great freedom in defining the shape and structure of the mesh, at the cost of computational resources. Both the nanostructure itself and the space around the nanostructure are discretized. The calculation is computationally expensive, as the discretization of the structure and surrounding space must be fine enough to resolve the features of the structure or of the EM response.

An EM plane wave is used as the excitation source and the response of the structure is calculated using Maxwell's equations at each node. The toroidal dipole structures in Chapter 5 were modelled using COMSOL Multiphysics® FEM. More details on the simulations performed for the T4 array are given in Section 2.8.7.

2.7.3 BEM

The boundary element method was used for all of the nanostructures studied in this thesis. A Matlab toolbox, Metallic Nanoparticle Boundary Element Method (MNPBEM), provides the necessary implementation to solve Maxwell's equations. More detail on this toolbox can be found in [178, 179]; the parameters used for the simulations presented in this thesis are described in Section 2.8.8. In BEM, only the surfaces of nanostructures are discretized into a finite element mesh and Maxwell's equations are solved to find surface charges and interface currents in response to an electron beam or other EM source. The surfaces are defined as abrupt interfaces with separate media on either side defined by their dielectric function, which may be frequency dependent [177, 180]. The media inside each surface is assumed to be homogeneous.

Given the finite element mesh, dielectric functions, and EM source, the induced fields ($\boldsymbol{\varepsilon}^{\mathrm{ind}}(\boldsymbol{r}_{\mathrm{e}}(t), \omega)$) within the nanostructure are solved for and then used to calculate the energy loss probability, given in Equation 2.5, as a function of frequency, which is converted to electron energy loss. BEM relies on linear algebra techniques to solve the

equations on the nodes of the discretized surface mesh [69]. The plasmonic response is represented in terms of linear combinations of eigenvectors and eigenvalues [69].

The BEM simulations can be done in either the quasistatic approximation or by taking retardation into account. Retardation effects become important when there is a noticeable time delay between a field reaching one side of a nanostructure and the same field propagating to reach the other side, and affect the energy and behaviour of the LSPR. In the quasistatic approximation, the full set of Maxwell's equations do not need to be solved, but instead Poisson's wave equations can be used, making it computationally faster by a factor of six compared to the retarded approach [69].

2.8 Experimental Conditions

In this section the experimental conditions used to fabricate the samples, acquire EELS and CL data, analyze the data, and perform the simulations for the work shown in this thesis are detailed.

2.8.1 Electron Beam Lithography

The substrates used for LSPR studies must be compatible with TEM analysis techniques, so TEM grids from Norcada are used. The grids are silicon and each have a 3 by 3 arrangement of electron transparent windows with silicon nitride membranes, of thickness 50 nm. Thinner membranes are also available, but the thicker membranes are less likely to fracture during processing (as also found in [125]) and give a better yield after all the processing steps, something which is particularly important in the double-step EBL used for the 3D structures. An outline of the process flow for EBL of 3D structures is given in Figure 2.15.

Spincoating

Before spincoating, each TEM grid is plasma-cleaned for three minutes at 30 W in a combination of hydrogen, nitrogen, and argon gases to clean off residual contamination and enhance the wetting of the PMMA layer. A single drop of PMMA from the tip of a fine needle was deposited on each of the grids for spincoating. Spincoating of the TEM grid for a single planar layer (Sierpiński fractals and the first layer of the 3D VSRRs) was done at a spin speed of either 4000 RPM or 6000 RPM for 90 s using 950 kg/mol PMMA in anisole (3%). For better pattern definition and lift-off, a layer of 495 kg/mol PMMA in anisole (3%) is spun at 6000 RPM for 90 seconds before the layer of 950 kg/mol PMMA. The lower molecular weight layer underneath the higher molecular weight creates an undercut profile during exposure and development (Figure 2.16), improving the yield of lift-off (similar to [181]). The faster spin speed of 6000 RPM produces a smoother layer of electron beam resist over the silicon nitride windows. To prevent the vacuum of the spincoater from breaking the TEM grid

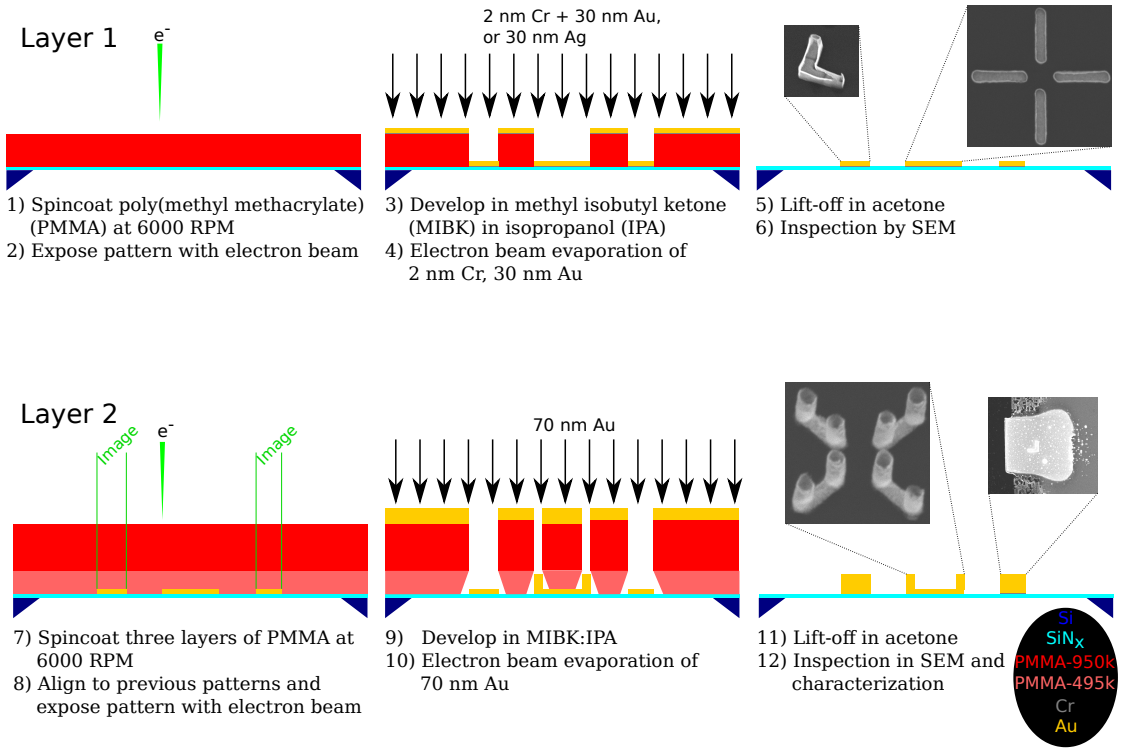

Figure 2.15: EBL processing steps for 3D nanostructure fabrication. Electron beam resist is spincoated and exposed according to a CAD pattern which includes sacrificial alignment marks; the resist is developed and metal is deposited before lift-off in acetone and inspection under the SEM; the process is repeated with a three layers of resist (495, 950, 950 kg/mol PMMA) and alignment to the previous pattern to deposit the pillars of the VSRRs.

windows, the grid was stuck onto a sticky pad, which was then stuck to a square glass coverslip to be placed on the spincoater chuck.

After spincoating, the grid was removed from the sticky pad and post-baked on a hotplate at 175°C for 5 minutes. This was done separately for each layer for multi-layer resists. The post-bake encourages any remaining anisole to evaporate and is above the melting point of PMMA, allowing it to flow and redistribute to a produce a smoother surface. The small size of the grid means that the resist coating is often not even and there tends to be significant build-up of resist bead around the edges of the grid, which can cause thickness variation over the surface of the grid and makes the quality and thickness of resist difficult to reproduce.

Patterning

After this, the grid is ready for lithographic patterning in the SEM, a JEOL-JSM 7000F equipped with Nanometer Pattern Generation System (NPGS) software. NPGS is an add-on system to a standard SEM column, which takes control of the SEM scan coils and beam blanker in order to pattern arbitrary shapes from CAD files [126].

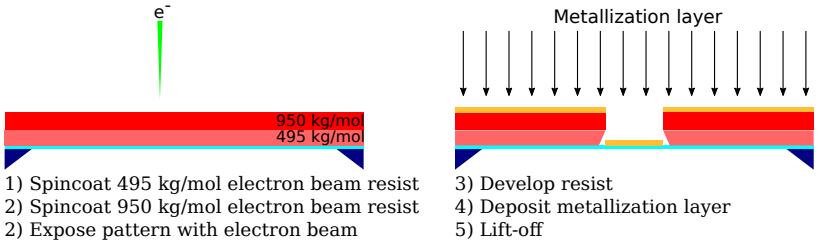

Figure 2.16: The use of two electron beam resist layers to create an undercut profile and improve lift-off.

DesignCAD^{TM} 2000LT or DesignCAD^{TM} 3D MAX (both from IMSI Design®) is used to make the CAD files for NPGS to read. The SEM is carefully aligned on the lowest current setting using the smallest objective aperture, aperture 4 (30µm diameter), to achieve the lowest beam current and smallest probe size possible. The SEM is operated at 30 keV, with approximately 20-25 pA of beam current at a 10 mm WD.

The exposure for each pattern is set in the NPGS program as an area dose. Usually, a CAD pattern with multiple copies of each desired structure is used to apply a range of doses and later select the best outcome. Typical dose ranges are from 300 to 800 $\mu C\,cm^{-2}$ in each pattern. Typical line spacings of the raster scan are set to 5-15 nm between writing points, or up to 50 nm for very large structures. Most patterns are written at SEM magnifications between 1000× and 4000×, corresponding to a field of view between 120 × 120 µm and 30 × 30 µm.

After exposure, the TEM grid is removed from the SEM and developed for 120 seconds in a solution of methyl isobutyl ketone in isopropanol (MIBK:IPA, 1:3) before rinsing in isopropanol and drying under a stream of nitrogen. The grid is then mounted on an SEM stub for metallization in an electron-beam evaporator.

Metallization and Lift-off

The grid is coated with 30 nm of silver (Chapter 3: Sierpiński fractals) or 2 nm of chromium and 30 nm of gold (Chapters 4, 5: VSRRs and toroidal structures) using a Gatan Precision Etching Coating System. The chromium acts as an adhesion layer between the gold and the silicon nitride [121], although it is known to increase surface plasmon damping [182]. Typical parameters used for coating are 150 pA of beam current, at 6 keV accelerating potential, with a rotation of 25 RPM and a rocking angle of $20°\,s^{-1}$ to a maximum of 5°. These conditions give a deposition rate of approximately 1 $Å\,s^{-1}$.

After coating, lift-off is performed in acetone, either by squirting acetone tangentially to the grid or leaving the grid in a spinning acetone bath on a stirplate until most of the material has been removed. The gold structures can be left overnight to soak in acetone if lift-off by the other methods proves difficult, but the silver structures

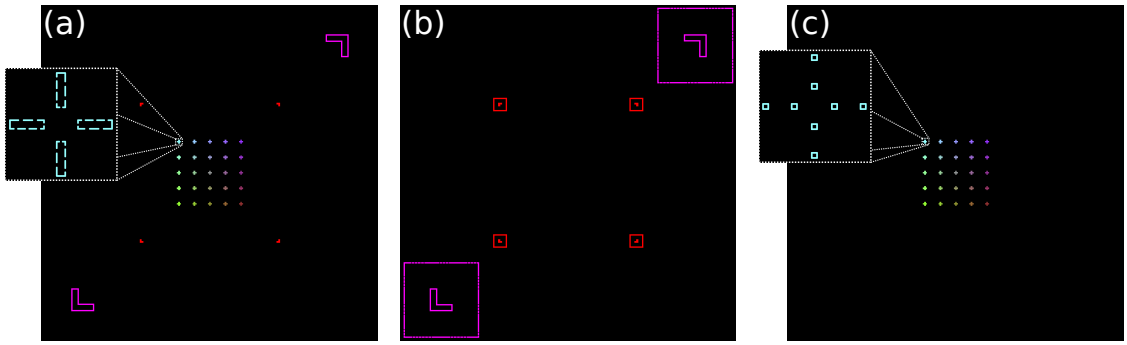

Figure 2.17: CAD patterns used to fabricated a T4 array of VSRRs. (a) The pattern for the first step includes six sacrificial 'L'-shaped alignment marks at two different scales (pink and red) and an array of the bottom bars for a toroidal array, each colour maps to a different exposure dose; (b) the pattern for the alignment procedure, the electron beam is scanned over the squares to create a local SE image and the alignment marks are manually aligned to the secondary electron image, then the transformation matrix is calculated from the movement of the alignment marks and applied to the following CAD pattern; (c) CAD pattern for exposing the pillars of the VSRRs on top of the bottom bars after alignment.

will react with impurities in the acetone and degrade quickly if left for too long in solution. After this, the grid is rinsed in isopropanol to remove the acetone (which can cause contamination build-up under the electron beam in the TEM) and dried under a stream of nitrogen. The silver samples degrade quickly from small concentrations of sulphur dioxide in the air or contaminants within the grid itself, so analysis of the silver samples must be done relatively quickly after fabrication, within a few days.

Three-Dimensional Structures

For the VSRRs, the EBL process must be repeated to deposit a second layer of gold and build the pillars on top of the bottom bar. During the first step for these structures, sacrificial alignment marks are added to the CAD pattern to be patterned around the base pattern (Figure 2.17(a)); alignment routines in NPGS image these alignment marks, using them to shift or rotate the next CAD pattern to be written (Figure 2.17(b, c)). Accuracy of the alignment routine is approximately 15 nm, based on observations of the common misalignment errors and the limits set during the process. Examples of the three CAD files required for the construction of a 3D nanostructure are shown in Figure 2.17.

The second layer for the pillars of the SRR needs to have thicker metal layers, so the spincoating must be modified to account for this. A layer of 495 kg/mol PMMA in anisole is spincoated at 6000 RPM for 90 s and post-baked. This procedure is repeated under identical conditions for two layers of 950 kg/mol PMMA. This is effectively a three-layer electron beam resist, which is much thicker than the single layer and so allows for a thicker metal layer to be deposited. It is also intended to produce a sloping resist profile with a wider base, as shown in Figure 2.16, with the

lower molecular weight PMMA on the bottom layer [128, 181]. Exposure conditions in the SEM must be modified accordingly, and exposure doses range between 800 and 3000 $\mu C\,cm^{-2}$. At such high doses, the resolution of the EBL process would normally be ruined by additional dose from BSE in the substrate, but using the 50 nm thick silicon nitride membrane as the support greatly reduces the BSE dose and makes such high doses possible without significant resolution degradation. Alignment is done first at low magnification using the larger set of alignment marks, then at the magnification with which the pattern will be written using the smaller set of alignment marks (Figure 2.17(b): pink and red sets). Alignment is done manually by imaging selected windows over the pattern area and adjusting the position of an alignment pattern overlay; NPGS then calculates the transformation matrix and applies it to all subsequent patterns.

After exposure, the same development routine is followed as for the single layer resist, followed by coating of 70 nm of gold in the electron beam evaporator under identical deposition conditions. Lift-off is faster with the thicker resist and can be done in the same manner as before. It has been found that the pillar diameter must be at least 100 nm, otherwise the pillars will not deposit properly, likely because of resist collapse in the high aspect ratio pattern. This process (Figure 2.15) results in the 3D VSRR or toroidal structures, ready for EELS analysis.

2.8.2 EELS

All EELS SI data was acquired on an FEI Titan 80-300 STEM equipped with a monochromator, image corrector, and Gatan Tridiem spectrometer (model 865), operated at 80 kV in STEM mode. For the experiment on the VSRR and toroidal arrays of VSRRs, the microscope was equipped with an SFEG and the monochromator was used in accelerating mode at a potential of 800 V and an excitation between 1.5 and 1.8 rad (more detail on the operation of the FEI monochromator and column can be found in Appendix B). Prior to the Sierpiński fractal study, the gun was replaced with an XFEG, for which the accelerating monochromator mode is disabled. For the fractals, therefore, a decelerating monochromator at a potential of 3000 V and excitation of 1.5 was used.

Typical spot sizes used are 7-9. The spot size is chosen largely based on the need to increase or reduce the beam current for the EELS acquisition. For the additive fractals, a beam current of approximately 100 pA was obtained on spot 9, while on the subtractive fractals, a beam current of approximately 250 pA was obtained using spot 7. Typical condenser aperture settings were either a rectangular slit or 2000 µm aperture in C1 and either a 10 or 30 µm aperture in C2. The slit in the C1 plane is used to cut the monochromated beam, but also greatly reduces the beam current. A small aperture in C2 can also be used to cut the monochromated beam for good energy resolution, in which case the slit is not needed.

Camera lengths of 57 mm (T4 data), 72 mm (VSRR, T5, T6 data), and 89 mm

(fractal data) were used, keeping the size of the projected spot small in order to collect the most current in the spectrometer. A 1 mm spectrometer entrance aperture was used for all datasets, with a typical 1 ms exposure time. The exposure time is limited by the mechanical shutter of the spectrometer, which cannot blank the beam faster than approximately 1 ms. A fast acquisition time reduces the likelihood of saturation on the ZLP and improves the energy resolution by acquiring faster than the electronic jitter in the beam, which blurs the spectrum if a long acquisition time is used. A dispersion of 5 meV/channel was used on the spectrometer for all datasets, except for the T4 data, for which a dispersion of 10 meV/channel was used. A spectrometer binning of 1×16 (spectrum $\times$ vertical binning) was used for all datasets except for the T4 array data, which was acquired with 1×32 binning.

EELS spectrum images are acquired simultaneously with dark-field signal from the ADF detector. The magnification of the STEM image was set based on the size of the structure under study, with typical values between 40 k$\times$ and 115 k$\times$.

Energy Resolution

With the SFEG equipped (VSRR, T4, T5, T6 datasets), the typical energy resolution, as determined by the FWHM of the ZLP, was between 50 and 60 meV. An example of the FWHM (in meV) for what can be considered good performance for the instrument is shown in Figure 2.18(a), showing the fluctuations in FWHM over an SI acquisition after filtering out pixels with low ZLP counts. For the T4 datasets, with a larger spectrometer dispersion, the energy resolution of the raw data was slightly worse, approximately 60-70 meV. Instabilities in the high tension supply (ripple) cause variation in the FWHM of the ZLP across a spectrum image (high frequency oscillations in Figure 2.18). The optimal energy resolution achieved on the SFEG was approximately 40 meV.

Upon switching the gun to the XFEG, the best achievable energy resolution was degraded to approximately 55 meV. Reducing the monochromator potential and deviating from standard operating conditions can further improve the energy resolution to 45 meV with a 5 meV/channel dispersion on the spectrometer, though this strategy was not used for any data shown in this thesis. For most experiments, an energy resolution of between 55 and 65 meV was obtained. Figure 2.18(b) shows the variation of the FWHM within an SI obtained with the XFEG. The energy resolution is observed to be slightly worse than that of the SFEG SI (a), but the stability of the ZLP is improved, with a less extensive tail in the histogram towards higher FWHM values.

2.8.3 EELS Analysis

The RLD algorithm was used on the acquired SIs to help deconvolve the effect of the microscope system PSF from the acquired spectrum [122], effectively improving the energy resolution to approximately 30-40 meV for most datasets. Deconvolution and analysis of the SIs was performed using custom Python software (Chapter 6 [183]). For

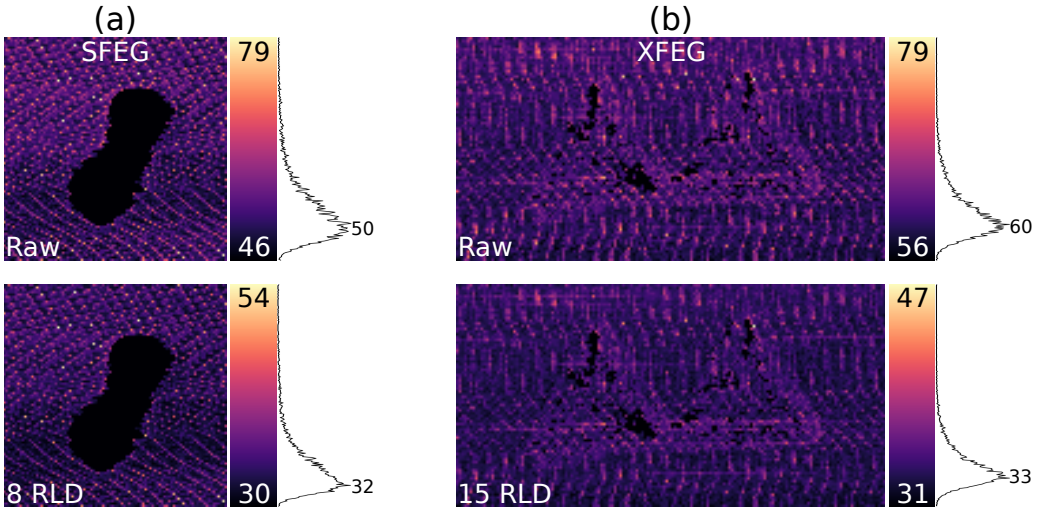

Figure 2.18: Comparison of the energy resolution of a typical spectrum image acquired with the SFEG and the XFEG. (a) The FWHM of the ZLP for each pixel of an SI acquired with the SFEG before (top) and after (bottom) eight iterations of the RLD algorithm; (b) FWHM of the ZLP for each pixel of an SI acquired with the XFEG before (top) and after (bottom) 15 iterations of the RLD algorithm. The colourbars and accompanying histogram to the right of each image show the colour mapping to the ZLP FWHM in meV. The FWHM values shown are linearly interpolated from the two spectrometer channels closest to half the intensity of the ZLP (on both positive and negative sides of the ZLP). Pixels with a ZLP of less than 30000 counts have been filtered out and appear as black.

data acquired with the SFEG, typically 8 RLD iterations were used, beyond which the noise begins to dominate the signal. The XFEG with a decelerating monochromator provides more beam current and the typical number of RLD iterations used on the fractal data was increased to 15. Before deconvolution, a threshold is applied to the SI to mask out the low intensity pixels, such as those over top of the nanostructure, so that the noise of these pixels doesn't dominate the SI after deconvolution.

Examples of the effect that RLD has on the effective resolution are shown in the lower row of Figure 2.18 for SFEG (a) and XFEG (b) datasets. Remarkably, the ability to apply more RLD iterations to the less-noisy XFEG data results in very similar effective FWHM values for the deconvolved SFEG and XFEG SIs. The RLD appears to have a greater benefit on the spectra with lower resolution (larger FWHM) within the SI, as observed through the reduction in the high-value histogram tail of the deconvolved datasets compared to the raw data.

EELS Difference Maps

Subtraction of the EELS resonance maps in Chapter 4 was done by rescaling the intensity of each map between 0 and 1 and performing a pixel-by-pixel subtraction.

Linewidth Fitting

Fitting of the linewidth of the dipolar peaks of the Sierpiński fractal to the experimental EELS data was done using the Python Astropy library [184]. Raw spectra were averaged over selected areas, then deconvolved with 15 RLD iterations. The three corners of each triangular prism were used to provide three datapoints in the fitting. A model composed of a power law and a Lorentzian peak was used to fit the ZLP tail and the dipolar plasmon peak within the energy region of the plasmon peak; the FWHM of the Lorentzian function was used as the linewidth of the plasmon peak.

The presence of the ZLP in an EELS experiment makes interpretation of the linewidth of a plasmon peak complicated: the ZLP is not only present as a large neighbouring peak with an extensive overlapping tail, but it is convolved with the signal from the sample. RLD is an iterative procedure to deconvolve the ZLP from the sample signal, but the algorithm relies on an approximation to the PSF of the microscope system [122] and does not perfectly remove the effect of the PSF from the acquired data. The linewidth of the dipolar plasmon peak was estimated for different numbers of deconvolution iterations, and it was found that although the values may still change as the number of iterations is increased (and deconvolution artifacts start to affect the results), the trend found between different structures remains the same. Contributions to the linewidth, even after several deconvolution iterations, include the PSF of the microscope and plasmon damping, which is strongly dependent on the fabrication and surface quality of the nanostructures. In the comparison of Sierpiński fractals presented in Chapter 3, all four samples were fabricated in parallel with each other, the EELS data was acquired on the same day using the same experimental conditions, and the same number of RLD iterations was performed using the same PSF reference.

Linewidth fitting of the magnetic and toroidal dipole peaks on the tilted T4 array in Chapter 5 was done using a similar procedure with a power law and two Lorentzian functions.

2.8.4 CL

CL data was acquired on a field emission SEM, an FEI XL-30 equipped with a Schottky FEG and operated at 30 kV. The SEM is equipped with an in-house CL mirror and optics collection system (Figure 2.19), the prototype of Delmic's commercial system [149, 153, 185–187]. The CL system has an aluminium parabolic mirror with an acceptance angle of 1.46π sr and a numerical aperture of 0.95, with a 600 µm diameter hole vertically above the mirror focus. The sample is located at the focal point of the mirror. The mirror collimates and directs radiation from the sample out of the SEM chamber through a transparent vacuum flange.

The light passes through an achromatic lens onto a Peltier-cooled CCD camera (Princeton Instruments (PI), PIXIS 1024B) for angular-resolved (AR) imaging. A pair of flip mirrors direct the CL radiation into multimode fibre optics to either a

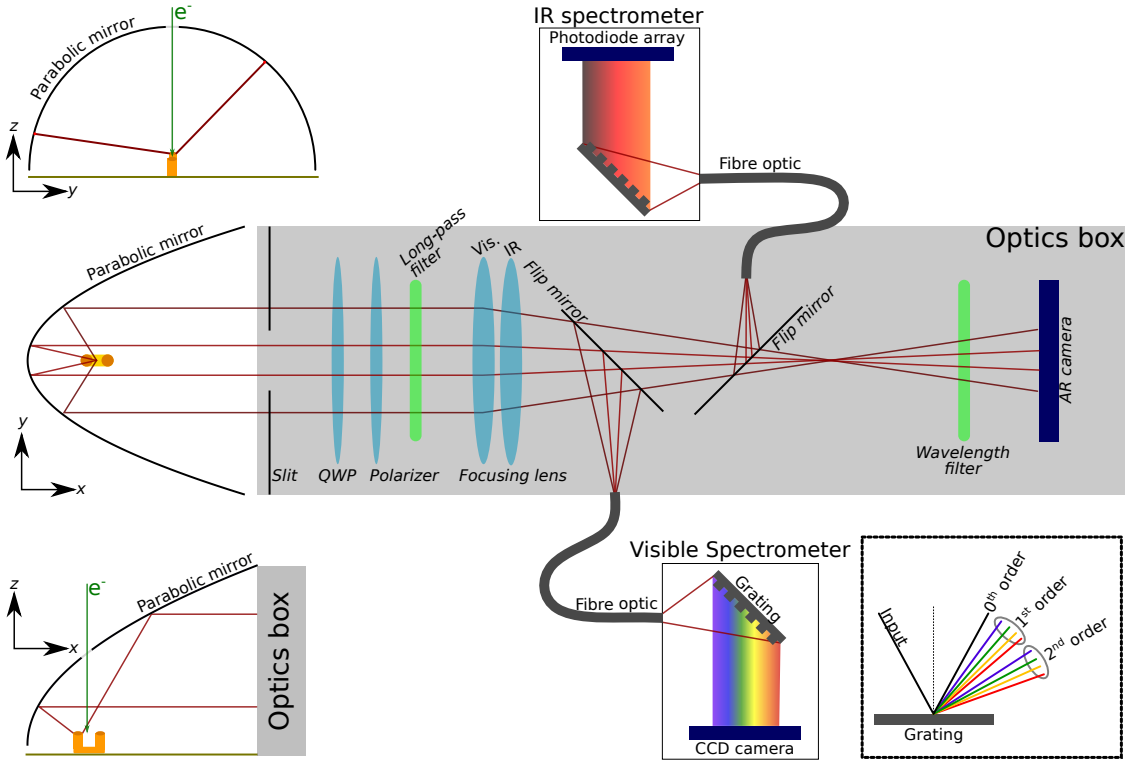

Figure 2.19: Schematic of the CL optics acquisition system, including front, top, and side views of the mirror-sample configuration (left column) and the layout of the optics box. All components in the optics box are removed or inserted into the optical beam path as needed for the experiment. A small schematic of the diffraction orders from the spectrometer grating is given in the lower right.

visible spectrometer (PI Acton SP2300i) or an IR spectrometer (PI Acton SP2300i). Each spectrometer possesses several diffraction gratings and a liquid nitrogen cooled silicon CCD array (visible spectroscopy: PI Spec-10 100B, 1340 × 100 pixels), or InGaAs photodiode array (IR spectroscopy: PI OMA V 1.7, 1024 × 1 pixels) [153].

When performing AR imaging, the visible light lens is used to transfer an image of the mirror onto the AR-CCD camera. Optionally, a quarter wave plate (QWP) and linear polarizer (LP) may be used to determine the polarization state as a function of emission angle, and a bandpass wavelength filter (BPF) may be inserted for some spectral information on the AR pattern. The LP filter used is ultra-broadband, rated from 300 to 4000 nm. The QWP chosen depends on the spectral range under study.

AR information is lost when performing spectroscopy, but much finer spectral resolution can be obtained. The slit can be used to select parts of the mirror for spectroscopy and is used when doing polarization-resolved spectroscopy to filter out light which has significantly changed polarization state after reflection off the mirror [185] before it is integrated in the spectrometer. The QWP and LP filter are used to determine the polarization state of the radiation. A visible focusing lens is used to focus light into a fibre optic to the visible spectrometer or pass the mirror image

Table 2.2: Quarter wave plate (QWP) and linear polarizer (LP) rotation settings to filter the polarization states of the emitted radiation for linearly (Vertical, Horizontal, 135°, and 45°) and left- and right-handed circularly (LHC, RHC) polarized light.

QWP	Polarizer	Polarization
0°	0°	Vertical
270°	90°	Horizontal
315°	45°	135°
45°	135°	45°
270°	45°	LHC
270°	135°	RHC

to the AR camera; likewise, an IR focusing lens is used to focus the radiation into a fibre optic to the IR spectrometer. Further descriptions of the CL optics hardware used can be found in [187].

Visible Light Spectrum Imaging

Spectrum images on a single VSRR (Chapter 4) were acquired using 7.5 nA of electron beam current (aperture 3, spot number 4) and an acquisition time of 1 s per spectrum. The SIs on the toroidal structure (Chapter 5) were acquired with approximately 6.5 nA of beam current (aperture 3, spot number 4) with an acquisition time of 300 ms. The spectrometer grating used has 150 groove/mm with a 800 nm blaze, and was centred at a wavelength of 700 nm (VSRR) or 750 nm (T4 array). Full vertical hardware binning and 2× (VSRR) or 1× (T4 array) spectral binning was used for the spectrometer CCD. The sensitivity of the visible light spectrometer and collection system is approximately 10-15 % [187]. A SE image is acquired simultaneously with the CL SI.

Determining the polarization parameters of the emitted spectrum requires the use of the QWP and LP combination. The differences in s and p reflection coefficients of the parabolic mirror mean that the polarization state of the light can change upon reflection, depending on the angle of incidence [185]. A 3 mm slit is used to block light from the sides of the mirror, keeping only light which has reflected off the mirror at close to normal incidence with minimal change in polarization, because there is no way to correct for the changes in polarization at different parts of the mirror once the radiation has been integrated and dispersed in the spectrometer. The QWP and LP filter are used in six different combinations (Table 2.2) to acquired six consecutive spectrum images. The QWP is efficient between 610 and 850 nm, limiting the spectral range at which circular polarization results can be trusted.

For the polarimetry SIs, the 800 nm blaze grating was used, centred at 750 nm. The beam current was reduced to 1.7 nA (aperture 3, spot number 3) to avoid melting the nanostructures during the repetitive acquisition process. An acquisition time of

900 ms was used for each spectrum in the SI. To collect the directional response of the VSRR, the VSRR was first oriented horizontally relative to the mirror, ensuring that the SEM scan rotation was set to 0, then the stage was rotated by 90° to change the orientation of the VSRR relative to the mirror. The spectrometer was set to a gain of 4, a readout rate of 0.1 MHz, and 2× spectral and full (100×) vertical binning. A full description of the Stokes parameters in angular and Cartesian coordinates can be found in Appendix A.

Visible Light Angular-Resolved Imaging

Angular-resolved images were collected by leaving the electron beam stationary in one location and integrating the light hitting the PIXIS AR camera. The slit, QWP, linear polarizer, and mirrors are removed, leaving only a focusing lens and a wavelength filter. 40 nm (FWHM) BPFs were used, centred at 850 nm, 700 nm, and 650 nm, as indicated the relevant figure in Chapter 4. A beam current of 7.5 nA was used (aperture 3, spot number 4) and the integration time was 10 s for each AR image.

Infrared Spectrum Imaging

In the IR the sensitivity of the collection system (0.01-0.1 %) is much lower than in the visible regime, partly due to limitations in the photodiode array hardware and partly due to misalignments of the optical components within the IR spectrometer [187].

Initially, a 150 groove/mm grating with a 2000 nm blaze centred at 1500 nm was used to acquire an SI in the IR with 7.5 nA of beam current (aperture 3, spot number 4) and a 15 s acquisition time per pixel. No hardware binning is possible in the IR spectrometer and there is only a single row of photodiode pixels. It was found that in this configuration the second order diffraction of the visible light wavelengths contributes noticeably to the spectrum (more discussion in Chapter 4).

A 980 nm long-pass filter was introduced into the beam path in order to acquire polarimetry datasets in the IR, while filtering out visible light. To increase the SNR, all spectral sensitivity was sacrificed by using the zeroth diffraction order of a 600 groove/mm grating with a 1600 nm blaze, concentrating all of the collected light into a few pixels in the centre of the photodiode array. Similarly to the visible light polarimetry acquisitions, six consecutive SIs were acquired using the QWP (1100-2000 nm range) and polarizer settings given in Table 2.2 and a 3 mm wide slit in front of the mirror. With the increase in SNR thanks to the concentration of radiation on the camera, a lower acquisition time of 2.5 s per pixel in the SI was used, with a beam current of approximately 7.1 nA (aperture 4, spot number 4). The IR SI was acquired with the sample rotated vertically relative to the mirror and SEM image, but the long acquisition time and high beam current damaged the sample before a second polarimetry set with a 90° stage rotation could be completed.

2.8.5 CL Data Analysis

CL spectral data must be corrected for the dark noise of the camera and for the system response efficiency. A dark reference was acquired by blanking the electron beam and collecting a spectrum with the same acquisition parameters as the dataset; a substrate reference accounts for both dark noise and emission from the substrate and was acquired using the same parameters by leaving the electron beam dwelling on the silicon nitride membrane far from any plasmonic nanostructure. Spikes of high intensity in the visible light datasets are corrected for by averaging the value of nearby pixels, on both the SI and AR cameras.

Spectrum Imaging

The system response for a set of grating settings has been calculated previously and loaded from a reference file [187]. The CL spectrum image data for both IR and visible light was processed in Python [183]. The substrate references were subtracted from the spectrum before applying the system response function.

In the polarimetry datasets, the six SIs were aligned manually to each other using the SE image to correct for drift in between acquisitions, before calculating the spatially resolved Stokes parameters. For the IR polarimetry datasets, all of the signal is concentrated in a few pixels in the centre of the photodiode array: the substrate reference was applied and then these central pixels were integrated at each pixel in the SI to retrieve a single spatial image for each IR polarimetry SI acquired. On the visible datasets, the Stokes parameters are retrieved as a function of both space and radiation wavelength. The Stokes parameters were calculated by performing pixel-by-pixel operations on the six SIs, following Equation A.7.

$$\begin{pmatrix} S_0 \\ S_1 \\ S_2 \\ S_3 \end{pmatrix} = \begin{pmatrix} P_H + P_V \\ P_H - P_V \\ P_{45} - P_{135} \\ P_{RHC} - P_{LHC} \end{pmatrix} = \begin{pmatrix} (QWP_{270}, LP_{90}) + (QWP_0, LP_0) \\ (QWP_{270}, LP_{90}) - (QWP_0, LP_0) \\ (QWP_{45}, LP_{135}) - (QWP_{315}, LP_{45}) \\ (QWP_{270}, LP_{135}) - (QWP_{270}, LP_{45}) \end{pmatrix} \tag{2.15}$$

Angular Resolved Imaging

The AR datasets were corrected for the emission from the silicon nitride substrate and plotted in polar coordinates using in-house Matlab code from the lab of Prof. Polman.

2.8.6 FDTD Simulation Parameters

FDTD simulations were performed on the Sierpiński fractal structures (Chapter 3) by Danielle M. McRae, under the supervision of Dr. Lagugné-Labarthet at the University of Western Ontario. The following section has been adapted with permission from

"Carving Plasmon Modes in Silver Sierpiński Fractals" [188].

FDTD modelling (Lumerical *Inc.*) was used to simulate the optical scattering cross-section, electromagnetic fields, and charge distributions of the Sierpiński fractals. The silver fractal structures were of sizes as indicated in the relevant figures in Chapter 3 and Appendix C, using a thickness of 30 nm. Inverse fractal structures were constructed by etching the same fractal structures in a silver layer of the same thickness. The structures were placed on a silicon nitride substrate. Materials were modelled using the dielectric functions of silver from Palik [113] and silicon nitride from Luke [189].

The Sierpiński fractal structures of 285 nm side length were meshed with a grid with sizes of 1.5 nm in the x- and y-directions and 2 nm in the z-direction. For the largest Sierpiński structures, a mesh of 6.5 nm was used for the x- and y-directions, while maintaining the 2 nm mesh in the z-direction. In the simulation region outside of the structure, the mesh was set to at least 10 mesh cells per wavelength. To truncate the computation region, perfectly matched layers (PML) were applied in the x-, y-, and z-axes. Symmetry boundary conditions were applied along the x minimum boundary when applicable, in order to reduce computation time.

2.8.7 FEM Simulation Parameters

Finite element method simulations of the T4 toroidal array were performed using COMSOL Multiphysics® by Dr. Ahmed Elsharabasy under the supervision of Prof. M. Bakr at McMaster University. An incident plane wave propagating from one side and polarized normal to the substrate was used as the excitation of the plasmonic nanostructure. The dielectric function of the nanostructure was modelled using a Drude model.

2.8.8 BEM Simulation Parameters

All BEM simulations were done using the MNPBEM Matlab toolbox [179]. The toolbox allows direct calculation of the EELS loss probability and the radiated fields for CL, in addition to surface charges and electric and magnetic field distributions at selected electron beam locations and loss energies.

Some examples of the meshes used for BEM simulations are shown in Figure 2.20. The meshes for the Sierpiński fractal structures, the planar SRRs, and the T4 array were defined using the built-in mesh generator in MNPBEM, while that of the VSRR was created in Blender 3D modelling software [190] and imported using an open-source code [191]. The MNPBEM mesh generator is designed for planar structures and struggles with the 3D structures of Chapters 4, 5. The mesh imported from Blender has well-defined features to mimic the sample, but is a dense mesh and requires a lot of memory, restricting the use of Blender meshes to the relatively simple isolated VSRR.

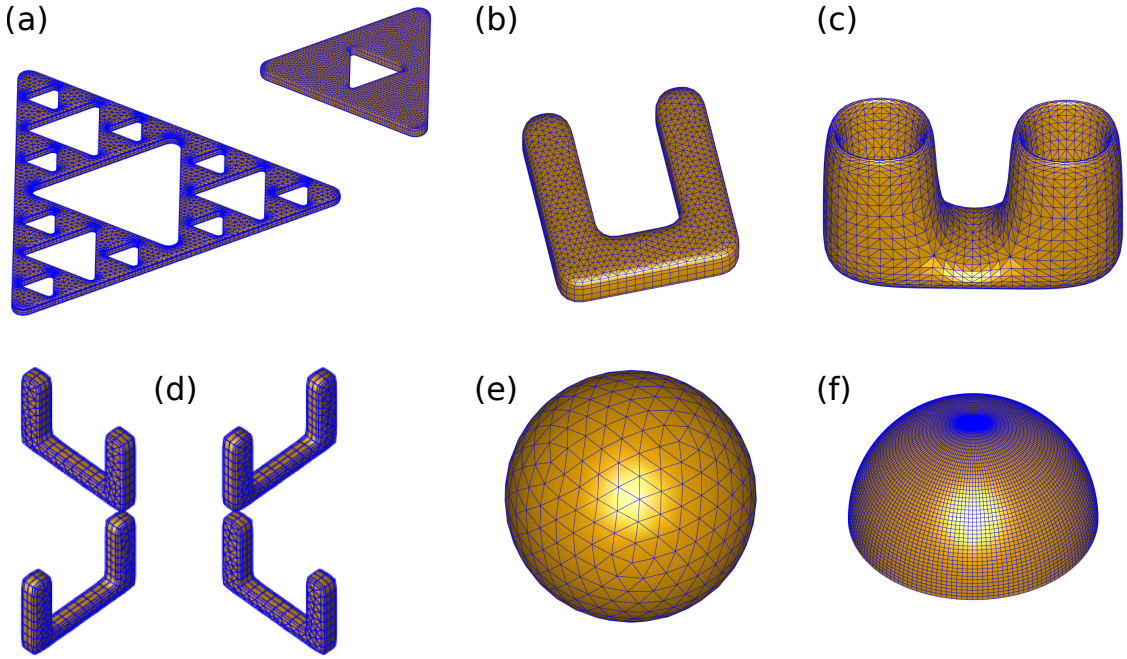

Figure 2.20: Example meshes used for MNPBEM simulations. (a) Two meshes used for the Sierpiński triangle eigenmode calculations; (b) MNPBEM-generated mesh used for planar SRR calculations; (c) Blender mesh used for the VSRR calculations; (d) MNPBEM-generated T4 array; (e) spherical mesh used to integrate the CL radiation from a nanostructure for spectrum or map calculations; (f) hemispherical mesh used for polarimetry calculations.

Fractal Calculations

The mesh sizes for the fractal structures (Figure 2.20(a)) were 310 nm on each side of the triangular prism for the smallest Generation 0 prisms and 620 nm for all of the other structures, except for Generation 3, which was made larger (1240 nm) to accommodate the extra small triangular apertures without errors in the mesh. Each fractal structure is 30 nm thick. The maximum mesh size (maximum allowed size of a discretized face) was set to 5 nm for the smallest Generation 0 prisms and Generation 1 prisms with small apertures (less than 70 nm on a side); 10 nm for the Generations 0.5, 1.5 and the remaining Generation 1 fractals; and 15 nm for the Generation 2 and 3 fractal structures. The fineness of the mesh was chosen to balance the definition of small features with the computational resources required by dense meshes. The dielectric function of silver from Johnson and Christy [110] was used for the fractal prisms, with the dielectric environment set to a constant value of 1.

Split Ring Resonator

The mesh for the planar SRR (Figure 2.20(b)) was defined using a maximum mesh size of 10 nm. The bottom bar has a length of 300 nm and breadth of 75 nm; the

pillars are 250 nm long; and the whole structure is 30 nm thick.

The VSRR mesh created in Blender (Figure 2.20(c)), was scaled so that the length of the VSRR is approximately 250 nm. The dielectric function of gold from Johnson and Christy was used for the nanoparticle; the dielectric environment was set to a constant value of 1.

To calculate the CL scattering cross-section, the far-field intensity as a function of energy around the structure is integrated over a full sphere (Figure 2.20(e)). The EELS and CL spectra are calculated by simulating an electron beam located at a given position and calculating either the EELS probability or CL scattering cross-section. The intensity maps are obtained by selecting the energy of a peak in the spectrum and calculating the EELS probability or CL scattering cross-section as the simulated electron beam position is changed, simulating a raster scan. The mirror symmetries present in the VSRR are used to reduce the computational time by calculating the response only over one quarter of the VSRR and extrapolating the results.

To calculate the Stokes parameters and AR images from the VSRR, the far-field radiation emitted was calculated using a hemisphere discretized into 50 segments along the θ direction and 150 segments along the ϕ direction (Figure 2.20(f)). The far-field electric and magnetic fields along the directions defined by the surface normals of the hemisphere are saved for each electron beam location and imported into Python [192]. In Python, the fields are transformed from Cartesian to spherical coordinates and the Stokes parameters are calculated to obtain the AR polarimetry plots. To calculate the spatially resolved Stokes parameters, a mask representing the mirror and slit is applied to the hemisphere, after which the Stokes parameters are calculated and averaged over the remaining mesh faces. More detail can be found in Appendix A

Fitting of the AR Stokes parameters of the VSRR dipolar mode to a pair of analytical dipole moments was done using least squares fitting from the curve fitting toolbox in Scipy v. 1.1.3, (Python 3.6). The S_3/S_0 parameter as a function of θ and ϕ is used as the reference for the fitting function. The vector components of the electric and magnetic dipoles, and the relative magnitude and phase of the magnetic dipole were left open as parameters to be optimized.

Toroidal Array

The T4 array (Figure 2.20(d)) was created using four rotated planar resonators. To reduce the computational time and cause an artificial blueshift of the LSPR modes into an area covered by the experimental dielectric function, the mesh used is relatively rudimentary. To aid in blueshifting the low energy modes, the size of the structure is scaled down to have VSRRs approximately 30 nm long and 20 nm high and silver [110] instead of gold is used as the material. A quantitative comparison with the experimental data is not needed at this point, and the approximation used should not change the nature of the LSPR modes found. A minimum mesh size of 2.5 nm is used for the T4 VSRRs. The response of the tilted structure was done by rotating the whole T4 array around the x-axis by 40°.

The electric and magnetic field vectors were calculated at a series of points on a plane defined by (x, y, z) coordinates, in response to electron beam excitation at a chosen location and the energy loss corresponding to the magnetic and toroidal dipole peaks, respectively.

2.9 Concluding Remarks

This chapter has covered the background theories and techniques that are used in this thesis work. Effort has been made to include references for relevant papers in the field or for helpful textbooks which explain the concepts in far more detail than is given here. More explanations on plasmon behaviour and previous studies from the group can be found in the theses of Dr. E.P. Bellido and Dr. D. Rossouw [193, 194], in addition to the other resources given in the references. Further descriptions of CL and the CL set-up can be found in the theses of Dr. Coenen and Dr. Brenny from the lab of Prof. Polman [187, 195]. Also given in this chapter are the experimental parameters used to fabricate, collect, and analyze the EELS and CL data presented in this thesis.

The concepts reviewed in this chapter are relevant to each of the results chapters (Chapters 3, 4, 5). Each results chapter also contains a small review of the concepts unique to that chapter.

Chapter 3

Sierpiński fractals

In this chapter, the spatial localization and energy of the LSPR modes of the first three generations of Sierpiński fractal nanoprisms are investigated using STEM-EELS, FDTD simulations, and BEM simulations, with the goal of further predicting the properties of LSPR modes in higher generations of fractals. STEM-EELS has proved itself to be a powerful technique in uncovering the LSPR behaviour of lithographed nanostructures with high spatial resolution [123]. The Sierpiński fractal uses the ever-popular triangular nanoprism, which has shown its usefulness in a variety of applications [196–198], as its basic building block.

The LSPR behaviour is studied in two types of fractals, referred to here as subtractive and additive fractals. In subtractive fractals, the whole structure is the same size for all generations, which are created by introducing and growing triangular apertures into the parent; the behaviour of LSPR modes and the importance of structural variables in subtractive fractals is explained using the equivalent circuit theory and the Babinet principle. In the additive fractal, successive generations of fractals are constructed by adding triangular prisms onto the previous generation, resulting in increasingly larger structures; hybridization theory is applied to explain the modes seen in higher fractal generations.

FDTD simulations were performed by Danielle McRae at the University of Western Ontario, under the supervision of Prof. François Lagugné-Labarthet.

3.1 Background

This section contains a brief review on some of the necessary concepts used specifically in this chapter to understand the behaviour of the plasmonic Sierpiński fractals. Following this section is the discussion of the experimental and theoretical results about the Sierpiński gasket. Of particular importance in the interpretation of the plasmonic response of the fractals are the Babinet principle, originating in antenna theory, and the equivalent circuit theory of LSPR.

3.1.1 Fractals

Fractals were first described mathematically in the late 1800s, but little attention was paid to them until Benoit Mandelbrot began to use computer programs to draw fractal geometries and found a startling likeness between fractals and the behaviour of the natural world: random fractals could be used to describe hilly regions, cloud formation, or coastlines, among other things [200]. Once ignored as a quirk of mathematics, fractals are now used in several applications, ranging from aesthetic designs [201]; to image compression algorithms [202]; to modelling of fluid mechanics [203], soil processes [204], or astronomical events [205]; to multiband antennas in the telecommunications industry [206, 207].

Non-random fractals are constructed from infinite loops of simple equations, creating, for instance, the Koch snowflake [208], Cantor sets, or the Sierpiński gasket [209]. Fractals are of non-integer dimension and represent an infinitely recursive pattern on progressively smaller length scales, although physical constructions of fractals must be truncated because of practical limitations to creating an infinitely recursive object.

This chapter will focus on the Sierpiński gasket and its use as a platform for supporting localized surface plasmon resonance modes. The Sierpiński gasket is a very interesting model system in which to explore the behaviour of plasmon resonances on multiple length scales.

3.1.2 Fractal Antennas

Fractal shapes are used in commercial telecommunications for broadband and multiband antennas. The drive to use fractal shapes as antennas came from a desire to make antennas frequency-independent. The fractal self-similarity on multiple length scales gives them the ability to couple to many different frequencies, since the wavelength that an antenna can couple to most efficiently is proportional to the size of the physical antenna structure. The fractal antenna is also known for its efficient use of space: comparing a simple loop antenna with a fractal antenna occupying the same space, the fractal antenna is able to couple to longer wavelength radiation and so use space more effectively. A fractal structure is electrically 'longer' than a simple straight wire or loop of equivalent spatial footprint, because of the highly convoluted

perimeter inherent to fractal geometries [210]. It is noted, however, that the benefits of using higher generations of fractals to couple to longer wavelengths eventually becomes negligible, as successive generations cause only negligible redshifts to the resonant wavelength [210].

Fractal antennas are also known to have smaller quality factors than comparable loop or wire antennas, because of their more efficient occupation of space, meaning that fractals have narrower peaks than the comparable patch or wire antenna. The quality factor of an antenna is a measure of how efficiently the antenna radiates energy vs storing energy, and, for many antennas, is proportional to the inverse of the bandwidth of the antenna [210]. In previous work, plasmonic fractal structures have been revealed to have self-similar hierarchical resonances dependent on the fractal generation [123, 211, 212].

Sierpiński Gasket

The Sierpiński gasket, or Sierpiński fractal, first described by W. Sierpiński [209] in 1915. The 0th generation (hereafter referred to as 'G0') of this fractal is an equilateral triangle. The first generation of the Sierpiński fractal is created by connecting the midpoints of the edges of the G0 equilateral triangle, dividing the G0 triangle into four equilateral triangles (Figure 3.1, Subtractive Fractals). The middle triangle is then removed, leaving behind three equilateral triangles of half the size as the original: this is the Generation 1 ('G1') fractal. The Generation 2 ('G2') fractal is created by repeating the process for each of the three small equilateral triangles, dividing them into four new, even smaller, triangles and removing the centre. Each successive generation has three times the number of small triangles as the previous generation; the smallest triangles are half the size of the smallest triangles of the previous generation, giving the gasket a scaling factor of two, a fractal dimensionality of 1.585. This creation algorithm results in a structure which maintains the same overall size, but develops smaller and smaller sub-units as the generations advance.

Alternatively, an additional equilateral triangle can be added to G0 as shown in Figure 3.1 (Additive Fractals), to create an intermediate structure (G0.5), to which another equilateral triangle can be added to create the G1 fractal, and so on. This algorithm results in a fractal which grows in size with each successive iteration, but the smallest triangle remains the same size. To construct the true Sierpiński gasket, either of these algorithms is repeated infinitely.

Unfortunately, practical considerations mean that any physically realized fractals must be truncated at a chosen generation, numbered according to the number of iterations of the algorithm required to make the structure. The properties and behaviour of a fractal antenna depend on the generation number; the self-similarity of their physical shape is mirrored in the electromagnetic frequency response [213]. A fourth generation Sierpiński gasket antenna possesses four frequency bands [214] and a fifth generation fractal supports five frequency bands [206], log-periodically spaced in frequency by the fractal scaling factor of 2 [213]. The multiple self-similar length scales

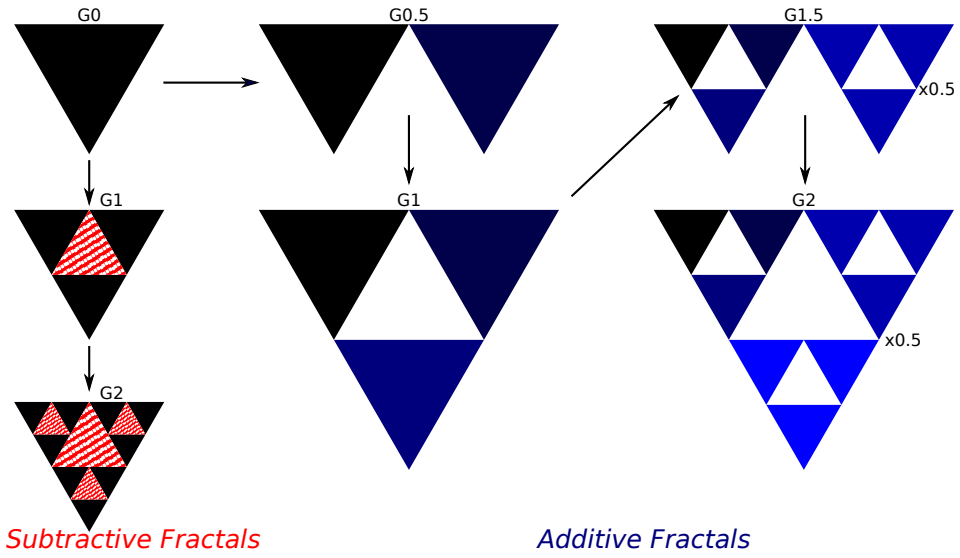

Figure 3.1: Creation of higher fractal generations via subtractive and additive algorithms. Triangular apertures are subtracted from Generation 0 to create Generation 1 and 2 subtractive fractals. More G0 parent units are added to make G0.5, G1, G1.5, and G2 additive fractals. The sizes of G1.5 and G2 fractals have been scaled down by $\times 0.5$ for easier display.

and corresponding multiband response of fractal geometries means that a single fractal antenna can couple to multiple different wavelengths, and so function as multiple antennas occupying the same physical space. Interestingly, the current distributions on Sierpiński gasket radio antennas scale according to the generation involved in the resonance at each band, with similar distributions at different length scales in different frequency bands [213].

In this work, the Sierpiński fractal antenna is scaled down to the nanoscale, to create multiband nanoantennas using LSPR. Previous work on plasmonic Sierpiński gaskets shows that, compared to a similarly sized triangular prism, the Sierpiński gasket shows enhanced field confinement [94, 215–217], either alone or in bowtie geometries. However, little attempt has been made to explain this enhanced confinement or to address higher order plasmon resonances in the fractal structure. The behaviour of LSPR will be studied in this chapter as the fractal generation is increased via both algorithms mentioned above: subtractive fractals, in which holes are carved into the G0 triangle; and additive fractals, in which additional G0 triangles are added to the previous structure to form the next generation, as shown in Figure 3.1.

3.1.3 Babinet Principle

The Babinet principle was developed regarding the behaviour of light passing through apertures. From the optics point of view, this principle states that the wave pattern received after light passes through a diffracting screen (Ψ_S) added to the wave pattern received from the complementary screen (Ψ_{CS}) is equivalent to the pattern resulting

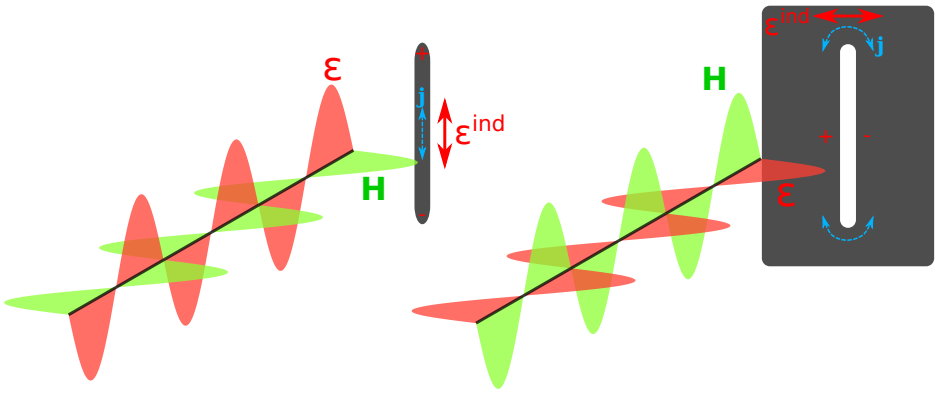

Figure 3.2: Complementary antennas resonate under orthogonal polarizations. Red arrows mark induced electric fields ($\boldsymbol{\varepsilon}^{\text{ind}}$); blue arrows mark induced currents ($\boldsymbol{j}$). The electric ($\boldsymbol{\varepsilon}$) and magnetic ($\boldsymbol{H}$) fields of the incoming EM waves are indicated.

from having no obstacles at all (Ψ_{UN}), and is a useful principle for the calculation of diffraction patterns (Equation 3.1). For instance, the diffraction pattern from a circular aperture is the complement of the diffraction pattern of a circular disk of the same size as the aperture, and adding both together will reveal the unperturbed wave [218]. Perhaps the simplest example of Babinet's principle is that the shadow cast by a screen is the complement of the shadow cast by the complement of the screen, and when the light from the two patterns is added together, there is no shadow.

$$\Psi_{\text{S}} + \Psi_{\text{CS}} = \Psi_{\text{UN}} \tag{3.1}$$

In electromagnetism and the interaction of light with absorbing media, however, Babinet's principle requires some modifications from its original form. The use of Babinet's principle was extended for applications in radio antennas by Booker [219], who realized that the polarization of light must be taken into account when considering the antenna's response in order to understand how the material becomes polarized under the incident light and in which direction the voltage across the antenna is applied. In a dipole antenna, such as a straight wire, the electric field of the incident light must be polarized parallel to the long axis of the wire to induce the desired response; however, for a slot antenna of the same dimensions, the magnetic field of the incident light must be parallel to the long axis of the slot, and the electric field of the light must be polarized perpendicular to the long axis of the slot to obtain the complementary response (Figure 3.2).

Applying Babinet's principle to a conducting screen requires the assumptions that the screen is (i) infinitely thin; (ii) perfectly conducting; and (iii) planar [219]. Babinet's principle applied to conducting planes also requires that, if the screen is exchanged with its complement, the electric and magnetic quantities involved must all be interchanged. If this is done, the transmission patterns of the screen and its complement are complementary.

On a dipole antenna, the incident electric field, polarized along the long axis, induces an oscillating electric dipole along the antenna. Similarly in the complementary slot antenna, the incident field, polarized perpendicular to the slot, induces an electric dipole across the slot, causing ring-like currents to flow around the ends of the slot and inducing an in-plane magnetic dipole along the long axis of the slot, as shown in Figure 3.2 [219, 220]. The slot antenna should have resonance at the same wavelength as the solid antenna, but in response to orthogonal polarization. If the dipole mode of a solid rectangular antenna is excited by vertically (horizontally) polarized light, the dipole mode of the complementary slot antenna resonates under horizontally (vertically) polarized light [219].

The application of Babinet's principle to nanoscale antennas, via the polarization response of LSPR, is still under active study in the plasmonics community. Qualitatively, there appears to be an agreement between the predictions of Babinet's principle and the behaviour of plasmonic antennas and plasmonic slot antennas [221, 222]. EELS is a polarization-insensitive technique, so cannot directly pick up the different responses to orthogonally polarized light in solid and slot antennas, but the technique is sensitive to the electric near-field of the LSPR and detects the change in orientation of the dipolar mode, causing the EELS maps of the solid and slot antennas to appear complementary to each other [221]. However, closer examination of the spectrum reveals spectral shifts between a nanoantenna and its complement [160, 223].

Plasmonic devices break some of the assumptions ((i) to (iii) above) required for a rigorous application of Babinet's principle to plasmonic antennas. In the radio regime, the thickness of the antenna is effectively infinitely thin relative to the wavelength of interest, but on the nanoscale, the thickness and surface roughness of the material are no longer negligible quantities relative to the wavelength of operation. The conductivity of the noble metals in the optical regime is also not 'perfect', whereas conductivity of antenna materials is much higher in the radio frequencies. Despite the difficulties in obtaining quantitative spectral agreement between plasmonic nanoantennas and their complement, Babinet's principle may still be used to discuss the behaviour of the fields of the two antenna configurations, under the knowledge that, because of the violation of the assumptions required to apply Babinet's principle, Babinet's principle is only an approximation and rigorous agreement should not be expected in plasmonic nanoantennas.

3.1.4 Equivalent Circuit Model

First proposed by Engheta *et al.* [224], the equivalent circuit model describes plasmonic and dielectric components as nano-elements of electrical RLC (resistor-inductor-capacitor) circuits based on their reaction to an applied optical field. At typical frequencies used in electrical circuitry noble metals are good conductors, but at optical or IR frequencies the conduction of the metal is through a different mechanism: that of the surface plasmon current or optical displacement current. The metal nanoparticle

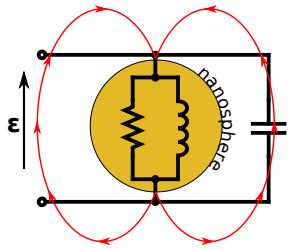

Figure 3.3: Equivalent circuit model for the dipolar mode of a plasmonic nanosphere under electric field (ε) excitation. Inspired by [224].

response to an applied electric field oscillating at optical frequencies can be described by its effective impedance [225]. It has also been shown that it is possible to use the circuit analogy to predict the position of a nanoantenna's resonance frequency, as well as shifts in this frequency caused by changes to the dielectric environment, by matching the effective imaginary impedance of the plasmonic antenna with that of the 'load', or dielectric filling a gap between parts of the antenna [226].

If the real part of the dielectric function of a nanoparticle is positive (*e.g.*, an insulator with no free electrons), then the nanoparticle acts as a capacitor and when a field is applied across it, there is a potential difference across the nanoparticle; if the real part of the dielectric function is negative, as is the case with plasmonic nanostructures, then the nanostructure acts as an inductor. The resistance of the nanocircuit comes from the imaginary part of the material's dielectric function. In a basic plasmonic nanoparticle, when the dipolar mode is excited by an applied field, electrons flow across the surface of the nanoparticle, which acts as a combined resistor-inductor (Figure 3.3). The electric field of the dipolar mode in the surrounding dielectric environment behaves as though the energy is stored in a capacitor, assuming that the dielectric environment has a positive dielectric value at the resonance energy: the dielectric environment acts as a capacitor between the two poles of the plasmonic dipolar mode.

The equivalent circuit theory is used to explain the spectral shifts seen in the subtractive Sierpiński fractal nanostructures as the central triangular aperture is introduced and its size is increased.

3.2 Results on Subtractive Fractal

The LSPR modes of the G0 triangle have been well characterized by Keast *et al.* and Campos *et al.* [227, 228]. The G0 prism supports both edge modes and cavity modes, some of which are degenerate pairs of orthogonally polarized resonances. Adding a triangular aperture into the G0 triangle has a significant effect on some of these modes; to understand this effect and the coupling of the aperture LSPR modes to the G0 LSPR modes, we will first examine the modes present on a triangular aperture in

a solid film (referred to hereafter as 'iG0').

3.2.1 Triangular Aperture

The triangular aperture is the complement of a simple triangular prism, and so the response of the iG0 structures can be predicted by applying the Babinet principle. The G0 prisms of interest have degenerate responses to both horizontally and vertically polarized light, so the iG0 apertures are expected to respond to both vertically and horizontally polarized light equivalently.

We fabricated a series of iG0 structures by patterning apertures inside a silver square of several microns. Comparing the primary EELS peak of these iG0 structures to equivalently sized G0 prisms reveals that although the G0 and iG0 structures may be expected to show EELS peaks at the same energy, there are spectral shifts with no clear trend evident across different sizes (Figure 3.4). Some G0 prisms are blueshifted by almost 200 meV (Figure 3.4(b)), others are redshifted by approximately 100 meV (Figure 3.4(c)), and some, the largest pair of complementary structures fabricated in this work, have dipole peaks with only a difference of 30 meV between G0 and iG0 dipolar modes (Figure 3.4(d)).

The dispersion curve for the primary peak energy of experimental and simulated G0 and iG0 structures is given in Figure 3.5(a). In the simulated structures, the lowest energy peak of the iG0 structure is consistently blueshifted relative to that of the G0 triangle of the same size, which we attribute to the effect of the silicon nitride substrate [222, 229]. The G0 prism and iG0 aperture have different field configurations; in the G0 prism, the dipolar field primarily surrounds the solid triangle (Appendix C, Figure C.3), while in the iG0 aperture, the electric fields traverse the inverse triangle (Figure C.1); the presence of the 50 nm thick SiN membrane may cause different energy shifts because of these differences in field configuration. We must also remember that these plasmonic nanostructures, fabricated from 30 nm thick silver films, are neither infinitely thin nor perfectly conducting, which does not fulfill the requirements of Babinet's principle [160].

Considering the variation in the experimental data, we may conclude that the fabrication quality of each of these structures has a dominant effect on the relative peak energies [223]. Although the same method of fabrication was used for both G0 and iG0, the defects which occur most commonly are different. We observe, upon examination of the ADF images (Figure 3.4), that there is often a flap of material along the edges from the coating and lift-off process, particularly in G0 structures. This material is visible as a region of higher brightness around the edges of the triangle. With the iG0 apertures, this does not occur as frequently, and the edges appear to be much more well-defined, although there is a thickness gradient of silver from the bulk film towards the aperture edges instead of an abrupt interface, due to shadowing during metal deposition. Despite this gradient, the edges of the iG0 aperture are often much cleaner than those of a G0 prism of the same size (*e.g.*, see the largest

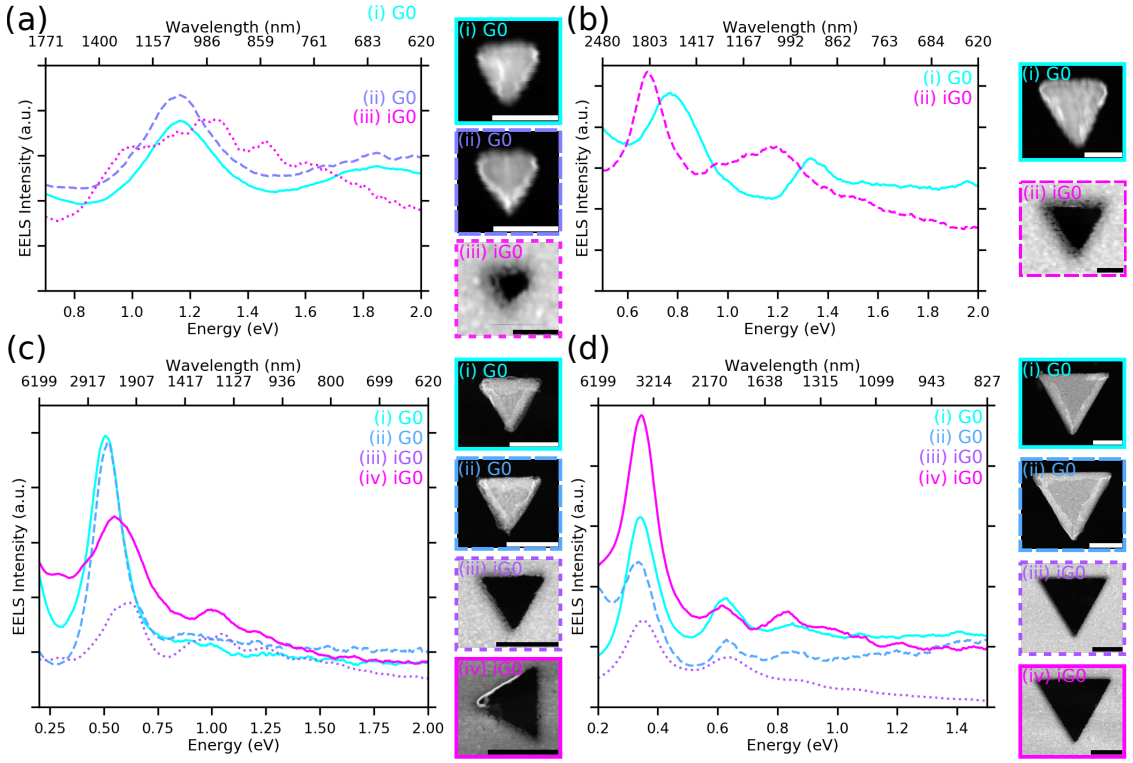

Figure 3.4: EELS dipole peaks for G0 and iG0 structures of different sizes. Structures of side length: (a) 150 nm (scalebars are 150 nm); (b) 285 nm (scalebars are 150 nm); (c) 550 nm (scalebars are 500 nm); and (d) 1100 nm (scalebars are 500 nm). ADF STEM images are shown to the right of each plot.

pair of complementary structures in Figure 3.5(b)). Fabrication defects also explain why the trend is not consistent between different pairs of solid and inverse triangles, since these defects are not controlled or consistent at different length scales, and why the variation seems to become greater at smaller sizes, which are more technically challenging to fabricate.

EELS profiles from the largest pair of solid and aperture nanostructures fabricated in this study are presented in Figure 3.5(c). There is a small blueshift between the primary peak energy of the G0 and iG0 structures, as predicted by the FDTD simulations, and the EELS maps for each edge mode appear to be complementary, agreeing with results on rectangular apertures [221]. The number of modes visible along the edges of each of these structures highlights the effect of the smoother edges of the iG0 structures (Figure 3.5(b,c)); more higher order edge modes are visible on the iG0 structure than the G0 prism.

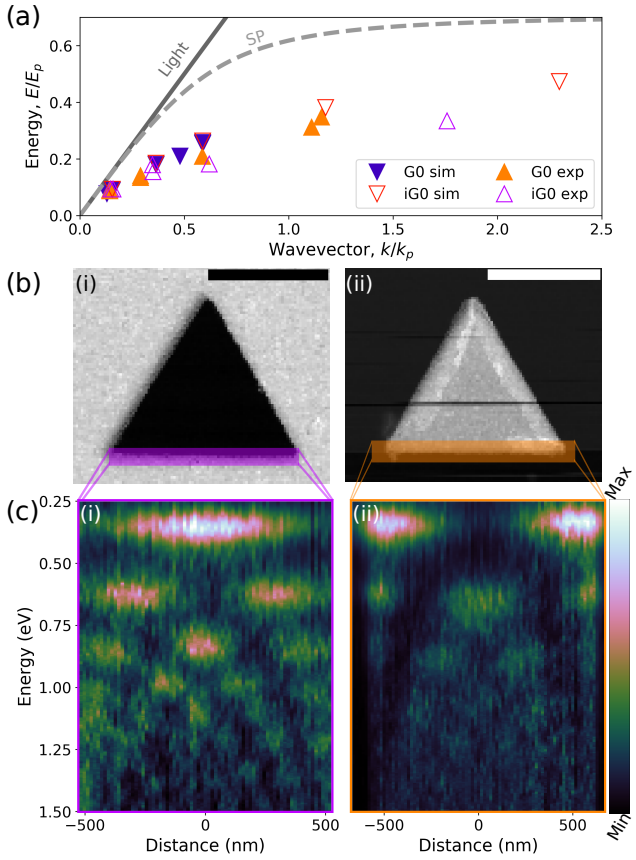

Figure 3.5: Dispersion curves and EELS profiles across an iG0 and G0 structure. (a) Dispersion curves for solid (G0) and inverse (iG0) triangles plotted as fractions of the plasma energy (E_p) and equivalent free-space wavevector k_p. (b) ADF images for (i) iG0 of side length 1130 nm and (ii) G0 of side length 1170 nm (scalebars are 750 nm). (c) EELS intensity profiles across one edge of (i) iG0 and (ii) G0, as highlighted in (b).

Surface Charges

Figure 3.6 shows calculated surface charges for the two lowest energy optical modes of the 285 nm side length iG0 aperture (a), the G0 structure of the same size (b) and a series of G1 triangles (c-e). The calculated surface charges reveal that both the G0 prism and iG0 aperture support degenerate orthogonal dipolar modes, as predicted by Babinet's principle. On the triangular aperture, charges are able to flow around the corners of the aperture (Figure 3.6(a)(i), charge flow indicated by green arrows), but are confined by the edges. The build-up of charges on one edge creates dipolar fields across the aperture, repelling mobile charges on the opposite side and turning the aperture into a capacitor. For higher order modes, a node or nodes are created along each edge, but the corners are not capable of confining charge, so no charge build-up or strong EELS signal is seen at the corners of the iG0 aperture (Figure 3.5(c)(i), Figure 3.6(a)(i)), resulting in the complementary EELS signal and

charge distribution when compared to the solid G0 structure, which effectively confines charges in the corners (Figure 3.5(c)(ii), Figure 3.6(b)). The field configurations for the two degenerate dipolar modes and second optical modes for the solid and aperture triangles are given in Appendix C (iG0: Figure C.1, C.2; G0: Figure C.3, C.4).

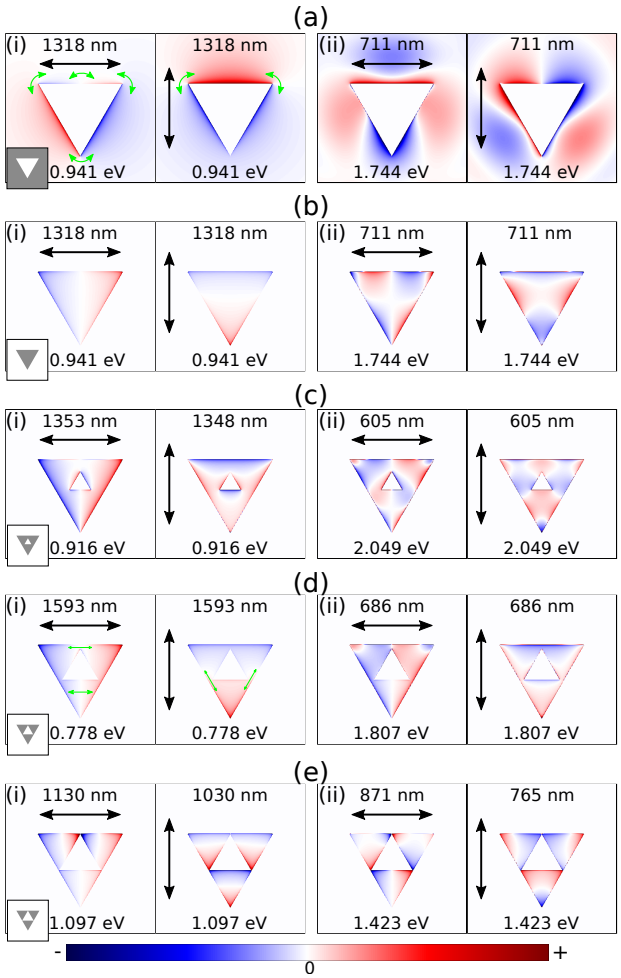

Figure 3.6: FDTD calculated surface charges for 285 nm iG0, G0, and G1 structures with increasing aperture sizes; polarization, wavelength, and energy of the excitation are indicated on each plot. (a) First two optical peak energies of an iG0 aperture in a solid film (green arrows indicate direction of current flow); (b) a solid G0 triangle; (c) a G1 fractal with a 73 nm aperture; (d) a G1 fractal with a 120 nm aperture (10 nm conductive channel); and (e) a G1 fractal with no conductive coupling. Structure geometries are shown in the inset for each row.

3.2.2 Generation 1

A series of fractal structures with a side length of approximately 285 nm was fabricated with increasingly large central apertures to study the evolution of LSPR modes

as the fractal generation is increased from G0 to G1. Experimental EELS spectra for this series of fractals are shown in Figure 3.7(a); plasmon maps at the peak energies indicated in the spectra are presented in Figure 3.7(b). The first four structures (i-iv) are the same size, within 10 nm, and the final structure (v) is half the size of the other four. All structures were fabricated in parallel on the same TEM grid. The experimental data is complemented by simulations of G0 and G1 fractals with increasing central aperture size, for which the spectra are shown in Figure 3.7(c) accompanied by surface charge (Figure 3.6(b-e)) and electric field calculations (Appendix C, Figure C.3-C.10). Eigenmode calculations (Figure 3.8) provide details on dark LSPR modes as the aperture size is increased, and clearly show individual modes, without the hindrance of spectrally overlapping mode contributions.

Edge Modes

In this series of fabricated triangular prisms, the dipole mode (Figure 3.7(a)(i-iv: peak 1)) redshifts after the aperture is introduced (ii: 0.78 eV) and grown in size (iii, iv: 0.74 eV, 0.73 eV). The shift in the dipole mode cannot be attributed to differences in the size or film quality, so must be an effect of the introduction of a central aperture in the solid G0 triangle. This trend is confirmed by the redshift of the simulated dipolar modes in the spectra of Figure 3.7(c)(i-v) and in the change in energy of eigenmodes (E1 and E2) in Figure 3.8. The EELS probability distribution, which is proportional to the normal component of the LSPR electric field, of the dipolar mode shows no observable differences between the four structures presented in Figure 3.7(b)(i-iv: peak 1), suggesting that the aperture does not significantly modify the field distribution in the degenerate dipolar resonances. Indeed, FDTD simulations confirm that there is only a small build-up of charge around the edges of the aperture (Figure 3.6(c,d)(i)). The electric field distribution is very similar for G0 fractals (Figure C.3) and G1 prisms with a small (Figure C.5) and large aperture (Figure C.7). Within the aperture, the electric fields are similar in topology to those of the iG0 dipolar modes (Figure C.1).

In the case where conductive coupling across the fractal is broken and the fractal is no longer a single solid structure, there is a strong blueshift and splitting of the degeneracy of the primary dipole modes (Figure 3.7(c)(vi)). The dipolar modes of each of the G0 parent units form new hybridized modes when there is no conductive coupling between them (Figure 3.6(e)). This case will be discussed in more detail further on, for larger samples of side length 1200 nm.

The second order edge mode (Figure 3.7(a)(i-iv: peak 2)) exhibits little, if any, shift in energy as the G0 structure is evolved to G1 (peak 2 in (i): 1.35 eV, (ii): 1.36 eV, (iii): 1.34 eV, (iv): 1.36 eV), changing by no more than 20 meV between the four structures. Despite the stable peak energy, the EELS distribution changes upon adding the aperture into the fractal structure, (Figure 3.7(b)(i-iv: peak 2)). Whereas this mode is a second order edge mode in G0, the central anti-node along each edge changes shape once the aperture is introduced and there is some EELS

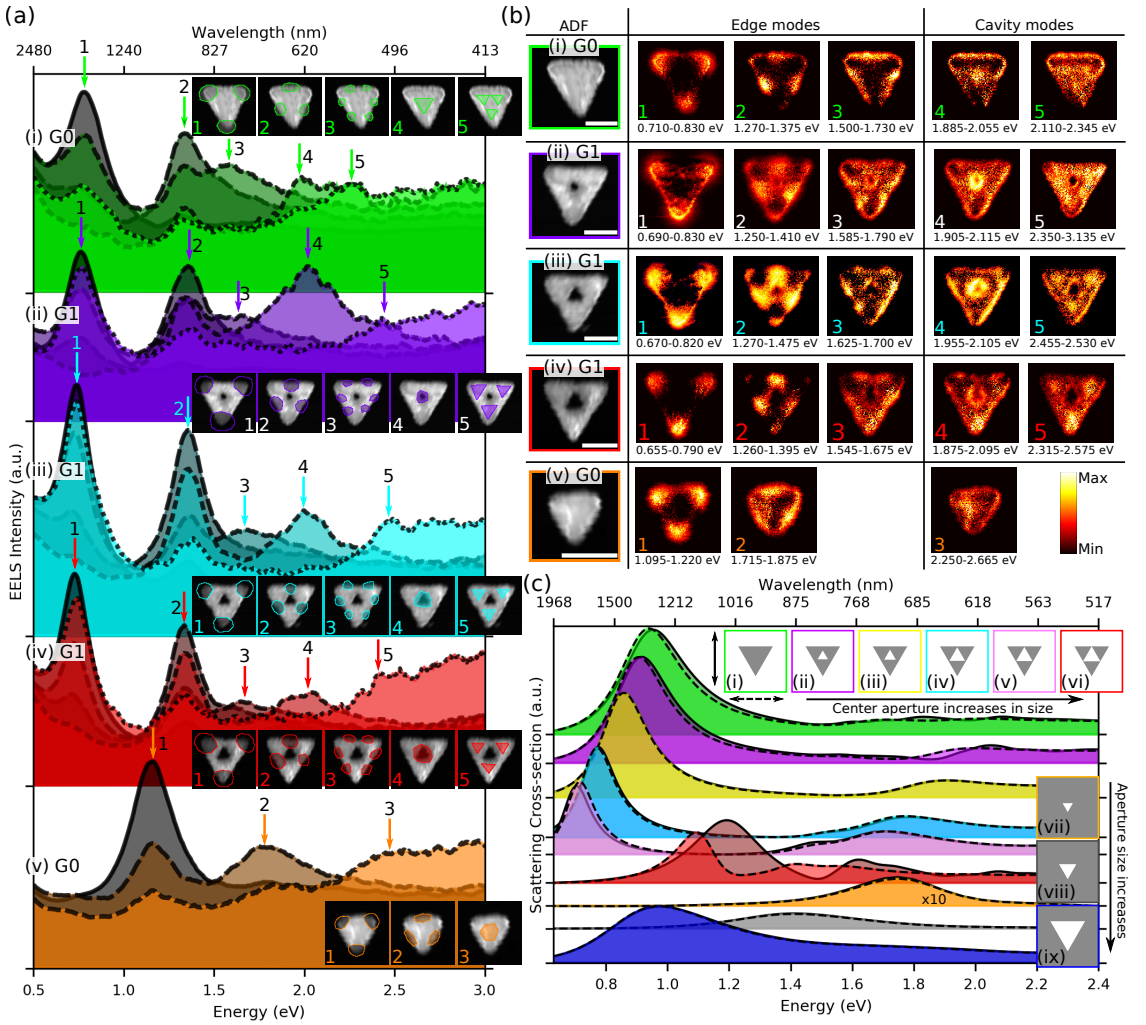

Figure 3.7: EELS and FDTD results for the evolution of LSPR modes as G0 is transformed to become G1 by the addition and growth of a small aperture in the centre. (a) Experimental EELS spectra averaged over the areas highlighted in the insets for (i) G0 prism, (ii) G1 fractal with a small circular aperture, (iii) G1 fractal with a larger triangular aperture, (iv) G1 fractal with a slightly larger triangular aperture, (v) G0 prism of half the size as the G0 structure in (i). (b) EELS intensity distribution extracted from the numbered peaks over the indicated energy range, scalebars in the ADF-STEM images are 150 nm. (c) Simulated vertically (solid line) and horizontally (dashed line) polarized spectra of the structures shown in the insets: (i) 285 nm G0 structure; (ii) 285 nm G1 structure with 73 nm central aperture; (iii) 285 nm G1 structure with a 95 nm central aperture; (iv) 285 nm G1 structure with a 120 nm aperture (10 nm conductive channel); (v) 285 nm G1 structure with a 133 nm aperture ($\approx$ 6 nm conductive channel); (vi) 285 nm G1 structure with no conductive coupling; (vii) 73 nm triangular aperture in a film; (viii) 142.5 nm triangular aperture in a film; (ix) 285 nm aperture in a solid film.

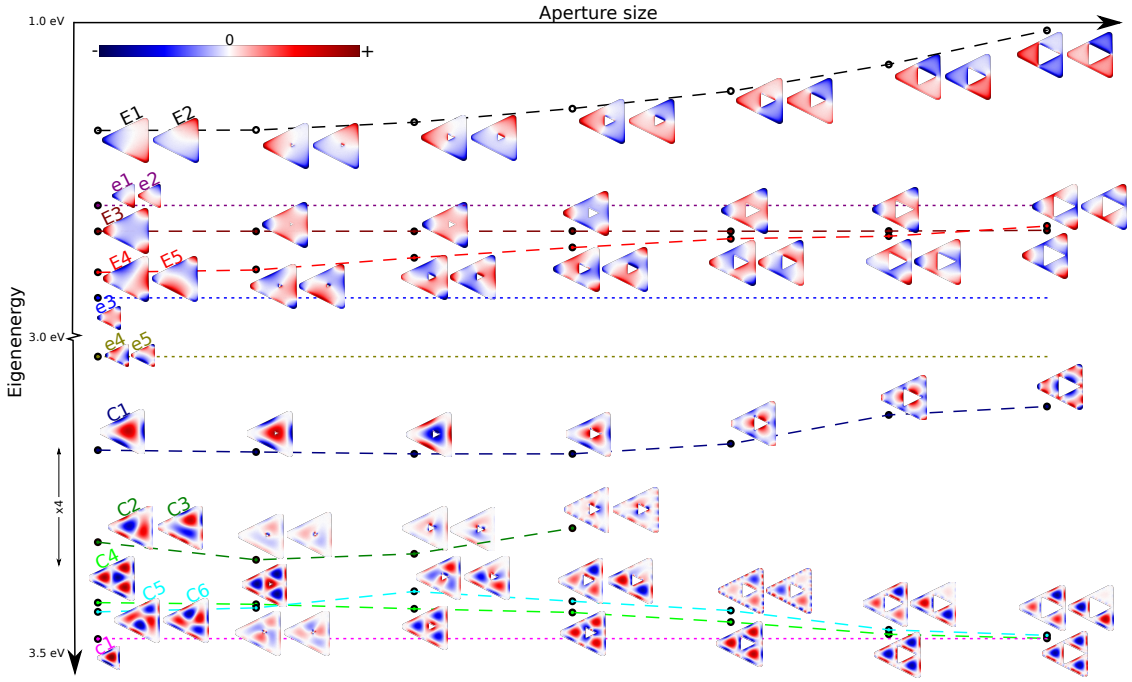

Figure 3.8: Evolution of the eigenmodes as a triangular aperture is introduced and grown inside a G1 fractal. The energy scale for the cavity modes (bottom) was expanded by ×4 relative to the energy scale for the edge modes (top), to make the energy differences more visible. Dashed lines indicate the energy evolution of each mode as the aperture size is increased. Modes along the dotted lines are those of a prism of half the size of the prisms along the dashed lines. Edge modes and cavity modes are labelled in order of increasing energy as 'E' and 'C', respectively, or 'e' and 'c' for the half-sized prism.

intensity around the central aperture. The energy of this mode is stable, but the electric field distribution has changed due to the presence of the aperture. This edge mode is a dark mode and does not appear in the optical FDTD simulations, though it is seen in the eigenmode calculations (Figure 3.8: E3), in which the surface charges do not indicate a significant change of topology around the aperture of the G1 fractal.

The third order edge mode of the G0 and G1 fractals (Figure 3.6(b-d)(ii), 3.7(a,b)(i-iv: peak 3)), which has three nodes and four anti-nodes along each edge of the triangle, presents an immediate blueshift of 100 meV upon the insertion of a small aperture in the centre of the triangle, from 1.6 eV to approximately 1.7 eV. Upon increasing the size of the aperture, there is little change in the peak energy: the third order mode appears within 10 meV for all three of the G1 triangles presented in Figure 3.7(a)(ii-iv). This higher order mode is revealed by simulations to be two degenerate modes with orthogonal polarizations (Figure 3.6(b-d)(ii), Figure C.4, C.6, C.8). Eigenmodes of this structure predict a sudden redshift as soon as the central aperture is introduced, followed by smaller redshifts as the size of the aperture increases (Figure 3.8: E4, E5), converging to a series of coupled dipolar modes on the three G0 parents (e1, e2).

Cavity Modes

Two cavity modes are visible in the EELS data from the fabricated triangles presented in Figure 3.7(a,b)(i-iv: peaks 4, 5). The lowest energy cavity mode (peak 4), at 1.98 eV in the G0 structure, presents shifts of approximately 20 meV across all four different fractal structures, therefore it can be concluded that the energy of this mode is not affected by the aperture. However, the EELS intensity changes from the central cavity mode in the G0 triangle (Figure 3.7(b)(i: peak 4) to become an apparent edge mode around the aperture in the G1 fractals (Figure 3.7(b)(ii-iv: peak 4). Eigenmode simulations reveal that the surface charges of this mode are merely accommodating the central aperture (Figure 3.8: C1) without changing the overall node and anti-node distribution until the aperture is of a comparable size to half of the G1 fractal. Once the central aperture is large enough, the charge distributions on each of the G0 parent units inside the G1 fractal converge towards those of the third order edge mode on the half-size G0 parent (compare C1 with e4, e5 in Figure 3.8).

The second cavity mode (Figure 3.7(a)(i-iv: peak 5)) presents an immediate blueshift of 140 meV between the G0 (i) and the G1 structure with the smallest aperture (ii). With a larger triangular aperture (iii, iv), the second cavity mode presents a blueshift of 70 meV, a much smaller shift than was seen on introducing even a small aperture in the structure. On the G0 triangle, the second cavity mode appears (Figure 3.7(b)(i: peak 5)) as expected of a simple triangle [228]; in the G1 structure, the second cavity mode peak shows high EELS signal in the centre of each of the smaller G0 fractal units (Figure 3.7(b)(ii-iv: peak 5)).

Comparing the second cavity mode of the G1 triangle (Figure 3.7(a)(iii,iv: peak 5) to the first cavity mode of a half-size G0 triangle (Figure 3.7(a)(v: peak 3)), the energy of the peak is very similar, within 30 meV. The similarity in the topology and energy indicates that the self-similarity of the fractal structure is coming into play and suggests that the first order cavity mode of the G0 parent (Figure 3.8: c1) evolves into a higher order cavity mode of the G1 fractal. Eigenmode calculations suggest that the second cavity mode peak in the EELS data is derived from a combination of the third and fourth order cavity modes of the parent G0 fractal (Figure 3.8: C4, C5, C6). As the aperture in the G1 fractal becomes larger, the eigenenergies and surface charge distributions of these high order cavity modes converge to the first order cavity mode of the half-sized G0 parent (c1). Due to the symmetry of the EELS excitation, these higher order cavity modes are indistinguishable from each other.

3.2.3 Babinet Principle

The Babinet principle can be used to explain the redshift of the dipolar modes and to interpret the interaction between the G0 parent and the central iG0 aperture. As discussed above, both the G0 and iG0 structures support two orthogonal degenerate dipolar modes. Because of this orthogonal degeneracy, the vertically (horizontally) polarized mode in the G0 fractal can be excited under the same conditions as the

complementary horizontally (vertically) polarized mode in iG0. Previous work has shown coupling between solid structures and their inverse, based on spectral and spatial overlap of the fields [220]. Although there is not a strong spectral overlap between G0 and the dipolar modes of the small central aperture (Figure 3.7(c)(i,vii,viii)), there is a strong relationship between the electric field distributions in the G0 prism and iG0 aperture (Figure C.1, C.3), allowing the aperture modes to couple to the solid G0 modes in the G1 structure and shifting the energy of the G1 dipole modes. The symmetry of both the triangle and aperture means that both of the degenerate dipolar modes shift equally in energy when the triangular aperture is introduced. As the size of the aperture increases (Figure 3.7(c)(vii-ix)), there is more spectral overlap and stronger coupling to the triangle dipolar modes, resulting in stronger redshifts. When the aperture cuts off conductive coupling, it can no longer support aperture LSPR modes, since current cannot flow around the aperture corners. Another example to support this argument is presented below, in which the symmetry is broken and the degeneracy of the aperture modes is lifted.

Interestingly, the second order edge mode does not appear to be affected by or couple to aperture modes. We suggest that since this mode is a dark mode, coupling via the Babinet principle may not apply here. The third order edge mode (second peak in the FDTD simulations) does reveal coupling between G0 modes and iG0 modes: the G0 and iG0 dipoles are anti-aligned with each other (Figure 3.6(c,d)(ii), Figure C.6, C.8), reducing the net dipole moment of the structure, similarly to the screened bonding dipole mode seen by Wen *et al.* [92] on a simpler structure. As the central aperture becomes larger, this mode changes to resemble three individual coupled dipole modes on each of the G0 parents within the G1 fractal (Figure 3.6(d,e)(ii)). The charge transfer plasmon theory developed by Wen *et al.* points to junction conductivity as a key factor in shifting the energy of the LSPR modes involved. However, the structure under study in this work is more complicated due to the presence of two conductive junctions across the structure and the capacitance of the aperture, which must be taken into account.

Asymmetrical Babinet

In the case of the Sierpiński triangle, adding a triangular aperture into the middle of a G0 structure to create a G1 fractal does not change the symmetry of the overall structure. There are two orthogonal dipolar modes in the Sierpiński triangle for all fractal generations, assuming conductive coupling is maintained. To emphasize that each dipolar mode of the solid triangle is coupling to the orthogonal mode of the central aperture, the case where the symmetry is broken on introducing an aperture into a different structure is presented in Figure 3.9. This example also highlights that the shifting of the modes caused by the addition of a central aperture is not unique to the fractal structure.

The two degenerate dipole modes of a simple silver square are shown in Figure 3.9 A. Introducing a small square aperture into this square maintains the symmetry of the

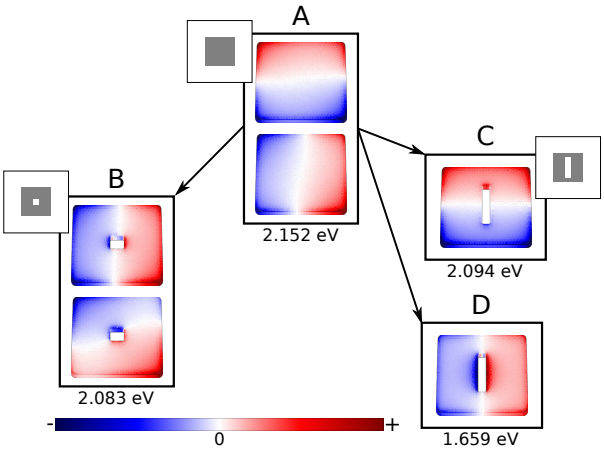

Figure 3.9: Change in the dipolar eigenmodes when a symmetrical and an asymmetrical aperture is added to a square prism. Dipolar eigenmodes of a silver square (A), a silver square with a small square aperture (B), and a silver square with a rectangular aperture (C, D).

structure and degeneracy of the dipole modes, redshifting both equally (Figure 3.9 B). A rectangular aperture introduced into the centre of the square breaks the symmetry and the degeneracy of the dipolar modes on the new structure (Figure 3.9 C,D). According to the Babinet principle, the lowest energy mode of the central aperture will couple to horizontally polarized light, orthogonal to the long axis of the aperture (the Babinet equivalent of a nanowire coupling to polarized fields along its length) [219, 221]. The vertical polarization, on the other hand, will couple to the aperture in the orthogonal direction, the equivalent of orthogonally polarized light coupling to the weaker transverse mode in a nanowire of the same dimensions as the aperture. Since the lower energy mode on the aperture is excited by fields polarized across the smallest dimension of the aperture, this mode couples to the horizontally polarized LSPR mode of the square (Figure 3.9 D) and the other mode, by similar arguments, couples to the vertically polarized LSPR dipole mode (Figure 3.9 C). The horizontally polarized case has a larger capacitance across the aperture than the vertically polarized case, resulting in a stronger redshift of the horizontal dipole mode. Alternatively, the coupling between the square dipolar mode and the slot dipolar mode is stronger in the case of the horizontally polarized LSPR modes because of greater spectral overlap, presenting a greater redshift for the more strongly coupled modes, as seen in Figure 3.9.

3.2.4 RLC Equivalence

The equivalent circuit theory provides a more thorough description of the behaviour of the LSPR mode in the complicated structures under study. As discussed above in relation to the aperture modes, the aperture acts as a capacitor, building up charge on the edges and supporting dipolar electric fields across the hollow aperture. Putting the

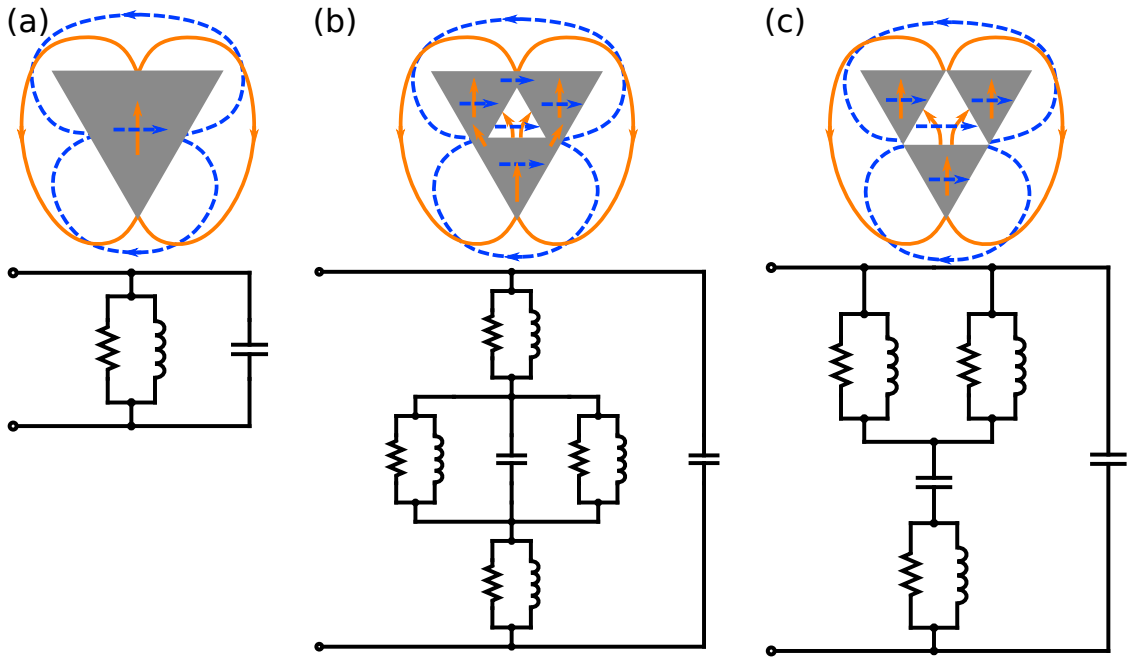

Figure 3.10: Simplified equivalent circuit diagrams for G0 and G1 dipolar modes. Energy flow (top row) of the dipolar response to horizontally (blue arrows) and vertically (orange arrows) polarized light and equivalent circuit diagrams (bottom row) representing the dipolar modes of (a) G0 prism; (b) G1 fractal with a small aperture, maintaining conductive coupling between G0 parent units; and (c) G1 fractal with a large aperture, cutting off conductive coupling between parent units. Electrical sources are left out of the diagrams for simplicity.

aperture into the G1 fractal introduces this capacitance in parallel with resistive and inductive components from the surface charges oscillating across the nanostructure [224]. In an RLC (resistor-inductor-capacitor) resonant circuit, adding a capacitor in parallel with the RL component increases the capacitance of the circuit and decreases the resonant frequency, explaining the redshift seen in the G1 fractal.

Simplified equivalent circuit diagrams are presented in Figure 3.10 for the dipolar modes of a G0 triangle; a G1 triangle with a small central aperture, allowing current to flow between G0 parent units; and a G1 fractal with a large central aperture which cuts off conductive coupling between G0 parent units. The top row of the figure represents a simplification of the flow of energy (arrows) through and around the structure, in the form of surface current or energy stored in capacitive fields across the central aperture or between the anti-nodes of the dipolar mode.

In the G0 triangle, the two dipolar modes are degenerate: they exhibit the same resonance energy, so must exhibit the same circuit characteristics. When the central aperture is introduced, we expect that the differences in conductive pathways across the device might cause splitting of the dipolar mode energies (Figure 3.10(b)), but this is not the case. To explain this, the individual components of the equivalent circuit must be considered. For the vertically polarized mode, the capacitance of the aperture

might be expected to be higher than that for the horizontally polarized response, because of the larger area of the aperture when projected along the vertical direction, which should reduce the resonance frequency of the vertically polarized mode relative to the horizontally polarized mode. However, the inductance along the conductive pathways also changes: for the vertically polarized mode, both of the conductive paths around the aperture are narrower than those for the horizontally polarized mode. Narrower conductive junctions in the vertical case result in an increase of the self-inductance of each junction, resulting in an overall reduction in the circuit inductance via the addition of two higher inductance values in parallel. For the horizontal case, the capacitance may be lower than that of the vertical case, but the inductance is higher because of the presence of one broad junction and one narrow junction around the central aperture. The lower circuit capacitance has the opposite effect on the position of the resonance as the higher inductance, which overall results in the same resonance frequency for both modes.

As the aperture is increased in size, the capacitance is increased and the resistance and inductance of the conductive junctions is increased as the channel narrows. Increasing the aperture capacitance reduces the resonance frequency, which is reflected in a stronger redshift of the dipole peak. When the aperture reaches the limit at which it cuts off conductive coupling across the G1 fractal, the fractal response transitions to that of a set of three coupled triangles, similar to the transition seen in several previous studies [92–96]. Applying the equivalent circuit model to this case (Figure 3.10(c)), the capacitive aperture is in series with the current oscillating in each of the G0 parent units on either side of the aperture, and the two parallel RL components of the narrow junctions are eliminated. Introducing a capacitor in series into an RLC circuit reduces the overall capacitance and increases the resonant frequency; the dipolar mode is blueshifted. The splitting of the degeneracy of the dipolar modes seen in Figure 3.7(c)(vi) is due to differences in the relative orientation of the different dipole modes and differences in capacitance of the aperture in different directions. The vertically polarized mode has a higher series capacitance (lower total capacitance) than the horizontally polarized mode, producing a greater blueshift in the resonance frequency.

The equivalent circuit model can be extended to consider the location of the nodes and anti-nodes of the LSPR. On the dipolar mode, the aperture is placed on an LSPR node and has a strong effect in diverting the current flow, resulting in peak shifts. There is no strong change in the charge distribution of the dipolar mode when the aperture is introduced, which is reflected as having no observable effect on the EELS intensity distribution over the structure. On the second edge mode, the anti-nodes are in the centre of each edge, with nodes partway between the centre and the corners (Figure 3.8: E3). Introducing the aperture does not greatly affect the current flowing through the nodes of the second order edge mode, so does not change the equivalent circuit significantly from that of the second edge mode of the G0 parent, and no energy shift is seen. On the third order edge mode (two degenerate edge modes),

the node structure is more complex, but the aperture in the G1 fractal is placed on top of a resonance node (Figure 3.6(c,d)(ii), Figure 3.8: E4, E5), and so affects the current flow, changing the RL components of the circuit and causing the observed energy shift.

3.2.5 Linewidth

Changes in the path that the surface currents travel caused by the introduction of an aperture modify the damping characteristics of the system, as the flowing charge is confined to a narrower path. For an RLC circuit, the damping characteristics are proportional to the resistance and inversely proportional to the inductance in the circuit. As the width of the conductive path is shortened, both the resistance and the inductance through this path increase. The self-inductance of the current flow increases at a faster rate than the resistance, resulting in net lower damping in the equivalent circuit and an increased resonance lifetime, reducing the linewidth of the LSPR modes, as seen in both experimental EELS data (Figure 3.7(a)(i-iv: peak 1)) and optical simulations (Figure 3.7(c)(i-v)). Briefly, raw spectra were averaged over the areas shown in Figure 3.11, then deconvolved using fifteen RLD iterations before fitting with a Lorentzian and power law combination. Further details of the fitting procedure are given in Chapter 2, Section 2.8.3.

For the fractals shown in Figure 3.7 and Figure 3.11, there is a clear trend of reducing linewidth as the aperture size inside the G0 parent is increased, from 0.281 to 0.196 eV. The same trend of decreasing linewidth with larger G1 apertures is also observed in the FDTD simulations, giving confidence that the experimental trend is not merely a factor of fabrication quality or the effectiveness of the deconvolution algorithm. The linewidth of the simulated peaks was calculated based off the full-width at half-maximum (FWHM) of the peak: for the G0 of 285 nm, the FWHM is approximately 0.25 eV (Figure 3.7(c)(i)), becoming progressively smaller to 0.11 eV for the G1 with the largest aperture (v), before conductive coupling is severed.

The equivalent circuit model accounts only for losses within the material and not for radiative damping. The simulated scattering cross-section of the dipolar mode noticeably decreases over the series of fractals presented in Figure 3.7(c)(i-v), from 1.8×10^{-13} m^{-2} for the G0 dipolar peak, to approximately 1.2×10^{-13} m^{-2} for the G1 peak in (v), indicating a reduction in the ability of the mode to couple to radiation and thereby a reduction in radiative damping. Examination of the fields of the G1 fractal (Appendix C, Figure C.7) reveals that there is an opposing dipole in the $\boldsymbol{\varepsilon}_z$ fields, which is weaker in the G0 triangle. Going from the basic G0 parent to the G1 fractal, therefore, results in an improved quality factor through the reduction in linewidth, at the expense of reduced scattering cross-section.

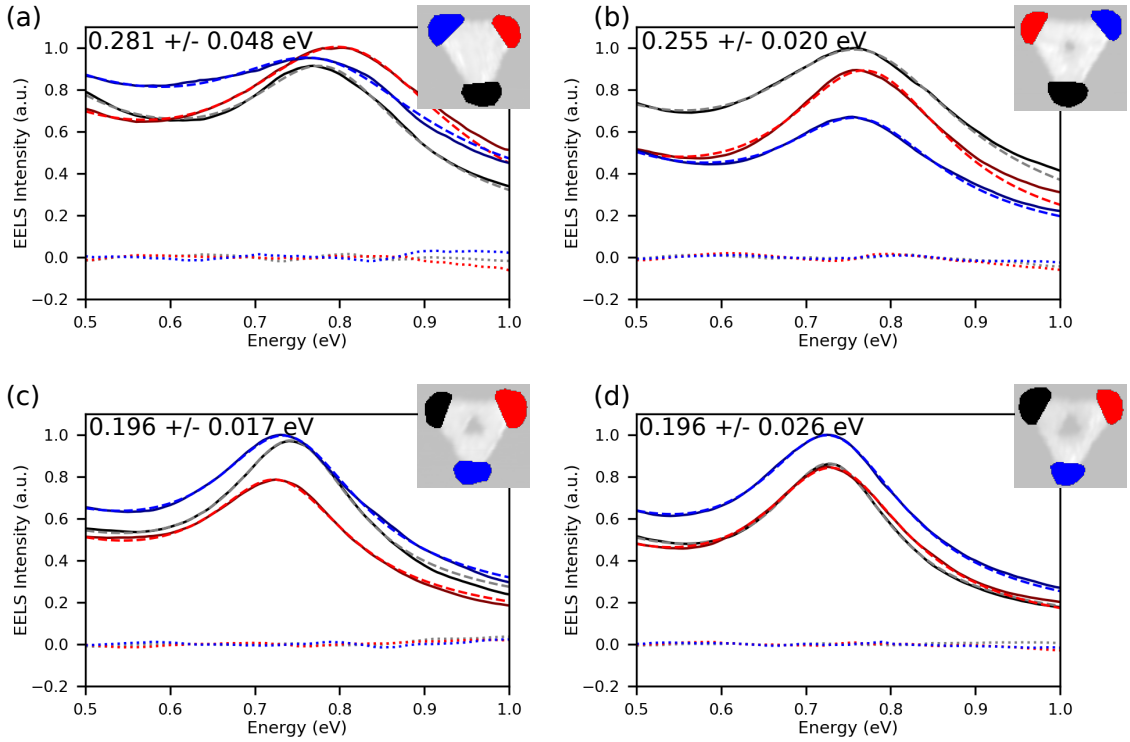

Figure 3.11: Fitting of the linewidth of the G0 and G1 dipolar modes using a combined power law and Lorentzian model. (a) G0; (b, c, d) G1 fractal triangles. Experimental EELS spectra were extracted from the areas coloured in the inset: solid lines are experimental data after 15 RLD iterations, dashed lines are the fitted model, dotted lines are the residuals of the fit for the respective colour. Fitted FWHM of the Lorentzian is shown in the upper left for each plot.

3.2.6 Generation 2

We will extend the results from the previous discussion on G0 and G1 fractals to interpret the modes present in the Generation 2 (G2) fractal. A series of triangles (G0, G1, G2) with a side length of approximately 575 nm was fabricated, as were the apertures of the G2 fractal inside a solid film (referred to hereafter as 'iG2') (Figure 3.12). The G0 triangle, of side length 578 nm, has a primary peak energy of 0.515 eV (Figure 3.12(a)(i): peak 1), while on a slightly smaller G1 fractal (534 nm), the redshift of the dipolar mode from interactions with the central aperture is stronger than the expected blueshift from the reduction in size of the fractal: the peak redshifts by approximately 25 meV to 0.480 eV (Figure 3.12(a)(ii): peak 1). A more significant peak shift of 80 meV from the G0 parent is observed on the G2 fractal (of side length 557 nm), which has a dipolar peak at approximately 0.420 eV (Figure 3.12(a)(iii): peak 1). The same trend is seen in another set of fabricated structures of similar size (not shown) and FDTD calculations of G0, G1, and G2 (Figure 3.13(a)(i-iii)), to emphasize that this trend is not unique to these specific nanostructures.

It is interesting to note that there is a strong peak redshift of the second order

edge mode, from 0.92 eV on the G0 fractal (Figure 3.12(a)(i): peak 2) to 0.815 eV on the G2 fractal (Figure 3.12(a)(iii): peak 2). Many higher order edge modes can also be detected, as well as a first order cavity mode, the EELS intensity maps of which are shown in Figure 3.12(b). Before further analysis of the peaks in the G2 fractal, it is informative to consider the modes of the combined apertures of G2 (Figure 3.12(a)(iv),(c)).

iG2 Apertures

The iG2 apertures were fabricated in a solid silver film to explore the possible coupling between the modes of this aperture configuration and the modes of the G0 parent. In the experimental data, two strong peaks and a shoulder in between them are observed at low energy (Figure 3.12(a)(iv: peaks 1-3)). FDTD calculations of the iG2 apertures also show two modes of equal strength (Figure 3.13(a)(iv)); the surface charges of these modes reveal that they correspond to a pair of degenerate modes centralized on the large central aperture (Figure 3.13(b: 0.574 eV)) and two degenerate modes exciting dipoles across the smaller triangular apertures (b, 1.091 eV).

There are some differences between the experimental (Figure 3.12) and simulated (Figure 3.13) G2 and iG2 nanostructures; the EELS data shows the two lowest energy peaks of the iG2 structure framing the dipolar peak of the equivalently sized G2 triangle, whereas the simulated data presents two iG2 peaks at a higher energy than the dipolar modes of the equivalently sized G2 triangle. Examination of these trends provides an interesting case to apply the RLC circuit model. In both EELS and FDTD datasets, two peaks of approximately equal strength are observed at different energies. FDTD simulations reveal that these peaks correspond to excitation of the aperture mode across the large central aperture in the iG2 structure, and the excitation of aperture modes across the smaller apertures, respectively.

The key to understanding the difference in the energy relationship when compared to the G2 triangle is noticing that the conductive coupling across the structure is different between the experimentally fabricated iG2 structure and the simulated iG2 structure. In the fabricated iG2, the apertures are connected to each other and charge cannot flow in between the apertures, but must collect at the edges, acting as a capacitor, or flow around the outsides of the smaller apertures. In the simulated structure, there is a conductive channel separating the large and small apertures, allowing charge to flow through this path. Similarly to the case of the G1 fractal, the conductive coupling across the structure greatly affects the energy of the modes. In the G1 case, when the conductive coupling is broken, the dipolar peak is blueshifted relative to the G0 of the same size; when the conductive coupling is broken in the iG2 structure, the dipole peaks are redshifted relative to the case with conductive channels. When the conductive channel between the smaller apertures and larger apertures is broken in the experimental iG2, charge is still able to flow around the outer edges of the small apertures, so the capacitance added by the extra gap should be considered as adding a capacitance in parallel with the rest of the equivalent

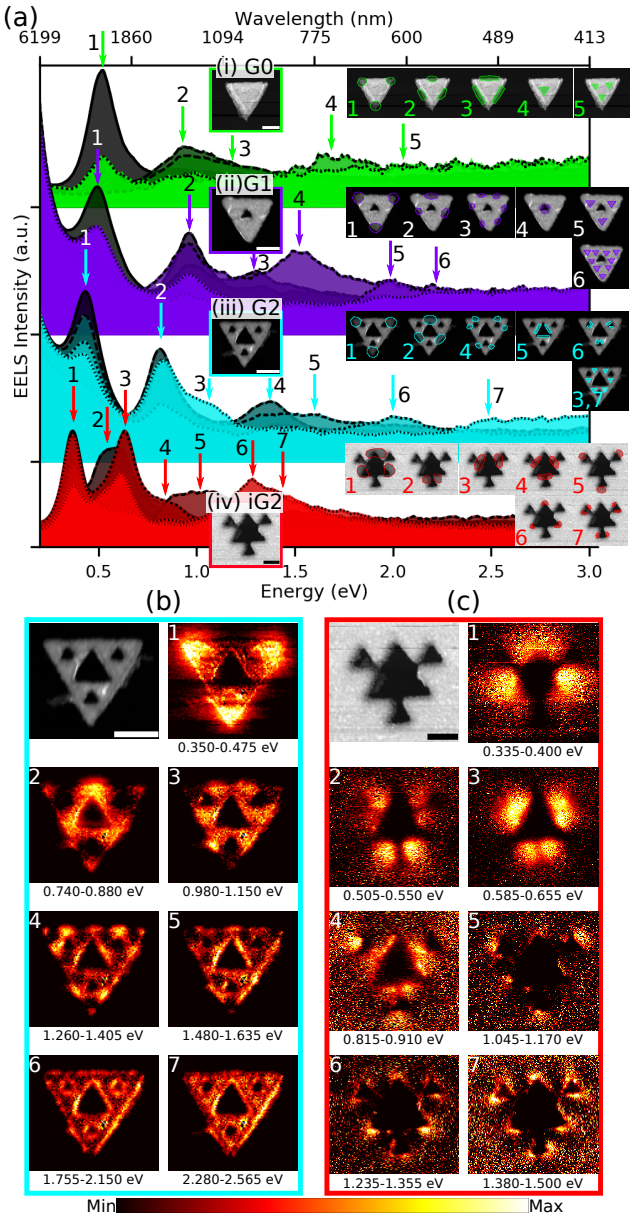

Figure 3.12: EELS spectra and intensity maps for G2 and iG2 fractals. EELS spectra (a) for (i) G0, (ii) G1, (iii) G2, and (iv) iG2 fractals (ADF-STEM images with 250 nm scalebars are inset, numbered insets highlight the areas over which spectra were averaged). (b, c) ADF images (top left, scalebars are 250 nm) and EELS intensity maps for the peaks indicated in (a)(iii, iv), averaged over the energy range noted for (b) G2 and (c) iG2 and individually normalized.

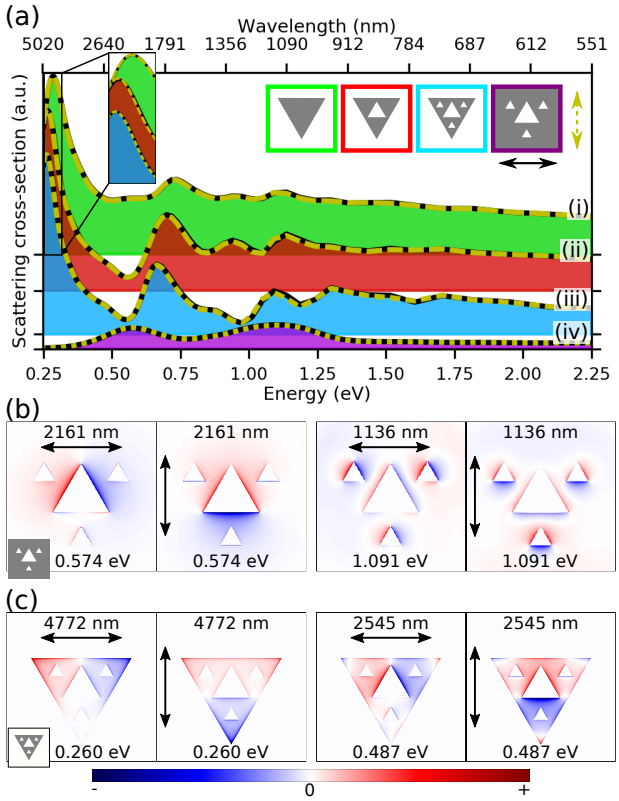

Figure 3.13: Optical FDTD results for spectra for G0, G1, G2, and iG2. (a) Simulated spectra; (b) surface charges for the first two peaks of the iG2 apertures (wavelength, energy and excitation polarization are indicated on each plot); (c) surface charges for the first two peaks of the G2 (wavelength, energy and excitation polarization are indicated). The side length is 1290 nm for all solid triangles, iG2 is a set of apertures of the same size as the apertures of the G2 structure, set in a continuous silver film.

circuit. Adding a capacitor in series increases the effective capacitance and reduces the resonant frequency, redshifting the dipole peak relative to the G2 triangle dipolar modes. In the simulated structure, there is a conductive channel in between the small and large apertures, resulting in an overall lower capacitance for this structure and a higher energy dipolar mode.

G2 Edge Modes

The redshift induced by increasing the fractal order from G0 to G2 dominates over the blueshift expected from reductions in the size of the fractal, for small size variations. At some limit, the blueshift from the use of a smaller structure is expected to fully cancel out the redshift resulting from the subtractive fractal topology. Similarly to the case for the G0 prism and iG0 apertures, the G2 prism and iG2 apertures each possess degenerate orthogonal dipole modes (Figure 3.13(b,c)), enabling coupling between the solid triangle and the iG2 aperture modes for both polarizations. The vertically

(horizontally) polarized dipole mode of the solid triangle couples to the horizontally (vertically) polarized complementary mode on the iG2 apertures because of the strong overlap in the electric field distributions (Appendix C, Figure C.11, C.12). With the addition of three smaller apertures in the iG2 set, the primary aperture modes are redshifted and the iG2 dipolar fields are extended to incorporate the smaller apertures, strengthening the coupling between the iG2 dipole modes and the solid G0 dipole modes. As a result, the G2 dipolar mode is more strongly redshifted than that of the G1 fractal of the same size. Using the equivalent circuit analysis, adding the three smaller apertures adds additional parallel capacitance into the circuit, reducing the resonance frequency.

The dipolar mode on the smaller apertures, the second iG2 peak, may be able to couple to higher order modes in the G0 structure, causing the redshift seen in the second order edge mode of G0 (Figure 3.12(a)(i-iii): peak 2). Adding the three smaller apertures onto nodes of the second order edge mode forces the flow of surface current to change, introducing additional capacitances into the resonance and redshifting the peak. More generally, this confirms the trend seen in the analysis of the G0 to G1 fractal transition: when apertures are placed on LSPR nodes, the current flow must change and the energy of the peak shifts. When the aperture is placed on an anti-node of the resonance, the LSPR accommodates the aperture and pushes charge to the aperture edges, changing the field configuration without causing a large shift in energy.

Higher order edge modes are affected to different degrees by the G2 apertures, with shifts in energy or EELS intensity distribution, depending on the location of the nodes and anti-nodes with respect to the additional apertures. Some of these higher order modes may also couple to higher aperture order modes on either the central aperture or the three smaller apertures in G2, via the Babinet principle. It is also interesting to note that as the fractal generation increases, the peak intensity of higher order modes relative to the primary dipolar mode also increases, as does the sharpness of the higher energy peaks (compare, *e.g.*, peak 2 in Figure 3.12(a)(i) with peak 2 in (iii)).

G2 Cavity Modes

Similarly to the evolution of the cavity modes in the G0 and G1 examples seen above, the primary cavity mode of G0 becomes localized around the central aperture in G1. In the G0 and G1 presented in Figure 3.12(a), the first cavity mode of G1 is redshifted (ii: peak 4) relative to that of the G0 (i, peak 4). There is a small defect on the aperture of this G1 prism, which may cause the strong redshift seen. Progressing to G2, this cavity mode (iii: peak 5) is at a similar energy to that of the G0 structure, with strong EELS intensity around the edges of the central aperture (Figure 3.12(b): peak 5).

The energy of the second cavity mode of the G0 prism Figure 3.12(a)(i: peak 5) is relatively stable as the fractal generation is increased, although the mode intensity

is weak in the G0 structure and the precise peak location is difficult to determine. Between the G0 and G1, as discussed above in Figure 3.7, the second cavity mode is similar in EELS intensity, whereas in the G2 fractal (Figure 3.12(a,b)(iii): peak 6), the EELS intensity is localized around the smaller apertures.

A third cavity mode, which is not visible as an independent peak in the G0 or G1 structures, is observed in the G2 structure as a cavity mode of the smallest triangles within the G2 fractal (Figure 3.12(a)(iii),(b): peak 7), with a similar energy as that of the first order cavity mode of a triangle four times smaller (Figure 3.7(a)(v: peak 3)).

As with the edge modes for the fractal structure, when the aperture or apertures are placed on an anti-node of the LSPR, the surface charges, as seen through the EELS intensity distribution, move to accommodate the apertures without significantly changing the energy of the LSPR mode. The self-similarity of the fractal structure also affects the behaviour of the cavity modes: the first cavity mode accommodates the central aperture, but is relatively unaffected by the three smaller corner apertures in the G2 fractal; the second order cavity mode creates higher EELS intensity around the smaller corner apertures; and the third order cavity mode, not easily visible in G0 or G1 structures, appears as expected of a triangular cavity mode on the smallest triangles within the G2 fractal.

3.3 Results on Additive Fractals

Following the analysis in the previous section on subtractive fractals, this section will address the behaviour of plasmon modes in additive fractals of increasing size. We will consider Generation 0, 1, and 2 fractals, as well as topological intermediaries which break the threefold (C_3) symmetry, halfway between Generations 0 and 1 (labelled as 'G0.5'), and between Generations 1 and 2 (labelled as 'G1.5'), as shown in Figure 3.1. Each successive generation is larger than the previous, though the fundamental G0 parent remains the same size, and adds an additional response band to the spectrum through hybridization of the plasmon modes of the parent generations. The modes of parent fractal generations hybridize to form new modes in higher generations, demonstrating the origin of the multiband capabilities and complex spectral response of the fractal nanoantenna using eigenmode calculations combined with EELS and FDTD results. Figure 3.14 shows the hierarchy of LSPR modes detected through EELS in each of the aforementioned generations, each of which will be dealt with in turn.

3.3.1 Generation 0

The G0 nanoprism, of side length 578 nm, exhibits the well-known set of LSPR modes, as discussed in the previous section and other works [227, 228]: a degenerate pair of dipolar modes at the lowest energy (Figure 3.14(a,b)(i): peak 1 (0.52 eV)),

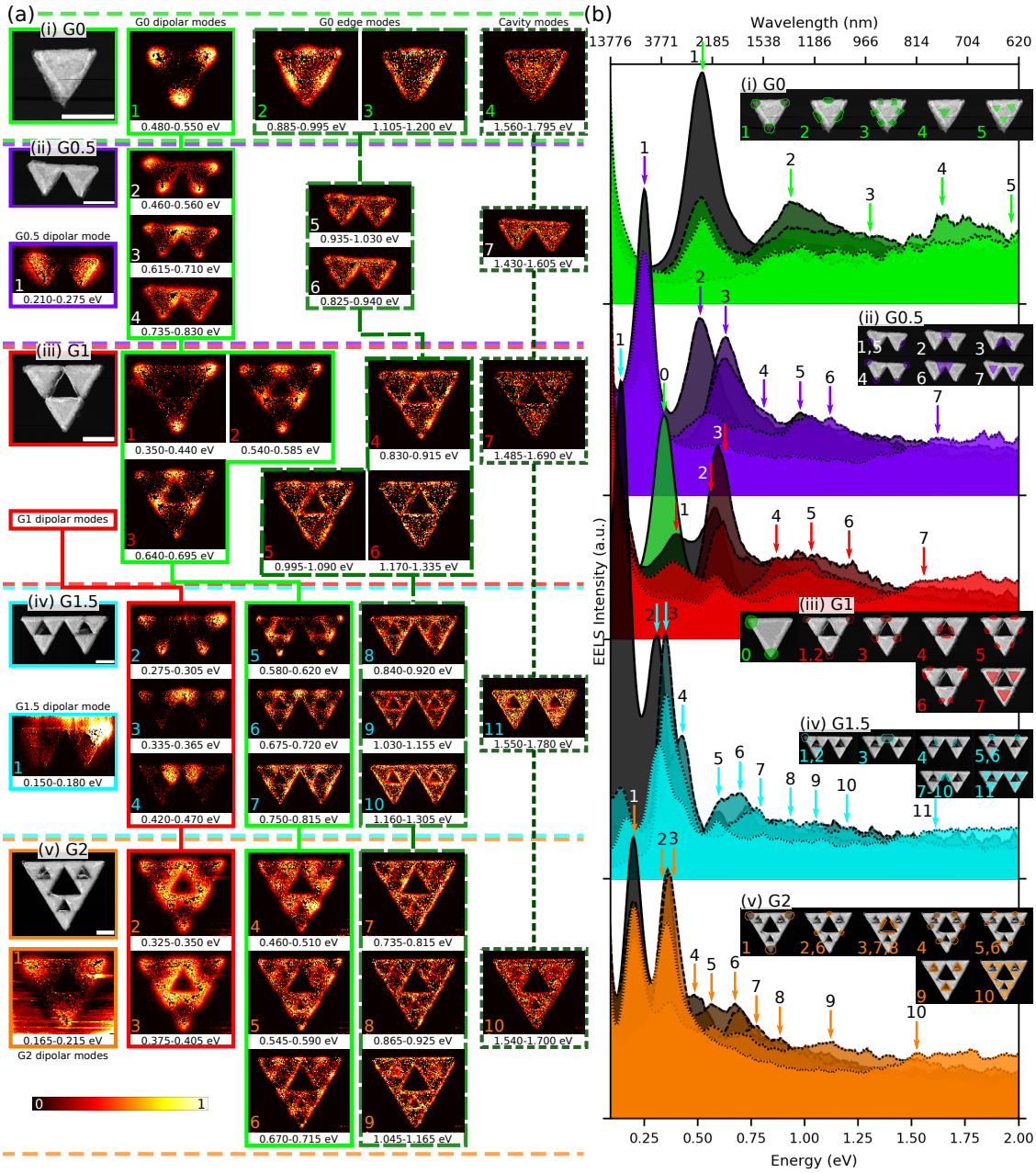

Figure 3.14: Experimental EELS data for G0, G0.5, G1, G1.5, and G2 structures. (a) ADF-STEM images and EELS maps averaged over the energies indicated for the labelled peaks; all scalebars on STEM images are 500 nm; each EELS maps is individually normalized according to the colourscale in the lower left; connecting lines follow the hybridized descendant modes of the top mode through successive fractal generations. A placeholder box is used instead of the G1 dipolar maps, which are not observed because of the lack of conductive coupling. (b) EELS spectra for each of the structures in (a); insets indicate the areas from which each spectrum was extracted in the EELS spectrum image; each spectrum is normalized to the height of the ZLP.

followed by higher order edge modes (peaks 2 (0.94 eV), 3 (1.15 eV)) and finally cavity modes (peak 4 (1.67 eV), 5 (1.98 eV)). The G0 nanoprism is the most basic structural building block and its dipolar modes form the basis for the plasmon resonances of descendant generations.

3.3.2 Generation 0.5

Using two G0 prisms to build an intermediate topology, we obtain the G0.5 structure. With one side twice as long as the G0 building block, the G0.5 structure possesses a strong peak at lower energy (Figure 3.14(b)(ii): peak 1 (0.25 eV)) than the G0 dipole peak (Figure 3.14(b)(i): peak 1 (0.52 eV)), followed by a cluster of three peaks close to each other in energy ((ii): peaks 2 (0.51 eV), 3 (0.63 eV), 4 (0.82 eV), and higher order edge modes ((ii): peaks 5 (0.98 eV), 6 (1.12 eV)).

The importance of conductive coupling between components in fractal structures has been emphasized in Section 3.2. Conductive coupling between the prisms in this G0.5 structure is maintained, allowing a new dipolar mode across the whole structure to be sustained at low energy (Figure 3.14(a)(ii)): peak 1). Since the C_3 symmetry present in the original equilateral triangle has been broken, there is only a single dipole mode in G0.5: the degeneracy and polarization-independence of the dipolar modes of the G0 parent have been broken. The two degenerate dipoles of the G0 parent hybridize to form four new eigenmodes in the G0.5 structure (Figure 3.15). From these four eigenmodes, three peaks are visible in the EELS data, identified by high EELS intensity around the corners of the G0 parents (Figure 3.14(a,b)(ii): peaks 2, 3, 4). The response from the G0 dipolar modes has split into multiple peaks, forming a broader band in the new structure.

At higher energy than these modes, there are broader peaks from edge modes on the triangular G0 parents (Figure 3.14(a,b)(ii): peaks 5, 6). There is also a cavity mode at comparable energy to the G0 cavity mode (peak 7 (1.61 eV)). The cavity modes of each of the G0 parent units within the G0.5 structure might be expected to hybridize to same-charge and opposite-charge cavity modes (similarly to higher order cavity modes seen in Figure 3.8). However, these are indistinguishable in conventional EELS data because it is not possible to differentiate symmetric and anti-symmetric cavity modes with different phases without resorting to beam-shaping techniques [166]. Small energy splitting between hybridized cavity modes, combined with more hybridizations of higher order cavity modes from each G0 parent result in severe modal overlap and the appearance of a broad continuum of EELS signal above 1.5 eV (Figure 3.14(b)(ii): peak 7). Instead, the cavity mode peaks appear as a broad continuum of signal.

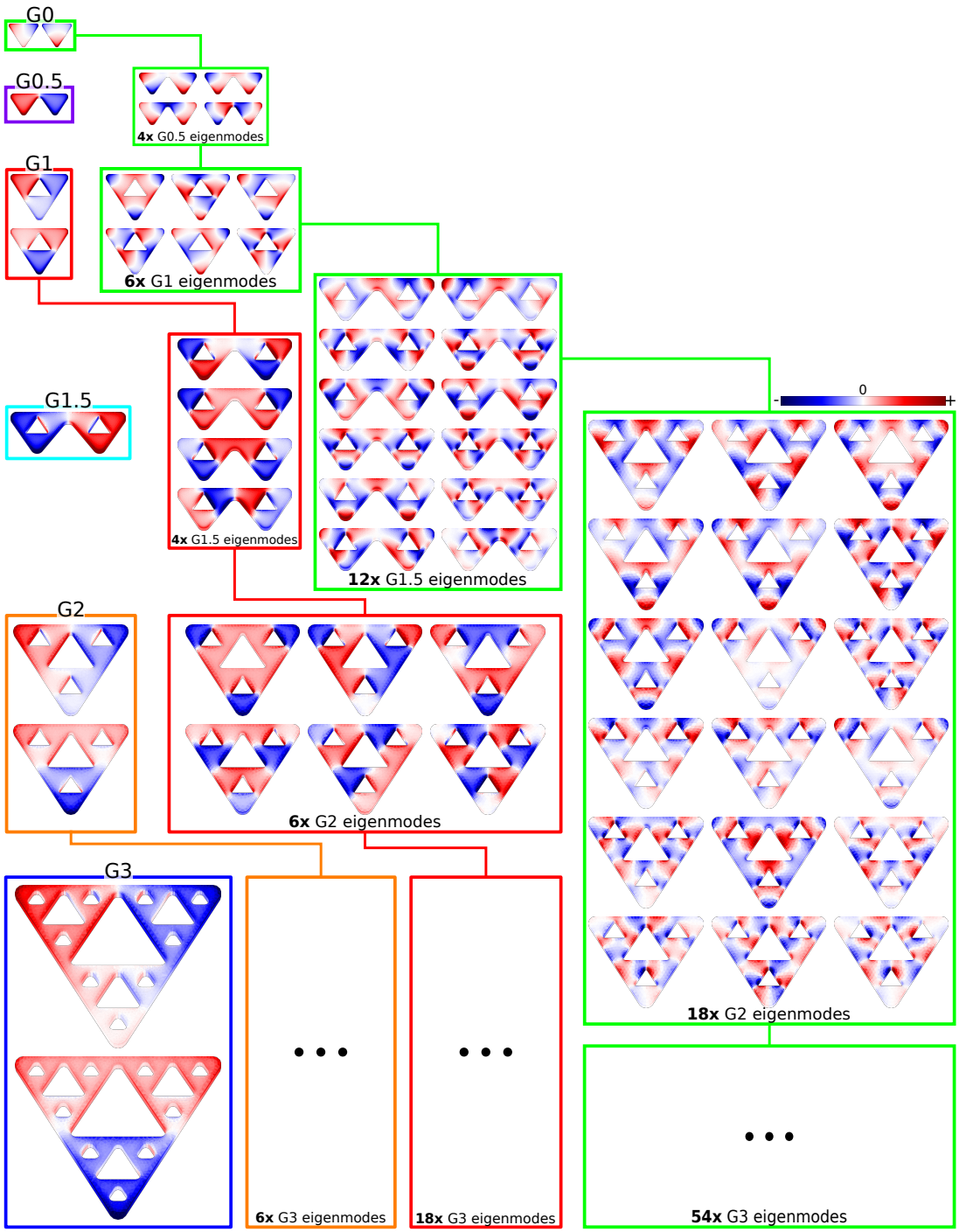

Figure 3.15: Eigenmode calculations of the hybridization of dipole modes of parent units as the fractal generation is increased incrementally from G0 to G3. Connections show the hybridization dependence of dipole modes from previous generations, as determined by the number of surface charge nodes within each parent unit. Each element of the figure shows the surface charge distribution for the respective eigenmode; the colourscale for each is normalized individually.

3.3.3 Generation 1

Completing the G1 structure by adding another G0 parent prism to the G0.5 nanostructure creates another set of hybridized modes. There are two new degenerate dipole modes in the G1 triangle (Figure 3.15) at a lower energy than the dipole modes of a similarly sized G0 structure (*e.g.* Figure 3.7, 3.12) and six new modes from hybridizations of the G0 parent dipolar modes (Figure 3.15). In the experimentally fabricated G1 fractal presented in Figure 3.14(a,b)(iii), perfect conductive coupling across the structure is not maintained and instead of new, lower energy dipolar modes, we see a set of three closely spaced peaks between 0.38 eV and 0.65 eV. Impaired conduction is known to cause, instead of the expected redshift, a blueshift of the lowest energy mode [92–96]. These peaks are hybridized modes from coupled dipoles on each of the G0 parents (Figure 3.6(e)), as evidenced by the blueshift of the primary G1 peak compared to that of an equivalently-sized G0 prism (Figure 3.14(b)(iii): peak 0 (0.34 eV)).

With impaired conductivity across the whole G1 structure, the dipolar G0 modes split in energy to form peaks 1, 2, and 3 in Figure 3.14(b)(iii). Notably, the combination of the second and third peaks has a stronger EELS signal than the first, with high intensity at the tips of the G0 parents in the centre of each G1 edge (Figure 3.14(a)(iii): peaks 2, 3), indicating that it may be possible to use the conductivity between fractal parent units to control the relative strengths of different spectral response bands. Higher order edge modes (peaks 4, 5, 6 (between 0.84 and 1.25 eV)) and the first cavity mode (peak 7 (1.52 eV)) can also be detected in this G1 fractal. Similarly to the G0.5 case, we expect multiple cavity mode configurations from hybridization on the three parent units and we do not see a single distinct cavity mode peak, but only the onset of signal on the faces of the G0 parents within the G1 fractal, beginning at approximately the energy of the primary G0 cavity mode.

3.3.4 Generation 1.5

In the G1.5 structure, built from two G1 parent units or six G0 grandparent units, and shown in Figure 3.14(a,b)(iv), there is conductive coupling across the whole structure. A single dipole mode is present at 0.165 eV (Figure 3.14(a,b)(iv): peak 1); similarly to the G0.5 intermediate structure, the C_3 symmetry of the standard Sierpiński fractal is broken and the dipolar mode is polarization-selective along the long axis of the G1.5 structure (Figure 3.15). In the experimental data, the energy of the G1.5 dipolar mode is approaching the limits of the instrument resolution, and some artefacts are visible in the peak map (Figure 3.14(a)(iv): peak 1). Within this map, small high frequency modulations are visible, caused by fluctuations in the shape of the ZLP of the microscope due to ripple in the high tension supply tank. There is also high intensity towards the top of the image caused by distortions to the spectrum from the flyback of the electron beam as it rasters over the sample. Despite these artefacts at the edge of the frame, the presence of the EELS peak is significantly correlated with

the outer corners of the G1.5 structure.

At higher energy, there are three peaks in the EELS data between 0.3 and 0.42 eV (peaks 2-4) and four eigenmodes (Figure 3.15) arising from hybridization of the two degenerate dipole modes of the G1 parent fractal, broadening the spectral response in this energy range compared to the G1 parent. Dipolar modes from the G0 grandparent hybridize in the G1.5 structure to form 12 new eigenmodes (Figure 3.15). Experimentally, these eigenmodes are very close to each other in energy and spatial distribution; they form a spectral band slightly blueshifted from the G0 dipolar response, in the form of a series of peaks between 0.5 and 0.82 eV (Figure 3.14(a,b)(iv): peaks 5-7) with high intensity at the tips of the G0 grandparents, resembling peaks 2-4 of the G0.5 structure. The next spectral band in the EELS data, from 0.84 to 1.30 eV, contains edge modes from hybridization of the higher order G0 grandparent edge modes (peaks 8-10), followed by a broad signal starting at 1.55 eV (peak 11) from hybridization of G0 cavity modes. Cavity mode hybridization is very complex in higher order fractals, as there are now six G0 parents, and the modes are truly blurred out and indistinguishable from the EELS data.

3.3.5 Generation 2

By stepping from G1.5 to G2, the C_3 symmetry is restored and there are again two new degenerate dipole modes across the whole prism (Figure 3.14(b)(v): peak 1 (0.19 eV); and Figure 3.15). Adding the third G1 triangle to the fractal blueshifts the dipolar mode of G2 relative to G1.5 and restores the polarization insensitivity. The low energy of the dipolar peak and the large size of the G2 structure (now 2290 nm along each side) results in some instrumental artefacts appearing in the lower corners of the peak map (Figure 3.14(a)(v): peak 1) from misalignment in the descan system of the microscope. Clear evidence of the presence of the dipolar mode remains in the high EELS intensity at the corners of the G2 prism. Optical simulations confirm that the G2 possesses two orthogonal, degenerate dipolar responses when conductive coupling is maintained across the whole structure (Figure 3.16(a,b): peak 1). Electric field responses for each of the peaks presented in Figure 3.16 can be found in Appendix C, Figure C.12- C.19.

The dipole modes of the G1 parent hybridize in the G2 structure to form six eigenmodes, from which only two peaks are resolvable in the EELS data acquired (Figure 3.14(b)(v): peak 2 (0.34 eV), 3 (0.39 eV)) and the optical simulations (Figure 3.16(a,b): peak 2, 3). As revealed by the optical simulations, each of these peaks is a pair of orthogonal degenerate modes. The second peak of this pair (peak 3) has the strongest scattering cross-section and, notably, is sharper then the similar peak on either G0 or G1 of the same size (Figure 3.16(b)(iii-v)) and stronger than the dipolar peak of the G1 parent (Figure 3.16(b)(ii)). The Sierpiński fractal structure, when used as a radio antenna, shows multiband optical responses [213]; the increasing definition of peak 3 in the optical spectra and in the EELS signal indicates that the response of

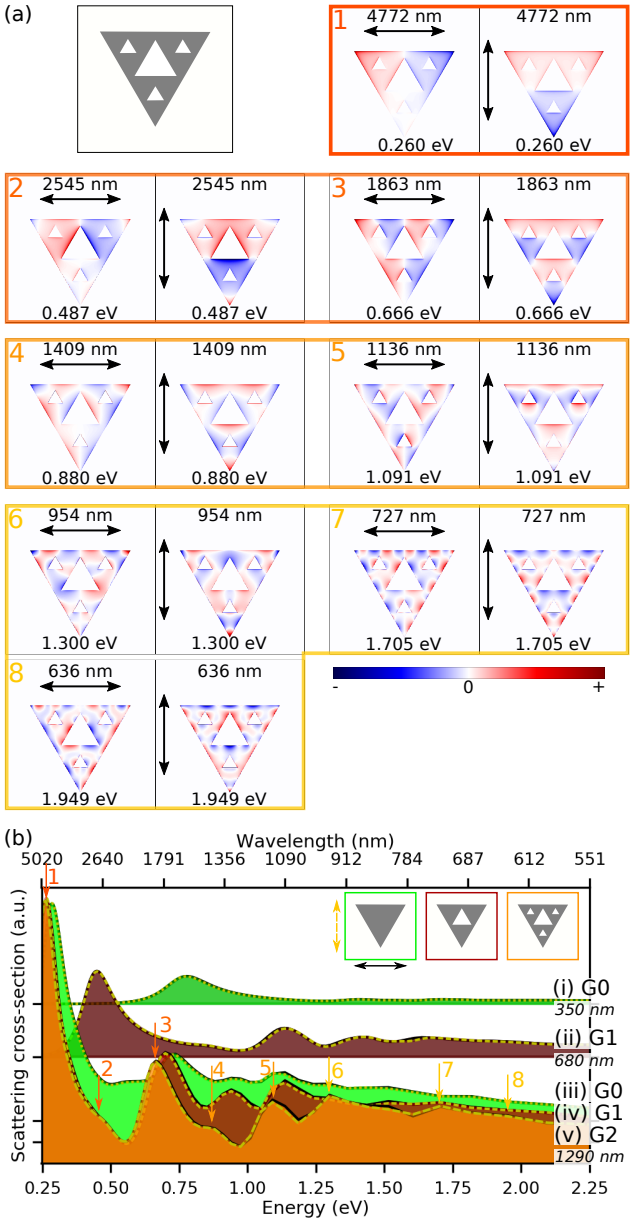

Figure 3.16: Optical FDTD simulations for three fractal generations. (a) Surface charge density distributions at the indicated wavelength, energy, and polarization, grouped by hybridization origin of plasmon modes, for a G2 fractal of side length 1290 nm; (b) spectra for (i) G0 fractal of side length 350 nm (green), (ii) G1 fractal of side length 680 nm (dark red), (iii, iv, v) G0 (green), G1 (dark red), and G2 (orange) fractals, respectively, of side length 1290 nm for vertical (yellow dashed lines) and horizontal (black solid lines) polarized light at normal incidence. Each individual distribution plotted in (a) is scaled individually according to the colour scale shown in the lower right.

higher order modes can rival that of the dipolar mode in fractal nanoantennas.

Dipolar modes from the G0 grandparent hybridize to form 18 eigenmodes (Figure 3.15) in the G2 structure. The high symmetry of the structure and the close energy spacing of all of these modes means that most of these modes are indistinguishable experimentally; three peaks can be distinguished in the EELS data between 0.46 and 0.71 eV (Figure 3.14(b)(v): peaks 4, 5, 6), and we identify these as arising from hybridization of the G0 dipolar modes by the localization of EELS signal around the corners of the G0 grandparent units and the proximity in energy to the G0 grandparent dipolar peak. Optically, two pairs of degenerate modes arise from G0 dipolar mode hybridization (Figure 3.16(a,b): peaks 4, 5), though the LSPR modes may be close enough in energy that the responses are mixing with each other and individual modes cannot be easily separated anymore. Although the first of these peaks (peak 4) is optically weak, the second is a clearly defined peak with a stronger scattering cross-section than the dipolar peak of the G0 grandparent (Figure 3.16(b)(i)).

At higher energy than these peaks is a broad amalgam of peaks identified as hybridizations of edge modes of the G0 prism (Figure 3.14(a,b)(v): peaks 7, 8; Figure 3.16(a,b): peaks 6-8) and aperture modes around the edges of the G2 apertures (Figure 3.14(a,b)(v): peak 9), which come from perturbed cavity modes of previous generation structures (see discussion on subtractive fractal cavity modes in Section 3.2.2). The final identifiable spectral response (peak 10) is identified as a descendant of the G0 primary cavity mode (Figure 3.14(a,b)(i): peak 4).

3.3.6 Predicting Recursive Modes

Using the experimental results supported by calculations, we can, in a manner extensible to other hierarchical structures, predict the recursive trend of LSPR modes in increasing generational orders of fractals. There are two degenerate dipole modes on the G0 parent which hybridize to form $2(3^l)$ modes on an lth generation fractal with 3^l G0 parent units. Each successive fractal generation acts as a larger parent unit for the next generation, revealing similar LSPR behaviour to the G0 hybridized modes, but on another length scale; in higher fractal generations, modes arising from hybridization of the G1 dipolar modes will number $2(3^{l-1})$. The trend is confirmed by examining the predicted eigenmodes of a Generation 3 (G3) ($l = 3$) fractal structure (Figure 3.15), which has $2(3^0) = 2$ degenerate dipole modes; $2(3^1) = 6$ dipole modes resulting from hybridization of the G2 parent unit dipolar modes; $2(3^2) = 18$ eigenmodes resulting from hybridization of the G1 grandparent unit dipolar modes; and $2(3^3) = 54$ eigenmodes resulting from hybridization of the G0 great-grandparent dipolar modes. Extrapolating from these results, we may predict that, for instance, a Generation 8 fractal will have two degenerate dipole modes, six modes resulting from hybridization of the Generation 7 dipole modes, and so on, down to 13,122 eigenmodes arising from hybridization of the G0 dipolar modes. We also note that, because of the C_3 symmetry of each full fractal generation, each pair of dipolar modes in the

Sierpiński fractal actually represents a set of six degenerate dipole modes, which can be obtained by rotations of 120°.

Experimentally, many of these different hybridized modes will be degenerate or indistinguishable from each other after taking into account instrument resolution and intrinsic peak width, especially for the higher order modes present in the smaller parent units of each generation. Each successive fractal generation adds a new band to the response spectrum, while maintaining and broadening the response from all of the previous generations. The localized hotspots for each mode can be predicted through knowledge of which band the mode is in: the hotspots for each mode, as visualized through EELS, tend to occur at locations relevant to the fractal parent units from which that band arises, as observed in the current example of the Sierpiński fractal and in other self-similar hierarchical geometries [123, 211, 212, 230].

Resonance Patterns in Hierarchical Geometries

The fractal nature of the structures contributes to some of the unique properties of the plasmon response spectrum. The symmetry of many deterministic fractals is consistent across all length scales [231]; the repetitive self-similar symmetry of geometrical fractals such as the Sierpiński is evident from inspection of different generations. Each successive generation maintains the C_3 symmetry of the previous generations. The self-similarity of the geometrical symmetry is also reflected in the anisotropy of the plasmon response across the different spectral bands in each generation. Each of the plasmon modes in which the charge distribution breaks the C_3 symmetry is partnered with a degenerate mode which responds to the opposite polarization (Figure 3.16), thereby maintaining the anisotropy of the response regardless of generation number. We may also predict that in higher generations, the fractal geometry ensures that each plasmon resonance mode either has C_3 symmetry or orthogonal degeneracy. Considering the G1 fractal, we notice that the charge distribution and EELS map of the hybridized modes from the G0 dipole maintain the same symmetry as higher order edge modes on the simple G0 nanoprism, but with stronger scattering cross-sections; these symmetries are repeated through all generations.

In addition, the repetition of the G0 parent unit is reflected in the strength of higher order plasmon modes. Compared to other hierarchical structures, such as a simple chain of coupled nanoparticles [232, 233], higher order modes in the Sierpiński fractal structure have a stronger response relative to the dipole peak, a trend which is more evident in higher generations (Figure 3.14(b), 3.16(b)), and is confirmed in Cesaro fractals [211], Koch fractals [123], and Cayley trees [212], among others [234].

The self-similar recursive trend described herein is possible only because of the conductive coupling between the parent prisms in each fractal generation, allowing charge to flow completely into or out of each parent unit. Breaking the conductive coupling within the Sierpiński fractal eliminates the low energy dipolar modes and leads to sets of three-way, or n-way hybridized modes based on coupling between the parent units, as seen in the G1 fractal presented in this work. The presence

of defects in the structure which impair conductive coupling provides another way to manipulate the spectral response of the fractal structure. Introducing defects blueshifts the response and promotes the intensity of higher order peaks over the lowest energy peak.

The intermediate topologies (G0.5 and G1.5) present interesting cases in which the dipolar peak is strongly redshifted relative to succeeding fractal generations of the same size, and the dipolar degeneracy is broken, leading to a polarization-sensitive response. Despite the dipolar redshift and breaking of the C_3 symmetry, these halfway structures still present a similar multiband response from hybridization of the modes of the parent generations; the intermediate structures present themselves as candidates for multiband, polarization-sensitive sensing platforms.

Not only do the dipolar modes of G0 hybridize, but the higher order G0 edge and cavity modes can also hybridize when higher fractal generations are built. When apertures are added to the G0 structure to create G1 and higher, the mode behaviour becomes very complex and the distinction between edge and cavity modes becomes blurred. For instance, when an aperture is added to G0, the lowest energy G0 cavity mode changes and behaves like an edge mode around the central G1 aperture. The lowest energy cavity mode of the G0 prism hybridizes to form multiple cavity modes with small energy differences in the additive Sierpiński fractal. For example, in G0.5, there are two G0 parent units and the lowest energy G0 cavity mode hybridizes to form symmetric and anti-symmetric modes. In the G1 fractal, there are three G0 parents and a three-way hybridization of the lowest energy G0 cavity mode. Each successive generation increases the number of modes seen in this spectral region. The natural plasmon linewidth, instrumental peak broadening, and the close energy spacing of so many hybridized cavity modes means that the spectral features above 1.5 eV are all blurred into each other and no clear peaks can be distinguished as the fractal generation advances. Cavity modes are also known to have relatively weak EELS signal compared to other modes [79, 228].

The cavity modes are excited when the electron beam passes through the faces of the G0 parent prisms. Unfortunately, the scattering of the electron beam is strongest when it passes through the nanostructure, degrading the SNR for the cavity modes. Each of the spectra in Figure 3.14(b) has been normalized to the ZLP, emphasizing the noise in the cavity mode spectra relative to spectra integrated over regions outside the nanostructures. The low SNR also explains the comparatively noisy EELS intensity maps of the cavity modes in Figure 3.14(a). A similar argument can be made for some of the higher order edge modes (*e.g.* peaks 8, 9, 10 of G1.5 in Figure 3.14(b)(iv)), which are integrated over very small areas and so have a poorer SNR than a larger integration area would provide. With the higher order fractal generations, the sheer number of modes present in the spectrum makes identifying individual peaks at higher energies very difficult, even with the local excitation provided by EELS spectrum imaging techniques.

3.4 Concluding Remarks

Following two different approaches, we have investigated the behaviour of LSPR in Sierpiński fractal triangles using EELS and a combination of FDTD and BEM simulations. It was found that the primary dipolar energy can be redshifted by increasing the generation number of a subtractive fractal, while maintaining the same physical footprint. With the Sierpiński triangle, two degenerate dipole modes of the triangle are able to couple to dipole modes on the central aperture, solely because symmetry is maintained and because of the degeneracy of the two orthogonal modes on both the triangle and the aperture, qualitatively obeying the Babinet principle. If the symmetry and degeneracy is broken on either the aperture or the triangle, the degeneracy of the dipolar modes is broken. The energy shift of the dipolar mode is dependent on the size of the apertures and the width of the conductive channels linking the different parent units of the fractal: larger apertures and more narrow conductive pathways lead to a stronger redshift of the dipole mode.

The peak strength of higher order mode peaks relative to that of the primary dipolar mode has been shown to increase with higher fractal generations, and even to become stronger than the primary dipolar mode when the conduction across the structure is highly impaired. The relative strength of different peaks may be controllable by manipulating both the fractal generation number and the width of the conductive channels.

Increasing the generation number of the fractal or the size of the apertures may be an efficient way to redshift the dipolar modes of the peaks, but there is a practical limit to the highest generation used for a given spatial footprint. With higher generations, the G0 units and conductive channels between parent units must become smaller and smaller, and even disregarding the limits of current fabrication technologies, eventually charge will no longer be able to flow efficiently across the structure and the junction conductivity will become too low to observe a redshift.

When an aperture introduced into the G0 triangle interrupts an anti-node of the LSPR, there is a stronger energy shift of the mode compared to the case when the aperture is placed on a LSPR node. Conversely, when the aperture is on a surface charge node of the LSPR, the energy of the mode is stable, but the EELS distribution changes as charge builds up around the aperture edges. This conclusion leads to a greater ability to control and design the plasmon behaviour of any structure: to shift the energy but maintain a similar footprint and field distribution, an interrupting feature can be placed on a node of the LSPR; to maintain a peak at the same energy, a feature may be placed on an anti-node of the structure.

In the additive fractal, the basic elements of a fractal structure can be used to effectively design multiband spectral responses with predictable localized hotspots in hierarchical structures. Through fine-tuning of the fabrication parameters, defects can be introduced to further manipulate the spectral response; by reducing conduction between the parent units, the signal from higher order peaks can be enhanced and the

energy of the lowest order peaks can be blueshifted. The possibility of defect engineering combined with the polarization-sensitivity of the intermediate topologies with distinct symmetries provides interesting opportunities for multiband sensing platforms or second harmonic generation with rich polarization-dependent spectral responses by, for instance, leaving only one conductive channel in a G1 fractal.

Each previous generation within a fractal structure contributes a spectral response band through hybridization of its dipolar modes; the number of eigenmodes arising from each parent unit can be predicted by applying a simple equation. Similar modes are seen on different length scales within the fractal structure, exhibiting a hierarchical response which is strongly linked to the hierarchical geometry and use of fundamental building blocks. This makes the fractal structure a strong candidate for multiband sensing applications across the spectrum; more spectral bands with strong scattering probabilities can be added by increasing the number of iterations used to construct the fractal. The complex fractal structures constructed from basic building blocks show predictable responses, providing valuable tools for the manipulation of plasmon modes and engineering design strategies for tuning the multiband response.

Chapter 4

Split Ring Resonators

This chapter concerns the split ring resonator (SRR), a well-known and studied antenna used for its ability to create a magnetic dipole moment when stimulated by light. The ability to create a magnetic dipole moment in response to light makes the SRR a good candidate for metamaterial applications. The SRR has been studied on many length scales, from a radio antenna to a microwave antenna, down to the nanoscale plasmonic antenna. Most studies on the nanoscale have focused on the planar split ring resonator because of its compatibility with nanofabrication techniques; in this chapter, we will discuss a vertical SRR (VSRR) plasmonic nanoantenna. By changing the orientation of the SRR, new opportunities for coupling with the magnetic dipole moment arise and, as will be discussed later in the chapter, a different series of higher order plasmon modes is emphasized.

Portions of this chapter (Figure 4.1, 4.3, 4.4, 4.5, 4.11, 4.12 and the corresponding discussion sections, including Section 4.2.4 on Correlative Spectroscopy) have been adapted from I. C. Bicket, E. P. Bellido, S. Meuret, A. Polman, and G. A. Botton, "Correlative electron energy loss spectroscopy and cathodoluminescence spectroscopy on three-dimensional plasmonic split ring resonators," *Microscopy (Oxf)*, vol. 67, pp. i40–i51, Mar. 2018, by permission of The Japanese Society of Microscopy [235].

4.1 Metamaterials

Metamaterials are artificially constructed materials which exhibit new and exotic properties that are difficult or impossible to find in naturally occurring materials. The concept of metamaterials applies to many different fields of science, ranging from mechanical to electromagnetic properties. In optics, metamaterials are designed to create properties such as a negative refractive index.

The refractive index is a macroscopic property, averaged over many unit cells in a crystal, or over many metamolecules in a metamaterial. The refractive index ($\tilde{n}$) is calculated using the relative electric permittivity (ϵ_{r}) and the relative magnetic permeability (μ_{r}) (Equation 4.1).

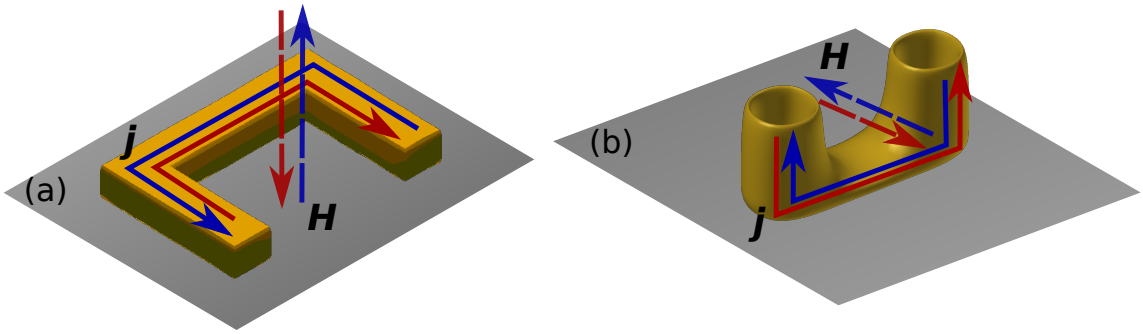

Figure 4.1: Split ring resonators in the (a) planar and (b) vertical (depicted with hollow pillars to mirror fabricated structures) orientations. $\boldsymbol{j}$ and $\boldsymbol{H}$ indicate the direction of current flow and the induced magnetic fields, respectively, on the LC resonance mode of the SRRs.

$$\tilde{n} = \pm\sqrt{\epsilon_{\mathrm{r}}\mu_{\mathrm{r}}} \tag{4.1}$$

An optical metamaterial possesses sub-wavelength metamolecules which modify the average permittivity or permeability, thereby changing the effective refractive index. Work by Veselago in the 1960s [236] predicted that materials with a negative refractive index could exist if both the permittivity and permeability are negative, in which case the negative square root in Equation 4.1 is used. In a material with a negative permittivity and permeability, the group velocity and the phase velocity of electromagnetic waves propagate in opposite directions through the material; the Doppler effect is reversed; Cherenkov radiation is emitted in the opposite direction; and the refractive index is negative. However, there are no naturally occurring materials with simultaneously negative permittivity and permeability. Only when the concept of metamaterials was introduced could such a material be designed [52, 54].

A negative permittivity can be found in natural materials in the frequency band below the plasma frequency of a conductive metal [60], or engineered at lower frequencies in artificial materials using, for example, a lattice of thin conductive wires [237, 238]. A metamaterial with an artificially negative magnetic permeability can be created using SRRs [239]. An SRR can be pictured as a conductive ring which has been broken in one location, creating a gap in the ring; current flowing around the split ring supports a magnetic dipole through the centre (Figure 4.1) while capacitance builds up across the gap in the ring, balancing the inductance from the circularly oscillating current to achieve LC (inductor-capacitor) resonant behaviour. The effective permeability drops below 0 on the high frequency side of this resonance. Combining the SRR with a lattice of conductive wires creates a metamaterial with a simultaneously negative permeability and permittivity, thereby giving it a negative refractive index and creating a 'left-handed' medium [54]. At higher frequencies, the negative permittivity found in conductive metals can be combined with the SRR design to create left-handed materials [52].

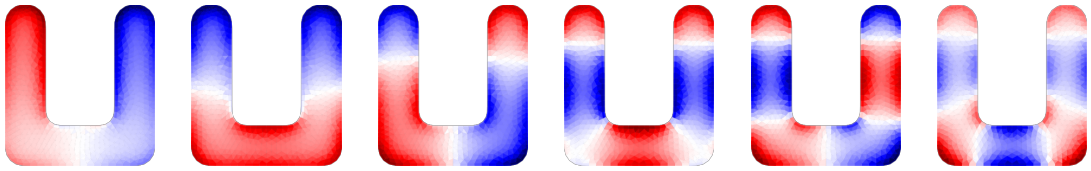

Figure 4.2: First six LSPR eigenmodes of the planar SRR.

4.1.1 Split Ring Resonator Antennas

Because of its ability to create an artificial magnetic dipole moment and thereby a negative permeability metamaterial, the SRR is a prime candidate for creating left-handed metamaterials. If the SRRs are placed on the sides of cubic unit cells, the optical response is isotropic [239], but in a planar array of resonators fabricated on a substrate, the optical response is anisotropic. In the original work, the SRRs operated in the microwave regime and were several cm or mm in size. To achieve resonance in the infrared (IR) or visible spectral regimes, the SRR must be scaled down to the nanoscale and fabricated from a plasmonic material. Scaling down the SRR requires increasingly complex fabrication techniques: from macroscale assembly of millimetre size SRRs [55]; to photolithography on the micrometer scale [240, 241]; to electron beam lithography for nanoscale structures [242–245].

Planar resonators

On the nanoscale, the easiest SRR to fabricate is planar (Figure 4.1(a)), lying flat on the substrate to create an anisotropic metamaterial. In the planar SRR, the magnetic dipole moment is normal to the surface, making it difficult to couple this magnetic moment directly to incoming light [246,247], though it can be excited indirectly using the electric field of normally incident light polarized across the gap in the split ring [248]. To couple to the magnetic fields of incoming light, however, oblique excitation must be used [246]. In the planar SRR, odd and even resonances couple to orthogonal polarizations of light [247], or to an electron beam. The resonance modes of the planar SRR resemble those of a bent nanowire in terms of node and anti-node distribution (see eigenmodes in Figure 4.2), though coupling between the SRR tips causes energy shifts and small modifications to the charge distribution [242, 244].

Vertical resonators

Coupling to the magnetic field of incident light is easier in a VSRR, because its resonant magnetic moment is parallel to the substrate (Figure 4.1(b)). When normally incident light is polarized across the split ring gap, the electric field of the light couples to the electric dipole moment between the tips of the split ring, and the magnetic resonance of the VSRR couples directly to the magnetic field of the incident light [248, 249], increasing the magnetic energy density compared to the planar SRR [248].

When incident light is polarized along the gap, it cannot couple to the magnetic resonance [249].

The in-plane magnetic dipole moment also means that the VSRR can be used to couple to other nearby VSRRs to create, for instance, bonding and anti-bonding magnetic dipole modes in hybridized structures [248], or the toroidal dipole mode studied in Chapter 5. If either the length of the bottom bar or the height of the arms is increased, the magnetic resonance undergoes a redshift [249].

Fabrication of the VSRR has been achieved on the millimetre scale [250], micrometer scale [251], and nanoscale [248,249,252], becoming progressively more challenging as the length scale is reduced. The VSRR studied in this work was fabricated using a double patterning step electron beam lithography procedure, as described in Chapter 2, Section 2.8.1. Based on observations and tilting of the fabricated VSRRs in the electron microscope, it appears that the VSRRs have hollow pillars (as represented in Figure 4.1(b)).

4.2 Results and Discussion

Fabrication produces VSRRs with a base length of approximately 300 nm with small upright pillars. Correlative EELS and CL were performed on the same VSRR for direct comparison of the spectromicroscopy results (Figure 4.3), each technique contributing unique information about the LSPR modes of the VSRR. Simulations were done in MNPBEM to confirm the nature of the LSPR modes and supplement the experimental data. Further investigations were done on another VSRR concerning the polarization properties of the light emitted by the VSRR over the spectrum of plasmon resonances supported by the structure. A detailed explanation of the polarization properties of light and the Stokes parameters can be found in Appendix A.

In the EELS data (Figure 4.3(a-d, i)), there is a strong peak in the near-IR at 0.69 eV (1.8 µm), localized around the tips of the VSRR. This is the magnetic dipole mode, the lowest energy and strongest mode in both EELS and CL, based on the simulated spectral response (Figure 4.4), indicating that it has the strongest net dipole moment of the VSRR modes and thereby strongest radiative coupling. The energy is out of the accessible range of the CL spectrometer used for the data presented in Figure 4.3(e-i), but the peak is clear in the EELS data.

At higher energy than the magnetic dipole peak, there is a broad spectrum of higher order modes between 1 eV and 2.5 eV (495 to 1240 nm wavelength) which are difficult to distinguish in the EELS data. At least two peaks can be made out (Figure 4.3(c,d)), but the nature of these modes is difficult to pinpoint from the EELS data and it is not clear if there are more overlapping peaks inside this signal. The CL data between 1.25 and 3 eV reveals three major peaks (1.375 eV, 1.73 eV, 2.12 eV) localized around the rims of the VSRR pillars (Figure 4.3(f-h)).

In the simulations, the strongest peak in both EELS and CL is located at 1.035 eV. Higher order modes start after 1.9 eV and extend to approximately 2.4 eV, corre-

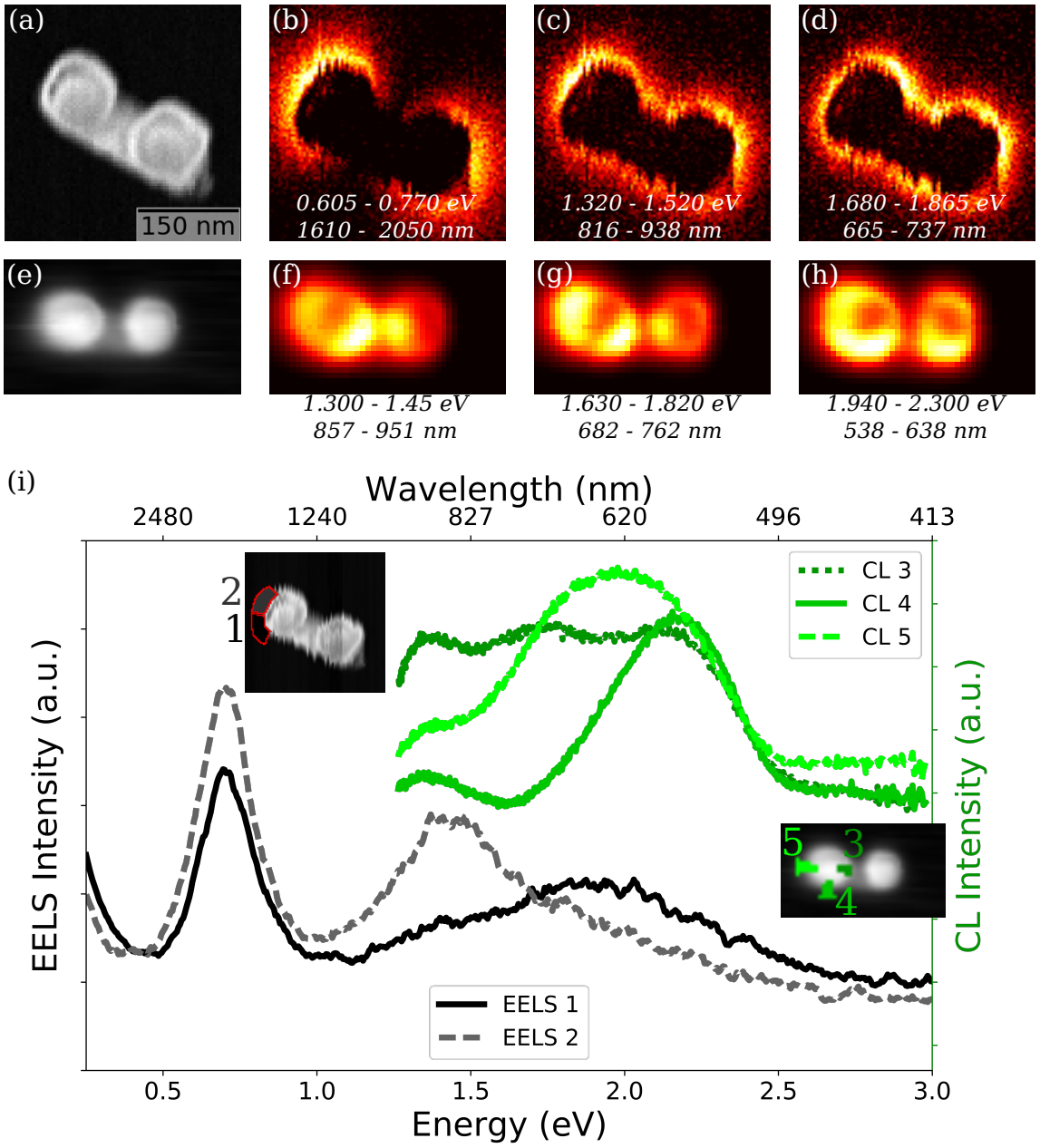

Figure 4.3: Experimental EELS and CL maps and spectra for an isolated VSRR; (a) ADF image of the VSRR (top down); (b)-(d) EELS intensity maps for the first three peaks; (e) SEM image of the VSRR (top down); (f)-(h) CL intensity maps for the three visible LSPR peaks (CL mirror is located towards the top of the image, opening to the bottom); (i) EELS spectra (black) and CL spectra (green) obtained from the areas shown in the insets.

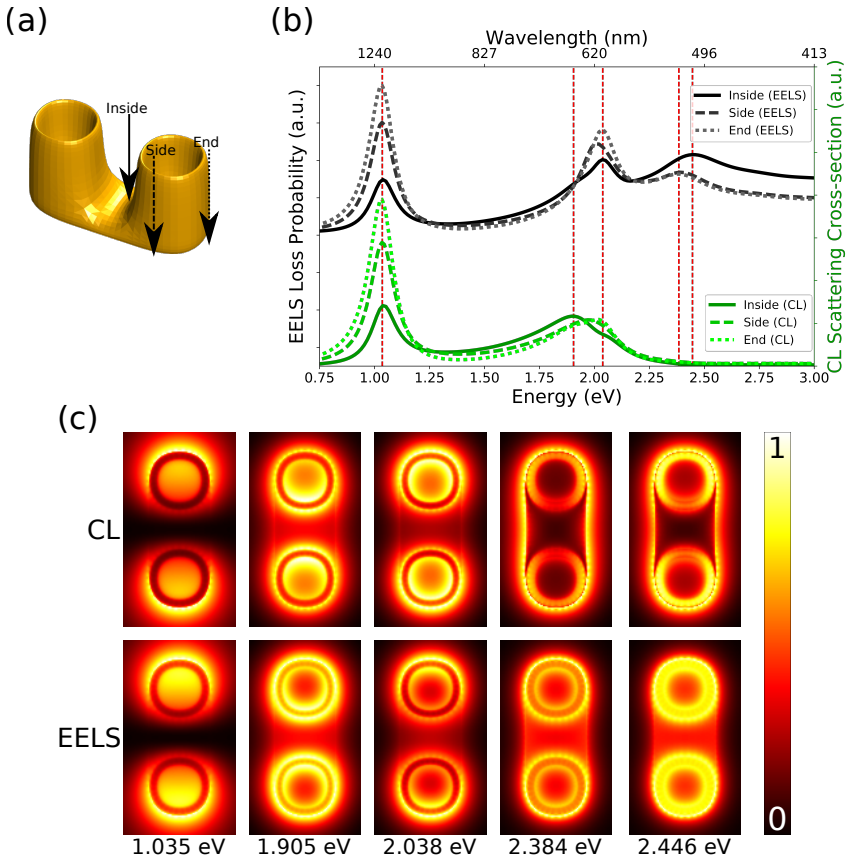

Figure 4.4: MNPBEM simulations of an isolated VSRR; (a) The simulation mesh for the single SRR with hollow pillars; (b) Calculated EELS and CL spectra for the locations marked by arrows in (a); (c) EELS and CL maps for the energies marked on the spectra by red dashed lines.

sponding to visible light between 650 and 500 nm. There is a strong overlap between all the peaks in this region and it is difficult to separate the individual resonances, but four main peaks at 1.905, 2.038, 2.384, and 2.446 eV are identified and their spatial intensity maps shown in Figure 4.4(c) for both EELS and CL, showing, similarly to the experimental data, localization of the modes around the rims of the VSRR pillars.

Before beginning to discuss the different modes present in the sample, the differences in energy between the simulated peaks and the experimental peaks will be addressed. The mode energies of the simulations (Figure 4.4) are blueshifted compared to those in the experimental data (Figure 4.3). This may be attributed to the presence of the substrate [253], which was not taken into account during simulation, and to differences in the simulated structure relative to the fabricated structure. The substrate causes additional damping of LSPR modes and changes the dielectric environment around the structure, thereby changing the mode energy. The dimensions of the simulated structure may be slightly different from those of the fabricated VSRR; small defects present in the experimental structure may particularly affect the higher

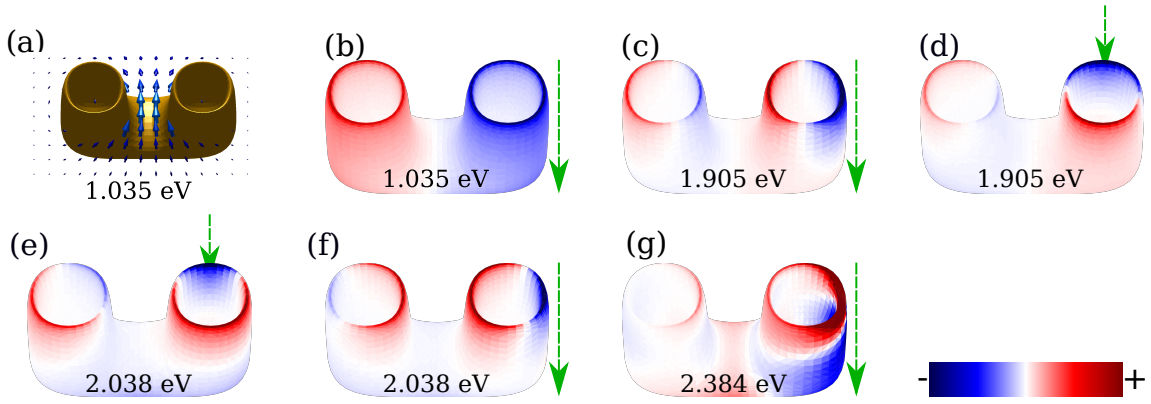

Figure 4.5: MNPBEM surface charge simulations of an isolated VSRR. (a) Magnetic field vectors for the primary SRR mode at 1.035 eV; (b)-(g) Calculated surface charges for the single split ring resonator at the indicated energies, the green arrow indicates the position of the electron beam.

order modes. In particular, it seems that the pillars are closer together in the fabricated SRR than in the simulated model, which may increase the coupling between the pillars and make the different LSPR modes around the rims more evident in the experiment. The simulations have approximated the pillars as hollow cylinders, but it is difficult to gauge the level of filling inside the as-fabricated pillars based on STEM projections or SEM imaging.

4.2.1 Magnetic Dipole Mode

The lowest energy mode detected in EELS, at 0.69 eV, has a broad evanescent field which matches that seen in the simulation data at 1.035 eV. Based on previous studies of the SRR [242, 244], this mode is expected to be the magnetic dipole mode; calculations of the magnetic field vectors at this energy confirm this assignation (Figure 4.5(a)). Surface charge calculations (Figure 4.5(b)) confirm that this mode also possesses an electric dipole along the long axis of the VSRR.

Although the magnetic dipole mode is out of reach of the CL spectrometer used to acquire the data in Figure 4.3, there is another CL spectrometer which works in the near-IR. The results of a spectrum image (SI) acquired with this spectrometer are shown in Figure 4.6(b-d). On the IR spectrometer, composed of an array of InGaAs photodiodes, the magnitude of the dark noise is evidenced by the black spectrum in (c), despite cooling the spectrometer to liquid nitrogen temperatures. The system correction factor, which shows the number of incoming photons required to obtain one count on the spectrometer and reflects the inverse of the detector quantum efficiency (DQE), is highly non-linear in the IR spectrometer, and has a peak of poor conversion efficiency above 1600 nm (black curve in (d)). Both of these factors make the acquisition and interpretation of CL data in the IR a very challenging task.

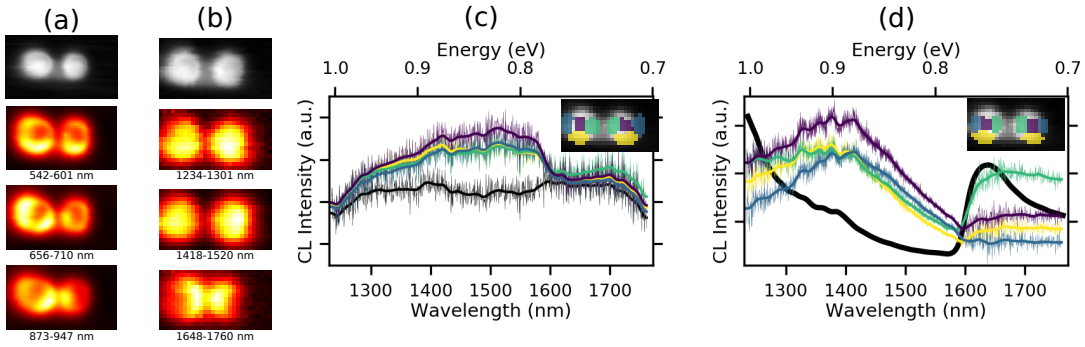

Figure 4.6: Visible and IR CL spectrum imaging showing higher diffraction orders on the IR spectrometer grating. (a) Extracts from an SI in the visible regime, as shown in Figure 4.3(f-h); (b) spatial intensity maps from an SI acquired in the IR with an acquisition time of 15 s; (c) raw IR spectra averaged over the areas indicated in the inset (black line is the dark reference, with the electron beam blanked); (d) IR spectra after correcting for contributions from the substrate, dark noise, and the quantum efficiency of different detector channels (black curve shows the shape of the system correction factor as a function of wavelength). Spectra are averaged over the areas shown in the inset. For (c) and (d), the solid line passing through each data set represents the data after a Gaussian smoothing filter with a standard deviation of 10 channels is applied.

The poor signal-to-noise ratio (SNR) can be improved by using longer acquisition times or higher electron beam currents to induce more emission from the sample. However, increasing the acquisition time (already at a long 15 s per pixel) results in worse drift and the deposition of more carbon on the sample in the relatively poor vacuum of the SEM chamber. Increasing the beam current, from approximately 6.5 nA, for the acquisition shown in Figure 4.6, to 30 nA quickly melts the VSRR.

The interpretation of signal obtained with this spectrometer is further complicated by the presence of second order diffraction from the dispersive grating. The spectrometer grating diffracts light according to integer multiples of its wavelength, $l\lambda$; usually the first order diffraction is chosen, as it contains the most intensity, but it is possible for second order diffraction to appear at 2λ in wavelength. If the DQE favours shorter wavelengths over longer wavelengths, then the second order diffraction of visible light can dominate the signal over first order diffraction from IR light. This effect is seen in the SI presented in Figure 4.6; the response in the IR SI (b) mirrors that of the higher order LSPR modes in the visible regime (a). Interestingly, the mode distribution is not precisely the same, which may be a result of overlapping signal between the second order visible signal and the first order IR signal. The CL signal for the dipolar mode is expected to have high signal (Figure 4.4(c)) near the outer edges or over top of the pillars, which may contribute some intensity to the purple spectrum in Figure 4.6(c,d).

Above 1600 nm, where the spectrometer efficiency is particularly poor, the second order diffraction from the modes in the visible regime appears to dominate the signal. Around 1500 nm, there is some signal which has high intensity in the centre of the pillars and does not belong to any of the rim modes shown in (a); this signal may

actually belong in the IR, but it is overlapping with second order diffraction from the visible regime. It is difficult to state where the IR peak may be located because of this interference and the high variations in spectrometer efficiency as a function of wavelength.

To reduce the contributions from second order diffraction of shorter wavelengths, a 980 nm long-pass wavelength filter is introduced before the grating. To combat the low DQE and low SNR, and because it is expected that there is only one peak in the IR for the VSRR based on the EELS data, the zeroth order diffraction of the spectrometer grating is used. This means that all light going into the grating is sent directly onto the spectrometer without dispersion, hitting only a small number of photodiodes. By doing this, the spectral dimension of the SI is totally lost, but the SNR is greatly improved and polarimetry measurements are possible.

IR Polarimetry

Using the 980 nm long-pass wavelength filter and a 1600 nm grating set to transmit the zeroth diffraction order, six different data sets are acquired with six different quarter wave plate (QWP) and linear polarizer (LP) settings, in order to retrieve the full polarization state of the light emitted in the IR, as explained in full detail in Appendix A. The SEM images are shown in Figure 4.7(a), showing that the VSRR did not melt during acquisition. Stokes parameters (see Appendix A, Sections A.1.1, A.1.2 for more detail) calculated from the six experimental data sets are shown in Figure 4.7(b). The polarized S_0 relative to the unpolarized S_0 shows that most of the light that is emitted from the VSRR is polarized. Unpolarized light may result from incoherent emission from the sample or substrate, errors in the alignment of the six images to each other, inefficiencies in the QWP or LP, or noise-based fluctuations in the acquired signal.

The S_1 component indicates that the light is strongly and dominantly vertically polarized, along the long axis of the VSRR. The S_2 pattern has much lower intensity relative to S_1 and reverses sign on the top and bottom halves of the image. The S_3 parameter, an indication of circular polarization, shows a quadrant pattern as the electron beam is scanned over the VSRR, switching signs when the electron beam crosses a symmetry axis. Dividing the S_1, S_2, and S_3 Stokes parameters by S_0 gives the relative contribution to the emission at each pixel. S_1 contributes most strongly when the electron beam impacts the VSRR. In aloof, off-axis excitation S_2 and S_3 become relatively stronger, though still weaker than S_1.

The simulated spatially-resolved Stokes parameters (Figure 4.7(c,d)) agree that the emission is most strongly polarized linearly along the long axis of the VSRR. The calculated S_2 parameter shows a quadrant pattern when the VSRR is oriented vertically relative to the mirror (this orientation will be referred to as 'VSRR-v') (c), and a single sign reversal in the horizontally oriented VSRR (this orientation shall be referred to as 'VSRR-h') (d). For both orientations, S_3 shows a quadrant pattern similarly to the experimental data.

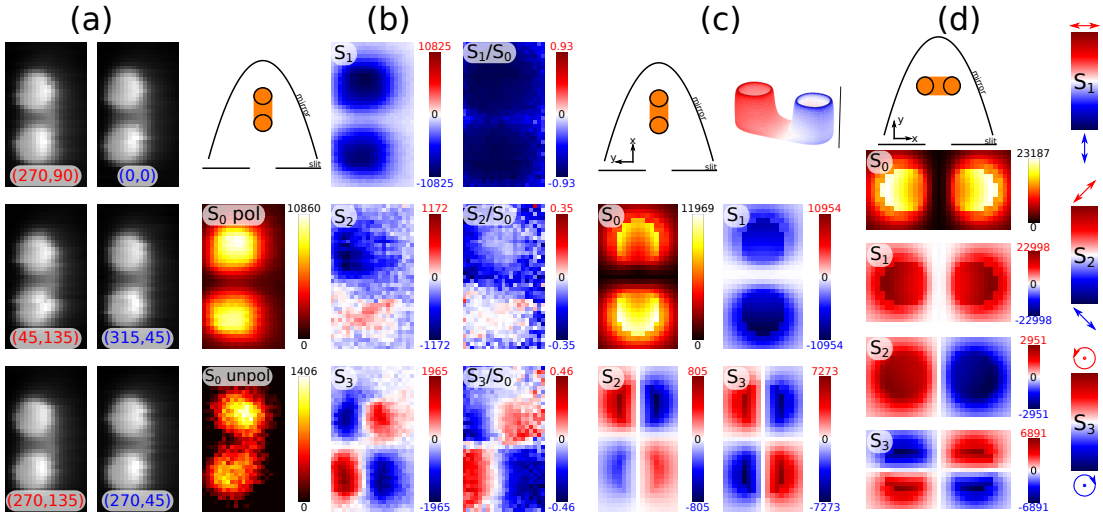

Figure 4.7: Spatially resolved Stokes parameters of VSRR magnetic dipole mode. (a) SEM images of the VSRR acquired simultaneously with each of the six polarization state SIs, the (QWP, LP) settings are indicated in the labels; (b) spatially-resolved Stokes parameters calculated from acquisitions of the integrated IR light with $\lambda > 980$ nm; (c) simulated spatially-resolved Stokes parameters for a VSRR oriented vertically relative to the mirror (VSRR-v); (d) simulated spatially-resolved Stokes parameters for a VSRR oriented horizontally relative to the mirror (VSRR-h). To the right are shown the polarization vector directions for each of the Stokes parameters, with the propagation vector out of the page.

Although the comparison between simulation and experiment is not perfect, there is a remarkable correlation. For both results, the light emitted from the VSRR is dominated by linearly polarized light along the long axis of the VSRR. The dipole mode of the VSRR can be broken down into an electric dipole along the long-axis and a magnetic dipole perpendicular to this, in the same plane through the gap of the split ring. Both electric and magnetic dipoles emit light in a donut-shaped radiation pattern (see Appendix A) normal to the dipole vector. The electric dipole should emit light towards the sides of the VSRR, polarized along the long-axis, while the magnetic dipole should emit light towards the ends of the VSRR, also polarized along the long-axis.

The comparison between experimental and simulated S_2 parameter maps is much less robust. The experimentally calculated S_2 (for a VSRR oriented as VSRR-v) more closely resembles that of VSRR-h, in which the S_2 parameter switches sign on each half of the VSRR. S_3 has a complete reversal of sign when comparing the experiment to the simulation. Observing the simulated angular-resolved (AR) emission patterns helps to clarify why the simulated VSRR behaves in this manner, but does not explain the mismatch relative to the experiment.

Despite the difficulty in finding precise agreement between experiment and simulation, the quadrant patterns of S_3 and S_2 on the simulated VSRR-v indicate some interesting behaviour when the electron beam is moved off of one of the symmetry

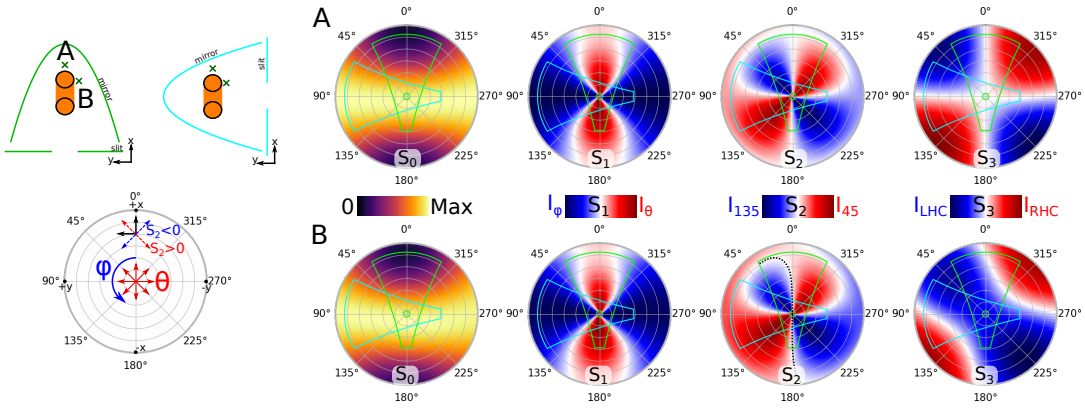

Figure 4.8: Simulated angle-resolved Stokes parameters of the SRR dipole mode at two beam locations, as shown in the upper left (A and B). Coordinate systems for S_1 and S_2 in polar coordinates are shown in the lower left. The projection of the collection mirror on the angle resolved plots is outlined in green and light blue.

axes of the VSRR. When the electron beam is on either the long or short symmetry axis, S_3 goes to 0, indicating that there is no net circular polarization collected by the mirror. However, when the beam is moved towards the corner of the VSRR, some circularly polarized light is collected by the mirror and the S_2 parameter emits more strongly towards the end of the VSRR.

Modelling the Angular-Resolved pattern

Plotting the AR patterns for the Stokes parameters at two different beam locations helps us to identify what is happening when the beam is on or off the VSRR symmetry axis (Figure 4.8). At location A, the electron beam is placed on a mirror axis of the VSRR where the magnetic dipole mode is strongly excited. At this beam location, the S_0 parameter qualitatively matches that of an electric dipole oriented along x ($\boldsymbol{p}_x$), with some additional emission towards $\phi = 0°$ and $\phi = 180°$ which prevents S_0 from becoming 0 as θ goes to 90°.

The S_1 Stokes parameter also appears to be dominated by $\boldsymbol{p}_x$. Although a pure $\boldsymbol{p}_x$ dipole is symmetrical towards $\phi = 0°$ and $\phi = 180°$, the asymmetrical location of the electron beam towards $\phi = 0°$ changes the emission symmetry [89], favouring a stronger emission and stronger θ polarization pointed away from the electron beam (towards $\phi = 180°$). Both mirror orientations (green and blue) pick up light polarized along the long axis of the VSRR. The asymmetry in emission appears to be even stronger when the electron beam is moved to location B, off the symmetry axis, even in the S_0 pattern.

The directional asymmetry is more obvious in the S_2 patterns. The S_2 pattern is distorted from that of $\boldsymbol{p}_x$ emission, with larger lobes in the direction away from the electron beam excitation. At location A, the positive and negative S_2 values precisely

cancel out for VSRR-v (green mirror), but for VSRR-h (blue mirror), the positive S_2 will dominate the signal. The sign of S_2 switches when the beam is moved to the other end of the VSRR and the S_2 lobes favour the other direction, resulting in the two-lobed S_2 pattern seen for VSRR-h in Figure 4.7(d). When the electron beam is moved off the symmetry axis to location B, there is an additional asymmetry in the S_2 pattern, highlighted by the black dashed line, which means that the positive S_2 will dominate slightly for the off-axis location in VSRR-v, explaining the quadrant pattern seen in Figure 4.7(c). For the VSRR-h, the pattern pointing away from the electron beam location remains the same and the sign of S_2 remains the same as for location A.

For a pure electric dipole, S_3 is 0 at every emission angle, but the addition of a phase-shifted magnetic dipole moment causes the emission of some circularly polarized light. When the electron beam is on-axis, at location A, the RHC and LHC are symmetrical and integrating over the mirror gives a net zero circular polarization. Collecting light emitted at $\phi = 45°$, however, would reveal strong circular polarization. When the electron beam is moved off-axis, to location B, the pattern of S_3 changes and LHC polarized light dominates both mirror orientations. As the electron beam crosses either of the symmetry axes on the VSRR, the sign of S_3 switches, explaining the quadrant pattern seen in the spatial maps of S_3 in Figure 4.7.

Viewing the AR plots at different electron beam excitation points helps to explain the patterns seen in the spatially-resolved Stokes parameters. The location of the electron beam induces asymmetrical excitation of the LSPR modes which distorts the AR plots. If the beam is off a symmetry axis in the VSRR, the distortion may cause the dominance of positive or negative S_2 and S_3 according to the beam location. These plots also demonstrate the sensitivity of the Stokes parameters to the precise beam location and mirror position. It may be that this sensitivity, or an error in the simulation code, causes the differences between simulation and experiment seen in the spatial maps in Figure 4.7, or the simulation is underestimating the contribution of the magnetic dipole moment.

Fitting the Dipole Moment

The AR patterns shown in Figure 4.8 indicate that the emission is dominated by an electric dipole oriented along x, but the presence of non-zero circular polarization indicates that the VSRR magnetic dipole moment, with a phase delay relative to the electric dipole, is also contributing to the emission. Based on the geometry of the VSRR, we create a basic model of the emission using the combination of an electric dipole with a magnetic dipole.

The emission from electric and magnetic dipoles is modelled as two oscillating waves related to each other by their relative phase (δ: the phase delay between the electric and magnetic dipoles) and magnitude, as explained more fully in Appendix A. Using the S_3 emission pattern normalized to the total emission (S_0) (Figure 4.9(a)), the relative phase and magnitude of the electric and magnetic dipole moments can

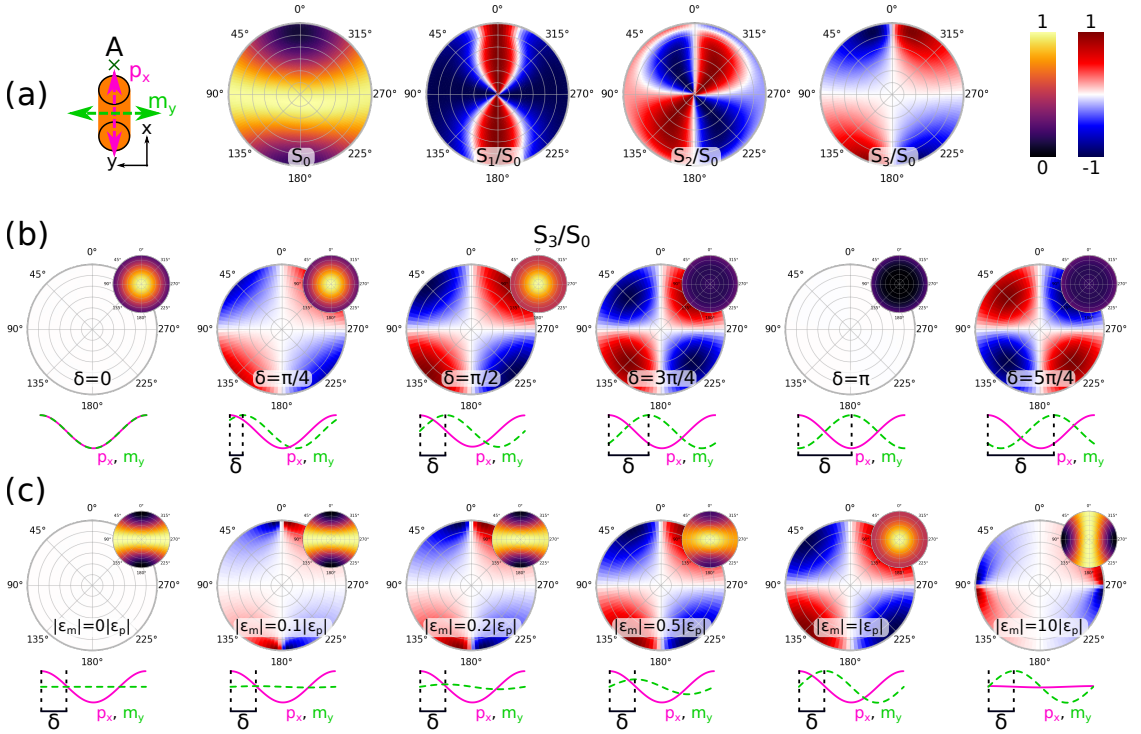

Figure 4.9: Normalized Stokes parameters and circular polarization angle-resolved patterns for the interference of an electric dipole and an orthogonal magnetic dipole moment. (a) Normalized Stokes parameters for the VSRR, with electron beam location A indicated by an ×; (b) Normalized S_3 parameter for different phase shifts applied to the magnetic dipole relative to the electric dipole moment; (c) normalized S_3 parameter for different magnitude ratios of the emitted electric fields from the magnetic dipole and from the electric dipole. Insets in the upper right of the polar plots in (b) and (c) show the S_0 parameter. The sinusoidal curves below each plot show the phase delay and relative magnitude of the emission from the electric and magnetic dipoles.

be inferred. Figure 4.9(b,c) shows the change in the S_3/S_0 AR plot as the phase delay between the two dipoles ($\boldsymbol{p}_x$ and $\boldsymbol{m}_y$) is changed and as the magnitude ratio is changed, based on analytical calculations of the combined emission pattern of both dipoles.

With no phase delay or a phase delay of $\delta = \pi$, there is no circular polarization emitted in any direction (Figure 4.9(b)). As the phase delay is increased from 0, circularly polarized emission first appears near $\theta = 90°$, then the local maximum moves upwards in θ to approximately 45°. The RHC and LHC switch signs when the phase delay of π is exceeded.

If the phase delay is kept constant at $\pi/2$ and the ratio of the magnitude of the radiated fields from the magnetic and electric dipoles is changed, the local maximum of S_3/S_0 moves around ϕ (Figure 4.9(c)). When the magnetic dipole emission is very small, the circular polarization is strongest at the angular location where the radiated fields from the electric dipole are weak and those from the magnetic dipole are strong,

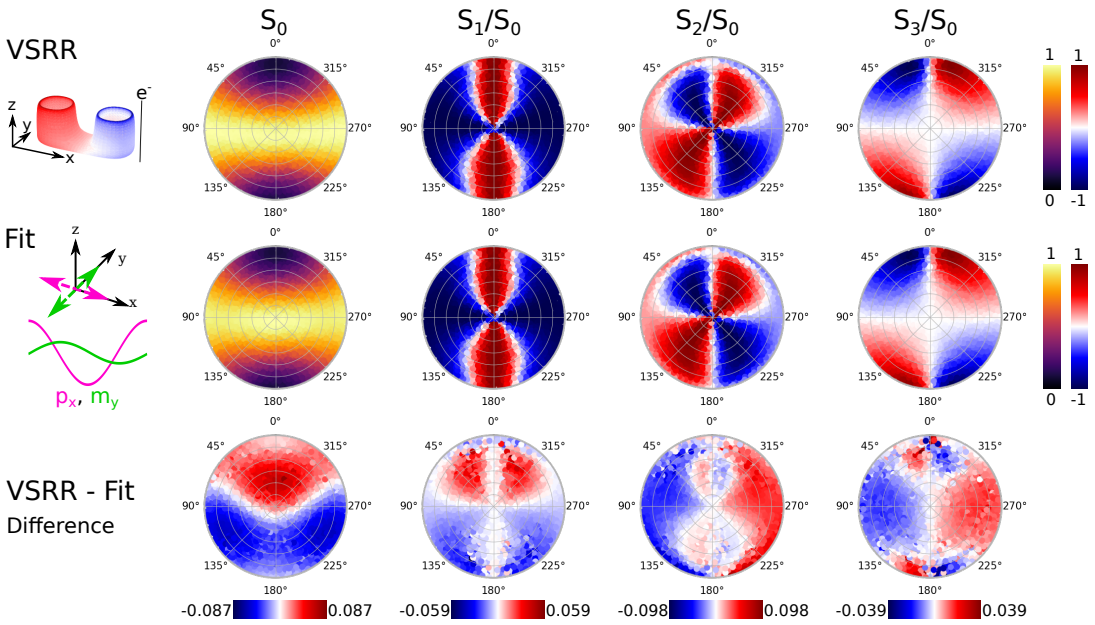

Figure 4.10: Fitting of the emission of analytical dipoles to the magnetic dipole mode of the VSRR. Top row shows the angular-resolved normalized Stokes parameters from the simulated VSRR; middle row shows the Stokes parameters calculated from a numerical fitting of the VSRR patterns using an electric dipole and a magnetic dipole; bottom row shows the numerical difference between the simulated and fitted patterns.

and perhaps more comparable in strength. When both dipoles emit equally strong fields, the strongest circular polarization occurs in-plane at 45° between both dipole vectors; here both dipoles contribute equal fields polarized in orthogonal directions, with a phase delay of $\pi/2$. If the magnetic dipole becomes stronger than the electric one, the local maxima of S_3/S_0 moves towards the angular location where the fields from the magnetic dipole are weakest and those of the electric dipole are strongest.

These trends in the S_3/S_0 AR pattern provide a means of deriving the phase delay and magnitude ratio of the fields radiated from the $\boldsymbol{p}_x$ and $\boldsymbol{m}_y$ dipoles. Although it is not shown in this figure, the maximum of S_3/S_0 is also a local minimum of S_2/S_0 along the θ direction.

Fitting of the upper hemisphere of the simulated S_3/S_0 AR plot to a combination of analytical electric and magnetic dipoles returns the parameters for an electric dipole oriented along x, and a magnetic dipole oriented along y which is emitting fields approximately 0.33× the magnitude of those emitted from the electric dipole, with a phase delay of 93°. The AR Stokes patterns from the simulated VSRR mode, and the pair of fitted dipoles are shown in Figure 4.10.

There is some error in the fit (lower row), because the emission is not perfectly described by a simple pair of analytic point dipole moments, but there is remarkably good agreement between the simulated and fitted Stokes parameters. Higher order EM multipole moments are neglected, although these are expected to have a negligible

effect on the emission of the magnetic dipole mode of the VSRR [247].

The observed phase delay agrees with the $\pi/2$ delay calculated by [247] and could be used to give some interesting insights on the dynamics of plasmonic excitation and emission. Intuitively, at the moment in time when the electric dipole is strongest, the charges are collected at either side of the VSRR. The mobile charges are then subjected to high potential energy from the charge separation and are accelerated back in the opposite direction. When the charges are in motion, the magnetic dipole grows in strength, becoming strongest when the charges are flowing the fastest and the electric dipole is at its weakest, resulting in a 90° phase delay between the electric and magnetic dipole oscillation.

An IR AR camera was not available when the experiments were being performed, but is necessary in order to to verify these simulated results experimentally and derive the phase delay and relative magnitude of the emitting dipoles in the VSRR structure. AR data in the IR would also reveal more clearly the origins of the S_2 and S_3 patterns in the spatial maps in Figure 4.7 and perhaps explain the differences between the experiment and simulation. The simulation could be underestimating the contribution of the magnetic dipole, or the presence of the thin silicon nitride substrate may change the emission pattern sufficiently to change the patterns in the experimentally acquired data.

With the link between the magnetic dipole and the surface current flowing in the VSRR, the interference patterns of the magnetic dipole and electric dipole may be an interesting way to probe the dynamics of the LSPR mode and its interaction with the electron beam without needing femtosecond timescale experiments. Time-resolved simulations, however, may be useful to further probe this interaction. There is some indication that the phase delay between the magnetic and electric dipole emission may be a function of damping parameters within the material. For instance, changing the damping parameter within a Drude model used for the dielectric function of the simulated VSRR causes small changes to the phase delay between the magnetic and electric dipole emission. Working backwards from an experimental dataset might allow the user to derive the Drude parameters of the material used. Although more work remains to be done to understand this relationship and to achieve a better match between simulation and the experimentally derived Stokes parameters, the magnetic dipole mode of the VSRR is identified and the relationship between the electric and magnetic dipole moments inside the VSRR have been derived.

4.2.2 Coupling of Rim Modes

Moving on from the magnetic dipole mode to the higher order modes localized around the rims of the VSRR pillars, the CL spectrometer can be used to full advantage to discover the nature of these modes (Figure 4.3). In the EELS maps, it is difficult to separate the peaks in the visible region of the spectrum, though it appears that at approximately 1.42 eV, there is a mode more strongly localized at the ends of the

pillars, and at higher energy there is a mode or modes with strong signal near the sides of the pillars. The CL intensity maps (1.375 eV, 1.73 eV, 2.12 eV) show the mode structure much more clearly, but there is some asymmetry in the maps between the left and right pillars, and from the top to the bottom of the image.

In the first two maps (Figure 4.3(f,g)), the asymmetry may be attributed at least partially to asymmetries present in the structure as-fabricated; compared to the ideal VSRR, the fabricated structure contains some defects which may affect the emission strength of the rim modes. The higher order modes have smaller effective wavelengths and so are more affected by small defects in the fabricated structure than longer wavelength modes are. For instance, the height of the pillar may not be exactly equal all around the circumference, affecting the electron beam interaction probability and emission strength at different locations around the pillar rim. In particular, the left pillar of this VSRR appears to have greater intensity in all of the CL intensity maps, so may be smoother or better defined than the right pillar. Asymmetry in the emission maps may also come from the asymmetrical collection parameters; the mirror is located towards the top of the CL image with its opening towards the bottom. The dipole mode showed a preferential emission direction relative to the electron beam and so might the higher order modes of the VSRR, which could explain the asymmetries between the top and bottom of the CL intensity maps.

The calculated surface charges (Figure 4.5(c-f)) reveal that higher order modes in the VSRR are different from those of a planar SRR; there are pairs of coupled dipoles around the pillar rims, dependent on the energy and location of the electron beam. The width of the pillars relative to their height supports these modes at low enough energy that they make up the second spectral band after the magnetic dipole, instead of higher order SRR modes (Figure 4.2). The pillar proximity allows dipoles across the rims to couple to each other and create hybridized modes [254]. In a perfect VSRR with ideally shaped pillars (Figure 4.5(c)), there is a longitudinal bonding (LB) mode across the two pillar rims overlapping in energy and complicating the interpretation of a transverse mode (Figure 4.5(d)). At higher energy, there is a transverse anti-bonding (TAB) mode (Figure 4.5(e)) and longitudinal anti-bonding (LAB) mode (Figure 4.5(f)) overlapping with a second-order SRR mode (see eigenmodes in Figure 4.2, [244, 255]). The next highest energy peak in the simulation is a fourth-order SRR mode (Figure 4.5(g)).

Calculating the eigenmodes of the VSRR in order of increasing energy eliminates the confusion caused by overlapping peaks (Figure 4.11). In the ideal VSRR, the magnetic dipole mode is the lowest energy, followed by an LB mode across the pillar rims, a transverse bonding (TB) mode, TAB mode, LAB mode, then a second-order SRR mode (Figure 4.11(a)). However, performing some mutations on the shape of the pillar to represent fabrication defects changes the order of the pillar rim modes and the appearance of the higher order resonances (Figure 4.11(b-d)). Despite the different ordering of eigenmodes caused by pillar defects, some consistencies remain: the magnetic dipole mode is always the lowest energy resonance and the coupled

bonding modes are always at lower energy than the coupled anti-bonding modes.

In the lowest energy mode visible in CL, at 1.375 eV in the experiment (Figure 4.3(f)) and 1.905 eV in the simulation (Figure 4.4), there is high intensity in between the two pillars, in the centre of the structure. This is the LB mode of the coupled pillar rims (Figure 4.5(c)). In the typical example of LB modes in coupled dimers, the fields in the centre of the dimers, although strong, are invisible to the electron beam [164], since they are mostly perpendicular to the direction of the propagation. In the case of the VSRR, the presence of the metallic bottom bar may force changes to the electric field configuration of the LB mode, allowing the electron beam to interact with this mode in between the coupled pillars. It would be very challenging to retrieve any EELS signal from the insides of the pillars due to the strong scattering of the transmitted electron beam as it passes through the thickness of the VSRR. In the simulated spectrum, this mode is, at most, a shoulder on the peak of the other rim modes (Figure 4.4(b)) in the EELS spectra and may therefore have very weak coupling to the electron beam. Despite this, the LB mode possesses a strong net dipole moment and has strong CL signal.

In the simulations, the next highest energy peak is the LAB mode at 2.038 eV, overlapping with the TAB mode in energy. At this energy, there is higher intensity towards the outer ends of the pillars in the simulated EELS and CL maps. In the CL data, this corresponds with the resonance at 1.73 eV (Figure 4.3(g)). The tails of the peak at 1.375 eV overlap in this energy range, but by subtracting the lower energy map from the higher energy map (Figure 4.12(a)), the differences between the resonances are made clear; the higher energy resonance has high intensity at the outer edges and the lower energy LB resonance contributes the intensity seen towards the middle of the VSRR. In a small enough structure, the LAB mode is non-radiative due to cancelling fields from the two opposing electric dipoles, but the large size of the VSRR means that retardation plays an important role and non-dipole modes can couple to propagating radiation [87–89]. In addition, the conductive coupling of the pillars and the charges flowing over the rest of the VSRR, or even structural defects in the nanostructure, may affect the radiation from the LAB mode [256].

The highest energy peak in the CL data, at 2.12 eV (Figure 4.3(h)) can be immediately identified as a transverse rim mode, though it is not possible to pinpoint it as either the TB or TAB mode based on the symmetry seen in the CL map. In the simulations, the TB and TAB modes are mixed with the LB and LAB rim modes and cannot be easily separated (Figure 4.5(c-f)). The surface charge distribution at 1.905 eV hints that the TB mode is near this energy, but overwhelmed by the LB mode, while at 2.038 eV, the TAB mode can be identified when the electron beam is placed to the side of one pillar. Without the use of tomography, it is difficult to know what the shape of each pillar rim is like, so the precise ordering of the LB, TB, LAB, and TAB modes cannot be established from simulation. In this VSRR, it appears that at least one of the transverse modes is at higher energy than both LB and LAB modes, based on the high CL signal at the sides of each of the pillars in the experiment.

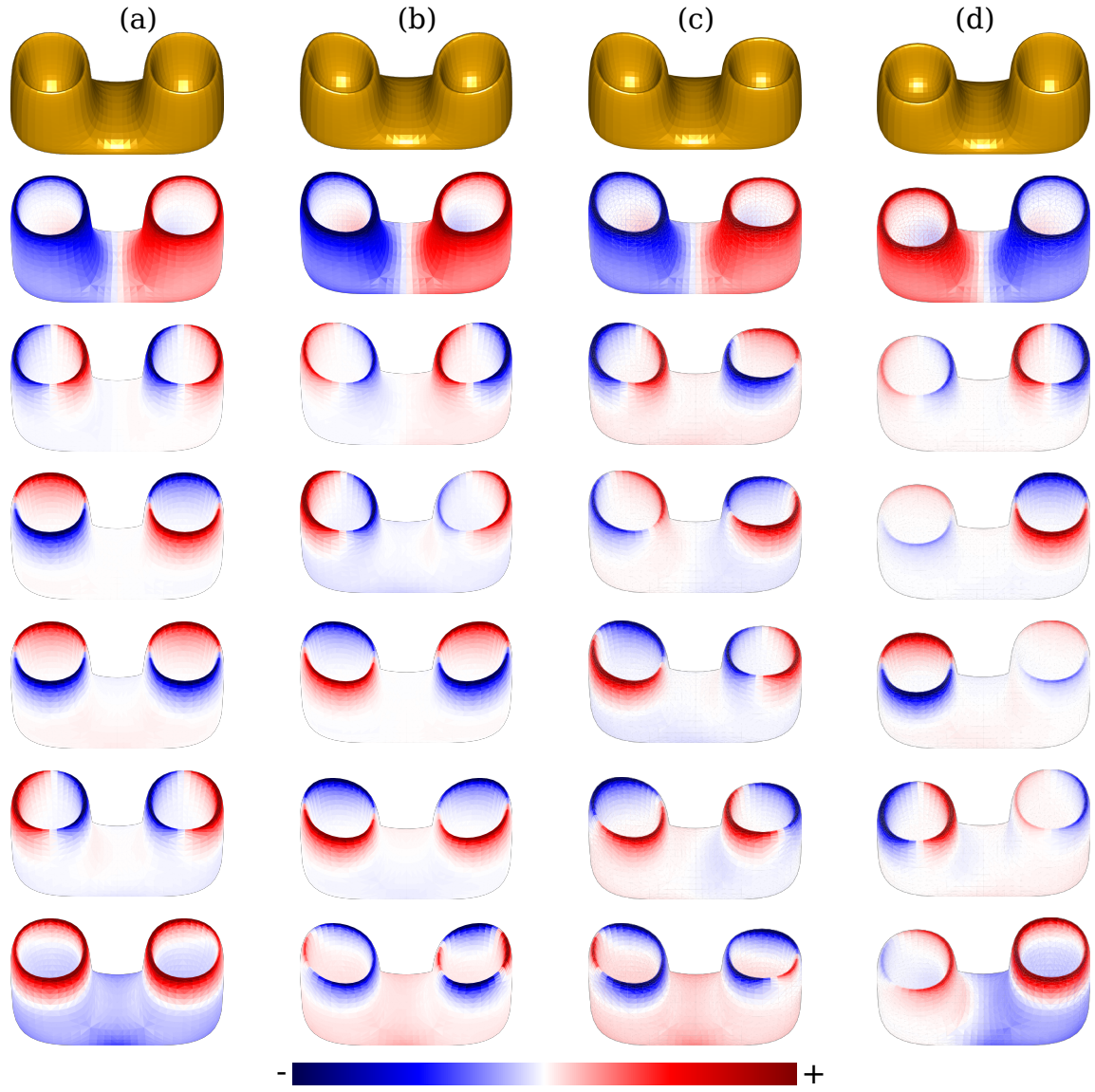

Figure 4.11: The first six calculated eigenmodes for single SRRs with common fabrication defects. (a) An ideal SRR; (b) an SRR with the insides of both pillars shortened; (c) an SRR with one pillar shortened on the inside; (d) an SRR with one short pillar. The top row shows the mesh used for each structure. The second through seventh rows show calculated eigenmodes in order of increasing energy for each column.

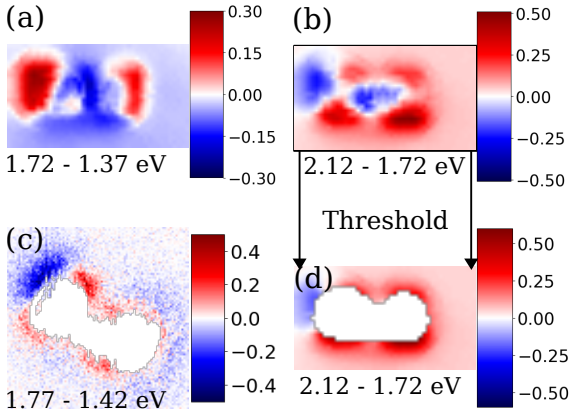

Figure 4.12: Difference maps created by normalizing and subtracting neighbouring peaks in EELS and CL data for the VSRR shown in Figure 4.3. (a) Subtraction of CL map centred around 1.37 eV from that centred around 1.72 eV; (b) subtraction of CL map centred around 1.72 eV from that centred around 2.12 eV; (c) subtraction of EELS map centred around 1.42 eV from that centred around 1.77 eV; (d) CL map in (b) with a threshold applied for easier comparison to the EELS difference map presented in (c). The EELS and CL maps used are shown in Figure 4.3.

The second peak in the EELS data (Figure 4.3(c): 1.42 eV) is identified as a longitudinal mode based on high intensity at each end of the VSRR. The tight confinement of the LSPR fields at high energies makes it difficult to distinguish the differences between this peak and the next, at 1.77 eV, but subtracting the two normalized intensity maps from each other clarifies the structure of each (Figure 4.12(c)). The clear similarities between this difference map and the difference map between the two highest energy CL peaks (Figure 4.12(b,d)) identifies this EELS peak as the LAB mode, the same as the 1.72 eV peak in the CL data.

The highest energy peak in the EELS data (1.77 eV), likewise, is identified as the same transverse mode as that present in the CL data at 2.12 eV. There is more EELS intensity around the sides of the pillars, and the agreement in the difference maps of the EELS data and the two highest energy CL peaks is clear, particularly when the pixels in which the electron beam hits the VSRR are masked out of the CL map (Figure 4.12(d)). As with the CL data, however, EELS is not sensitive to the phase and the TB and TAB cannot be distinguished from each other from the data presented in Figure 4.3. Polarized CL measurements may be able to distinguish some differences in the response of the TB and TAB modes.

Although the spatial intensity maps agree with the correspondence of these LSPR modes, there is a significant energy shift between the EELS data and CL data on the same VSRR. Energy shifts between CL and EELS have been observed in previous work [165]. EELS is a technique which detects the near-field of the plasmon, while CL collects the far-field scattered radiation. Damping of the LSPR mode can cause the near-field spectra to be redshifted relative to the far-field spectra, with higher damping causing larger redshifts [257]. The dielectric environment of the VSRR may

also have changed as thicker layers of carbon are deposited under the electron beam in the relatively poor SEM chamber vacuum during CL acquisition.

The mode at 2.384 eV in the simulations (Figure 4.5(g) and Figure 4.4(c)) appears to be a resonance attributable to a fourth-order SRR mode. This mode, and other SRR modes (Figure 4.2) may have weaker coupling to the electron beam than the planar SRR because of the orientation of the VSRR. The EELS peaks detected are also approaching the limit at which interband transitions within gold set in and begin to damp the plasmon modes, so these higher order SRR modes may simply be at too high energy and too highly damped to be detected.

Around 2.4-2.5 eV in the simulations, EELS signal arises from the bulk of the gold, which we attribute to the interband transitions of gold [111, 115]. The signal in the EELS map at this location is brighter where the thickness of the gold is higher, and the CL signal is negligible.

Polarimetry on the Rim Modes

CL polarimetry data in the visible regime was acquired on a different, but fabricated to identical parameters, VSRR using six different SIs with different (QWP, LP) settings, first on a horizontally oriented VSRR (VSRR-h), then, following a stage rotation, on the same VSRR oriented vertically (VSRR-v). From these twelve datasets, the spatially-resolved Stokes parameters as a function of wavelength were calculated (Figure 4.13). It must be noted that the QWP is of limited efficiency outside the range of 610-850 nm (1.46-2.03 eV), which will affect the accuracy of the S_3 calculation outside this range. In the spectra from the horizontally and vertically polarized SIs on VSRR-v and VSRR-h (Figure 4.13(c)), four peaks can be identified at 1.35 eV (920 nm), 1.65 eV (750 nm), 2.07 eV (600 nm), and 2.21 eV (560 nm).

The lowest energy peak, at 1.35 eV, is relatively low intensity, but is strongest when the electron beam is located on the inner edge of the top pillar in VSRR-v (Figure 4.13(b)). Light emitted from this location is dominantly polarized along the long-axis of the VSRR (hereafter referred to as longitudinally polarized), for both VSRR-v and VSRR-h, mostly in the direction towards the top of VSRR-v with some small intensity out the sides, which is picked up in the VSRR-h configuration (Figure 4.13(a)). In VSRR-v, the strongest emission comes from the topmost pillar, with longitudinal polarization. On the bottom pillar, the emission is more strongly polarized across the short axis of the VSRR (hereafter referred to as transversely polarized light) and the longitudinal polarization is weaker. There is also a peak in the VSRR-h spectrum near this wavelength when the electron beam is located near the insides or bottoms of the VSRR-h pillars. At the bottoms of the VSRR-h pillars, the light emitted is transversely polarized, primarily in the direction away from the electron beam across the VSRR-h. Transversely polarized light dominates the emission in VSRR-h except at the insides of the pillars, where longitudinal polarization dominates.

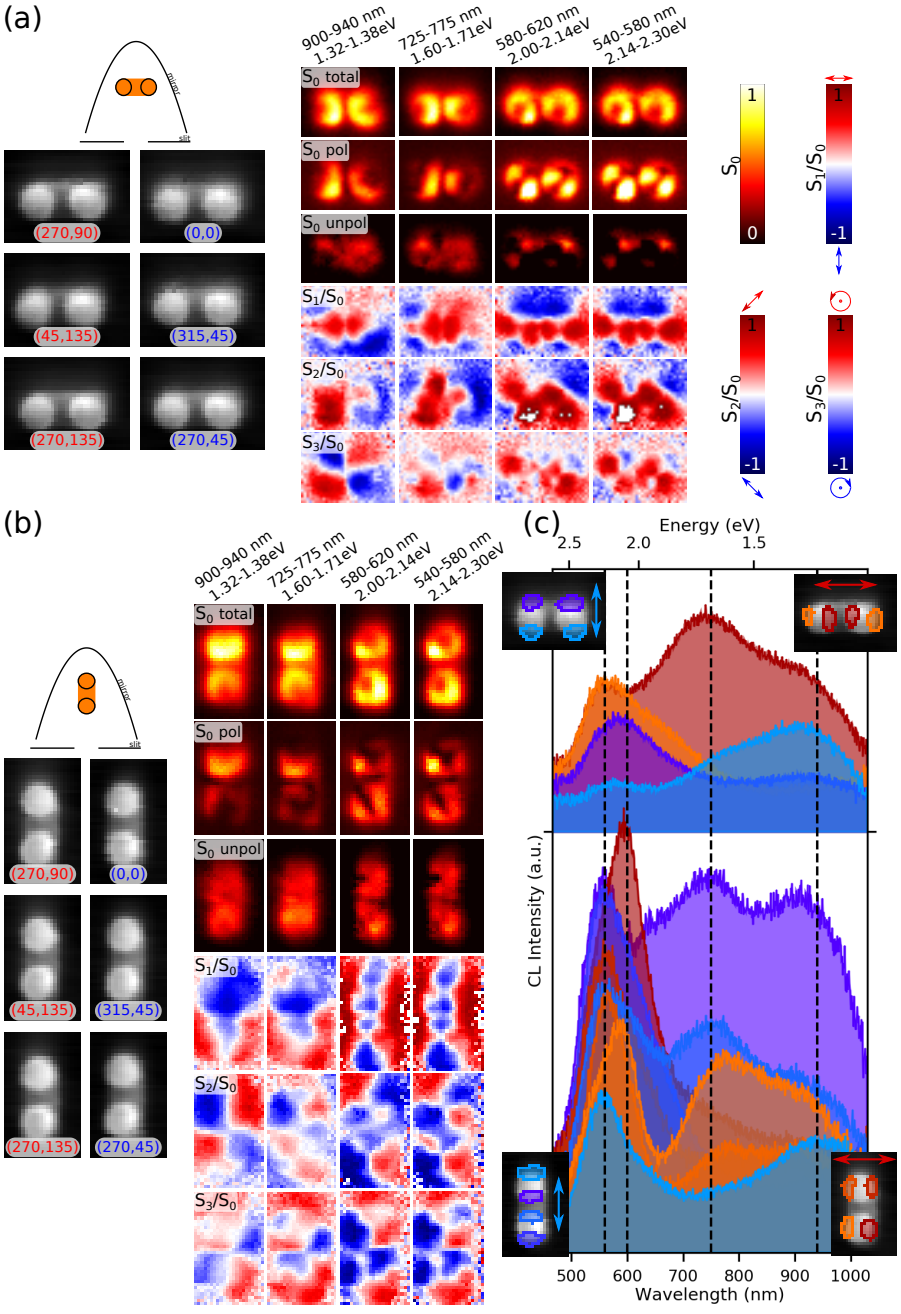

Figure 4.13: Experimental spatially-resolved Stokes parameters in the visible regime of the spectrum for an isolated VSRR. (a) Spatially resolved Stokes parameters for a horizontally oriented VSRR (VSRR-h) for selected wavelength ranges; (b) spatially-resolved Stokes parameters for a vertically oriented VSRR (VSRR-v) for selected wavelength ranges; (c) spectra extracted from vertically and horizontally polarized SIs of VSRR-h and VSRR-v, averaged over the areas indicated in the insets. Left panels in (a) and (b) show the mirror orientation and SEM images acquired simultaneously with the six SIs for each (QWP, LP) setting, as indicated.

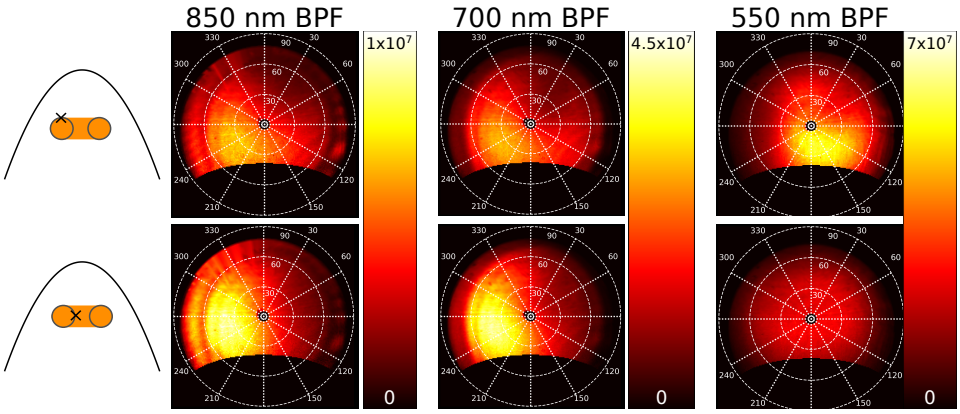

Figure 4.14: Experimental wavelength-filtered angular resolved emission plots for a VSRR. The centre wavelength of the band-pass filter (BPF) used is indicated above each pair of plots. The location of the electron beam (×)) and acquisition configuration for each row is indicated in the left column.

Some circularly polarized light is picked up when the electron beam is off the symmetry axis of the VSRR, in both VSRR-h and VSRR-v configurations, as well as some 45° and 135° linearly polarized light, in patterns which remarkably resemble the simulated patterns in Figure 4.7(c,d) for the magnetic dipole mode. Similar patterns are observed in the dipole mode of a nanowire, so it is likely that the emission at this energy is dominated by an electric dipole oriented longitudinally in the VSRR. Where the emission from this dipole is weak, polarization states from an overlapping transverse mode or off-resonance dipoles across the rim may be observed, such as in the bottom pillar of VSRR-v.

The strong linear polarization resembles an in-plane electric dipole, but the direction of emission does not. Interference from other dipole or multipole moments can cause directional scattering away from the electron beam [167, 186, 258] (see also Appendix A). Based on simulations, the second-order and even the third- or fourth-order SRR modes overlap spectrally with the rim modes in the VSRR (Figure 4.5) and can affect the angular scattering distribution of the rim modes, causing the directional beaming that is apparent from the two orthogonal datasets in Figure 4.13.

An AR emission image (on a different VSRR, to avoid melting of the nanostructure) with a band-pass filter (BPF) centred at 850 nm is presented in Figure 4.14. It shows directional emission, strongest when the beam is located on the inside of one of the pillars, directed away from the electron beam, but on the same side of the VSRR, at approximately 45° from the surface normal. The BPF is not centred on the peak at 920 nm or at 750 nm, and there may be some spectral shifts between the different VSRRs used for the polarimetry acquisitions and the AR experiment, so this emission is likely a mixture of the two lowest energy CL peaks.

The angular emission profile filtered around 700 nm is slightly brighter and more focused than the AR profile filtered at 850 nm, with more intensity near 30° from the

surface normal (Figure 4.14). The emission pattern rotates slightly when the electron beam is off to one side of the pillar, but is much weaker than when the beam is on the inside of one of the pillars. There are small changes to the angular emission, but it appears that the same resonance mode is still dominating the emission, likely corresponding to the mode at 1.65 eV (750 nm) in Figure 4.13, remembering that the spectral data was taken from a different VSRR.

At the 1.65 eV peak, the polarimetry maps do not change drastically from the 1.35 eV peak, though the S_2 and S_3 features are less well-defined and more complex at higher energy. In VSRR-h, the longitudinally polarized emission dominates even more strongly over the S_1 map, while the transversely polarized emission is weaker, implying that this peak at 1.65 eV may belong to the LB mode of the coupled rims. The peak at 1.35 eV has more transversely polarized components and the signal at this energy may be the result of a transverse rim mode (likely the TB mode) overlapping with the large tail of the LB mode at 1.65 eV. This is supported by the additional curvature around the sides of the pillars seen in the S_0 maps at 1.35 eV compared to those at 1.65 eV, particularly in VSRR-h.

At higher energy, there are two closely spaced peaks with a significant amount of spectral overlap, distinguishable from each other in the vertical and horizontal linearly polarized spectra in Figure 4.13(c). The S_0 maps for both of these peaks show a diagonal dipolar pattern on each of the pillar rims in VSRR-h. The other Stokes parameter maps also look very similar to each other, though the features in S_3 are slightly better defined at 2.21 eV than at 2.07 eV. However, this is beyond the efficient range of the QWP and the polarization state shown in the S_3 map may be more reflective of the S_2 polarization state, since the linear polarizer settings are the same for both acquisitions.

When the electron beam is on the longitudinal axis, either on the insides or outsides of the pillars for both VSRR-v and VSRR-h configurations, the light emission is strongly longitudinally polarized (visible in the S_1 maps), whereas when the electron beam is located on the sides of the pillars, there is a strong transverse polarization dominating the collected light. The spectral signal in this region may be a mixture of longitudinal and transverse coupled rim modes, which would help to explain the tilted appearance of the S_0 map across each pillar. The spatially-resolved Stokes parameters are much more localized around the pillar rims than in the lower energy modes. Based on simulations and dimer coupling theory, these two peaks are expected to be TAB and LAB modes, noting that the transversely polarized emission is slightly stronger on the 2.07 eV mode than on the 2.21 eV mode in VSRR-h. Both modes are so close in energy, however, that it is difficult to conclusively assign labels to these peaks, remembering also that the coupling of dipolar rim modes is greatly dependent on the precise shape and height of each pillar and there may not be a distinctive set of nicely defined LB, LAB, TB, and TAB modes.

The AR emission pattern, with a BPF centred at 550 nm (Figure 4.14) shows that when the electron beam is located on the side of one pillar, the emission is primarily in

the opposite direction compared to the lower energy modes and the VSRR is emitting light towards the opening of the mirror, approximately 30° from the surface normal, which could indicate the dominance of a transverse mode in the collected light. When the electron beam is placed near the insides of one of the pillars, there are much lower levels of emission, directed roughly upwards.

4.2.3 Prospects

The spatially-resolved Stokes parameter plots (Figure 4.7, 4.13) reveal the relationship between the LSPR near-fields that interact with the electron beam and the polarization of light emitted in a specific direction or, through reciprocity, between incident light from a given direction with a specific polarization and wavelength and the z-components of the electric fields ($\boldsymbol{\varepsilon}_z$) of the LSPR excited by that incident light. For example, Figure 4.13(a) indicates that longitudinally polarized light of around 900 nm wavelength, incident from the side of the VSRR, will excite plasmon modes with strong near-field enhancements near the centres of the pillars (red patches of the S_1/S_0 plot at 900-940 nm wavelength). Circularly polarized light incident from the same direction with the same wavelength will excite LSPR with strong $\boldsymbol{\varepsilon}_z$ field enhancements in the corners of the structure: *e.g.*, the upper left and lower right blue patches in the S_3/S_0 plot for RHC polarized light. This technique of spatially mapping the Stokes parameters can give insight on the usability of a structure for polarization-sensitive spectroscopic analyses. This is, based on a thorough examination of current literature, the first demonstration of this kind of experiment to date.

The VSRR, in the spatially-resolved Stokes plots, shows a stronger circular polarization response than a simple nanowire (Appendix A, Section A.4.1) on both the magnetic dipole mode and on the rim modes. The presence of the orthogonal phase-shifted electric and magnetic dipoles could make the VSRR a good candidate for enhancing signal in circular dichroism spectroscopy of chiral molecules for various photochemistry applications [259, 260]. Interference of multipole moments in the rim modes extends this potential to the visible regime. The vertical pillars provide a differently oriented surface compared to more classic planar or spherical nanostructures for binding molecules in SERS experiments, and combined with the knowledge of the polarization-dependent near-field distribution, the VSRR proposes itself as an interesting substrate for polarization-sensitive SERS studies.

The directional beaming of the emission from the rim modes of the VSRR suggests the application of this structure as an optical antenna to couple far-field radiation into or out of plasmonic waveguides. Directional emission of radiation reduces the amount that is lost to the surrounding environment and enhances the selectivity of a receiving antenna towards a specific incident direction. Use of a resonant antenna enhances coupling of incident light into linear plasmon waveguides [261]. With multiple rim modes which emit light of different polarization in different directions at different wavelengths, the VSRR could be used to couple far-field signals into or out of multiple

plasmonic waveguides branching out in various directions, transducing multiple signals with the use of a single nanostructure.

4.2.4 Correlative Spectroscopy of 3D Structures

Both EELS and CL bring their own unique advantages to the study of LSPR modes; we have shown the value of using both techniques in conjunction when studying a 3D nanostructure. EELS covers a broad energy range and reveals the whole spectrum of resonance modes in a single SI acquisition. EELS detects both bright and dark modes, but plasmon peak extraction suffers from proximity to the zero loss peak (ZLP) and its broad tails. When studying a 3D nanostructure, another weakness is revealed in EELS as a transmission technique: the thickness of the structure causes a lot of scattering of the electron beam, resulting in low signal reaching the EELS spectrometer. EELS is not able to detect the fine spatial structure of the LSPR modes within the 3D sample because of this scattering, and only aloof excitation yields information on the LSPR structure.

The LSPR fields detected in EELS come from a combination of inelastic delocalization of low energy loss processes and the extent of the evanescent field of the LSPR itself. Delocalization in the low-loss regime can restrict the achievable spatial resolution in EELS [262], making low energy plasmon modes appear broader spatially than predicted [263]. The spatial broadening of the lowest energy modes also comes from the sloping background of the ZLP; this effect is reduced after RLD is applied [122]. These delocalization factors actually prove to be helpful in detecting LSPR modes in 3D structures, over which much of the signal is scattered by the thick specimen, by increasing the signal obtained in the aloof beam configuration.

The low energy LSPR modes, such as the magnetic dipole mode in the VSRR, will have the longest plasmon wavelength which, in combination with the dielectric functions of the metallic structure and the surrounding medium, affects the LSPR field confinement [264]. Regardless of the thickness of the sample, an aloof electron beam will be able to interact with at least the lowest energy modes. Higher energy modes tend to be more tightly confined to the metal and are harder to detect in samples which scatter a lot: the electron beam must be very close to or on top of the structure to interact with the LSPR field and excite a resonance. This implies that for EELS on thick or highly scattering samples, the tightly confined modes are very difficult to probe due to poor SNR over top of the structure. With lighter elements or thin 2D samples, scattering of the electron beam is less of a problem and with sufficient current, tightly confined modes and cavity modes are accessible with EELS.

Comparing the spatial resolution of STEM-EELS and SEM-CL, a much higher resolution is obtained using a STEM instrument than is achievable with an SEM. With the modes studied in this work, it does not appear that the LSPR features are smaller than the SEM-CL spatial resolution can identify.

CL signal from the 3D structure does not rely on the detection of evanescent fields

through aloof excitation, but can be used to provide missing information on the mode structure of tightly confined modes over top of the structure. Unfortunately, the spectral range in CL is much more limited than that in EELS, which can mean that some modes are out of reach of CL detection. For the modes that it can detect, CL holds a wealth of information, including the angle at which light is emitted from the LSPR mode and, if the lengthy experiment can be performed without damaging the sample, information on the full polarization state mapped either over angular space or at different excitation locations.

From a practical point of view regarding the experimental parameters, the exposure time and beam current must be higher for CL than for EELS to obtain a good SNR, bringing additional problems related to sample drift and contamination build-up. CL signal relies on both excitation and emission probability, while EELS signal is detected from only excitation of the LSPR. Fabricating the sample on an electron-transparent substrate brings some advantage to the CL experiment as well; with a thin membrane supporting the VSRR, there is very little background CL signal from the substrate to contend with.

An interesting point to note for the study of a 3D structure is in the theoretical link between the EELS signal and the electromagnetic local density of states (EMLDOS), as established by Kociak and García de Abajo [265]. Included in the derivation is an assumption of invariance of the sample along the beam propagation direction (z): the structure is assumed to be planar. Building 3D nanostructures like the VSRR breaks the symmetry along this direction and the assumption of z-invariance no longer holds, which may have some interesting implications for the relationship between EELS signal and the EMLDOS of the structure: the relationship is unlikely to be as simple as in the 2D case.

4.3 Concluding Remarks

In this chapter, an isolated upright nanoscale split ring resonator was fabricated and its plasmon modes were studied using correlative EELS in a monochromated STEM and CL in an SEM, complemented with simulations of the LSPR response under electron beam excitation. The use of both experimental techniques offers more insight on the resonance modes than either technique can if used alone. In the EELS data, the magnetic dipole moment has a strong peak at 0.69 eV, which is too far into the IR for the CL spectrometer to easily detect. By using a long-pass wavelength filter and integrating all signal into only a few channels on the CL spectrometer, we can detect this mode and acquire polarimetry data to derive the spatially-resolved Stokes parameters at different electron beam locations over the VSRR.

The dipole mode emission is primarily polarized along the long axis of the VSRR, as expected from the predicted combination of electric and magnetic dipoles. When the electron beam is off the symmetry axis, the polarization distribution of the collected emission changes and some circular polarization is detected. Simulations

demonstrate that a basic model of the VSRR dipole mode can be constructed using two orthogonal electric and magnetic dipole moments; the phase delay and relative magnitude of the fields emitted from each of these dipoles can be calculated using angle-resolved polarimetry measurements. The interference of electric and magnetic dipoles in the VSRR may prove to be an interesting platform for studying LSPR dynamics and interactions with the electron beam without the need for femtosecond-resolved techniques.

The higher order modes are difficult to distinguish in the EELS data, but by comparing with the CL data and BEM simulations, higher order rim modes are identified around the VSRR pillars. The pillar rims support coupled dipole modes, which form longitudinal and transverse bonding and anti-bonding pairs, although these pairs are very sensitive to the precise shape of the pillars, something that is difficult to control in the fabrication of the VSRR. Difference maps are used to help distinguish the structure of overlapping LSPR modes, obtaining good agreement between EELS and CL peaks. The mode assignments are confirmed by comparison with calculated spectra, EELS and CL intensity maps, and surface charge density distributions using the MNPBEM software.

Spatially-resolved Stokes parameters for the visible regime of the spectrum are presented, with tentative identification of a low energy TB and LB mode, and two higher energy peaks which are likely TAB and LAB modes. The spectral overlap between all of the peaks continues to make interpretation of the Stokes parameter maps challenging, but using the polarization of the emission helps to more firmly identify the higher order rim modes on the VSRR structure.

The 3D nanostructure makes an interesting case for the comparison of EELS and CL data, in which each technique fills a gap and compensates for the deficiencies of the other to provide more complete information on the LSPR behaviour. EELS struggles with SNR due to the high scattering of the electron beam transmitted through the VSRR, but this is not a factor for CL, in which a good SNR can be obtained over the whole structure independent of the structure thickness. CL signal, however, is limited to the spectral range covered by the spectrometer, whereas EELS covers the full spectrum of interest in a single acquisition. Performing both techniques on the same nanostructure requires compatibility with TEM measurements, but gives a direct correlation between the signals obtained with each technique.

Chapter 5

Toroidal Array

In this chapter, four vertical split ring resonators (VSRR) are arranged in a circular array (abbreviated as 'T4'). The vertical orientation of the SRRs is required in order to have in-plane coupling of the magnetic dipole moments of each VSRR. The magnetic dipole modes on the array of VSRRs couple to form two hybridized modes: a magnetic dipole mode, and a toroidal dipole mode. Higher order modes appear similar to those of the individual VSRRs studied in Chapter 4.

The toroidal dipole is a little-known member of the EM multipole family, which is difficult to find or create experimentally. It has so far received comparatively little attention and many of its potential uses still remain unexplored. The current challenge is to create a strong toroidal dipole moment that is not overwhelmed by the presence of a stronger EM dipole, and so to isolate the response of the toroidal dipole. The T4 array studied in this chapter promises to exhibit a toroidal dipole isolated from electric and magnetic dipole moments, but overlapping with an electric quadrupole. We proposed two modified versions of this structure, with five and six VSRRs (named 'T5' and 'T6', respectively), to reduce the contribution from the electric quadrupole and enhance the contribution of the toroidal dipole moment.

5.1 Toroidal Dipole

The first mention of the properties of the toroidal dipole moment is traced back to Zel'dovich in 1957 [266], who derived an EM moment which did not fit into the current theories of electromagnetism, and dubbed it the 'anapole' moment. Zel'dovich's system consists of a set of virtual particles with spin components, elementary magnetic moments, forming a ring in a plane. In this configuration, the net electric and magnetic dipoles are both zero. Analogous to a spherical capacitor, in which fields inside the system are non-zero but there are no external fields, the external field of the anapole is zero. Unlike the scalar capacitor response, the anapole moment is a vector quantity [266]. The toroidal dipole is not precisely the same as Zel'dovich's anapole, but both the toroidal dipole and the anapole violate time and space reversal

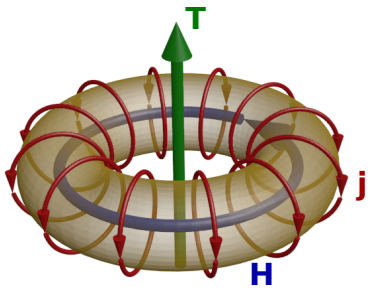

Figure 5.1: Toroidal dipole moment ($\boldsymbol{T}$) of a torus, created by alternating poloidal currents $\boldsymbol{j}$, which induce circular magnetic field vectors, $\boldsymbol{H}$.

symmetry and are vector quantities with no external static EM fields [108].

Zel'dovich's anapole is parameterized to suppress radiation [105,108,109], whereas the toroidal dipole moment, described in the multipole expansion by Dubovik [105], has radiative vector potential described by Equation 5.1a. The toroidal dipole moment has almost the same radiative properties as an electric dipole moment (Equation 5.1b [105]) including the same angular distribution, except for a $\pi/2$ phase shift and an ω^4 dependence on frequency, making it impossible to determine the difference between an electric and toroidal dipole based on the radiative fields alone [105,108].

$$\boldsymbol{A}_{T_1}(\boldsymbol{x},t) = \frac{\mu_0\omega^4}{4\pi x^3}[\boldsymbol{x}^2\boldsymbol{T_0} - \boldsymbol{x}(\boldsymbol{x}\boldsymbol{T_0})]\cos(\omega(t-x)) \tag{5.1a}$$

$$\boldsymbol{A}_{P_1}(\boldsymbol{x},t) = \frac{\mu_0\omega}{4\pi x^3}[\boldsymbol{x}^2\boldsymbol{p_0} - \boldsymbol{x}(\boldsymbol{x}\boldsymbol{p_0})]\sin(\omega(t-x)) \tag{5.1b}$$

The similarities can be further generalized to state that the radiation from toroidal multipoles is equivalent to that of electric multipoles of comparable order, except for a difference in the intensity as a function of frequency and a similar phase shift to the dipolar case [105]. In most systems, the toroidal dipole moment is neglected in favour of the electric and magnetic dipoles, but if a toroidal system can be designed to suppress the electric and magnetic dipoles and quadrupoles, the toroidal dipole moment may dominate the radiative properties of the system, such as in, for example, a toroidal solenoid with poloidal currents (Figure 5.1) [105,108].

Poloidal currents on the surface of a torus create magnetic fields which are contained inside the torus and precisely cancel out, leaving a net zero magnetic dipole moment. The toroidal dipole vector is found by applying the right-hand-rule to the ring of magnetic moments, and points along the symmetry axis of the torus [105]. The equation for the toroidal dipole moment as a function of the currents and position is given in Equation 5.2 [105].

$$\boldsymbol{T}(t) = \frac{1}{10}\int (\boldsymbol{x}(\boldsymbol{x}\cdot\boldsymbol{j}) - 2x^2\boldsymbol{j})d^3x \tag{5.2}$$

Although the toroidal dipole does not interact with a static external EM field, it can interact with an external current passing through the torus or with a time-varying external EM field [105,108,109]. Because the radiative properties of the toroidal dipole are very similar to an oscillating electric dipole, a non-radiative configuration can be achieved by introducing an electric dipole parallel to the axis of symmetry of the torus (an anapole); this system has zero radiated field strength, but still has a non-zero vector potential outside the system, allowing many other interesting experiments of the Aharonov-Bohm effect [108, 109, 267–270]. The fields will only be perfectly cancelled out, however, if the dimensions of the electric dipole and toroidal dipole are infinitesimally small [109, 267].

Since the toroidal dipole violates time and space inversion symmetry, it has been suggested that it also violates the reciprocity theorem of electromagnetism, thereby breaking the symmetry between receiving and transmitting antennas [271].

Experimental measurement of the toroidal dipole remains a difficult challenge, since the toroidal dipole responds to the curl of the magnetic field and not to homogeneous or static EM fields [108]. It could, in theory, be measured by controlling the curl of an applied time-dependent magnetic field and measuring the torque on the sample as the toroidal dipole tries to align itself [108,272]. The toroidal dipole is also expected to enhance second harmonic generation (SHG), suggesting that SHG could be used to measure the presence of the toroidal moment [273]. Higher order toroidal multipoles will interact with higher order derivatives of EM fields [109].

5.1.1 The Toroidal Dipole in Condensed Matter

The toroidal dipole can be found in particle physics, the field in which Zel'dovich first derived it; leptons and quarks possess a toroidal dipole moment, as might other elementary particles or atomic nuclei [266, 274]. The basic description of the toroidal moment can be simplified to a ring of elementary magnetic dipoles, which can be created with the appropriate arrangement of atomic spins [108,273,275]. Some special classes of materials may support a toroidal dipole moment through spin vortices or orbital currents [108, 272, 273].

Multiferroic materials, including antiferromagnets, ferrimagnets, and magnetoelectric materials can in some specific cases produce a non-zero toroidal dipole moment [272]. For instance, if the spatial inversion symmetry is broken in a pair of antiferromagnetic dimers, they may exhibit a net toroidal moment [272, 273]. It is also possible to use the toroidal dipole to describe orbital antiferromagnetism [108] or to produce magnetoelectric effects [108, 275]. Some systems possessing both electric and magnetic dipoles can produce a vector $(\boldsymbol{p} \times \boldsymbol{m})$ with the same symmetry properties as the toroidal dipole moment, which is often mistaken for the toroidal dipole [108, 272]. The existence of the toroidal dipole suggests the possibility of a ferrotoroidic class of materials, in which spins spontaneously arrange themselves in a head-to-tail arrangement over a large domain, creating a net toroidization [273, 275].

On a slightly larger scale, the toroidal dipole may also be created using magnetic particles dispersed in a fluid, provided that the magnetic particles have strong dipole-dipole interactions that cause them to form a head-to-tail ring arrangement, which is most stable when the toroidal moment is at is maximum [276]. The magnetic vortex is created by the head-to-tail arrangement and the magnetic field is confined by the ring, thus allowing denser packing of magnetic storage media by reducing the interaction distance between neighbours [276].

Toroidal dipole phenomena in condensed matter are usually very difficult to observe; the signature of the toroidal dipole is difficult to find and is overwhelmed by electric or magnetic dipoles. Most of the toroidal dipole moments found in condensed matter are static toroidal dipoles, which, while still interesting to study, do not have the same set of intriguing properties as dynamic, or time-varying toroidal dipole moments.

5.1.2 Toroidal Dipoles in the Microwave Spectrum

The design of metamaterials is a promising route to creating a dynamic toroidal dipole moment. Sub-wavelength components are engineered to emphasize the toroidal dipole moment and suppress other EM multipole moments by creating a vortex of magnetic dipoles in a metamaterial which operates at a frequency determined by the size and material of the metamolecule. Interest in creating a metamaterial with a toroidal dipole moment has increased over the past few years, on both the macroscale and the microscale. Macroscale metamolecules are easier to fabricate than micro- or nano-sized metamolecules and typically operate in the GHz or THz region of the spectrum (radio and microwaves).

Theoretical studies to create the toroidal dipole have been done on a set of double bar antennas arranged in a ring, with broken geometrical symmetry to promote the toroidal dipole moment under linearly polarized light [277], and on a planar double ring structure which has been copied and rotated to create a torus-like structure [278]. Use of a dielectric metamaterial eliminates Ohmic losses, and a toroidal dipole is created by a relatively simple arrangement of four dielectric cylinders [279]. Spoof plasmon polaritons, low frequency waves which mimic the field confinement of SPPs and are created using waveguides patterned in metals [70, 280], have also been used to create a non-zero toroidal dipole moment using defects in a metal groove array, in which both the toroidal dipole and the electric quadrupole contribute to the resonance mode of the defect [281]. A ring arrangement of bilayer SRRs with their gaps towards the centre of the ring produces a strong toroidal response in the third order resonance peak [282]. A higher order toroidal dipole moment has also been demonstrated in a metamaterial composed of L-shaped coupled SRRs, with two lower order magnetic dipole and electric quadrupole resonances [283].

The anapole, created by combining the toroidal dipole with an electric dipole, has been demonstrated in silicon nanodisks, dielectric metamaterials which produce both

electric and toroidal dipole moments [269], and in dumbbell shaped apertures cut into a metal plate, copied, and rotated to create a toroidal void [284]. The anapole has no radiated EM fields, but adding a dielectric substrate below an anapole configuration causes directional radiation into the substrate [270].

The simplest means of obtaining a toroidal dipole would appear to be to fulfill the geometrical picture of a torus with wire windings around it. Although this is the most intuitive physical representation of Figure 5.1, it is also flawed because helical windings around a torus will have a net non-poloidal current component, which creates a net magnetic dipole moment in addition to the toroidal dipole moment [271]. Special care must be taken in the winding of the wires to cancel out the additional current components by, for example, adding an extra loop of wire or using a double winding [285].

Four copper windings arranged with toroidal symmetry provide an approximation to the toroidal solenoid [286]; this metamolecule shows strong evidence of a negative refractive index and circular dichroism in its resonant bands. In this example, retardation is important to create the toroidal dipole moment: when the wire coil dimensions are comparable to the wavelength of light, sections on opposite sides of the structure work together. Induced currents on opposite sides of the structure flow in opposite directions at any given time, creating the necessary magnetic dipole vortex for the toroidal dipole moment. The response of this metamaterial is dominated by the electric and magnetic dipole moments, but the toroidal dipole is of comparable strength to the electric quadrupole moment [286].

Removing the electrical connection between copper windings to form a structure of four rings suppresses the magnetic dipole moment; splitting each of these rings makes a metamolecule composed of four SRRs with a toroidal dipole moment at one resonance frequency [107]. This configuration supports a magnetic dipole moment and a toroidal dipole moment at different resonant frequencies. Breaking the symmetry of the SRR arrangement, such that two neighbouring SRRs have their gap at the top and the other two have their gap at the bottom ('up-up-down-down' configuration), allows an incident wave polarized along z to induce circular currents in the split rings while the magnetic field of the incident light interacts with the magnetic dipoles in each of the split rings. At the lower energy resonance, the phase delay of the light wave hitting the 'front' and 'back' of the structure produces a head-to-tail vortex of magnetic dipoles in the split ring loops, creating the toroidal dipole moment. At higher energies, the split ring loops interact with in-phase components of the photon's magnetic field, so all induced magnetic dipoles point in the same direction, producing a net magnetic dipole moment in the whole structure [107]. A similar metamolecule was later used by Raybould *et al.* to create a metamaterial with strong circular dichroism, using an 'up-down-up-down' arrangement of SRRs to achieve structural chirality [287].

In these structures composed of SRRs, the toroidal dipole moment is at the same energy as either the magnetic [107] or electric [287] quadrupole moment, but isolated

from either electric or magnetic dipole moments. The SRR-based structure enhances the toroidal dipole moment such that it is detectable and of comparable strength to the quadrupole response. Stacking an array of SRRs has also been shown to enhance the toroidal dipole moment response over that of other multipole moments by breaking spatial symmetry [240].

Rotating each SRR by 90°, such that their long axes form a ring, creates an electric toroidal dipole moment (G in Table 2.1) [288]. Similarly to the magnetic toroidal dipole ($\boldsymbol{T}$) case, the electric toroidal moment is achieved due to the relationship between the phase of the incident light that each SRR experiences.

5.1.3 Optical Toroidal Dipoles

Moving the frequency of the toroidal dipole to the optical regime of the spectrum requires scaling down the fabricated size of the metamolecules to the nanoscale, where fabrication of a toroidal solenoid-like structure is much more challenging. A plasmonically active torus does not result in a toroidal dipole mode, as the dominant LSPR modes resonate around the toroidal direction, alternating between non-zero magnetic and electric dipoles on odd and even eigenmodes, and there is nothing to favour resonances around the poloidal direction [289].

Instead, other geometries must be engineered to be compatible with the toroidal moment and to suppress electric and magnetic dipoles at the same time. A toroidal response has been demonstrated in the near-IR using a stacked array of asymmetrical double bars [290], a pair of stacked double disks [291, 292], and a system of three plasmonic nanoparticles in which the toroidal dipole overlaps with an electric dipole response [293, 294].

Other demonstrations make use of the Babinet principle: the electric dipole formed in plasmonic nanoparticles becomes a magnetic dipole moment in the complementary nanostructures, including a VSRR underneath a dumbbell-shaped aperture, which produces an in-plane toroidal dipole moment [295], or a circular system of nanoholes in a silver sheet [296–298]. Interestingly, the toroidal dipole moment found in this system has weak radiative properties but possesses a broadband emission feature at the toroidal resonance, as studied by CL [298]. Simulations on this hole-based structure suggest that the heptamer of holes supports a dark toroidal mode with weak far-field coupling in an energy region dominated by other dipole modes. The toroidal mode can only be created using a near-field oscillating electric-dipole source, but the system achieves two toroidal modes at different energies [296,297], including a mode with a pair of coupled toroidal dipoles [298]. This is one of the few examples of a toroidal dipole mode studied using electron spectromicroscopy techniques, namely EELS and CL.

The SRR approach holds some promise for creating the toroidal dipole moment at optical frequencies. An array of four SRRs has already been shown to support a toroidal dipole isolated from either the magnetic or electric dipoles in the microwave

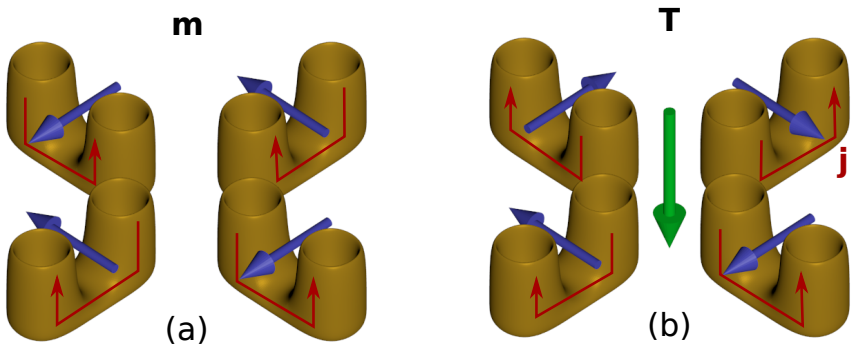

Figure 5.2: Magnetic and toroidal resonances on an array of four VSRRs ('up-up-up-up' configuration). Current ($\boldsymbol{j}$) directions on the front and back pair of VSRRs are (a) in-phase for the magnetic dipole moment, $\boldsymbol{m}$, and (b) anti-phase for the toroidal dipole moment, $\boldsymbol{T}$. The pillars of the VSRRs are depicted as hollow to mimic the fabricated structures.

regime and it is possible to fabricate VSRRs on the nanoscale, making some allowances for the additional fabrication challenges. Simulations on a nanoscale array of SRRs, in both an 'up-up-down-down' and an 'up-up-up-up' configuration reveal that both of these support an isolated toroidal dipole response near optical frequencies [58, 299]. The order of the resonances changes: in the latter configuration, the magnetic dipole occurs at the lowest energy resonance while the toroidal dipole occurs at the second resonance, overlapping with an electric quadrupole [299]. The electric quadrupole dominates the radiative response at the second resonance. Coupling between pairs of resonators is stronger in the first ('up-up-down-down') configuration and the energy difference between toroidal and magnetic dipole modes is higher, but the latter configuration ('up-up-up-up') is much more feasible for nanoscale fabrication.

The production of a toroidal dipole moment requires a phase delay between the field hitting the front pair and that hitting the back pair of VSRRs, causing the induced magnetic dipoles of each resonator pair to oscillate in anti-phase. When the VSRR dipoles of the front pair are in anti-phase with the back pair, ring-like magnetic fields are created, producing a toroidal dipole moment (Figure 5.2(b)). The charge configuration at this resonance and four-fold symmetry of the array produces an electric quadrupolar moment. Likewise, when the induced dipoles are all oscillating in-phase with each other, a magnetic dipole is created (Figure 5.2(a)). Both the magnetic and toroidal modes arise from coupling between the front and back pairs of SRRs. As the SRRs are brought closer together, the energy difference between the two resonances increases, but the strength of the toroidal dipole mode declines [299].

Additional simulations on the 'up-up-down-down' configuration show the potential use of the toroidal resonance in a lasing spaser application [58]. Here the toroidal dipole peak shows better spatial coherency and narrower beam diversion with a lower gain threshold than the magnetic dipole mode in the same structure. This would allow use of a lower level of gain for loss compensation, signal amplification, or surface plasmon lasing, though there is a trade-off between the radiation loss (lasing appli-

cation) and the quality factor of the peak, which broadens when the radiation loss is enhanced.

5.2 Results and Discussion

Due to the constraints imposed by nanofabrication techniques, the '4-up' configuration of VSRRs (T4) was chosen for experiments. The VSRRs in the T4 array were fabricated using the same techniques used for the isolated VSRR described in Chapter 4. FEM simulations with dimensions matching those of a fabricated VSRR were performed by Ahmed Elsharabasy under the supervision of Dr. M. Bakr at McMaster University, to complement EELS studies and BEM simulations on this T4 structure. EELS was performed on a variety of T4 structures, in the top-down orientation and with a stage tilt applied to the sample in order to retrieve information on the 3D localization of LSPR fields. Some preliminary results are also presented on similar arrays of five and six VSRRs (T5 and T6), in which the four-fold symmetry no longer exists.

5.2.1 Fabrication

Accurate alignment techniques in electron beam lithography (EBL) allow a second deposition layer to be placed on top of the first, within 10-15 nm, to create the upright VSRR arms. The height of each individual pillar is difficult to control, as small variations in the thickness of the electron beam resist change the shadowing conditions during metallization. The quality of each pillar is dependent on many parameters, including the smoothness and thickness of the EBL resist, the dose received during exposure, shadowing during metallization and the quality of the metallization layer, and the success of the lift-off procedure. The pillars are hollow, indicating that the deposited gold coats the sides of the electron beam resist walls, rather than filling in the developed cavity fully.

Fabrication of the T4 array is perhaps more challenging than that of an isolated VSRR, because it requires four VSRRs to come out with good quality. Even with very small distances between neighbouring pillars, on the range of a few hundred nanometers, there can be a great variation in the quality of the pillar after the fabrication procedure. In the examples seen in Figure 5.3, it is seen that perfect uniformity, even on a single toroidal array, is very difficult to achieve.

All of the structures presented in Figure 5.3 were fabricated in a single fabrication batch on a single TEM grid. Tilting the sample stage allows us to see the defects and the true structure of the pillars. Often the ends of the pillars are ragged, as they may have broken off from the metallization film on top of the e-beam resist during lift-off, or sometimes a single pillar collapses inwards or is otherwise malformed.

Accounting for the stage tilt angle, the height of the pillars is measured to be approximately 250 nm in the tallest case (Figure 5.3(c)), though there are several

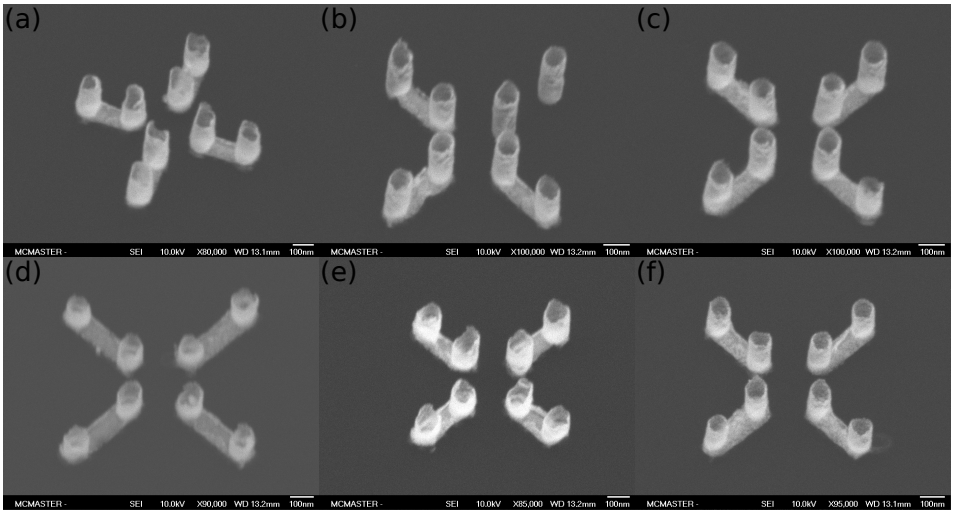

Figure 5.3: SEM images of fabricated T4 arrays, taken at 35° stage tilt, all on a single TEM grid.

examples of shorter pillars in different structures. Each individual SRR was designed to be 300 nm long, but some overexposure during EBL or misalignment of the second patterning step to the first increases the length of the SRR bottom to approximately 330-350 nm, with a pillar diameter of approximately 120-150 nm, varying between different structures with different exposure doses.

5.2.2 Experimental EELS

EELS was performed on the T4 array shown in Figure 5.3(c) (also shown in Figure 5.4(a)), revealing two low energy peaks at approximately 0.58 and 0.67 eV (Figure 5.4(c)). The first of these, at 0.58 eV, has a high EELS intensity around the outside edges of the VSRR pillars and the second has higher EELS signal towards the centre of the structure around the inside edges of the VSRR pillars (Figure 5.4(b)). The EELS distributions for this pair of modes are similar to the EELS distributions seen in the classic example of bonding and anti-bonding modes in nanoparticle dimers [164, 300], in which the bonding mode has high EELS signal at the farthest edges of two coupled nanoparticles and the anti-bonding mode shows high intensity in the centre, near the gap between the two nanoparticles. Both of these dipole modes in the T4 structure are, in fact, formed from the coupling and hybridization of VSRR dipolar modes with each other.

At higher energy in the spectrum, it is more difficult to identify different modes. Another peak at 1.29 eV has high EELS intensity towards the centre of each VSRR bar, but much of the signal between 1.2 and 2.5 eV merges to appear as one broad peak with no clearly identifiable hotspots. There may be another broad peak in the VSRR centres at approximately 1.7 eV, after which the EELS intensity drops at this location. EELS signal around the inner and outer pillars, however, remains high up

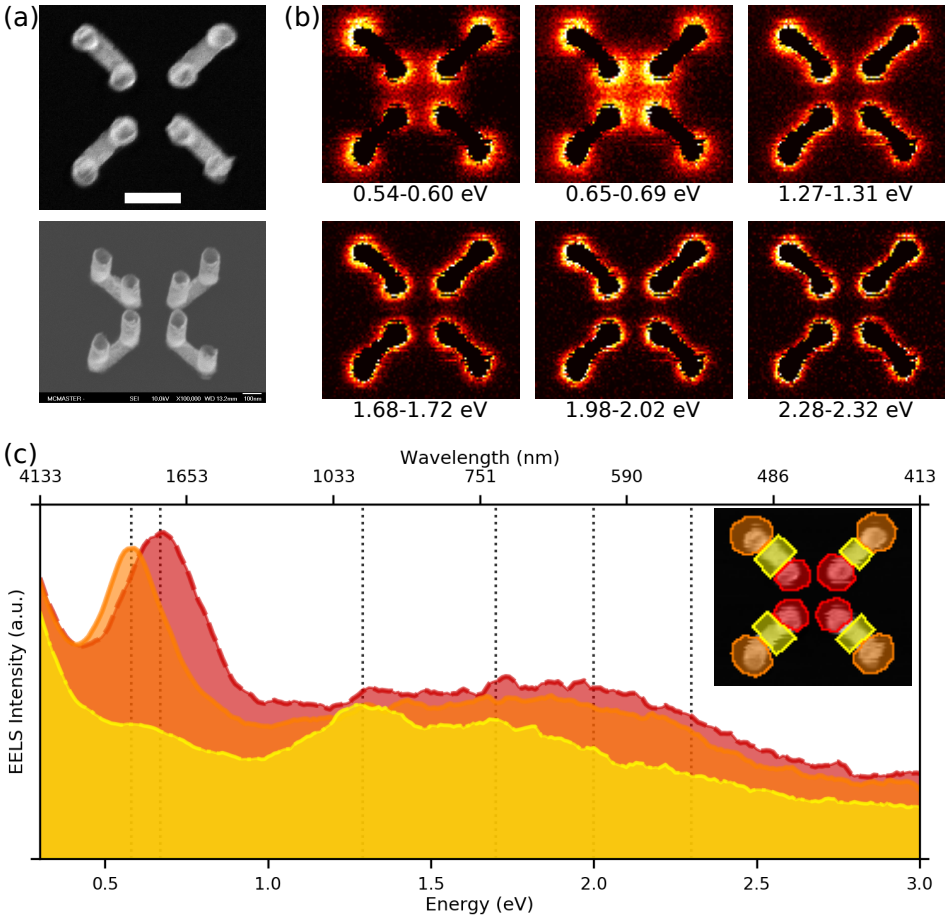

Figure 5.4: EELS results for a T4 array. (a) STEM-ADF (top, scalebar is 250 nm) and SEM images (bottom, 35° tilt); (b) EELS intensity maps extracted from the indicated energy ranges; (c) EELS spectra averaged over the areas indicated in the inset.

until around 2.5 eV, when interband transitions in gold begin to dominate the optical response and damp the plasmon resonances.

5.2.3 FEM Simulations

The basic dimensions of the simulated structure were chosen to match those of the T4 structure presented in Figure 5.4. Although the simulated pillars are not hollow, these features are well below the effective plasmon wavelengths of the lower order modes and should not affect them significantly. A plane wave polarized along the z-direction propagates from the side and the spectrum is calculated from 100 THz to 240 THz (0.41-0.99 eV). Three peaks are found in the simulated spectrum, at 0.56, 0.61, and 0.66 eV (Figure 5.5(a)). The distance across the central gap in the simulation mesh is 230 nm, and the height of each pillar is 240 nm.

At the lowest energy is a magnetic dipole mode, followed by two toroidal dipole

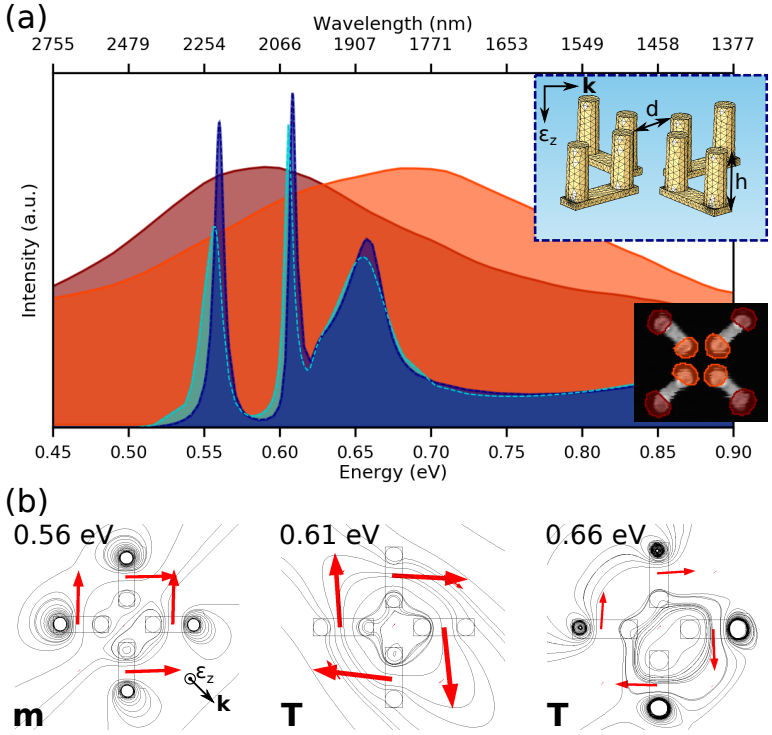

Figure 5.5: FEM simulations of a T4 array. (a) Simulated spectra (dark blue) for a T4 with (d = 230, h = 240) overlaid on the experimental EELS spectra (red, orange), insets indicate the propagation direction and polarization of the simulated plane wave and the areas over which EELS spectra were averaged, light blue spectrum is the calculated spectra for a T4 array of the same dimensions with one outer pillar shortened to 195 nm; (b) simulated magnetic field vectors and contours for each of the three peaks in (a) on the dark blue spectrum showing a magnetic dipole mode ($\boldsymbol{m}$: 0.56 eV) and two toroidal dipole modes ($\boldsymbol{T}$: 0.61, 0.66 eV).

modes at higher energy, identified by their circulating magnetic field vectors (Figure 5.5(b)). On the magnetic dipole mode, the field lines are concentrated around the outer pillars, whereas for the first toroidal mode, the magnetic field contours are more spread over the whole structure. The toroidal dipole peak at 0.61 eV has a slightly higher scattering cross-section than the magnetic dipole and is observably thinner. The third peak has strong magnetic fields around the outer pillars of the VSRRs as well, but exhibits the circulating magnetic field vectors of a toroidal dipole moment. On the low energy side of the second toroidal dipole peak, there is a small contribution from an electric dipole moment, while on the high energy side, the response resembles an electric quadrupole. The electric multipole moments may interfere [258] with the scattering response of the toroidal dipole, enhancing the response on the low energy side and reducing it on the high energy side and making the toroidal peak asymmetrical.

The light blue spectrum in Figure 5.5(a) shows the calculated response if one of the outer pillars in the simulation mesh is shortened to a height of 195 nm to mimic

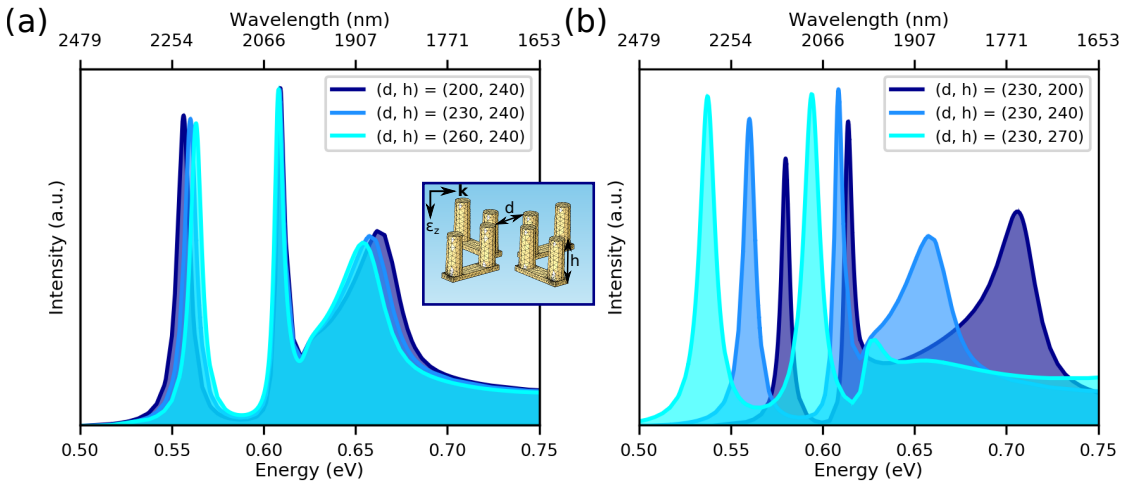

Figure 5.6: FEM simulated spectra of a T4 array with changing geometrical parameters. (a) Simulated spectra with changing gap between VSRRs; (b) simulated spectra with changing pillar height. Dimensions are given in the legend in nanometres.

the imperfections of the structure shown in Figure 5.3(c). There is a small redshift in all of the peaks and a reduction in the scattering cross-section, particularly on the low energy magnetic dipole mode, but no significant change to the spectrum, indicating that the toroidal response is robust against small defects in the fabricated pillars.

The EELS response is subjected to broadening from the instrument PSF (point spread function) and the natural linewidth of the plasmon mode, which may experience higher damping in the as-fabricated structure relative to the Drude model approximation used in the simulation. In addition to the much broader response in the EELS spectrum compared to the calculated spectrum, there is a small blueshift in the experimental EELS spectrum relative to the simulated spectrum, particularly on the magnetic dipole peak. The small energy separation and large peak width of the EELS peaks means that there are only two peaks distinguishable in the data and it is not possible to determine if there are two overlapping toroidal peaks present in the EELS data, or only one centred at 0.67 eV.

Changing Dimensions

Small changes to the dimensions of the T4 array were done in the simulated mesh (Figure 5.6). Specifically, the gap between the VSRRs was changed by ±30 nm, and the height of all eight pillars was changed by ±40 nm.

As the VSRRs are brought closer together (Figure 5.6(a)), the magnetic and toroidal modes are pushed further away from each other in energy, as expected when the coupling strength between the pillar fields increases [299]. The first toroidal dipole mode at 0.61 eV is relatively stationary as the VSRRs are brought closer together. Instead, the magnetic dipole and the second toroidal dipole peak are pulled in towards

the first toroidal peak when the VSRRs are further apart, or pushed away when the VSRRs are brought closer together: the magnetic dipole redshifts by approximately 7 meV in the datasets shown in Figure 5.6 as the VSRRs are pushed closer together, and the second toroidal peak blueshifts. The response strength of the magnetic dipole and the second toroidal peak increases slightly as the VSRRs come closer to each other, but the response of the first toroidal peak changes very little.

As the height of the arms increases (Figure 5.6(b)), all of the modes are redshifted. The magnetic dipole redshifts by approximately 20 meV when the height of the pillars is increased by 40 nm, with a redshift of 43 meV between the smallest and tallest pillars, whereas the first toroidal peak redshifts by a lesser amount, moving only 20 meV between the smallest and tallest sets of pillars. It appears that increasing the height of the VSRR pillars redshifts the whole spectrum and increases the coupling strength between individual VSRRs, pushing the magnetic and toroidal dipole modes further away from each other in energy. The optical response of both the two lowest energy peaks increases as the pillar height is increased, but the strength of the magnetic dipole mode increases by a greater amount. The redshift of the whole spectrum may be explained by considering the size of each of the VSRRs: as the size of each VSRR is increased by increasing the pillar height, the dipole mode can be expected to redshift as the structure accommodates a longer effective wavelength. The increasing gap between the magnetic and lowest energy toroidal peak implies that the coupling between VSRRs is made stronger by the increased pillar height. Increasing the pillar height increases the surface area of the VSRR facing the other three VSRRs, which may increase the coupling strength of the electric fields from accumulated charge in each VSRR. Increasing the height of the pillars increases the effective length of the split ring, which may in turn increase the magnetic flux through the centre of each of the VSRRs, thereby increasing the magnetic coupling around the whole T4 structure and causing a greater energy splitting of the magnetic and toroidal dipolar modes. A previous study on coupled SRRs have shown that coupling through the magnetic moment is stronger than coupling through electric dipoles [55], indicating that the contributions from the increased magnetic field coupling may be of greater consequence than electric dipole coupling.

As the pillar height increases, the second toroidal peak redshifts more strongly than either of the other two, and drops in scattering intensity. The peak exhibits some Fano-like characteristics in the asymmetry of its shape and when the pillar height is increased, a shoulder develops on the peak at around 0.628 eV, which becomes a full peak and dominates the spectral region after the first toroidal dipole moment when the pillar height is increased to 270 nm.

The energy shift between the experimental T4 array and the simulated spectral response could be explained by inaccuracies in the measurement of the height of the T4 pillars, especially since the spectrum seems to be very sensitive to this parameter. Despite changes to the pillar height, the magnetic and the first toroidal mode still exist in the T4 structure, although they may shift in energy. The second toroidal peak

appears much more sensitive to the pillar height, almost disappearing completely when the pillars are made 30 nm taller than the original case, which could explain why this peak is not seen in the experiments or the simulations by Huang *et al.* [299], who used different design parameters.

5.2.4 Simulated EELS

BEM simulations are used to simulate the EELS response of a simplified T4 structure with solid pillars. Unlike the FEM simulations, the BEM simulations are more limited in terms of the mesh size which can be simulated, but the BEM program directly calculates the EELS response of the structure. The BEM simulations further confirm the mode order presented by Huang *et al.* [299] and the FEM simulations, although only one toroidal peak is present in the BEM spectrum. This is not entirely unexpected, given the dependence of the second toroidal peak from the FEM simulations on the pillar height, and the reduced size of the BEM simulation mesh. Figure 5.7 presents simulated EELS maps at the two lowest energy peaks of a simplified T4 structure, and the magnetic and electric field vectors induced by a given electron beam location.

The BEM simulations confirm that the lowest energy mode produces a net magnetic dipole and has high EELS intensity towards the outer pillars of the VSRRs, as seen in the experimental maps at 0.58 eV (Figure 5.4(b)). There is also an electric dipole response induced at this energy (Figure 5.7(a)(iii)).

The second peak in the simulation has high EELS intensity around the inner VSRR pillars, agreeing with the experimental maps in Figure 5.4(b). When the electron beam is placed near the centre of the structure, circulating magnetic fields are induced in the VSRRs (Figure 5.7(b)(ii)), while the electric field vectors reveal no net dipole moment.

5.2.5 Tilted Excitation

The EELS probability is proportional to the component of the electric field of the LSPR which is parallel to the electron beam [69]. Tilting the stage so that the sample is in a different orientation relative to the electron beam exposes different LSPR electric field components to excitation [242, 301], giving more information on the distribution of LSPR in a complex 3D structure such as the T4 array. The stage tilt was chosen such that two of the VSRRs are end-on and two are side-on in projection (Figure 5.8).

When the specimen stage is tilted, the relative probabilities of the magnetic dipole and toroidal dipole mode switch, so that the toroidal dipole peak is higher when averaged over a similar location on the sample as the original, untilted data (Figure 5.8(c)). The tilted EELS maps of the magnetic and toroidal dipoles show that the fields of each mode extend up the outsides of the VSRR pillars, instead of being localized only at the top or bottom (Figure 5.8(b)).

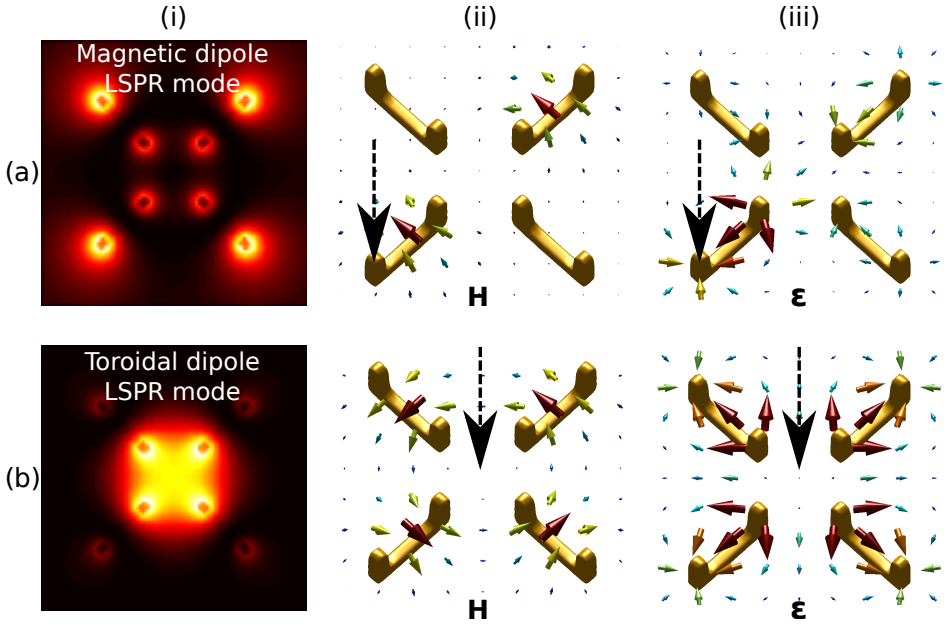

Figure 5.7: BEM simulations of the EELS response and induced magnetic and electric fields of the T4 array. (a) Simulated response of the magnetic dipole peak energy: (i) simulated EELS map, (ii) magnetic field vectors, (iii) electric field vectors; (b) simulated response on the toroidal dipole peak energy: (i) simulated EELS intensity map, (ii) magnetic field vectors, (iii) electric field vectors. Electron beam location in (ii) and (iii) is indicated by the black arrow.

The intensity of the magnetic dipole mode is strongest on the outside edges of the side-on VSRRs (pillars A1, C1 as labelled on the ADF image) and around pillar D1, but is much weaker around pillar B1. Pillar B1, in the tilted projection, is over top of the bottom bar of the VSRR and there is too much scattering of the electron beam to detect any signal near the top of this pillar, although no strong evanescent fields are detected along its sides either.

On the toroidal dipole mode, the intensity around the base of pillar D2 is reduced, but the EELS signal extends up the sides of the other three inner pillars and seems particularly strong in between pillars B2 and C2, and pillars B2 and A2, indicating strong electric fields parallel to the beam between the coupled pillars. The toroidal dipole peak is at the same energy for both the top-down and the tilted samples. The magnetic dipole peak appears to have a small blueshift, which may be a result of the reduced coupling strength to the electron beam and its proximity to the tail of the toroidal dipole mode.

The electric field vectors, calculated in the BEM software, of the tilted T4 array under electron beam excitation are shown in Figure 5.9. On both of the two low energy dipole peaks, the anti-node of charge density is located at the tops of the pillars and this is where the strongest electric fields are present.

The side-on VSRRs (A and C in Figure 5.8(b)) still possess strong electric field components along the electron beam direction pointing towards the tips of the pillars

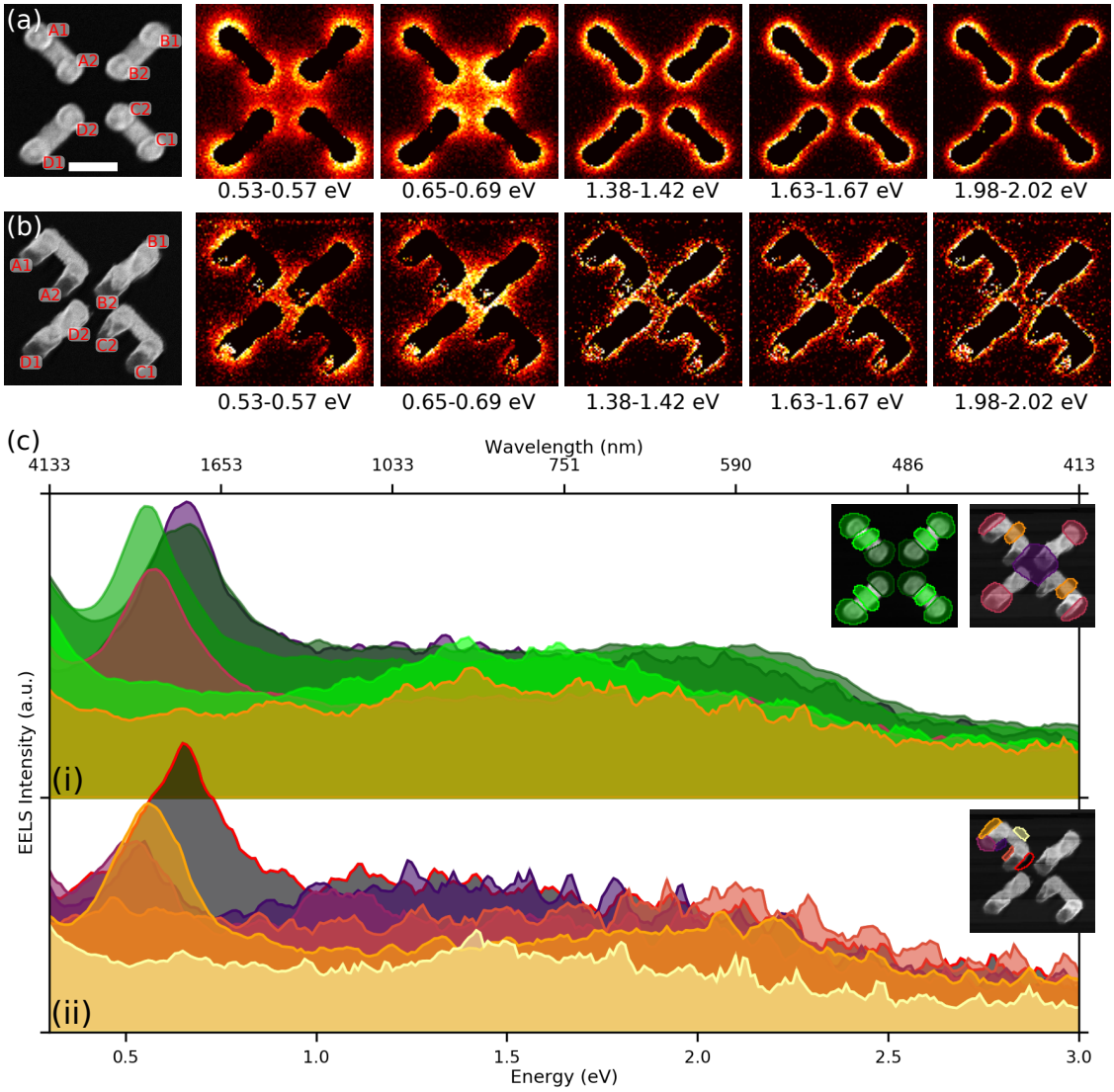

Figure 5.8: EELS results for a top-down and a tilted (stage tilt of $(\alpha, \beta) = (35°, -10°)$ T4 array. (a) Top-down STEM image (leftmost, scalebar is 250 nm) and averaged EELS intensity maps for the energies indicated; (b) STEM image (leftmost image) and EELS maps for the same T4 array with stage tilt; (c) Spectra from both the top-down (i) and tilted (i, ii) toroidal array, averaged over the areas shown in the insets.

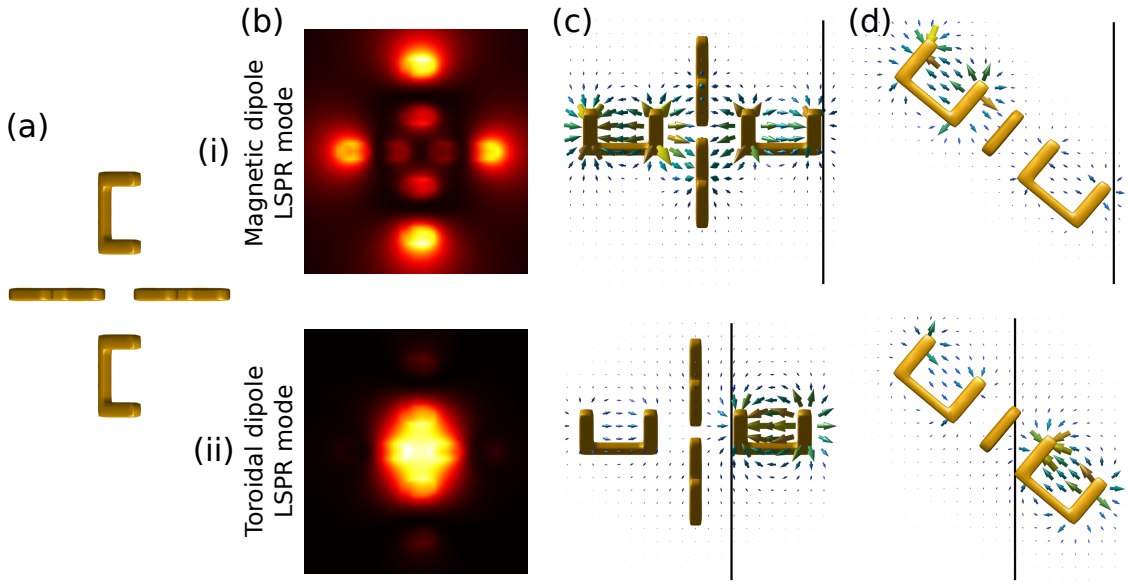

Figure 5.9: Simulated EELS response and electric field vectors for magnetic and toroidal dipole modes of a tilted T4 array. (a) Projection of the tilted mesh; (b) EELS probability maps for the magnetic dipole (i) and toroidal dipole (ii) moment on the tilted samples; (c, d) Electric field vectors induced by the electron beam (black line) at the magnetic dipole peak (i) and the toroidal dipole peak (ii).

(Figure 5.9(c)) and there is strong signal (Figure 5.8(b)) along the length of the pillar for both magnetic and toroidal modes.

For the end-on VSRRs (B and D), however, the tip has the strongest near-fields interacting with the electron beam. When the beam hits the base of pillar B1 or D2, there is a low excitation probability of the dipolar modes because of the low electric fields near the pillar base (Figure 5.9(d)(ii)). When the beam impacts the tops of pillar B2 or D1, however, there is a high electric field due to the charge accumulation near the tips of the pillars, and thereby a greater interaction probability (Figure 5.9(d)(i)). This introduces the asymmetry seen in the maps of Figure 5.8(b). In the simulations, the magnetic dipole mode also has a lower excitation probability than the toroidal mode when the sample is tilted.

The plasmon fields of the bonding mode in between the gap of two coupled plasmonic nanoparticles are normally invisible in an EELS experiment because, although the electric fields are strong, they are perpendicular to the electron beam [164]. As demonstrated on a single planar SRR by von Cube *et al.* [242], tilting the sample can make these fields visible. The primary mode on an SRR has an electric dipole configuration across the long axis of the SRR and a magnetic dipole through the gap (as discussed in Chapter 4). In the toroidal array, the magnetic dipoles of each VSRR couple to each other and hybridize to give the magnetic and toroidal dipole modes.

When the stage is tilted, the electric fields of the dipole between the two pillars of the end-on VSRRs (B and D) have a component parallel to the electron beam. In

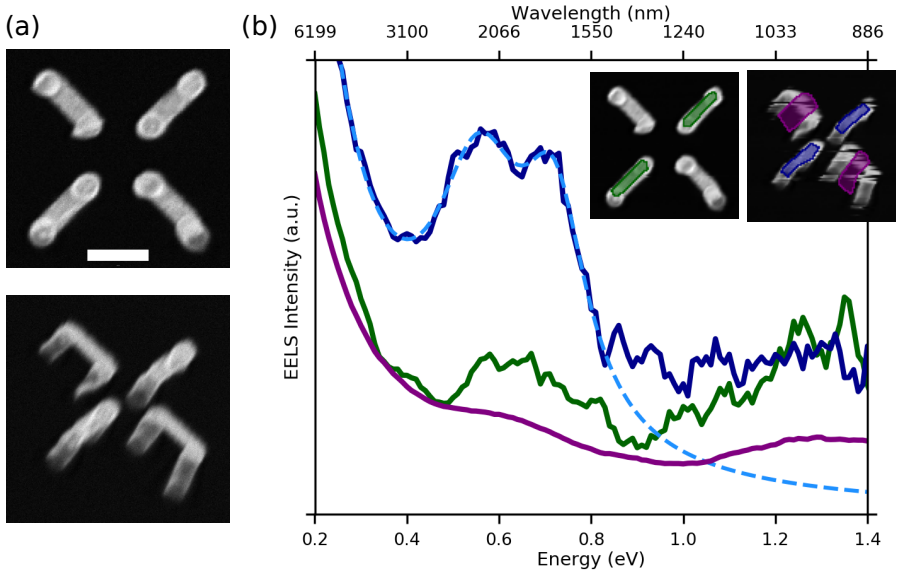

Figure 5.10: Change in EELS intensity of the primary two modes upon tilting of the T4 array. (a) STEM-ADF images of the T4 array (top), scalebar is 250 nm, and the same T4 array tilted to an angle of $(\alpha, \beta) = (40°, -10°)$; (b) spectra averaged over the areas indicated in the inset, dashed blue line indicates a fitted function including a power law and two Lorentzian functions. Spectra were averaged over the area selected, then normalized to the spectral integral before 8 iterations of RLD.

the side-on VSRRs (A and C), the electric dipole fields between the pillars are still perpendicular to the electron beam and the dipole can only be detected where the electric fields curve around the outsides of each pillar.

Unfortunately, retrieving signal from the end-on VSRRs is challenging because of the high scattering of the electron beam travelling through the projection of the pillar on top of the bottom bar. Nevertheless, by averaging a spectrum over both end-on VSRRs before applying 8 iterations of the RLD algorithm, two peaks can be detected in the spectrum despite the noise (Figure 5.10). The peak heights of the magnetic and toroidal dipole modes are very similar to each other in this case and both are retrieved from the same area, confirming the electric field configuration suggested by the VSRR electric dipole model. Applying the same procedure to either the same T4 array with no stage tilt, or to the side-on VSRRs shows very little signal from the two dipole peaks, averaging over similar locations.

The pair of peaks detected in the end-on VSRRs can be fitted using a combination of a power law, for the ZLP tail, and two Lorentzian peaks. The fitted Lorentzian peaks are centred at 0.557 eV with a FWHM of 0.24 eV, and at 0.720 eV with a FWHM of 0.17 eV, agreeing very well with the peak locations of this T4 array. Interestingly, the toroidal dipole peak ($Q = E_{\text{centre}}/\text{FWHM} = 4.2$) has a higher quality factor than the magnetic dipole peak ($Q = 2.3$), although the SNR here is not high and application of the RLD algorithm is limited because of the poor SNR.

Tilting the toroidal array also allows us to see structural defects which are not

obvious in the top-down projection of a typical micrograph. For instance, in the VSRR array shown in Figure 5.10, the outer bottom right pillar is revealed to be particularly tall and slightly crooked, and the inner top left pillar appears to have collapsed in on itself. Despite the imperfections in the fabricated structure, this T4 array still shows strong plasmon coupling to give the hybridized magnetic and toroidal modes, though the defects might affect the peak width.

The tilted views of the VSRR array also support the inference that the pillars are hollow inside, since the electron beam does not experience as much strong scattering as would be expected from solid pillars. In fact, the electron beam is scattered more by passing through the bottom bar, which is a nominal 30 nm of gold, than it is by passing through the tilted pillar, suggesting that the walls of the pillar are very thin. Comparing the relative scattered intensity through the bottom bar and the pillars in the tilted ADF image shown in Figure 5.10(a) allows us to estimate that each pillar wall is approximately 10 nm thick.

5.2.6 Higher order modes

At higher energy than the two dipole modes, above 1 eV, there is very little EELS intensity at the bottoms of the pillars of the VSRRs (Figure 5.8(b)). In the normal orientation, the structure of the signal above 1 eV is difficult to make out (Figure 5.4(b), 5.8(a)).

At around 1.34 eV, a signal can be distinguished at the centre of the VSRR bars (Figure 5.8(c)) (or at 1.29 eV in the T4 array presented in Figure 5.4). In the tilted images, this signal is strong around the bottom bar itself, indicating that this could be the second order SRR mode (see SRR eigenmodes in Figure 4.2), with three anti-nodes spaced around the SRR. EELS signal from the anti-nodes around the VSRR ends is hard to separate from all of the other modes which cluster at these locations, but in the centre of the bar, the peak stands out.

Based on the analysis of the isolated VSRR presented in Chapter 4, rim modes might be expected around the tops of the pillars on each VSRR in the T4 array. There is some signal on the outer edges of the VSRRs (Figure 5.8(c)(ii)) between 1 and 1.5 eV, which could belong to a combination of higher order SRR modes and pillar rim modes.

Near the tops and sides of the pillars the EELS intensity is higher towards the higher energies, between 1.5 and 2.5 eV, unlike the bottom bar location or near the bottoms of the pillars (Figure 5.8(b),(c)(ii)). The localization of these modes around the tops and sides of the pillars implies that these might be rim modes similar to those seen in the isolated VSRR. The extent of the evanescent fields outside the VSRR structure is noticeably reduced as the energy loss increases; higher energy LSPR modes have shorter free-space wavelengths and more tightly confined fields, and the delocalization associated with low-loss EELS is lower at higher energy. Both of these factors make it challenging to distinguish the higher energy loss LSPR modes. The

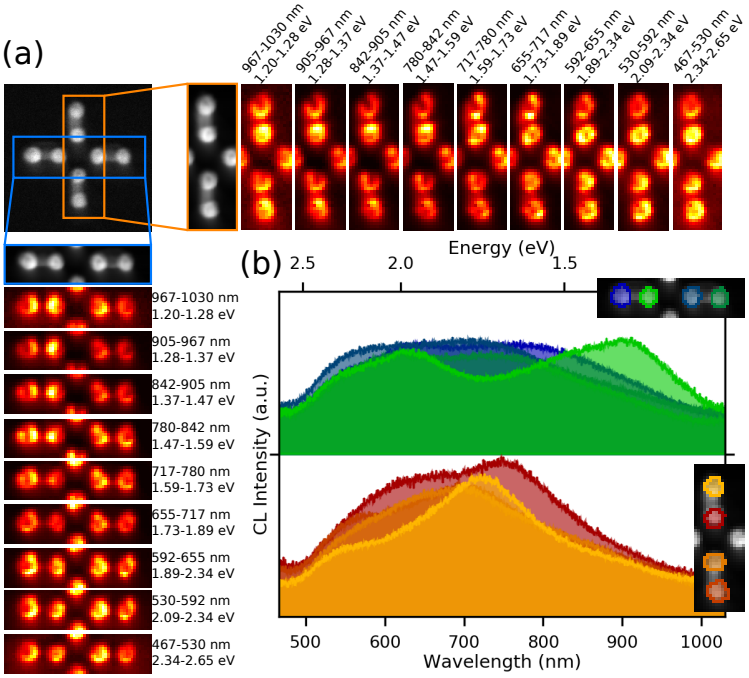

Figure 5.11: CL spectrum imaging on the T4 array. (a) Top left is the SEM image of the T4 structure, with the extracts showing the areas mapped for spectrum imaging, the CL intensity is integrated over the wavelength range indicated, along the top row and left column. (b) CL spectra averaged over the areas indicated in the insets.

noise on the spectra in Figure 5.8(c)(ii) is noticeably higher than that in (i), because the spatial averaging is done over fewer pixels in order to be more selective of the location.

CL on the T4 array

As shown in Chapter 4, where EELS struggles to reveal the nature of tightly confined higher order modes, CL enables easy visualization of the localized fields of radiative LSPR modes. The CL spectrum of a T4 array is complex, revealing a variety of resonances primarily localized around the pillar rims (Figure 5.11).

At low energy (long wavelength), there is a peak at approximately 1.37 eV (905 nm). This mode is strongest on the inside left pillar and emits primarily transversely to the horizontal VSRRs.

In between 780 and 550 nm, there is a complex series of overlapping peaks. Nevertheless, at low energy, there appears to be a longitudinal bonding (LB) mode between the two pillars on each individual VSRR, based on a comparison to the CL intensity maps of Chapter 4. As the energy increases, the CL intensity surrounds the rims of each pillar, the result of overlapping coupled rim modes.

In the T4 array, there are eight pillar rims and, having noted previously the diffi-

culty in obtaining consistently sized pillars, the defects in the pillar rims may play an important role on the LSPR modes of the high energy region of the spectrum where the LSPR wavelength is more comparable to the small details of the pillar shape. If all pillars were the same, it might be expected that both of the inner pillars and both of the outer pillars on the horizontal datasets would have the same CL response. Based on the spectral response averaged over each pillar, this is not the case, likely due to fabrication defects on each individual pillar. It may also indicate that the pillar rim modes are coupled only within each VSRR and do not couple strongly across the gaps between VSRRs in the T4 array.

Above 2.5 eV, interband transitions in gold dominate the spectrum, damping the LSPR response too strongly for resonances to appear.

5.2.7 Defeating the electric quadrupole

The four-fold symmetry of the T4 array has a low energy magnetic dipole mode and a higher energy toroidal dipole mode overlapping with an electric quadrupole mode, as shown by Huang *et al.* [299], which dominates the radiative spectrum. In order to suppress the electric quadrupole and further isolate the toroidal dipole from other multipole contributions, two configurations of VSRRs are proposed: one with five SRRs and five-fold rotational symmetry (T5 array) and one with six SRRs with six-fold rotational symmetry (T6 array).

The toroidal dipole in the T4 array occurs when the charge distribution on the VSRRs is rotationally symmetrical. This overlaps with an electric quadrupole, which is created by the four-fold rotational symmetry of the electric dipoles on each of the VSRRs.

If the five-fold and six-fold VSRR arrays support a similar mode in which the charge distributions are rotationally symmetrical, a set of similarly circular magnetic dipoles can be created (Figure 5.12). However, the extra VSRRs present in the structure mean that the four-fold symmetry has been eliminated and the electric quadrupole contributions may be suppressed.

T5 and T6 arrays have been fabricated for EELS characterization (Figure 5.13). Both structures have two low energy peaks, though it is possible that there are more than two closely spaced resonances inside these peaks which are not resolvable.

On the T5 array, there is a peak at 0.665 eV with high intensity around the outsides of the VSRRs. Another peak is identified at 0.70 eV, which is quite broad relative to the first, but has more intensity around the insides of the VSRR pilars.

The T6 array also has two distinguishable primary peaks; the first localized primarily around the outsides of the pillars (0.665 eV) and the second localized around the insides of the pillars (0.78 eV). The intensity of the low energy peak on the T6 array is higher than that on the second peak, and the second peak is much broader than the first. The lowest energy peak also has some EELS intensity near the inside of the structure, and appears as a shoulder on the higher energy peak in the spectrum

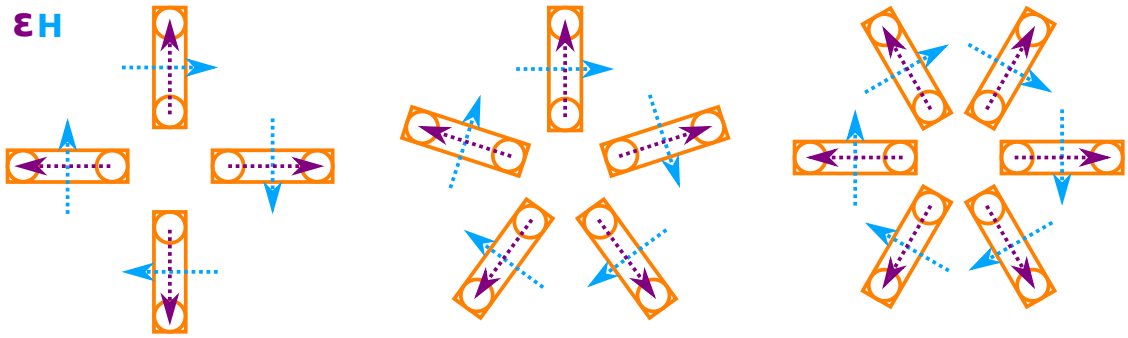

Figure 5.12: Schematic of electric and magnetic field vectors for the toroidal dipole resonance of four-fold, five-fold, and six-fold VSRR arrays. View is top-down, with the orange figures representing each VSRR; purple vectors represent electric dipole vectors; blue vectors represent magnetic dipole vectors.

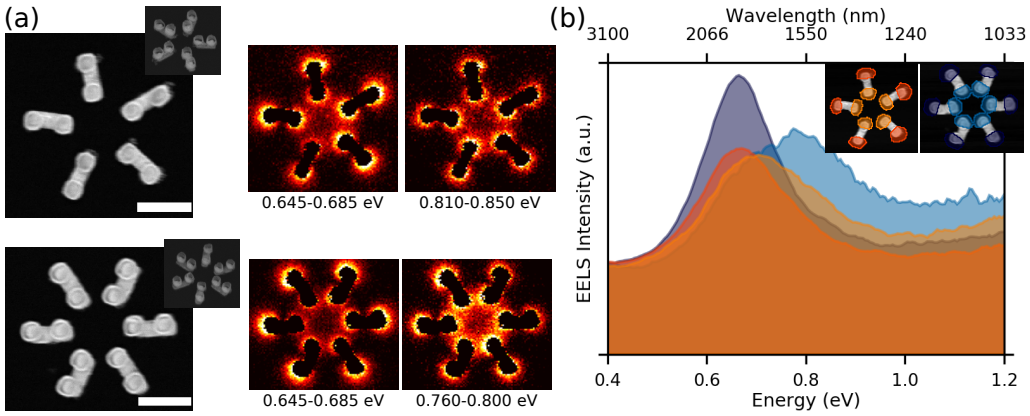

Figure 5.13: EELS data for T5 and T6 arrays. (a) STEM-ADF images (scalebar is 250 nm), inset shows a tilted SEM image, and EELS maps averaged over the energy shown for T5 (top) and T6 (bottom) toroidal arrays; (b) EELS spectra averaged over the areas shown in the insets for T5 (orange) and T6 (blue) arrays.

averaged over the insides of the pillars.

There may be more non-degenerate peaks from hybridization of the individual VSRR dipolar modes in the T5 and T6 arrays than there are in the T4 array, which could broaden the spectral response in this region because of peak overlap. The lowest energy peak of the T6 array is noticeably the highest and sharpest peak out of both the structures presented in Figure 5.13.

Damping mechanisms broaden the peak width of an LSPR peak through shortening the lifetime of the plasmon, and include radiative damping, interface scattering, and Ohmic damping within the material [196, 302, 303]. Both the T5 and T6 arrays shown in Figure 5.13 were fabricated in parallel on the same TEM grid, so have similar film quality. Inspection of the STEM and SEM images reveals no obvious differences in the quality of the structure, and the energies of the peaks are well below the onset

of interband transitions. Convolution of the PSF of the EELS system can complicate linewidth interpretation [304], but since both of these datasets were acquired under identical conditions, within a few hours of each other, it is unlikely that instrumental contributions account for the differences in peak linewidth.

All other things being similar, the different configuration and rotational symmetry of the T5 and T6 arrays may result in stronger radiative damping on the T5 peaks relative to the T6 peaks. The second T6 peak is also broader and less intense than the first, which could either be due to additional radiative damping, or spectral broadening from multiple overlapping peaks.

The T5 and T6 arrays presented in Figure 5.13 are nominally the same size as each other, with only the addition of an extra VSRR in the T6 array. Although the diameter of the central gap is the same for both arrays, the additional VSRR in T6 decreases the distance between neighbouring VSRRs. This increased proximity of the VSRRs may be responsible for the greater energy splitting seen in the peaks of T6 compared to T5, promoting greater coupling of the magnetic moments of the VSRRs. Despite this, the energy of the primary peak is almost precisely the same for both T5 and T6 structures. Only the energy of the second peak blueshifts when an extra VSRR is added to form T6. The trends seen in the data presented here are confirmed in datasets on other examples of T5 and T6 arrays (not shown), but simulations on the response of T5 and T6 remain to be done to confirm the possibilities of these structures as supporters of the toroidal dipole moment. Based on symmetry arguments, the T5 and T6 arrays should suppress emission from the electric quadrupole at the proposed toroidal dipole mode, but EM multipole calculations of the scattering off these structures is required to confirm this.

5.3 Concluding Remarks

The coupling of magnetic dipole modes of four VSRRs in a circular arrangement produces a low energy magnetic dipole mode and a higher energy LSPR mode supporting a toroidal dipole moment. The magnetic dipole moment is produced when two of the VSRRs oscillate out-of-phase with the other pair, resembling the configuration of a hybridized bonding mode between two pairs of VSRRs. The anti-bonding mode between the two pairs produces the toroidal dipole moment, when all four VSRRs are oscillating in phase with each other.

Tilting the T4 array allows the electron beam to probe different components of the electric fields of the LSPR modes, thereby changing the relative excitation probabilities of the magnetic and toroidal dipole modes and revealing more of the structure of the LSPR mode fields around the 3D array. The tilted excitation configuration also improves the identification of higher order modes on the VSRR and on the rims of the pillars. CL is used to confirm that higher order coupled rim modes are present on the pillars of the VSRRs in the toroidal array, similarly to the isolated VSRR. Further electron-beam experiments on these structures could include the use of vortex beam

experiments, in which the electron beam carries a magnetic moment [305,306], though it is likely a monochromator will be required to detect the low-energy toroidal dipole peak.

Future work on these arrays of VSRRs (T4, T5, T6) remains, including additional simulations to better understand the complex modes present in the 3D coupled geometry and the interaction of the electron beam with these fields in the straight and tilted orientations. This type of structure, in which both electric and magnetic dipoles couple together, holds great promise for its ability to create different electromagnetic multipole moments, including the toroidal dipole moment. Performing a multipolar decomposition (*e.g.* [247, 307, 308]) on the scattered spectra of these structures can further improve understanding of these exotic multipolar moments and the additional moments that can be created through manipulation of these geometries.

Chapter 6

Data Analysis with SIAn

During the course of this thesis work, a Python program (named 'SIAn' for Spectrum Image Analysis) was written to fulfill the data processing needs that come with trying to visualize and understand 3D spectrum image datasets in both EELS and CL. The program was written to speed up the Richardson-Lucy deconvolution through using parallel processing on a multiprocessor computer, and to enable a unique and flexible way of navigating 3D datasets.

The accuracy and trustworthiness of a piece of science depends not only on the use and understanding of the hardware in the lab and the scientist's ability to interpret the data, but also on the quality of the software used to acquire, analyze, or visualize the scientific data. Errors in the software can modify the results in unexpected ways and may mislead the scientist into making the wrong interpretation. When so much care is taken over the fabrication and data acquisition conditions in the lab, the software used to analyze and display the data might be expected to live up to similar standards, yet the data processing step is often undervalued in the scientific experiment.

6.1 Scientific Programming

The progress of science relies heavily on the concept of reproducible science and peer review, as evidenced by the working practices of respected journals. There are now many specifications in place for reporting new experimental procedures or mathematical proofs and journals rely heavily on peer review to determine what is suitable for publishing. However scrutinized the experimental methods and results may be, the review of scientific code has not yet reached the same level of importance or the same standards of peer review and reproducibility [309–311], despite the large impact that software can have on the results obtained. If the code used is not made available and accessible to others in the community, the research is not truly reproducible, but the sharing of code brings up barriers such as providing sufficient understandable documentation and cleaning up the code so that it is readable by others [309].

Programs used by scientists may come from commercial packages, but these may be

buggy with slow updates if the market is small, the licensing requirements may change unexpectedly, or different non-compatible versions or updates may be released [312]. In the ideal case, the open source community has many people, usually experts in the application field, working on the same code base and any bugs will to be caught and fixed quickly [312].

In practice, however, many open source projects are developed by individual end-user developers, working alone to fit their own unique needs [312, 313] and often abandoning their projects once their need has passed. Large scale projects may suffer from a lack of leadership: when none of the individual developers understands the full program, bugs are easily introduced unnoticed. End user programmers have the specialized knowledge to be able to define what the code needs to do, but are usually novices in software engineering: the majority being self-taught without knowledge of best practices [313, 314]. With advances in computing hardware, the limit that scientists often encounter now comes more from their ability to produce reliable code than from the hardware it is run on, as they face a steep learning curve with more and more complex coding tasks [314, 315].

6.1.1 Coding in the Lab

Scientific programs written by an end-user developer are often undocumented and seem unreliable and confusing to anyone without conversational access to the author, making them inaccessible to other potential users [313]. A typical piece of code might start out as something small and simple, but then it is built upon until it is very large; beginning the documentation and refactoring the code to be more readable would take a lot of time and effort, which is usually deemed not worth it [316]. The short term nature of graduate student and post-doc contracts means that coding knowledge can easily disappear from a lab, making a once-useful or necessary piece of code worthless because nobody remembers how to use it [313]. Undocumented code causes nightmares for new students or researchers as code is passed through the generations of short term developers [315].

Coding is often not valued as a scientific endeavour and is instead seen as a secondary activity by scientists: something that is not an important part of research, but must be done in order to get back to the interesting science [310, 313]. Achieving fast results takes precedence over taking the time to test and document code, although scientists who spend a lot of time coding do start to value and appreciate the benefits of applying software engineering principles [316]. Mostly, however, testing of code is done by asking a colleague to try the program, comparing the results to similar programs, and making sure that the output of the code is qualitatively reasonable [313, 317]. Only if the program starts producing strange or outlandish results will the accuracy of the code itself be checked [317]; usually the code's merit is based on the reasonableness of the output, given the inputs and knowledge of the user [317–319].

6.1.2 Silent Faults

Producing a perfect computer program is nearly impossible, even for software engineering experts: even well-written and well-tested code may contain something like 1 fault per 10,000 lines of code [310]. With novice programmers, code is often full of silent faults, tiny errors which don't cause obvious problems but may cause small errors in the results [315]. Even in commercial programs, silent faults can cause vastly different outputs for different implementations of the same algorithm, each of which gives a believable output [311]. Small errors in the software propagate through the calculations and can cause significant changes to the end result, but are hard to detect [320] and as long as the output is within the realm of plausible answers, the defects in the code go unnoticed [310, 318, 321].

Scientific coding poses a particular challenge in finding the source of errors; the code represents a hardware calculation of an implementation of a numerical algorithm, which is an approximation to a mathematical model, which is a representation of a real-world phenomenon, and it is difficult to know at which stage the error lies [316, 318, 322]. While errors can come into play in any or all of these steps, scientists often focus on the validity of the model, rather than checking for faults in the code, which can be done through testing or inspection [318].

6.1.3 Challenges in Scientific Programming

With the high percentage of scientists who are self-taught programmers, scientific code is often messy, unreadable, not rigorously tested, and undocumented [315]. Other scientists who want to make use of an algorithm or reproduce an analysis see this poorly documented and messy code, then decide that it will be both easier and faster for them to write their own implementation rather than trying to understand what is going on in the original code [312, 315, 322].

This results in a lot of different versions of a single algorithm, each with its own set of silent faults making its output slightly different from the other implementations, making results seem unreproducible, and wasting time in repeated implementation of the same algorithms. Even within the field of software engineering, implementations of the same algorithm are error-prone; only five out of twenty software engineering textbooks surveyed by Pattis [323] had an error-free implementation of the binary search algorithm. How to encourage scientists to write more reusable code and improve the standards of scientific programming is an active topic of discussion in the literature. Suggestions include partnering the scientific developer with software engineers or training graduate student developers with formal courses or mentoring programs [315].

It is difficult to apply precisely the same development strategies to scientific applications as are used in software engineering applications [312, 324]. In software engineering, it is common to define the end requirements of a program before beginning to write the code; this is often not possible in scientific computing, where

the requirements may not be known in advance, or may evolve as the developer learns more about the process: as their understanding improves, their needs may change [316, 317, 321, 324]. Scientifically oriented programs are often developed in an exploratory manner and often the correct output is unknown, making it difficult to verify that the program is performing correctly [312, 313, 316]. Despite these difficulties, the scientific programmer has much to gain from taking advantage of software engineering practices and tools.

6.1.4 Tools of Program Development

Since many scientific developers learn through self-study with little formal education in software development [314, 316], they often lack knowledge of current practices in software engineering which help to make code development faster and the resulting code more trustworthy [325]. Tools used by software engineers, such as version control, unit testing and system testing, the use of development environments, automation of repetitive tasks, issue trackers, and code reviews are often totally unknown to scientific developers, because of a lack of education in these areas [314, 321, 325].

Version Control

Version control in scientific programming is frequently done by emailing files, manually copying them to new locations, or adding numbers or dates to the ends of filenames [321]. Automated version control systems simplify this process greatly [321]; every change made is saved in the history and it is always possible to revert back to previous versions if needed [326]. Systems such as Git, Subversion, or Mercurial can be linked to online repositories with public or private accounts, such as Github, Bitbucket, or SourceForge [321]; public accounts on these repositories encourage code sharing and can be linked to published results, as well as enabling multiple people to make changes to the same code in an organized fashion [326].

Testing

Testing of code is an important but frequently overlooked step in creating a software program. Low level tests include unit testing, in which small individual sections of code are tested independently of the rest of the program to make sure that it is returning the correct output for any input [321]. Unit testing is one way to catch silent faults in the code, and the completeness of the unit tests themselves can be tested through mutation testing, in which small errors are added into the original code to check if the unit tests catch the error [318]. Even a small number of these tests can catch a large number of faults in the code, particularly with careful test design [318].

Higher level tests, such as integration tests and regression tests, check the connections between different functions in the program and that the program's behaviour

does not change as updates are made to it or to the packages that it uses [321].

Many programming languages have built-in testing packages that can be used directly, and the testing process itself can be automated once tests are written [321]. For instance, in the Python language, the unittest package [327] is part of the standard Python distribution, but there are also other packages with additional features, such as the pytest package [328], that can be installed separately.

Exhaustive testing of code is generally not possible, particularly in scientific applications, where the true answer to the problem at hand is new, unknown scientific territory [313, 318, 319]. Because of this, writing tests does not guarantee that the correct answer will always be given, but it greatly enhances the confidence of the user that the code is behaving properly and they can turn their attention to scientific problem-solving [318]. Catching and fixing small errors improves the reproducibility of the results [311]. If it is not possible to truly know the correct answer, relative checks can be performed on the system to make sure that the output changes as expected if a change is made to the input [319].

Code Review

Code review involves simply reading the code. Either the developer or another colleague reads through the code, actively looking for visible bugs [318,321]. Code review is a form of testing that relies on inspection of the code by a knowledgeable person, and can be made easier through the use of development environments.

Development Environments

Integrated Development Environments (IDEs), such as IPython, Pycharm, or Spyder in Python, are independent programs compatible with one or more programming languages. They provide many useful features such as syntax highlighting, debugging tools, and variable tracking. Some languages, such as Matlab, also provide their own built-in development environments in the user interface. The IDE may be capable of, for example, basic error checking to catch mistakes before they have a chance to propagate through the code, such as checking that inputs to a function are of the correct type (*e.g.*, floats, integers, strings) and within the limits that the function is designed to accept [319, 321].

Documentation

Documentation of code is valuable not only to make the software usable by others, but also to help make the code maintainable by the developer's future self or counterpart. The documentation should explain what design decisions were made and why, so that future developers understand the history and avoid making the same mistakes [320,321]. Good documentation is accurate, free of ambiguity, defines exactly what the program is supposed to produce, and is easy to read and accessible to both end-users

and developers, thereby promoting reusability and maintainability of the code [329]. Defining the requirements and expectations of the software promotes reuse of the code and accuracy of the results [330, 331], whereas poorly written documentation can lead to the code being used for things outside its scope of applicability [315]. If documentation is poor, users will not read it, which in turn reduces the incentive for developers to spend time writing it [329].

Clear documentation not only helps future users and developers, but aids in the rational design of software, forcing the developer to treat the coding process as a design process, similarly to other large scale engineering projects [329, 332]. Writing out the requirements of the software helps the developers to keep on track to meeting those goals, and to catch and solve problems before the project is complete, saving time in future programming stages [320]. This is challenging in scientific programming, where the end requirements are difficult to pin down at the beginning of the project, but even post-dated documentation still helps future users to understand or maintain the code [330]. The process of documentation in scientific programming is still on ongoing research field, but several examples in the literature highlight the benefits of clear design documentation [332, 333].

Modular Design

Code that is modular is easier to test, read, and maintain: this means splitting up the code into smaller chunks. Each chunk takes an input, performs an operation, and returns an output independently of the rest of the program, with the advantage that each module can be modified separately and the program will continue to function as long as the inputs and outputs remain the same [321, 334]. Modular code also encourages the reuse of small functions and pieces of code in multiple applications, and allows a big project to be split up between different team members, saving time on the programming end [334].

6.1.5 Python for Scientists

Though there are many programming languages used in science, Python has quickly become a popular choice for scientists and engineers. In an object-oriented language (OOL) such as Python, different types of objects, each with its own set of associated properties, are stored as variables. The use of an OOL can help to reduce the barrier to starting to program and to the reuse of code; for instance, in an OOL, default values can be stored in objects, reducing the number of function inputs required from the user [322].

Python is an interactive interpreted language which doesn't require long compilation times and allows programmers to create quick exploratory scripts, possessing an expressive, easy-to-learn, and readable syntax [321, 335, 336]. Easily readable syntax makes it easy for new programmers to get started and relatively quickly build a simple working program. Python provides a flexible way to rapidly prototype or explore

algorithms and data. It is covered by free, open-source licensing which allows anyone to freely distribute and share any code they may write using the language, with the backing of a strong and supportive online community [335].

The language is portable between different platforms and installation comes with many built-in datatypes and a well-equipped standard library with many functionalities. Many more user-contributed modular libraries are available on the internet, many stored in a centralized database for easy access [335, 336]. Of particular use for scientists and engineers are the NumPy, SciPy, Matplotlib, and interactive IPython libraries [335–337].

NumPy

The NumPy library, developed in the 1990s, contributes the multidimensional array object and manipulation thereof to Python, and is one of the most well-used packages in scientific Python computing [335, 338]. NumPy is a computational array-based library built for fast vectorized operations, including standard arithmetic, matrix operations, sorting, slicing, indexing, and broadcasting multidimensional arrays with efficient memory storage and recall routines [335,339]. Although Python is interpreted code, it is able to interact with compiled code, and provides the user with an easy-to-learn façade over the more complicated, but faster, compiled code [335]. NumPy takes advantage of this; its array objects are stored in the same manner as compiled code and NumPy array operations are implemented in C to provide a huge boost to computation speed over standard Python operations [339].

SciPy

The SciPy package uses NumPy and provides additional functions useful to the scientific community, such as interpolation, optimization, and image processing routines for single or multi-dimensional arrays [335].

Matplotlib

Matplotlib was developed to provide an easily-usable library for creating 2D plots and data visualization and is now a widely used and supported plotting package [337]. Much of the Matplotlib interface is an imitation of Matlab's graphical plotting interface, which helps to support the transition to Python for new programmers who may have previously only ever used Matlab. Matplotlib provides a full suite of 2D plotting tools, including different types of plots, colourmaps and representations of data, annotations, text support, and interactive graphics capabilities [337].

IPython

IPython is an interactive command line tool, allowing scientists to test their ideas, look through their data, and try out different processing algorithms live [340]. It

provides many tools, including live access to the documentation, auto-completion of variable names and object attributes while typing, the ability to query objects to discover their properties, and detailed error tracing and debugging tools. IPython allows the programmer to experiment with their data and different algorithms, before incorporating their processing routine into a larger data processing program [340].

6.2 Spectrum Image Analysis with SIAn

All of the spectrum image (SI) data analysis performed in this thesis was done using a custom-built Python program, SIAn [183]. Other options for the analysis of EELS data include Digital Micrograph (DM), which provides on-line control of the EELS spectrometer and has some additional data analysis functionality; HyperSpy, an open-source Python library for multidimensional data analysis [341]; and a custom in-house Matlab code written by Dr. E.P. Bellido [122]. For CL data processing there is an in-house suite of Matlab functions belonging to the lab of Prof. Albert Polman, or Odemis [342], a Python-based interface used to both acquire and visualize CL data.

Digital Micrograph

DM is a proprietary software accompanying the Gatan spectrometers and providing functionality for controlling microscope hardware to acquire SIs. It possesses some signal processing routines, primarly aimed at core-loss EELS. Extraction of spectra from specific regions in a spectrum image can be done using rectangular boxes, but the Richardson-Lucy deconvolution algorithm is not coded into the program and must be scripted by the user in the DM scripting language. The student version of DM is much more limited in its signal processing functionality than the full, paid version.

HyperSpy

HyperSpy is open source and developed by microscopists, focusing on machine learning and component analysis of multidimensional datasets. Over the past few years, the development of HyperSpy has greatly accelerated as the number of contributors increases and the software becomes more trustworthy and adds functionality. Although the library is quite popular, it did not, at the beginning of the thesis work, meet the needs for low-loss EELS and CL SI processing. Specifically, the graphical user interface (GUI) for exploring data in HyperSpy is quite limited in its ability to extract spectra from specific areas. Although HyperSpy provides the RLD algorithm in its functions, when the decision to write SIAn was made, this implementation was prohibitively slow.

Matlab toolbox

The home-built Matlab toolbox was written explicitly for the purpose of performing the RLD algorithm on an individual spectrum or on spectrum images. The data and point spread function are exported from DM, imported into Matlab, then the RLD is performed before exporting the deconvolved data from Matlab back into DM or another program for visualization.

CL Software

Concerning the CL software, the in-house suite of Matlab scripts from Prof. Polman's lab is certainly comprehensive for all the tasks required to analyze CL spectrum imaging or angle-resolved data, but it is limited to the Polman lab's specialty of CL, and it does not handle EELS well. Odemis has more limited functionality, but presents a well-thought-out GUI for data visualization. Functionality for processing CL data was added into SIAn for easier comparison and side-by-side visualization with EELS data on the same nanostructures.

SIAn

Each of the options available offers a small part of the desired analysis routines and may be used in concert with each other, but it is highly desirable and much simpler to have a single piece of software which can handle all of the processing routines without needing to import and export different data formats between different programs. A Python library was written for the visualization and analysis of 3D spectrum imaging datasets obtained from CL and low-loss EELS. Data can be imported into Python using a freely available external library, such as HyperSpy [341], dm3lib [343], or dm3reader/dm4reader [344], and fed into SIAn for analysis and visualization.

6.2.1 Structure of SIAn

SIAn is largely built on top of NumPy [338, 339] and Matplotlib [337]. It was originally written in Python 2, but has since been upgraded to Python 3 following the deprecation of Python 2. The code is built as a library for users who are somewhat familiar with the Python programming language. Confidence in the results of the code are improved through the use of the Python unittest library and from comparisons with results from Digital Micrograph and the in-house Matlab deconvolution code. The code as-is is somewhat modular, to allow the re-use of functions for multiple different kinds of data. For instance, the GUI is not limited to the visualization of EELS spectrum images, but can be applied to any other spectromicroscopy technique such as CL. The same concepts of data navigation apply, only the spectral axis needs to be renamed. The modularity of the code makes it easier for new functions to be introduced or for old functions to be modified. More details on the testing, design,

and structure of SIAn can be found in the code repository [183]. SIAn is stored in a public repository on Github, taking advantage of Git's version control capabilities and automation of unit tests, and making the software available to contributors or users, under an open-source 3-clause BSD (Berkeley Software Distribution) license.

SIAn provides a library of useful functions specifically used to process low-loss EELS and CL data, including several common data processing functions, such as applying gain or background corrections and aligning spectra to a desired peak. The key features of SIAn are the parallelized implementation of the RLD algorithm and the GUI for navigation of the 3D spectrum image.

6.2.2 Richardson-Lucy Parallelization

The RLD algorithm has been described in detail in Chapter 2. This algorithm is computationally quite expensive, involving two convolution operations when performed on discretized datasets. As laid out in the code, the algorithm follows the steps shown in Figure 6.1, given the input of the number of desired iterations N_{it}, the point spread function (PSF) to be used, and the spectrum to be deconvolved. The original spectrum is used as an approximation to the ideal, or 'true' spectrum on the first iteration, but on all following iterations the result of the previous iteration is used. On a single spectrum, the algorithm typically works very fast, but when each pixel in a large SI must be deconvolved, the processing times can become distressingly long if each pixel is done in turn.

Each pixel in of the 2D spatial plane in a spectrum image is independent of all of the other pixels, since the RLD is acting along the spectral axis. This makes the implementation of the RLD algorithm an ideal case for utilizing the parallel processing capabilities of modern computers with multiple processing cores. To make use of parallel processing, SIAn uses the multiprocessing Python library and a program called 'handythread' from the SciPy Cookbook of user-contributed programs. The SI is divided into groups of pixels in the spatial dimension which are then assigned to different processors to perform deconvolution in parallel. The following section details the tests and improvements in timing that are obtained upon parallelizing the algorithm.

Parallelization Timing Tests

Timing tests were performed on a personal laptop computer running Linux Mint 19 Cinnamon (Cinnamon v. 3.8.9, Linux kernel v. 4.15.0-72-generic), with a quad-core (Intel© Core™ i7-4710MQ CPU @ 2.50 GHz ×4) processor with 8 threads, and 16 GB of RAM. All tests were run in the Jupyter Notebook server v. 5.2.2 interface, running IPython v. 7.10.1 in Python v. 3.6.9. No other tasks were performed on the computer during testing. Timing tests were performed using different numbers of RLD iterations (1, 2, 5, 10, 15, 20, 30), with serial and parallel processing, with different data spatial dimensions (1×1, 10×10, 100×100, 150×150 in the spatial

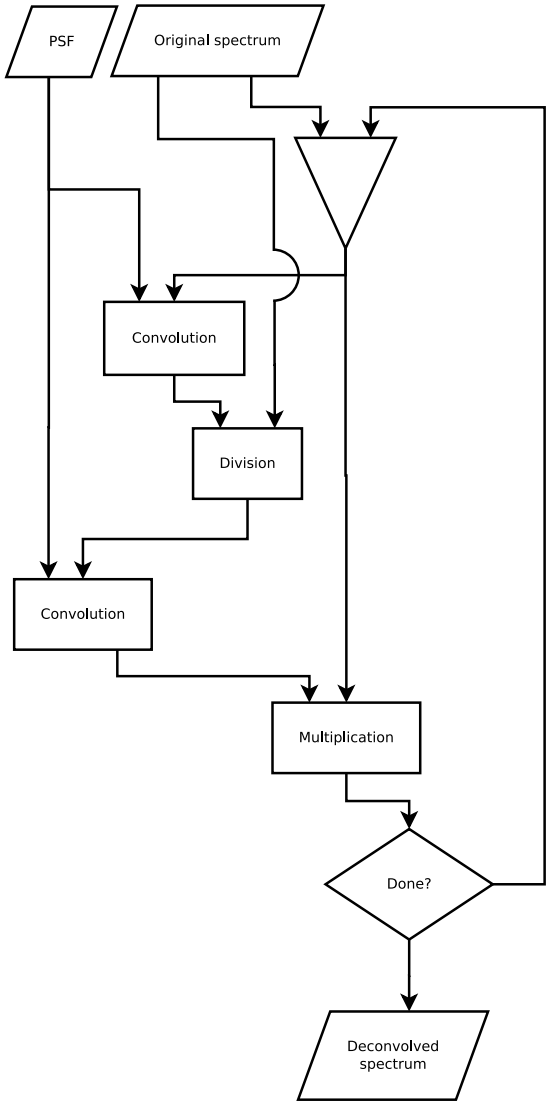

Figure 6.1: Chart showing the process flow for the Richardson-Lucy deconvolution algorithm for N_{it} iterations.

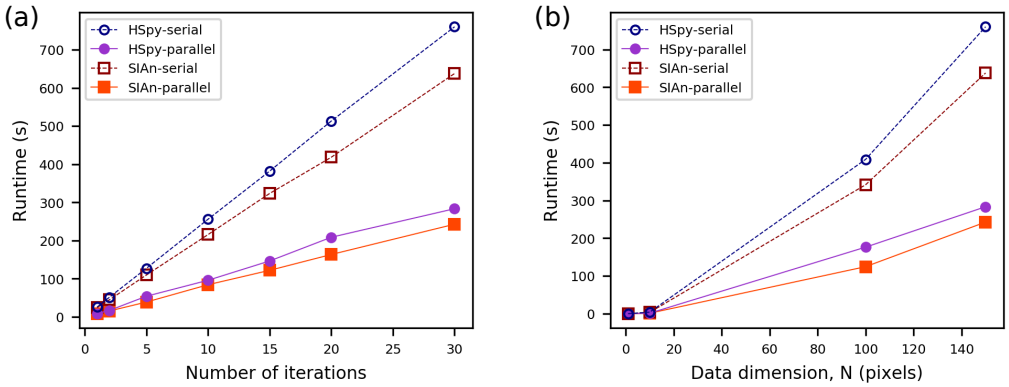

Figure 6.2: Runtimes for Richardson-Lucy deconvolution with 8 parallel threads (parallel) and with a single thread (serial) as (a) the number of iterations is increased for a dataset of dimensions $N \times N = 150 \times 150$ using both HyperSpy and SIAn; and (b) as the data dimension is increased from 1×1 to 150×150 for both Hyperspy and the developed code.

dimension, and 2048 in the spectral dimension); and using both HyperSpy's and SIAn's implementation of the RLD algorithm. The fastest time out of 20 trials was used as the result for each test to reduce variability from interference of other processes running on the computer [345].

An experimentally acquired SI and PSF are used for the tests to mimic the typical use conditions. The size of the SI is manipulated by cropping or tiling spatial pixels as needed to get an SI of the desired dimension. The PSF used is a 1D spectrum of length 2048. The serial timing tests were run by allowing the use of only a single processing thread; the parallel timing tests used all eight threads. The same dataset was used for all the tests performed with appropriate modifications to the spatial size as needed.

The results of the timing tests are shown in Figure 6.2. First looking at the difference in time between the serial and parallel processing in SIAn as the number of iterations is increased (Figure 6.2(a)), there is approximately a $3\times$ improvement in the runtime when all eight available threads are used in parallel compared to the serial result using one thread. For both serial and parallel processing, there is a relatively linear increase in the runtime for both HyperSpy and SIAn, though the slope is higher for serially processed runtimes. SIAn presents a small improvement in runtime over HyperSpy, which is particularly noticeable in the serial calculations. In the parallel calculations, SIAn has a small advantage over HyperSpy in the timing tests, but both programs are approximately $33 - 40\%$ faster when parallel processing is used instead of serial processing.

When increasing the size of the data by increasing the spatial dimensions and thereby the number of spectra which need to be deconvolved, the processing time required to perform the RLD algorithm on the whole dataset increases as shown in Figure 6.2(b). Notably, the additional time required by the parallelized implemen-

tation is less than that for the serial implementation, indicating that the parallel algorithm shows a greater improvement with larger data sizes than at smaller data sizes.

Interestingly, with a single spectrum (a $1 \times 1 \times 2048$ spectrum image), the parallel computing approach (36.4 ms for 30 iterations) is actually consistently slightly slower than the serial approach (35.8 ms for 30 iterations). This is because of the overhead associated with setting up parallel processing. When there is a single spectrum, there is only one serial calculation which needs to be run, as the spectrum image cannot be further divided into independent spectra to be run in parallel. Running the code to split the data into independent threads takes extra time, which is normally compensated for by the improvement in being able to run multiple things at the same time; in the case of a single spectrum, this improvement does not show.

Amdahl's Law

A simple view of the parallelization set-up might imply that the speed-up ought to be eight times faster than serial processing when eight processors are used to run calculations instead of one. This is not the case; adding more processors to the computation introduces a cost associated with the sharing out of the tasks and with using multiple processors to try and access the same memory locations [346]. There are also parts of the code which cannot be parallelized, but must be run in sequence. The additional costs mean that doubling the number of processors used does not double the performance of the system; Amdahl's law allows a rough prediction of the improvements which can be made to the performance by increasing the number of processors used [346]. This not only tells the user how much benefit can be gained from using better hardware, but also tells the developer the relative benefit of optimizing either the serial or the parallel portions of the code.

The RLD, as implemented by SIAn, contains some code which cannot be run in parallel with other code, particularly when using Python, which was not designed for parallel computing. Python possesses a Global Interpreter Lock (GIL), which only allows one Python Interpreter to run at a time; Python code that was written to run in parallel must wait in line for the GIL to become available, so that the Python Interpreter can translate the code to machine instructions. Each process must wait for the GIL to become available, so each process must be interpreted sequentially [347]. The multiprocessing library in Python has ways of working around the GIL restrictions and without these, parallelized code can actually take longer than serially run code because of added time spent inquiring after and waiting for the GIL to become available [347]. NumPy, as mentioned above, translates Python commands into compiled C code, so calculations run in NumPy are free of the restrictions imposed by the GIL and can be parallelized. Some of the other Python functions in the RLD implementation, however, must be run sequentially through the GIL.

Amdahl's Law provides a formula (Equation 6.1) to estimate the optimal speed-up of the code when an infinite number of processors are used for the problem, also

assuming that the problem is infinitely divisible into parallel processes [348]. The code is split into the fraction which must be run serially (ς), and the fraction which can be parallelized (χ) to estimate the performance (τ) improvement when using N_{proc} processing units over the performance when the code is run fully serially (τ_ς). The performance is a measure of instructions evaluated per unit time, so is inversely proportional to runtime [348].

$$\tau = \tau_\varsigma \frac{\varsigma + \chi}{\varsigma + \chi/N_{\text{proc}}} \tag{6.1}$$

Using the runtime data for eight cores ($N_{\text{proc}} = 8$) and for a single core, the amount of time which is spent on parallel code (t_χ) and on serial calculations (t_ς) can be found using the following system of equations (Equation 6.2), in which $t_{\varsigma,\text{tot}}$ is the total time to complete the serial calculations and $t_{\chi,\text{tot}}$ is the total time to complete the parallel calculations. The fraction of time spent on serial calculations is given by $\varsigma = t_\varsigma/t_{\varsigma,\text{tot}}$, and that spent on parallelizable calculations is given by $\chi = t_\chi/t_{\varsigma,\text{tot}}$.

$$t_{\varsigma,\text{tot}} = t_\varsigma + t_\chi \tag{6.2a}$$
$$t_{\chi,\text{tot}} = t_\varsigma + t_\chi/N_{\text{proc}} \tag{6.2b}$$

For both SIAn and HyperSpy, the fraction of time spent on parallelizable calculations (χ) in the serial calculation is approximately $70 - 75\%$ of the total runtime. The fastest either code can be run given an infinite number of CPUs is between 3.3 to 4 times faster than when it is run serially, although the approach to the optimal runtime is asymptotic with the number of additional processors used [348].

For 30 RLD iterations on the $150 \times 150 \times 2048$ spectrum image dataset, the optimal runtime will be approximately 186 seconds in SIAn. This is quite close to the actual runtime of 243 seconds, and adding more processors will not drastically improve the speed of the calculations for the end-user, but will make the calculation approximately one minute faster.

Future efforts to improve the runtime of the RLD algorithm should focus either on increasing the fraction of the program which is parallelizable, for instance by increasing the number of calculations done in NumPy instead of standard Python, thereby reducing the need for the GIL, or by speeding up the serial portion. Reducing the time spent on the serial portion will decrease the runtime for the whole computation by a greater factor than an equivalent speed-up of the parallel component.

6.2.3 Graphical User Interface

SIAn also includes a GUI with which the user can interact with their 3D data (Figure 6.3). The motivation for providing a user interface to navigate the datasets was that current spectrum imaging visualization programs limit the user in terms of the areas which they are allowed to select. DM allows energy slicing and extraction of

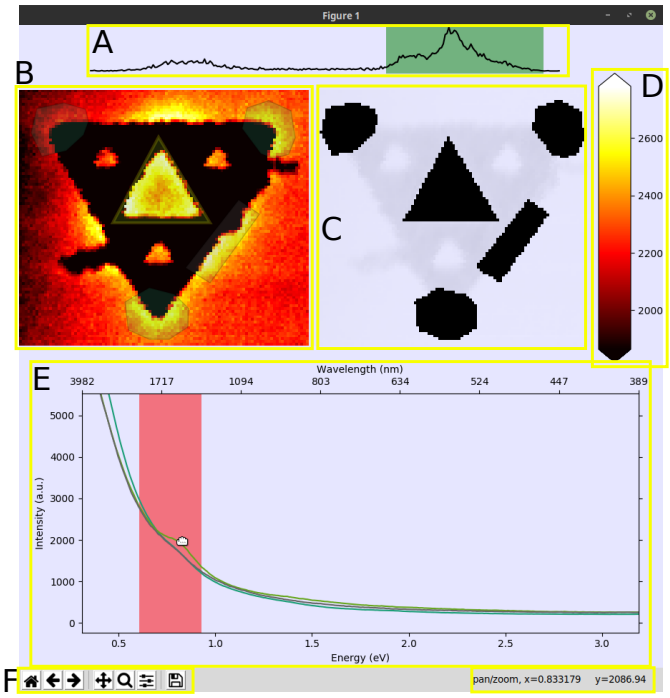

Figure 6.3: Example of the graphical user interface for visual spectrum image analysis and exploration.

spectra over spatial areas, but limits the user to rectangular areas; HyperSpy splits the 3D spectrum image into 2D spatial and 1D spectral dimensions and allows the user to navigate a single pixel at a time in one of these. The SIAn GUI separates the 3D dataset into a 2D image and a 1D spectrum and allows the user to select arbitrary pixels in the image, from which it averages the spectra and displays it or saves it to a CSV file, and to select arbitrary energy ranges, over which it averages the spectral intensity and displays or saves the spatial image.

The GUI is populated by five Matplotlib axes (labelled A-E in Figure 6.3). The image axis (B) shows an image of the two spatial dimensions of the SI. The user can draw patches in this axis of any arbitrary shape with three or more vertices, inside which the spectral pixels will be averaged and displayed as a spectrum in the spectrum axis (E). Multiple different areas can contribute to a single averaged spectrum (the three shapes around the corners of the triangle in (B) contribute to the blue spectrum in (E)), or the user can select different areas to contribute to different spectra (the triangular patch in B contributes to the green spectrum in (E), and the rectangular patch contributes to the gray spectrum in (E)).

The spectrum axis plots the currently active spectra and allows the user to select an energy span, shown by the red rectangle in axis (B), and display the spatial distribution of the peak intensity in the image axis.

The axis (C) to the right of the image axis also shows the spatial image, but is a

static view for the purpose of highlighting to the user which areas of the 2D image are currently being used to plot spectra in the spectrum axis, as the plotted spectra can be toggled on or off, making the corresponding black shapes in (C) appear and disappear.

The third axis in this row, axis (D), shows a colourbar for the image display in axis (B). It shows the numerical colourscale and intensity levels for the image in (B). The colourbar is updated when the colour limits are changed using the histogram in the topmost axis (A).

Axis (A) shows a histogram for the image displayed in the image axis, and can be manipulated to change the contrast limits of the displayed image, as shown by the green highlighted region in Figure 6.3.

The displayed image can be saved along with the colourbar, and the spectrum can be saved along with the specific area from which it was averaged. Currently the user interface is controlled through the use of the mouse and keyboard shortcuts, which are explained on the Github wiki page: `https://github.com/icbicket/SpectrumImageAnalysisPy`.

Two other features in the figure are built into Matplotlib. The box labelled F indicates the window controls, a 'Home' control to reset any view that has been changed; a navigation tool to move backwards and forwards between views of any axis that has been changed since the initialization of the figure window; a pan/zoom tool which allows free panning and zooming on any of the axes A-E with the use of the left and right mouse buttons; a magnification tool which can be used to select and zoom into specific areas of any axis; a subplot adjustment tool to adjust the boundaries of each of the axes in the figure; a save button to save the display; and a status indicator showing the currently selected tool and the coordinates of the mouse cursor in whichever axis it is in (in this figure, the mouse is in the spectrum axis E at 0.833 eV at an intensity of 2086.90).

Although the user interface relies heavily on keyboard shortcuts, it presents a unique way to navigate freely through both the spatial and spectral axes, as well as directly saving the data as seen in the display.

6.3 Conclusions

The software written during the course of this thesis work was written to meet a specific demand for analysis of 3D spectrum imaging EELS datasets. SIAn offers a parallelized implementation of the RLD algorithm, tested against results from other software, and a unique GUI which allows the user full freedom in simultaneously navigating both spatial and spectral dimensions of a spectrum image.

Parallelization of the RLD algorithm has the potential to reduce the execution time by $3.5 - 4\times$. The current improvement in speed in the data presented here is approximately $2.5 - 3\times$. This can be improved using more processing cores, but there

is a limit and it may be more beneficial to refactor the code to decrease the amount of time that must be spent on serial processing.

The SIAn GUI is designed to allow the user the freedom to simultaneously navigate through the spectral dimension and the two spatial dimensions in a spectrum image dataset. The GUI allows arbitrary selection of spatial pixels to average spectra over, and selection of an energy range on the spectrum to obtain and save an energy-filtered map. Currently, the software is programmed to display the appropriate axes for both EELS and CL data, but it is also possible to navigate other 3D datasets using this interface with small adjustments to the appropriate modules.

Chapter 7

Summary and Outlook

7.1 Summary

Over the course of this thesis, the behaviour of planar and non-planar plasmonic nanostructures has been studied using EELS in a monochromated STEM and CL spectromicroscopy in a SEM. Both techniques use a focused electron beam to probe the highly localized near-fields of plasmonic nanostructures.

In the Sierpiński fractal structure (Chapter 3), the coupling and interaction of LSPR modes within the structure is shown to cause spectral shifts or changes to the electric field configuration. The fractal antenna, useful for its multiband properties in the radio and microwave spectral regime, shows similar properties when scaled down to the nanoscale. By breaking down the fractal structure into its component parts and by using the Babinet principle, the equivalent circuit model, and hybridization theory, the behaviour of the primary mode and many of the higher order modes can be explained. The plasmonic behaviour of the Sierpiński fractal is driven by the coupling of in-plane electric multipole moments. For instance, the electric dipole mode of the aperture couples to the electric dipole mode of the solid triangle, and causes an energy shift in the dipolar peak. The aperture also affects higher order LSPR modes of the triangular prism: when the aperture is placed on a node of the LSPR pattern, the energy of the LSPR peak changes; and when the aperture is placed on an anti-node in the LSPR, the surface charge distribution changes to accommodate the aperture, thereby changing the electric field configuration.

Using a double-step EBL process, a non-planar vertical split ring resonator (Chapter 4) was fabricated. The LSPR modes of the VSRR are studied with both EELS and CL, retrieving information on the near-field and far-field properties of the magnetic dipole mode and higher order modes. The magnetic dipole mode is in the infrared spectrum and is challenging to study with current CL techniques, but by modifying the acquisition settings, the polarization state of this mode can be retrieved as a function of electron beam location. Modelling of the emission from this dipole mode indicates that the phase delay and magnitude ratio of the emitted fields between the

magnetic dipole and orthogonal electric dipole can be retrieved using the polarization properties of the CL emission. The vertical orientation of the VSRR emphasizes a different set of modes compared to the more standard planar SRR, and instead of the higher order SRR modes expected from literature, a set of hybridized longitudinal and transverse dipolar modes on the rims of the VSRR pillars are emphasized.

The vertical orientation of the SRR means that its magnetic dipole mode can be easily coupled to other nearby VSRRs. Chapter 5 discusses the coupling of four VSRRs to produce a low energy magnetic dipole mode and a higher energy toroidal dipole mode, both of which are identified through EELS studies. Tilting the sample under electron beam excitation shows a different point of view of the 3D electric fields surrounding these complex non-planar structures. As with the isolated VSRR, CL reveals that the higher order modes in the visible regime of the spectrum are dominated by hybridized dipole modes on the rims of the vertical pillars.

Finally, Chapter 6 describes a Python program written to analyze and visualize EELS and CL spectrum imaging data. Inside this code, the Richardson-Lucy deconvolution algorithm is parallelized to improve the runtime of this algorithm by approximately 3.5× over running the algorithm on a single processor. The Python program also encodes a unique graphical interface for navigating 3D spectrum imaging datasets with greater freedom than is currently provided by other software. This code is open-source and available for use on Github [183].

7.2 Outlook

EELS is a powerful tool for characterization of the near-field response of plasmonic nanostructures with high spatial and energy resolution. Recent advances in instrumentation make even lower energy regions of the electromagnetic spectrum accessible with EELS, down to the mid-IR. Combining EELS studies with electron beam lithography to fabricate customized nanostructures allows the user to study the fundamental behaviour of LSPR modes, thereby developing the toolbox required for intelligent design of plasmonic nanostructures geared towards specific applications.

Cathodoluminescence collects the far-field radiation from radiative LSPR modes with similar nanoscale spatial resolution to EELS. CL is a strong complement to EELS in the characterization of LSPR modes and can provide additional information on the multipole behaviour of each resonance inside the nanostructure. The information about far-field radiation also gives an indication of the behaviour of a nanostructure under optical illumination.

7.2.1 Extensions of the Thesis Work

For each of the chapters in this thesis, there remain unanswered questions or follow-up questions which arose during the study. The following sections describe some of these questions and suggest directions for future work.

Fractals

Further extensions to the work on Sierpiński fractals could include the study of the far-field response of the fractal structures or the application of the fractal as a multiband sensing platform. It would also be interesting to confirm the predicted behaviour of the LSPR modes (*i.e.* in terms of spectral shifts and electric field distributions) after addition of an aperture to a non-fractal structure.

Although there appears to be a qualitative agreement of the behaviour of complementary plasmonic nanostructures with the predictions of the Babinet principle, it is known that the Babinet principle was derived for far-field properties and requires specific polarization configurations for use with antennas. Some open questions remain on how accurately a technique such as EELS, which is polarization-insensitive and probes the near-field, not the far-field, can be used to comment on the applicability of the Babinet principle to LSPR.

Split Ring Resonators

Future work on the VSRRs could include time-resolved simulations to study the dynamics between the emission from the magnetic dipole and electric dipoles of the lowest energy LSPR mode. The magnetic and electric dipoles of these modes rely on flowing current and stationary charges, respectively, and the far-field interference of the radiation from these modes could provide an interesting avenue to retrieve information on the femtosecond-scale dynamics of the LSPR mode. Angle-resolved experiments in the IR would be very beneficial to this goal, given the dependence of the angle-resolved polarization state on the phase delay and magnitude ratio of the dipole pair.

There may also be some interesting opportunities in studying the physics of LSPR behaviour with off-axis electron beam excitation. Placing the electron beam away from a symmetry axis in the nanostructure changes the emission behaviour of the plasmon mode by modifying the angular distribution and polarization distribution of the emitted radiation.

Toroidal Dipole Moments

The toroidal dipole moment is anticipated, through literature review, to have interesting optical properties, such as circular dichroism or enhanced second harmonic generation (SHG). Future experiments on the T4 array of VSRRs should involve optical polarization experiments or SHG experiments to confirm these properties of the toroidal dipole.

Two new structures which have the potential to produce a toroidal dipole moment have been proposed in this thesis (T5 and T6 arrays). More studies remain to be done to determine the multipolar scattering properties of these structures. In particular, a multipolar decomposition performed on the scattering spectrum of each of the toroidal

arrays studied here would reveal the effect that changing the symmetry properties of the toroidal array has on the radiated multipole moments. Even if the toroidal dipole moment proves to be weak in the T5 and T6 structures, these arrangements of VSRRs may provide an interesting avenue towards accessing higher order electric or magnetic multipole moments. Additional simulations or optical experiments on the T5 and T6 structures would also be beneficial to unravel the EELS response of these nanostructures.

Python Coding

Coding of a software program is a virtually endless task: there are always improvements to be made in the reliability, usability, and performance of a software. Improvements include adding more tests on individual functions and extending the documentation. Further extensions to SIAn could open up its use for x-ray spectromicroscopy or other 3D spectromicroscopy techniques, as well as adding data processing functionality for other algorithms which are commonly used for EELS or CL datasets, including peak-fitting and background extraction.

7.2.2 Expanding Horizons

CL holds great promise towards unravelling plasmon behaviour, particularly in its ability to derive the angular emission profile and polarization state of emitted radiation. The interference of different multipole moments inside a plasmonic nanostructure changes the radiation patterns and can give insight on plasmon dynamics without the need for ultra-fast femtosecond experiments. As the knowledge base for CL grows, the technique can be applied to more and more complex structures to derive the multipolar composition of LSPR modes and the interaction of LSPR modes with far-field radiation.

Advances in EELS resolution [41] have pushed the lowest detectable energy into the mid-IR, allowing the detection of phonon polariton modes in ionic or dielectric nanostructures. It is also now possible to detect plasmon resonances even further down the dispersion curve, with more delocalized fields and longer propagation distances. As the energy of the plasmon decreases, it behaves more and more like light trapped on an interface, and experiments can come closer and closer to probing light in the electron microscope.

Another field opening up in plasmonics is the study of semiconductor materials. High levels of doping in semiconductors can be used to add enough free charge carriers to support LSPR in nanoparticles [349, 350]. The ability to control the free electron density through the doping level and band structure manipulation provides many new opportunities for the manipulation and study of plasmon behaviour. Future interesting work in this field might include studying the evolution of LSPR behaviour as a sample is cooled or heated. The number of free carriers in a semiconductor depends on temperature and the thermal energy required to promote electrons across

the bandgap, and so the plasmon response can change as a function of temperature in semiconductor nanostructures. The field of semiconductor plasmonics is still relatively new and there are many different properties to be explored in this field, including thermal behaviour, plasmon scattering off dopants or defects, differences in n- and p-type dopants, and the relationship with the effective mass of the charge carrier or with anisotropic band structures. All of these properties have the potential to be manipulated with semiconductor plasmonics.

An interesting concept, particularly suited to high resolution EELS, is the creation and study of a pn-junction from highly doped plasmonically active materials: can such a structure support a plasmon mode across the whole device, or does the depletion zone of the junction affect the behaviour? How is the plasmon behaviour affected by the presence of two opposite kinds of majority and minority charge carriers on either side of the junction?

Another interesting field that could make use of the high spatial resolution of the electron microscope is the field of atomic-scale plasmonics on few-atom clusters. Density functional theory calculations have shown resonance modes across few-atom clusters [351], in which the electronic density of states is discretized and cannot be treated as continuum bands. High resolution EELS could be used to study the collective electron behaviour in metallic nano-clusters as the electronic density of states evolves from discrete atomic orbitals to continuous metallic bands with increasing numbers of atoms in a cluster to answer some of the fundamental questions in plasmonics.

How many electrons does it take to make a plasmon?

Appendix A

Polarization Properties of Light

This appendix describes the polarization properties of light using the Stokes parameters. Some examples of the angular-resolved (AR) polarization patterns from analytical dipole moments are given, as well as some examples of spatially-resolved and AR Stokes parameters from cathodoluminescence (CL) simulations of basic plasmonic nanoantennas. Calculations of the Stokes parameters from electric field vectors were performed using custom Python software [192].

A.1 Polarization

The polarization of an oscillating electromagnetic (EM) plane wave refers to the direction and magnitude of the electric field vector over time at a fixed point in space [103, 352], or to the direction of vibration of the electric field component [353] at a given observation point in the far-field. The electric field vector is decomposed into two orthogonal components, both perpendicular to the propagation direction.

When spherical coordinates are used, the intuitive choices for the two orthogonal directions are the angular spherical coordinates, $(\hat{\boldsymbol{\theta}}, \hat{\boldsymbol{\phi}})$, resulting in an electric field vector decomposed as $\boldsymbol{\varepsilon} = \varepsilon_\theta \hat{\boldsymbol{\theta}} + \varepsilon_\phi \hat{\boldsymbol{\phi}}$ [103]. The radial component is negligible in the far-field [103]. The polarization state is described in terms of pairs of orthogonal vectors: linearly polarized (horizontal and vertical, or 45° and 135°) or circularly polarized (right-handed circular (RHC) and left-handed circular (LHC)) (Figure A.1(b)).

In general, a plane wave can be described as elliptically polarized. A polarization ellipse is used to describe the shape traced by the electric field vector of the light as a function of time and space (Figure A.1(a)) [99, 352]. Linear polarized light and circularly polarized light are special cases of elliptically polarized light. The electric field vector of linearly polarized light is stationary in time at a fixed ratio of two orthogonal linear components. For RHC and LHC polarized light, one of the two orthogonal components has a phase delay of $\pi/2$ relative to the other [99, 103].

Unfortunately, the physics communities and engineering communities have differ-

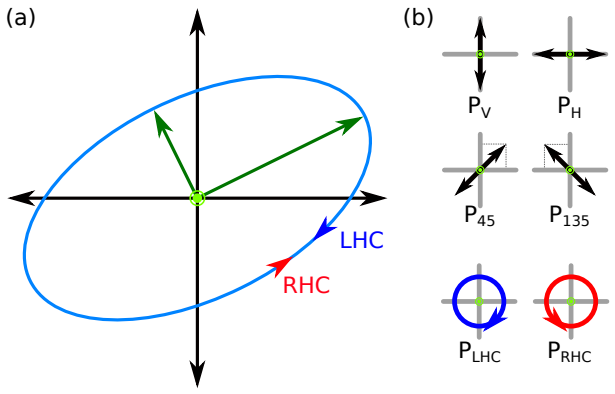

Figure A.1: Polarization states of light. (a) Polarization ellipse traced out by the electric field vector of an arbitrary photon over time, the direction determines the handedness of the polarization; (b) orthogonal polarization states, light is propagating out of the page in all cases.

ing definitions of circularly polarized light. In the optics and physics community, RHC polarization is defined as light with an electric field vector which rotates clockwise when the light is propagating towards the observer; electric fields rotating counterclockwise when propagating towards the observer are LHC [99, 353]. On the other hand, in the engineering community, the standard is that when the light is propagating away from the user, RHC light rotates clockwise and LHC rotates counterclockwise, such that when the thumb on the right hand points in the direction of propagation, the fingers curl in the direction of rotation for RHC polarized light, and likewise for the left hand and LHC light [104,352]. To maintain coherency with current literature on light emission from plasmonic nanoantennas (*e.g.* [150]), the convention defined by the IEEE is used in this thesis [104].

Poincaré Sphere

The Poincaré sphere is used to represent the polarization vectors of light (Figure A.2). Linearly polarized states are present on the equator, LHC and RHC are the north and south poles, respectively, in the IEEE convention; all states in between represent elliptically polarized states [99, 104]. Degenerate polarizations are present across the diameter of the sphere from each other [99]. Along one equatorial axis, vertically polarized light and horizontally polarized light are across from each other, while 45° and 135° linear polarizations define the orthogonal axis in the equatorial plane [99].

The position along the radius of the Poincaré sphere defines the degree of polarization (DoP); fully polarized light (DoP = 1) is present on the surface of the sphere; partially polarized light is described by points along the radius of the sphere (DoP < 1). If the wave is totally unpolarized, then there is no coherent amplitude or phase relationship between two orthogonal independent vector components, and the light is represented by the origin of the Poincaré sphere [99]. A beam of unpolarized

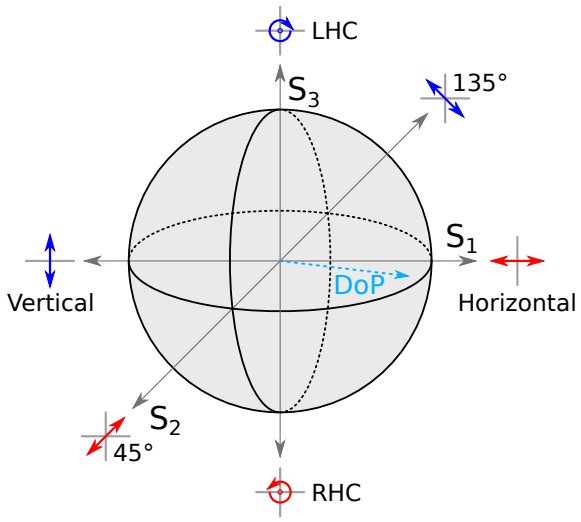

Figure A.2: Poincaré sphere. Points in the northern hemisphere represent elliptical left-handed circular (LHC) polarization; points in the southern hemisphere represent elliptical right-handed circular (RHC) polarization states. The north and south poles represent purely LHC and RHC polarized states, respectively. All linear polarization states are defined by points on the equator. Points on the surface of the sphere represent fully polarized light; points inside the sphere represent partially polarized light, according to the degree of polarization (DoP).

light can be decomposed into any two degenerate polarization states, but there is no coherent relationship and both states are independent of each other [99].

Experimentally, it is not practical to try and measure the evolution of the electric field vector over time; the necessary timescale is extremely fast and realistically all measurements must necessarily be time-averaged [99]. A practical way to define the polarization of light from measured quantities uses the Stokes parameters [99].

A.1.1 Stokes Parameters

The Stokes parameters (S_0, S_1, S_2, S_3) are a way of defining Cartesian axes on the Poincaré sphere (Figure A.2). S_1, S_2, and S_3 are three vectors which fully define the Cartesian location of a polarization state on the surface of the sphere, while S_0 defines the amplitude of the light, represented as the radius of the sphere [99, 353]. The four Stokes parameters are defined as follows.

- S_0: the intensity of the beam
- S_1: the difference in intensity between horizontally and vertically polarized light
- S_2: the difference in intensity between light polarized at 45° and at 135°
- S_3: the difference in intensity between RHC and LHC polarized light

If the light is fully polarized, the relationship between the Stokes parameters is given in Equation A.1a; for partially polarized light the relationship is given by Equation A.1b. For completely unpolarized light, S_1, S_2, and S_3 are all 0 and the radiation state is at the centre of the Poincaré sphere [99, 354]. Normalizing the sphere radius to S_0 makes the radius into the degree of polarization [354].

$$S_0{}^2 = S_1{}^2 + S_2{}^2 + S_3{}^2 \tag{A.1a}$$

$$S_0{}^2 > S_1{}^2 + S_2{}^2 + S_3{}^3 \tag{A.1b}$$

The DoP is defined by Equation A.2 and defines the fraction of light which is polarized (*i.e.* has a coherent phase and amplitude relationship between two orthogonal electric field vector components) [99]. The polarization of light can also be separated into the degree of linearly polarized light (DoLP) (Equation A.2b) and the degree of circularly polarized light (DoCP) (Equation A.2c) [355]. Fully polarized light has DoP = 1, while fully unpolarized light has DoP = 0 [99].

$$\text{DoP} = \frac{I_{\text{pol}}}{I_{\text{tot}}} = \frac{\sqrt{S_1{}^2 + S_2{}^2 + S_3{}^2}}{S_0}, 0 \leq \text{DoP} \leq 1 \tag{A.2a}$$

$$\text{DoLP} = \frac{\sqrt{S_1{}^2 + S_2{}^2}}{S_0} \tag{A.2b}$$

$$\text{DoCP} = \frac{S_3}{S_0} \tag{A.2c}$$

Considering a plane wave propagating along the z-axis in Cartesian coordinates, with x and y the two orthogonal axes on which to define the electric field vector ($\boldsymbol{\varepsilon} = \varepsilon_x \hat{\boldsymbol{x}} + \varepsilon_y \hat{\boldsymbol{y}}$), the Stokes parameters form the Stokes vector, given by Equation A.3 [99]. In this equation, ε_{0x} and ε_{0y} are the electric field vectors of the light projected along the x and y axes and δ is the phase delay between the two orthogonal x and y components.

$$\boldsymbol{S} = \begin{pmatrix} S_0 \\ S_1 \\ S_2 \\ S_3 \end{pmatrix} = \begin{pmatrix} \varepsilon_{0x}^2 + \varepsilon_{0y}^2 \\ \varepsilon_{0x}^2 - \varepsilon_{0y}^2 \\ 2\varepsilon_{0x}\varepsilon_{0y}\cos(\delta) \\ -2\varepsilon_{0x}\varepsilon_{0y}\sin(\delta) \end{pmatrix}, \delta = \delta_y - \delta_x \tag{A.3}$$

If the ε_x and ε_y vectors are expressed by Equation A.4, the Stokes vector can be transformed into a function of the electric fields and their complex conjugates, transforming Equation A.3 into the equivalent Equation A.5 [99].

$$\begin{pmatrix} \varepsilon_x(t) \\ \varepsilon_y(t) \end{pmatrix} = \begin{pmatrix} \varepsilon_{0x}\exp(i\delta_x) \\ \varepsilon_{0y}\exp(i\delta_y) \end{pmatrix} \tag{A.4}$$

$$\begin{pmatrix} S_0 \\ S_1 \\ S_2 \\ S_3 \end{pmatrix} = \begin{pmatrix} \varepsilon_x\varepsilon_x^* + \varepsilon_y\varepsilon_y^* \\ \varepsilon_x\varepsilon_x^* - \varepsilon_y\varepsilon_y^* \\ \varepsilon_x\varepsilon_y^* + \varepsilon_y\varepsilon_x^* \\ -i(\varepsilon_x\varepsilon_y^* - \varepsilon_y\varepsilon_x^*) \end{pmatrix} \tag{A.5}$$

However, regarding the far-field radiation from antennas, it is often preferable to work in spherical coordinates. The Stokes parameters given in Equation A.5 are relatively simply transformed to spherical coordinates by making the substitutions $\varepsilon_x \rightarrow \varepsilon_\theta$ and $\varepsilon_y \rightarrow \varepsilon_\phi$, giving Equation A.6 [99]. The linear polarization direction vectors in spherical coordinates are visualized on the surface of a hemisphere in Figure A.3.

$$\begin{pmatrix} S_0 \\ S_1 \\ S_2 \\ S_3 \end{pmatrix} = \begin{pmatrix} \varepsilon_\theta\varepsilon_\theta^* + \varepsilon_\phi\varepsilon_\phi^* \\ \varepsilon_\theta\varepsilon_\theta^* - \varepsilon_\phi\varepsilon_\phi^* \\ \varepsilon_\theta\varepsilon_\phi^* + \varepsilon_\phi\varepsilon_\theta^* \\ -i(\varepsilon_\theta\varepsilon_\phi^* - \varepsilon_\phi\varepsilon_\theta^*) \end{pmatrix} \tag{A.6}$$

The key benefit to using the Stokes parameters rather than the polarization ellipse to describe the polarization state of radiation is that the Stokes parameters are measurable quantities and can be determined by a set of independent measurements.

A.1.2 Measuring the Stokes Parameters

To measure the Stokes parameters, there are a variety of different methods [355]. One of the most straightforward is to acquire six different polarization states by performing six different measurements of the same radiation. To do this, a quarter wave plate (QWP) and a linear polarizer (LP) are used to create what is effectively a rotating polarimeter before the emitted light hits the detector [99, 150, 356].

The QWP is a birefringent, uniaxial material which introduces a phase shift between two orthogonal components of the electric field [353]. EM waves travel with different velocities along the different axes of the QWP, introducing an effective path difference of one quarter of the wavelength ($\lambda/4$) and resulting in phase retardation of one vector component relative to the other by $\pi/2$. This partial phase delay changes the polarization state of light and will, for example, transform light which is linearly polarized at 45° into RHC polarized light, or circularly polarized light into linearly polarized light.

The beam of light is then passed through a linear polarizer, which has different absorption coefficients along different axes of the material, so will preferentially absorb one of the orthogonal components of the light's electric field vector [99, 353]. The LP produces linearly polarized light and will linearly polarize unpolarized light, transmitting half of it according to the polarization axis of the LP [353].

The QWP changes the phase of the light, while the LP manipulates the amplitude; both are used in tandem to make a set of six measurements at different relative

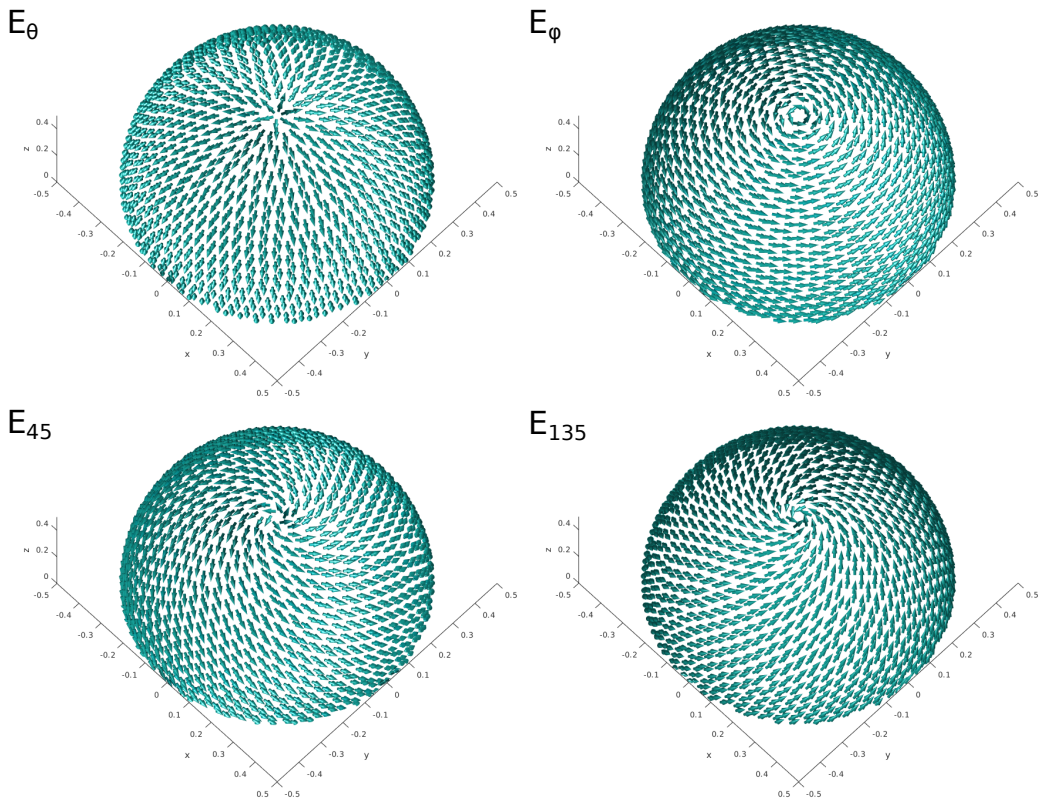

Figure A.3: Visualization of the direction vectors of linearly polarized light in spherical coordinates. Top row: direction vectors of ε_θ and ε_ϕ; bottom row: direction vectors for ε_{45° and ε_{135° polarized light.

rotation angles defined in Equation A.7 [99, 355]. Each of the Stokes parameters is given by a different measurement, as shown on the right-hand side, in which the subscripted numbers indicate the rotation angle of the QWP or LP in degrees.

$$\begin{pmatrix} S_0 \\ S_1 \\ S_2 \\ S_3 \end{pmatrix} = \begin{pmatrix} I_\mathrm{H} + I_\mathrm{V} \\ I_\mathrm{H} - I_\mathrm{V} \\ I_{45} - I_{135} \\ I_\mathrm{RHC} - I_\mathrm{LHC} \end{pmatrix} = \begin{pmatrix} (\mathrm{QWP}_{270}, \mathrm{LP}_{90}) + (\mathrm{QWP}_0, \mathrm{LP}_0) \\ (\mathrm{QWP}_{270}, \mathrm{LP}_{90}) - (\mathrm{QWP}_0, \mathrm{LP}_0) \\ (\mathrm{QWP}_{45}, \mathrm{LP}_{135}) - (\mathrm{QWP}_{315}, \mathrm{LP}_{45}) \\ (\mathrm{QWP}_{270}, \mathrm{LP}_{135}) - (\mathrm{QWP}_{270}, \mathrm{LP}_{45}) \end{pmatrix} \tag{A.7}$$

The QWP is only necessary to measure RHC and LHC polarized light. Determination of the linear polarization state of light by measurement of S_1 or S_2 requires only the LP, but the QWP is included in the ray path for the other measurements because it will absorb some fraction of the light, which must be accounted for in order to quantifiably compare the linearly polarized measurements with the circularly polarized measurements.

Other than the QWP and LP, the radiation after emission from the luminescing sample encounters other components which may change its polarization state before

it reaches the detector. The evolution of the electric field vectors traversing the collection system can be described with the Mueller matrix formalism, which describes the evolution of the polarization state using linear transformation matrices [353]. The Mueller matrix of each component is known or measured [150] and the polarization state of the collected light can be derived by reversing the linear transformations that the light has undergone by passing through the system.

The polarization state to be measured is set by the (QWP, LP) pair, so any optical components after this pair are unimportant regarding the polarization state. However, the polarization state may be changed before reaching the polarimeter set-up. In a CL experiment, the two components in between the emitting sample and the (QWP, LP) pair are the parabolic mirror used to collect emitted radiation, and the window in between the vacuum chamber of the SEM and the optical system. The window is not expected to change the polarization state of the light, but the parabolic mirror is known to affect the polarization of incident light upon reflection [185]. The reflection properties of the mirror depend on its complex Fresnel reflection coefficients, which in turn depend on both the angle of incidence and the polarization state of the incident light [150,185]. It is possible to calculate how the mirror changes the polarization state of light (the mirror's Mueller matrix) through knowledge of the Fresnel reflection coefficients of aluminium and the geometrical equation of the parabolic mirror, as explained by Coenen and Polman [185].

When performing AR polarimetry measurements, it is possible to fully calculate the polarization state at each point on the acquired image of the mirror or, by simulating the dipole moments, calculate the expected AR pattern by applying the appropriate Mueller matrix to the simulated radiation.

However, when performing spectral measurements, all light bouncing off the CL mirror is channelled into a fibre optic cable and dispersed in the spectrometer, with no knowledge of how much light reflected from which parts of the mirror. As a result, when doing polarized spectroscopic measurements, it is not possible to simply apply the Mueller matrix of the mirror (a function of incidence angle) to retrieve the polarization state on the sample. Instead, a 3 mm slit is introduced before the (QWP, LP) pair to block light reflecting from the sides of the mirror before it enters the optical set-up [185]. Light impinging the centre parts of the mirror has an angle of incidence close to the normal of the mirror surface. At this angle, the modification of the polarization state is negligible, whereas light impacting the sides of the mirror is incident at a greater angle and there is a greater modification to the polarization state of the light [185, 357].

The presence of the 3 mm slit, aligned to the centre of the mirror, improves the polarization contrast and the accuracy of the spectroscopic results [185]. A narrower slit may offer improved polarimetry accuracy, but narrowing the slit reduces the amount of light which is collected and reduces the signal to noise ratio; a 3 mm slit width is the balance between obtaining good signal and improving the polarization contrast [185]. The 3 mm slit is used in all acquisitions of polarized spectroscopic data.

Interpretation of polarimetry data is not trivial, and to fully understand the polarization state of the sample, it is beneficial to compare the experimental data with analytical or simulated radiation fields. The following sections describe the analytical dipole models and some simple simulation cases.

A.2 Analytical Dipole Radiation Patterns

At far enough distances, when the emitted spherical wavefronts appear almost flat, the far-field radiation from an antenna behaves like a plane wave [104] and therefore the antenna radiation can be described by terminology applicable to plane waves. The polarization of the wave is one such property of plane waves that is used to describe far-field radiation. The polarization may vary according to the direction of emission from the centre of the antenna; the polarization pattern describes the spatial distribution of polarization vectors over the radiation sphere of the antenna [103].

In the following sections, the analytical expressions for a pure electric and pure magnetic point dipole are used to calculate the radiation patterns for these cases. The orientation of the electric and magnetic dipoles will be altered to demonstrate how this affects the polarization distribution and interpretation of the CL results. Further examples of dipole or quadrupole emission patterns can be found in, for example, [167,358,359]. Importantly, plotting these ideal cases reveals how the choice of coordinate axes and dipole orientation affects the polarimetry results. The radiated far-field is calculated along evenly spaced (θ, ϕ) spherical coordinates to retrieve the angular emission of each analytical dipole or pair of dipoles. Figure A.4 shows the coordinate systems used for spherical coordinates and angular resolved plots of the Stokes parameters, including a visualization of the linearly polarized Stokes parameters on an AR plot, akin to the 3D plots shown in Figure A.3.

The radiative fields from an electric point dipole and those from a magnetic point dipole are very similar to each other. Duality between electric and magnetic fields means that with the substitutions given in Table A.1, the fields of an electric or magnetic source can be derived knowing those of the equivalent magnetic or electric source [86].

A.2.1 Electric Dipole

The electric and magnetic radiation fields from a linear oscillating electric point dipole ($\boldsymbol{p}$) are described by Equation A.8 [86]. In these expressions, $\boldsymbol{\varepsilon}$ and $\boldsymbol{H}$ are the electric and magnetic fields, respectively; ϵ_0 is the electric permittivity in vacuum; $i = \sqrt{-1}$ is the imaginary number; k is the wavevector of the radiation; ω the frequency of oscillation; $\boldsymbol{r}$ is the vector from the source to the observer; $r = |\boldsymbol{r}|$ is the scalar distance between the source and observer; $\hat{\boldsymbol{r}} = \boldsymbol{r}/r$ is the unit vector along $\boldsymbol{r}$; and the Green's function, $\mathrm{G}(\boldsymbol{r}) = \frac{\exp(-ikr)}{4\pi r}$ is the solution to the single frequency wave equation [86].

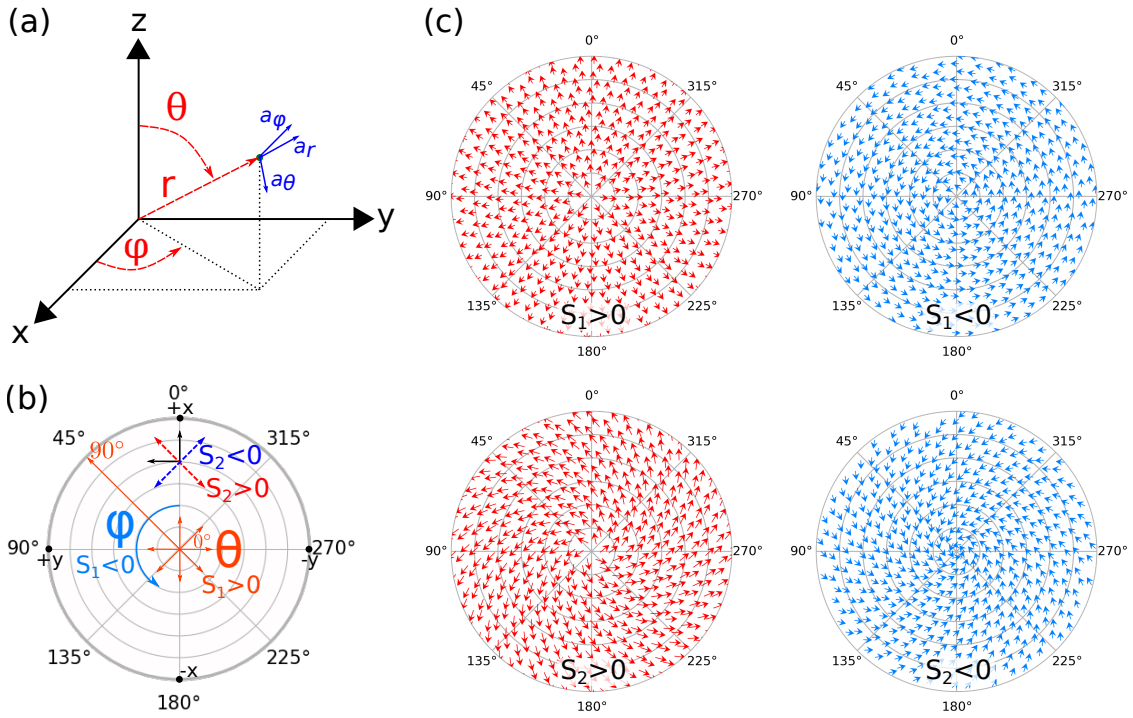

Figure A.4: Reference for the spherical and angular coordinate systems used. (a) Spherical coordinate system; (b) mapping of spherical coordinates onto the AR polar plot and definitions of the Stokes parameters on this plot; (c) AR plot visualization of the direction vectors corresponding to pure linear polarization along ε_θ ($S_1 > 0$), ε_ϕ ($S_1 < 0$), ε_{45} ($S_2 > 0$), and ε_{135} ($S_2 < 0$)), similarly to Figure A.3.

$$\boldsymbol{\varepsilon}(\boldsymbol{r}) = \overbrace{\frac{1}{\epsilon_0}\left(ik + \frac{1}{r}\right)\left(\frac{3\hat{\boldsymbol{r}}(\hat{\boldsymbol{r}}\cdot\boldsymbol{p}) - \boldsymbol{p}}{r}\right)\mathrm{G}(\boldsymbol{r})}^{\text{near-field}} + \overbrace{\frac{k^2}{\epsilon_0}\hat{\boldsymbol{r}}\times(\boldsymbol{p}\times\hat{\boldsymbol{r}})\,\mathrm{G}(\boldsymbol{r})}^{\text{far-field}} \tag{A.8a}$$

$$\boldsymbol{H}(\boldsymbol{r}) = i\omega\left(\underbrace{ik}_{\text{far-field}} + \underbrace{\frac{1}{r}}_{\text{near-field}}\right)(\boldsymbol{p}\times\hat{\boldsymbol{r}})\,\mathrm{G}(\boldsymbol{r}) \tag{A.8b}$$

Equation A.8 describes both the near- and far-fields coming off the oscillating dipole. All of the terms which fall off faster than $1/r$ are near-field components, while the far-field components are those terms which are proportional to $1/r$. In the far-field, the surface area of the surrounding sphere changes with r^2; the intensity, or power, of the EM field is proportional to $|\boldsymbol{\varepsilon}|^2$, so those components of the electric field which fall off with $1/r$ have constant power as r increases, and only these components contribute to far-field radiation [86, 104]. As the distance (r) from the antenna increases, the outward propagating wavefronts look increasingly flatter and flatter, until at sufficiently far distance from the source, they are treated as plane waves [104].

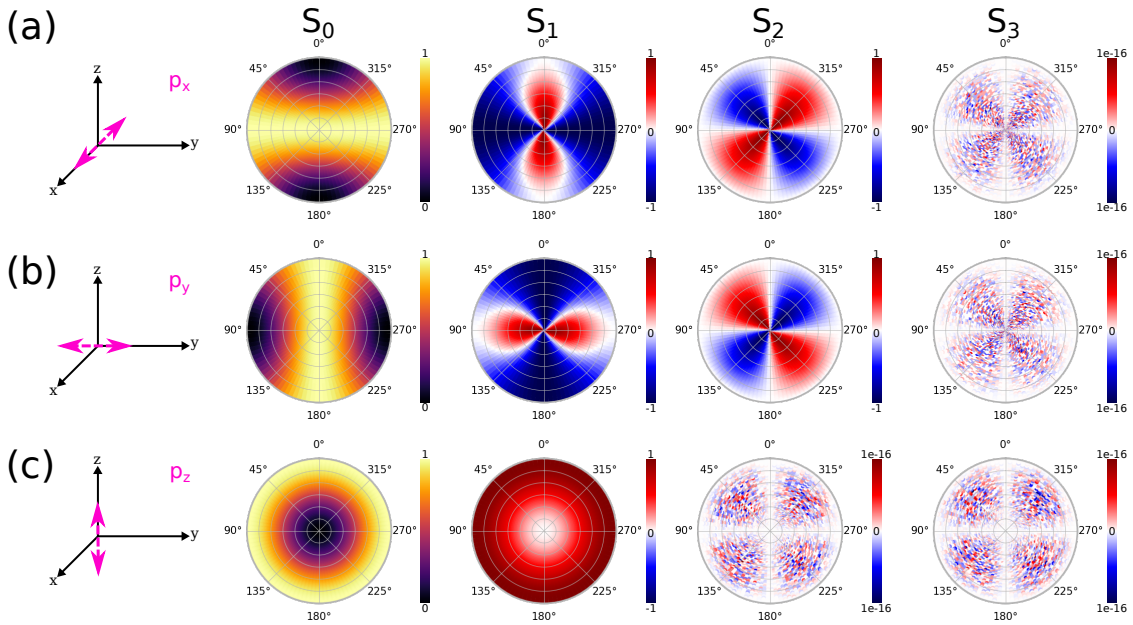

Figure A.5: AR Stokes parameters for an ideal electric dipole oriented along (a) x-axis, (b) y-axis, (c) z-axis. The left column shows the dipole orientation.

The far-field radiation of the electric point dipole is linearly polarized along the same axis as the dipole vector. The Stokes parameters of the radiation fields for an electric point dipole oriented along each of the x, y, and z axes are plotted in Figure A.5 as a function of the angle of emission, for the upper hemisphere ($z > 0$).

Most of the radiation for an electric point dipole is emitted perpendicularly to the dipole vector, with polarization parallel to the dipole vector. For a dipole oriented along the z-axis ($\boldsymbol{p}_z$), the ε_r and ε_ϕ components are negligible and the fields are wholly polarized along the z (θ) direction. A z-oriented dipole has also been studied experimentally by Coenen *et al.* [149] and Coenen and Polman [185]. Differences between the AR patterns in the literature and those calculated here are explained by

Table A.1: Exchangeable components of the electric and magnetic source equations

Electric Dipole	Magnetic Dipole
$\boldsymbol{\varepsilon}$	$\boldsymbol{H}$
$\boldsymbol{H}$	$-\boldsymbol{\varepsilon}$
ϵ_0	μ_0
μ_0	ϵ_0
η_0	$1/\eta_0$
$\boldsymbol{p}$	$\mu_0 \boldsymbol{m}$

the presence of a reflective substrate in the literature study, which modifies the angular emission pattern. Other than differences caused by the substrate, the analytically calculated radiation pattern agrees very well with experimental patterns.

If the electric dipole is in-plane (Figure A.5(a,b): $\boldsymbol{p}_x$ or $\boldsymbol{p}_y$), the dipole moment is no longer aligned with the zenith axis of the spherical coordinate system (z) and the Stokes parameters appear very different from the $\boldsymbol{p}_z$ case (Figure A.5(c)). In studies of antennas, there is some freedom in defining the zenith axis of the spherical coordinate system as convenient for the geometry and dipole moment of the antenna. In the case of CL, however, the zenith axis is aligned with the electron beam propagation direction. This allows the mirror and electron beam to be described in a fixed coordinate system which doesn't change depending on the sample, but can make the polarimetry patterns more challenging to interpret. The $\boldsymbol{p}_x$ and $\boldsymbol{p}_y$ dipoles in Figure A.5(a,b) are both purely linearly polarized along x and y, respectively, but because θ and ϕ are defined using z as the zenith axis, the S_1 pattern has different signs and the S_2 pattern is non-zero, unlike the angular emission from $\boldsymbol{p}_z$.

The S_1 and S_2 patterns make sense considering the orientation of electric field vectors over the radiation sphere. For example, considering a point on the y axis ($\theta = \pi/2, \phi = \pi/2$), the electric field from $\boldsymbol{p}_x$ is primarily oriented along the x axis, which at this point is parallel to ϕ and perpendicular to θ (see Figure A.4(b)). S_1 in spherical coordinates is the difference in intensity between light polarized along θ and light polarized along ϕ and at this point, the emission is dominated by ε_ϕ: S_1 is negative. At another point ($\theta = \pi/4, \phi = 0$), the electric field is still polarized along x, but the Cartesian x-axis is aligned with the spherical θ axis and perpendicular to the ϕ axis, so S_1 is dominated by light polarized along θ and is positive. Rotating the electric dipole in-plane rotates the radiation pattern by the same angle, as observed by comparing the angular emission plots for $\boldsymbol{p}_x$ and $\boldsymbol{p}_y$.

A.2.2 Magnetic Dipole

For an oscillating magnetic point dipole at the origin, the electric and magnetic fields are given by Equation A.9 [86]. In these equations μ_0 is the vacuum permeability; and $\boldsymbol{m}$ is the magnetic dipole moment; the other variables represent the same quantities as in Equation A.8.

$$\boldsymbol{\varepsilon}(\boldsymbol{r}) = -i\omega\mu_0\left(\overbrace{ik}^{\text{far-field}} + \overbrace{\frac{1}{r}}^{\text{near-field}}\right)(\hat{\boldsymbol{r}} \times \boldsymbol{m})\,\mathrm{G}(\boldsymbol{r}) \tag{A.9a}$$

$$\boldsymbol{H}(\boldsymbol{r}) = \underbrace{\left(ik + \frac{1}{r}\right)\left(\frac{3\hat{\boldsymbol{r}}(\hat{\boldsymbol{r}} \cdot \boldsymbol{m}) - \boldsymbol{m}}{r}\right)\mathrm{G}(\boldsymbol{r})}_{near-field} + \underbrace{k^2\hat{\boldsymbol{r}} \times (\boldsymbol{m} \times \hat{\boldsymbol{r}})\,\mathrm{G}(\boldsymbol{r})}_{\text{far-field}} \tag{A.9b}$$

Similarly to the case of the analytical electric point dipole, the electric fields of

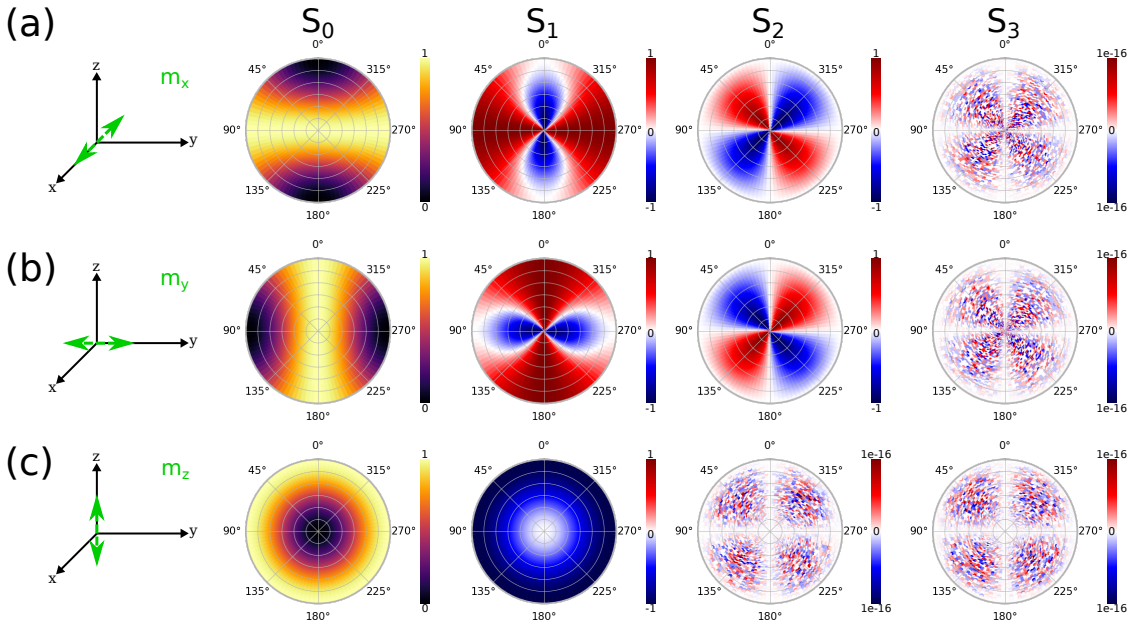

Figure A.6: AR Stokes parameters for an ideal magnetic dipole oriented along (a) x-axis, (b) y-axis, (c) z-axis. The left column shows the dipole orientation for each row.

a pure oscillating point magnetic dipole at the origin are calculated from the far-field components of Equation A.9. The emission patterns of the magnetic dipole (Figure A.6) are very similar to those of the electric dipole, although in general the ε_θ and ε_ϕ components are switched, affecting the S_1 and S_2 parameters. The dominant radiation direction remains the same. To distinguish between electric and magnetic dipole moments, the sign of the linear polarization given by S_1 appears to be enough.

The magnetic and electric dipoles can be linearly combined to create radiation polarized at a 45° angle (favouring S_2) or circularly polarized (strengthening S_3) radiation fields. Many simple antennas can be modelled using linear combinations of electric and magnetic dipole moments.

A.2.3 Two Parallel Dipoles

A pure $\boldsymbol{p}_z$ electric dipole produces fields which are fully polarized along ϕ, whereas the magnetic dipole with the same orientation produces electric far-field radiation fully polarized along θ. A linear combination of equal electric and magnetic oscillating point dipoles (Equation A.10), both oriented along the z-axis, produces far-field radiation with equal field components in both of the orthogonal directions, resulting in radiation polarized at a 45° angle.

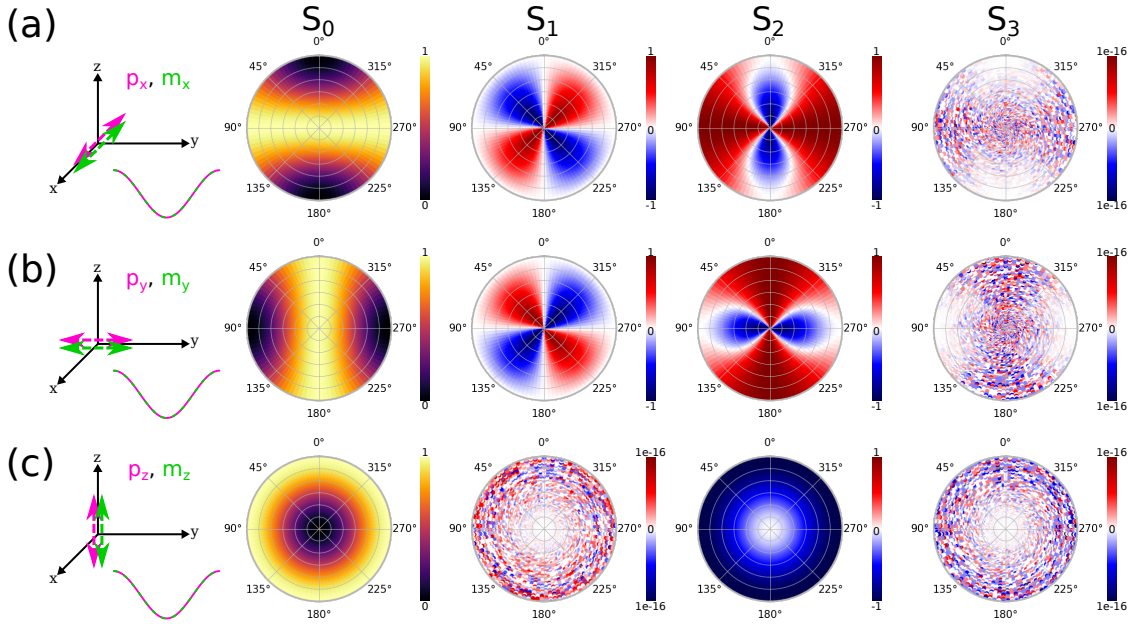

Figure A.7: AR Stokes parameters for an ideal electric dipole oriented parallel to an ideal magnetic dipole, both are oriented along (a) x-axis, (b) y-axis, (c) z-axis. The left column shows the dipole orientations and phase relationship (sine curve) for each row.

$$\boldsymbol{\varepsilon}(\boldsymbol{r}) = \boldsymbol{\varepsilon}_{\boldsymbol{p}}(\boldsymbol{r}) + \boldsymbol{\varepsilon}_{\boldsymbol{m}}(\boldsymbol{r}) \tag{A.10a}$$

$$= \frac{k^2}{\epsilon_0}\hat{\boldsymbol{r}} \times (\boldsymbol{p} \times \hat{\boldsymbol{r}})\,\mathrm{G}\,(\boldsymbol{r}) + \eta_0(k^2)\,(\hat{\boldsymbol{r}} \times \boldsymbol{m})\,\mathrm{G}\,(\boldsymbol{r}) \tag{A.10b}$$

Radiation of this polarization is dominated by the S_2 parameter when there is no phase shift between the dipoles (Figure A.7(c)). When both dipoles are rotated to be in the (x, y) plane, the S_1 and S_2 parameters appear similar to the S_2 and S_1 parameters of a lone $\boldsymbol{p}_x$ or $\boldsymbol{p}_y$ dipole, respectively (Figure A.7(a,b)). With no phase shift, the radiation is wholly linearly polarized and S_3 is negligible.

Phase-Shifted Dipoles

When a phase shift of $\pi/2$ is added to one of the two dipoles relative to the other (Equation A.11), the emitted light is fully circularly polarized and dominated by S_3, regardless of orientation (Figure A.8).

$$\boldsymbol{\varepsilon}(\boldsymbol{r}) = \boldsymbol{\varepsilon}_{\boldsymbol{p}}(\boldsymbol{r}) + \exp(i\delta)\boldsymbol{\varepsilon}_{\boldsymbol{m}}(\boldsymbol{r}) \tag{A.11a}$$

$$= \frac{k^2}{\epsilon_0}\hat{\boldsymbol{r}} \times (\boldsymbol{p} \times \hat{\boldsymbol{r}})\,\mathrm{G}\,(\boldsymbol{r}) + \eta_0(k^2)\exp(i\delta)\,(\hat{\boldsymbol{r}} \times \boldsymbol{m})\,\mathrm{G}\,(\boldsymbol{r}) \tag{A.11b}$$

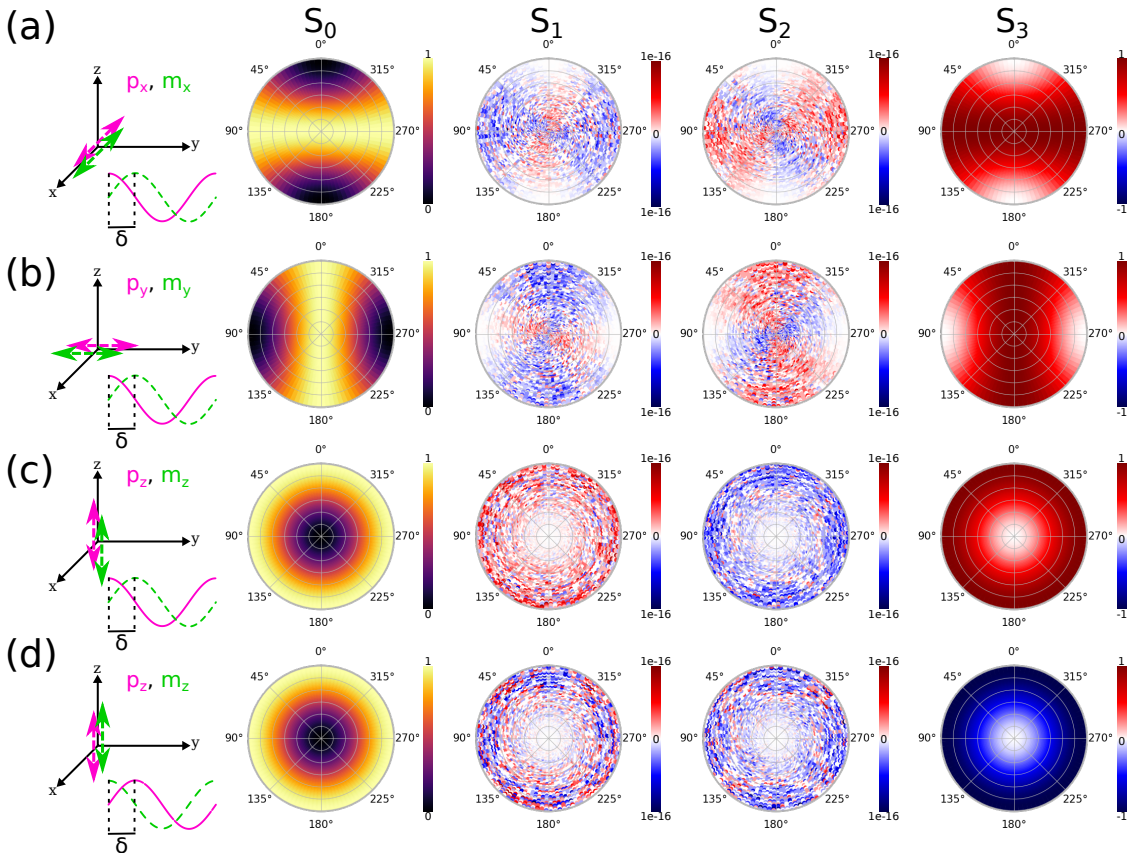

Figure A.8: AR Stokes parameters for an ideal electric dipole oriented parallel to an ideal magnetic dipole. Both are oriented along (a) x-axis, (b) y-axis, (c) z-axis, (d) z-axis. The magnetic dipole has a phase delay of $\pi/2$ relative to the electric dipole in (a)-(c) and in (d), the electric dipole has a phase delay of $\pi/2$ relative to the magnetic dipole. The left column shows the orientation of both dipole moments and their phase relationship, δ.

When the magnetic dipole is given a phase delay of $\delta = \pi/2$, the emitted radiation is RHC (Figure A.8(c)), and similarly, when the electric dipole is given a phase delay of $\pi/2$, the emitted light is LHC (Figure A.8(d)). The emission is strongest perpendicular to the dipole vectors, similarly to the lone dipoles.

When the vectors of the two dipole moments are rotated (*e.g.*, along x to along y), the primary emission axis rotates with it, but the polarization remains fully circular. Intermediate phase shifts ($0 < \delta < \pi/2$, $\pi/2 < \delta < \pi$) between the electric and magnetic dipoles give various degrees of elliptical polarization.

A.2.4 Two Orthogonal Dipoles

When an electric and a magnetic dipole moment are in-phase and orthogonal to each other, the light emitted is fully linearly polarized (Figure A.9). When both dipoles are in the (x, y) plane, the S_1 and S_2 parameters both display a quadrant symmetry

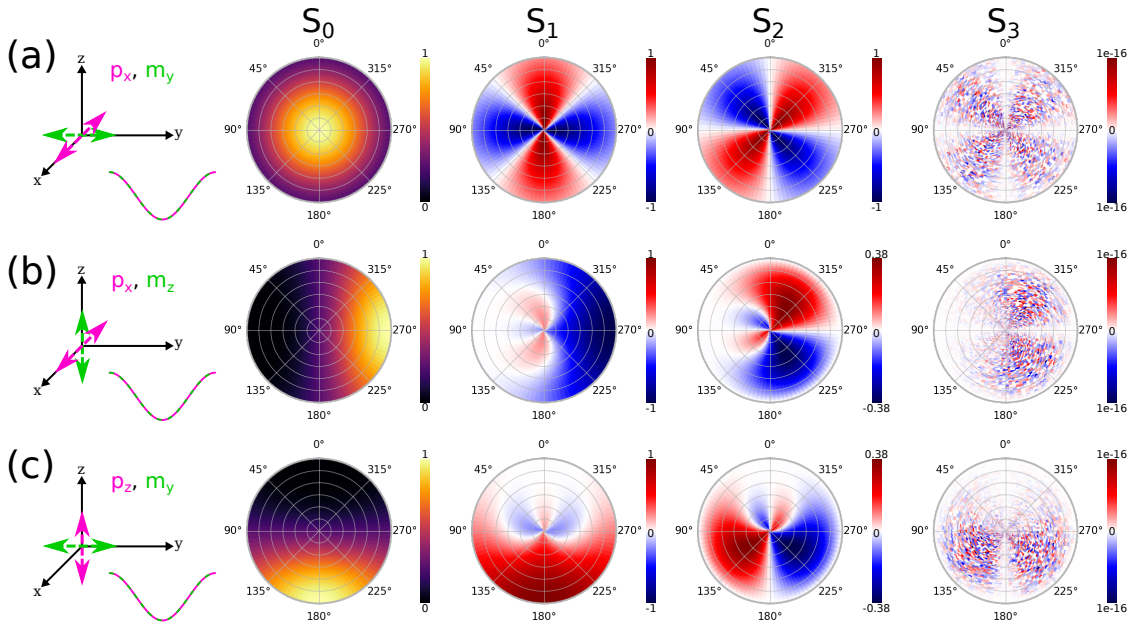

Figure A.9: AR Stokes parameters for an ideal electric dipole oriented orthogonally to and in-phase with an ideal magnetic dipole. The dipoles are oriented as follows: (a) $(\boldsymbol{p}_x, \boldsymbol{m}_y)$, (b) $(\boldsymbol{p}_x, \boldsymbol{m}_z)$, (c) $(\boldsymbol{p}_z, \boldsymbol{m}_y)$. The left column shows the orientations and phase relationship of both dipoles.

with strong emission towards the z-axis.

When one of the dipole moments is oriented along the z-axis, the symmetry in the S_1 and S_2 angular patterns is broken (Figure A.9(b,c)), although the emitted light is still directed towards the normal of the plane that the two dipoles lie in. When the dipole pair is $(\boldsymbol{p}_x, \boldsymbol{m}_z)$, as shown in Figure A.9(b), the emission is directed towards the negative y axis and is predominantly polarized along ϕ. Exchanging the orientations of the two dipoles switches the signs of S_1 and S_2. Rotating the dipole pair rotates the emission pattern (compare Figure A.9(b) and (c)).

Orthogonal Phase-shifted Dipoles

If one of the dipole moments is phase-shifted relative to the other, circularly polarized light is emitted. Figure A.10 shows the AR Stokes parameters for a series of electric and magnetic dipole moments, in which the magnetic dipole has a phase delay of $\pi/2$ relative to the electric dipole.

The interference of the emitted fields from two dipoles in the (x, y) plane gives strong linearly polarized emission along the positive z-axis (Figure A.10(a)), normal to both dipole moments. Towards the in-plane emission angle, circular polarization (S_3) dominates the emission. When one of the dipoles is oriented along z, a similar S_1 pattern to the lone electric or magnetic dipole in x or y emerges (Figure A.10(b,c)). The S_2 pattern retains its quadrant symmetry, and the S_3 pattern takes on a two-lobed pattern, strongest at 45° from the z-axis.

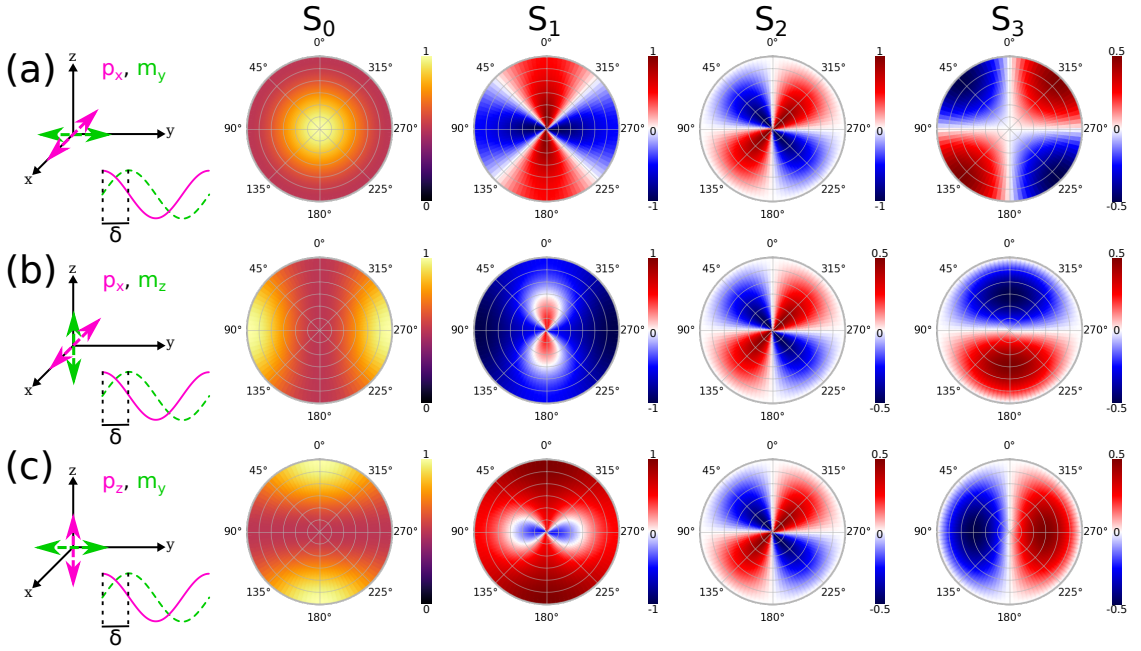

Figure A.10: AR Stokes parameters for an ideal electric dipole oriented orthogonally to an ideal magnetic dipole with a relative phase delay of $\pi/2$. The dipoles are oriented as follows: (a) $(\boldsymbol{p}_x, \boldsymbol{m}_y)$, (b) $(\boldsymbol{p}_x, \boldsymbol{m}_z)$, (c) $(\boldsymbol{p}_z, \boldsymbol{m}_y)$. The orientation and phase relationship is shown in the left column.

Although the strongest emission is still linearly polarized, the phase shift between the two dipole moments introduces some circular polarization in the emission.

Two electric dipoles

A combination of two electric dipole moments that are either in different directions or have different phases also changes the angular emission polarization patterns. Figure A.11 shows three different combinations of two electric dipoles ($\boldsymbol{p}_x$ and $\boldsymbol{p}_z$) with different phase shifts.

When both dipoles are in phase, the emission is tilted towards the negative x direction; the asymmetry is reflected in the S_1 and S_2 parameters, which appear similar to the patterns for a single electric dipole, but distorted. A $\pi/2$ phase shift between the two dipoles results in an S_1 pattern which resembles that of a single magnetic dipole, $\boldsymbol{m}_y$ (compare Figure A.11(c) with Figure A.6(b)). This configuration can be distinguished by the differences in the S_0 parameter and the presence of circular polarization (S_3), both of which favour the normal to the plane containing the two dipoles.

The presence of a phase shift between the emission from two dipoles, whether they are both of the same type or of different types, produces circularly polarized light in the angular emission pattern. Many of the different dipole combinations show similar patterns and can only be distinguished from each other by knowing

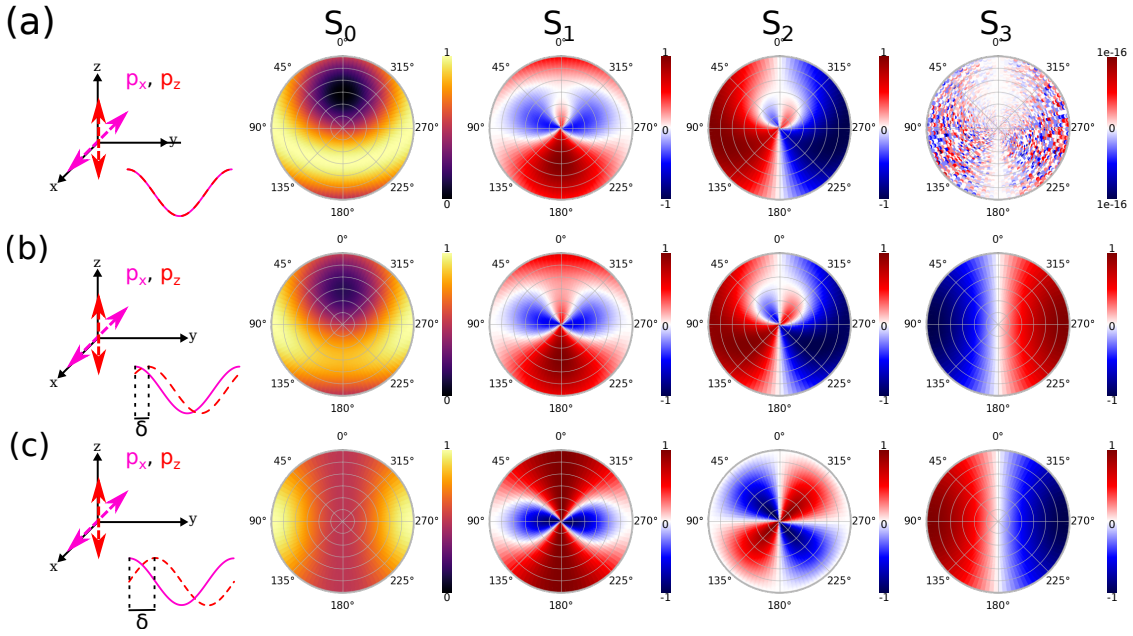

Figure A.11: AR Stokes parameters for two orthogonal ideal electric dipoles with different phase relationships, as follows: (a) 0; (b) $\pi/4$; and (c) $\pi/2$. Phase relationship and dipole orientations are indicated in the left column for each row.

the angular patterns of the full Stokes vector. Knowing some of the results from elementary dipole configurations can help to identify the dipole moments present in a sample under electron beam excitation.

A.3 Simulating Radiation Patterns

Using the MNPBEM toolbox [178, 179], the far-field response of a plasmonic nanostructure can be calculated for a given beam position and response frequency. Input to the far-field function in the toolbox requires the surface charge distribution over a mesh representing the nanoparticle, as well as the direction vectors along which to calculate the radiation emitted. The surface normals of a unit sphere are used to define the direction vectors; to save calculation time, the sphere is reduced to a hemisphere. The output from the far-field calculation function is the electric ($\boldsymbol{\varepsilon}(x, y, z)$) and magnetic ($\boldsymbol{m}(x, y, z)$) field vectors of the scattered far-field radiation, and the wavevector of the radiated EM fields.

The MNPBEM far-field calculation uses equation (50) from García de Abajo [69], which gives the far-field amplitude of the electric field using retarded potential calculations, taking into account the time it takes for an EM field to propagate from one point to another. The electric field is given in terms of vector ($\boldsymbol{A}$) and scalar (Φ) potentials by Equation A.12.

$$\boldsymbol{\varepsilon} = ik\boldsymbol{A} - \nabla\Phi \tag{A.12}$$

Taking retardation into account, the potentials are given by the volume integrals in Equation A.13 [355], in which $R = |\boldsymbol{r} - \boldsymbol{r}'|$, and the Green's function, $\mathrm{G}(r) = \frac{\exp\left(ikr\sqrt{\epsilon_A}\right)}{r}$, is the solution to the Helmholtz wave equation in the medium of interest.

$$\Phi(\boldsymbol{r}) = \int_V \frac{1}{\epsilon}\sigma(\boldsymbol{r}')\mathrm{G}(R)\mathrm{d}^3\boldsymbol{r} \tag{A.13a}$$

$$\boldsymbol{A}(\boldsymbol{r}) = \int_V \mu\boldsymbol{j}(\boldsymbol{r}')\mathrm{G}(R) \tag{A.13b}$$

The BEM method calculates the response of interface charge and current sources [69]: integrals are performed over surfaces, rather than over volumes, so the volume integrals from Equation A.13 are modified to become surface integrals (Equation A.14). In these equations, $\boldsymbol{j}_{AB}$ is the interface current on interface AB, σ_{AB} is the interface charge density, $\boldsymbol{s}$ is a point on the interface, and $\boldsymbol{r}$ is the observation point.

$$\Phi(\boldsymbol{r}) = \int_{AB} \frac{1}{\epsilon}\sigma_{AB}(\boldsymbol{s})\mathrm{G}_{AB}(|\boldsymbol{r} - \boldsymbol{s}|)\mathrm{d}\boldsymbol{s} \tag{A.14a}$$

$$\boldsymbol{A}(\boldsymbol{r}) = \int_{AB} \boldsymbol{j}_{AB}(\boldsymbol{s})\mathrm{G}(|\boldsymbol{r} - \boldsymbol{s}|)\mathrm{d}\boldsymbol{s} \tag{A.14b}$$

Returning to Maxwell's equations as expressed in terms of these potentials [61], the electric and magnetic fields can be expressed in terms of the vector and scalar potentials as shown in Equation A.15, in which c is the speed of light in vacuum. Equation A.15a represents the curl of the gradient of a scalar potential [61], implying that the term $\nabla\Phi$ in Equation A.12 contributes only to the longitudinal electric field and not to propagating far-field (transverse) radiation.

$$\nabla \times (\boldsymbol{\varepsilon} + \frac{1}{\mathrm{c}}\frac{\partial \boldsymbol{A}}{\partial t}) = 0 \tag{A.15a}$$

$$\boldsymbol{B} = \nabla \times \boldsymbol{A} \tag{A.15b}$$

When calculating far-field radiation, the longitudinal components of the electric field can be neglected. The far-field electric field vector is reduced to eliminate the contributions from the longitudinal scalar potential, removing the second term in Equation A.12.

The other term in Equation A.12 contains the vector potential, which has both transverse and longitudinal components. To remove the longitudinal components, first the vector potential is rewritten as Equation A.16 [69].

$$\boldsymbol{A} = \int_{AB} \frac{\exp(i(kr - k\hat{\boldsymbol{r}} \cdot \boldsymbol{s}))}{r} \boldsymbol{j}_{AB} \mathrm{d}\boldsymbol{s} = \frac{\exp(ikr)}{r} \int_{AB} \exp(-ik\hat{\boldsymbol{r}} \cdot \boldsymbol{s}) \boldsymbol{j}_{AB} \, \mathrm{d}\boldsymbol{s} \quad \text{(A.16)}$$

The integral is simplified on the right hand side, allowing the assignment of a new variable representing the total amplitude of the electric field (using Equation A.12 and neglecting the phase component), given in Equation A.17.

$$\boldsymbol{\varepsilon}_{\mathrm{amp}} = ik \int_{AB} \exp(-ik\hat{\boldsymbol{r}} \cdot \boldsymbol{s}) \boldsymbol{j}_{AB} \, \mathrm{d}\boldsymbol{s} \quad \text{(A.17)}$$

To obtain the far-field radiation amplitude, $\boldsymbol{\varepsilon}_{\mathrm{ff}}$, which should only contain the transverse electric field vectors, the longitudinal components are subtracted from the total amplitude, shown in Equation A.18.

$$\boldsymbol{\varepsilon}_{\mathrm{ff}} = \boldsymbol{\varepsilon}_{\mathrm{amp}} - (\boldsymbol{\varepsilon}_{\mathrm{amp}} \cdot \hat{\boldsymbol{r}}) \hat{\boldsymbol{r}} \quad \text{(A.18)}$$

The electric field of the far-field radiation is then given by Equation A.19, from which the far-field amplitude $\boldsymbol{\varepsilon}_{\mathrm{ff}}$ can be separated out. Further details can be found in [69].

$$\boldsymbol{\varepsilon}_{\mathrm{farfield}} = \boldsymbol{\varepsilon}_{\mathrm{ff}}(\hat{\boldsymbol{r}}) \frac{\exp(ikr)}{r} \quad \text{(A.19)}$$

The MNPBEM toolbox uses these equations for the far-field to calculate $\boldsymbol{\varepsilon}(x, y, z)$, keeping in mind that the nanoparticle surface and the collection sphere are discretized into distinct mesh faces. The far-field electric and magnetic field components along the directions defined by the normals to the faces of the collection sphere are calculated. The calculated fields and surface charges are then imported into Python [192] to calculate the Stokes parameters as a function of angle or simulated electron beam position.

A.3.1 Python Simulation Processing

The custom Python code transforms the $\boldsymbol{\varepsilon}(x, y, z)$ fields into spherical coordinates, $\boldsymbol{\varepsilon}(r, \theta, \phi)$, then calculates the Stokes parameters on each face of the collection sphere using the two angular components of $\boldsymbol{\varepsilon}$ as the two electric field components perpendicular to the direction of propagation ($\hat{\boldsymbol{r}}$), assumed to be outwards from the origin. Longitudinal components (ε_r) are very small and are neglected. At this point, the AR Stokes parameters can be plotted.

Cartesian to Spherical Coordinates

Calculations of the electric field done in MNPBEM give the electric field vector in Cartesian coordinates. To calculate the Stokes parameters from these fields, it is much

more convenient to transform the electric field vectors into spherical coordinates. In spherical coordinates, the emitted light propagates along r, and θ and ϕ represent two orthogonal directions which are also orthogonal to r. To transform point coordinates, a simple Cartesian-spherical transform can be used, given in Equation A.20 [360].

$$\begin{pmatrix} r \\ \theta \\ \phi \end{pmatrix} = \begin{pmatrix} \sqrt{x^2+y^2+z^2} \\ \arctan\left(\frac{\sqrt{x^2+y^2}}{z}\right) \\ \arctan\left(\frac{y}{x}\right) \end{pmatrix} \tag{A.20}$$

For the transformation of the electric field vectors from Cartesian to spherical coordinates, a more complex vector field transformation must be used, given in Equation A.21 [360].

$$\begin{pmatrix} \varepsilon_r \\ \varepsilon_\theta \\ \varepsilon_\phi \end{pmatrix} = \begin{pmatrix} \sin\theta\cos\phi & \sin\theta\sin\phi & \cos\theta \\ \cos\theta\cos\phi & \cos\theta\sin\phi & -\sin\theta \\ -\sin\phi & \cos\phi & 0 \end{pmatrix} \begin{pmatrix} \varepsilon_x \\ \varepsilon_y \\ \varepsilon_z \end{pmatrix} \tag{A.21}$$

It is also important to notice which axis (the z-axis, in this case) is used as the zenith axis in the spherical coordinate system. The electron beam is assumed to propagate from $+z$ to $-z$; the CL mirror opens towards the $-x$ direction. The angle θ is defined as the angle from the $+z$ axis. The angle ϕ is the angle from the $+x$ axis rotating towards the $+y$ axis (see Figure A.4(a)).

A.3.2 Wavelength-Filtered Images

The simulated electron beam can be raster-scanned over the nanoparticle mesh using a simple loop; at each pixel, the far-field electric and magnetic fields are saved to reconstruct a wavelength-filtered image of the Stokes parameters over space. At each electron beam position, the AR Stokes parameters can be calculated, as described above. A mask representing the mirror and slit combination used in the experimental SI acquisitions is used to filter out parts of the collection sphere mesh. The Stokes parameters are then averaged over the remaining mesh faces and a wavelength-filtered image of the Stokes parameters at each electron beam position is calculated for direct comparison with the experimental polarimetry SI datasets.

Comparison of Simulation with Experiment

The processes for both simulation and experimental acquisition of polarized CL spectrum images are complicated and careful consideration must be given to make sure that the simulated data is comparable to the experimental data.

In the experiment, electromagnetic radiation, $\boldsymbol{\varepsilon}(r, \theta, \phi)$ is emitted from the sample. Assuming the radial component is negligible, the electric field is simplified to $\boldsymbol{\varepsilon}(\theta, \phi)$. The radiation reflects off the parabolic mirror; the reflected beam is collimated and

propagates towards the exit window in the SEM chamber, effectively becoming a 2D image of the mirror ($\boldsymbol{\varepsilon}(x,y)$). The reflection is represented by the Mueller matrix of the mirror, $\boldsymbol{M}_{\text{mirror}}$, which is applied to the electric field coming off the sample and transforms the electric field into Cartesian coordinates. This radiation is then passed through a QWP and LP, with rotation angles given by Equation A.7, which can be represented by the known Mueller matrices of QWPs ($\boldsymbol{M}_{\text{QWP}}$) and LPs ($\boldsymbol{M}_{\text{LP}}$) [354]. After the polarizing filters, the radiation is integrated over the area of the mirror and slit ($A_{\text{collection}}$) using a focusing lens before it is sent to the spectrometer, where the light is dispersed by a grating and a spectrum of intensity over wavelength is acquired, $I(\lambda)$ (Equation A.22). Six acquisitions are performed, as described in Section A.1.2, and the Stokes parameters are calculated from these six acquisitions.

$$I(\lambda) = \left| \int (\boldsymbol{M}_{\text{LP}} \boldsymbol{M}_{\text{QWP}} \boldsymbol{M}_{\text{mirror}} \boldsymbol{\varepsilon}(\theta,\phi)) \mathrm{d}A_{\text{collection}} \right|^2 \tag{A.22}$$

In the simulation, the Stokes parameters are directly calculated from the emitted radiation ($\boldsymbol{\varepsilon}(\theta,\phi)$). Comparing this to the experiment requires the understanding that the polarization state is set early on in the optics system by the polarizers. After the QWP and LP, the polarization state of the light is set as one of the following states, represented by Equation A.23, depending on the particular measurement being done.

$$\boldsymbol{\varepsilon}(x,y) \in \{\varepsilon_H, \varepsilon_V, \varepsilon_{45}, \varepsilon_{135}, \varepsilon_{RHC}, \varepsilon_{LHC}\} \tag{A.23}$$

If the two orthogonal axes after mirror reflection, x and y, are assumed to be aligned with the horizontal and vertical polarization states, respectively, then the electric radiation fields can be represented by the relationships in Equation A.24, noting that the electric fields are complex values ($\varepsilon_x = \varepsilon_{x1} + i\varepsilon_{x2}$, $\varepsilon_y = \varepsilon_{y1} + i\varepsilon_{y2}$).

$$\begin{pmatrix} \varepsilon_H \\ \varepsilon_V \\ \varepsilon_{45} \\ \varepsilon_{135} \\ \varepsilon_{RHC} \\ \varepsilon_{LHC} \end{pmatrix} = \begin{pmatrix} \varepsilon_x \\ \varepsilon_y \\ \frac{1}{\sqrt{2}}(\varepsilon_x + \varepsilon_y) \\ \frac{1}{\sqrt{2}}(-\varepsilon_x + \varepsilon_y) \\ \frac{1}{\sqrt{2}}(\varepsilon_{x1} - \varepsilon_{y2} + j(\varepsilon_{x2} + \varepsilon_{y1})) \\ \frac{1}{\sqrt{2}}(-\varepsilon_{x2} + \varepsilon_{y1} + j(\varepsilon_{x1} + \varepsilon_{y2})) \end{pmatrix} \tag{A.24}$$

The circularly polarized electric fields are derived using Euler's formula ($\exp(i\theta) = \cos(\theta) + i\sin(\theta)$). RHC light has a $\pi/2$ phase delay on the ε_x component, which is equivalent to $\exp(i(\theta + \pi/2)) = -\sin(\theta) + i\cos(\theta)$, so the real and imaginary components of ε_x are effectively switched, with a negative sign on the real part. The Stokes parameters (Equation A.25) are calculated from the intensity of light, which is proportional to the square of the electric field ($I \propto |\boldsymbol{\varepsilon}|^2 = \boldsymbol{\varepsilon}^*\boldsymbol{\varepsilon}$).

$$\begin{pmatrix} S_1 \\ S_2 \\ S_3 \end{pmatrix} = \begin{pmatrix} \varepsilon_x\varepsilon_x^* - \varepsilon_y\varepsilon_y^* \\ \varepsilon_{45}\varepsilon_{45}^* - \varepsilon_{135}\varepsilon_{135}^* \\ \varepsilon_{RHC}\varepsilon_{RHC}^* - \varepsilon_{LHC}\varepsilon_{LHC}^* \end{pmatrix} \tag{A.25}$$

On inserting the electric field values from Equation A.24, Equation A.25 can be simplified to give the equivalent of Equation A.5 or A.6. This exercise demonstrates that the polarization state is set after the EM radiation passes through the QWP and LP and calculating the Stokes parameters before integrating over the area of the mirror is equivalent to calculating the Stokes parameters after the QWP and LP, with the switch of axes from (x, y) to (θ, ϕ), which are both equivalently orthogonal axes regarding the treatment of circular polarization.

Mirror Rotation

As evidenced in the above angular-resolved plots, the orientation of the component dipoles within a sample affects the orientation and symmetry of the emitted radiation. A different portion of the radiation sphere can be captured by rotating the sample stage in an experiment. To save simulation time, instead of rotating the nanostructure mesh and re-calculating the emission, the mirror and slit mask that is applied to the radiation can be rotated. This rotates the coordinate system relative to the sample and must be accounted for by changing the sign of the S_1 and S_2 Stokes parameters. The mirror rotation does not affect the sign of the S_3 parameter.

A.3.3 Summary of Simulation Procedure

In summary, the Stokes parameters are calculated from the simulated complex electric fields, then averaged over the mirror with the 3 mm slit imposed, to give one value for each Stokes parameter at each location of the simulated rastered electron beam, forming wavelength-filtered images of each of the Stokes parameters. A step-by-step summary of the calculation procedure for the simulated wavelength-filtered Stokes images is given below.

1. Calculate surface charges ($\sigma_{\boldsymbol{r}_\mathrm{e}}$) and currents ($\boldsymbol{j}_{\boldsymbol{r}_\mathrm{e}}$) at each face of the nanoparticle mesh in MNPBEM, at each electron beam scan position ($\boldsymbol{r}_\mathrm{e}$) for a chosen energy.

2. Using the surface charges and currents, calculate far-field electric field vectors for each electron beam scan position, in the direction defined by the normal vector to each face ($\boldsymbol{r} = (x, y, z)$) on the spherical collection mesh (Equations A.14-A.19).

$$\boldsymbol{\varepsilon}_{\boldsymbol{r}_\mathrm{e}}(\boldsymbol{r}) = \varepsilon_{x,\boldsymbol{r}_\mathrm{e}}(\boldsymbol{r}) + \varepsilon_{y,\boldsymbol{r}_\mathrm{e}}(\boldsymbol{r}) + \varepsilon_{z,\boldsymbol{r}_\mathrm{e}}(\boldsymbol{r})$$

3. Convert the electric field vectors to spherical coordinates (Equation A.21).

$$\boldsymbol{\varepsilon}_{\boldsymbol{r}_\mathrm{e}}(x, y, z) = \varepsilon_{r,\boldsymbol{r}_\mathrm{e}}(x, y, z) + \varepsilon_{\theta,\boldsymbol{r}_\mathrm{e}}(x, y, z) + \varepsilon_{\phi,\boldsymbol{r}_\mathrm{e}}(x, y, z)$$

4. Calculate the Stokes parameters as a function of electron beam position ($\boldsymbol{S}_{\boldsymbol{r}_\mathrm{e}}(\boldsymbol{r})$) at each sphere face (Equation A.6).

5. Apply mirror and slit mask and integrate the Stokes parameters over the remaining spherical collection mesh to get a single value for each Stokes parameter at each electron beam location ($\boldsymbol{S}_{\boldsymbol{r}_e}$).

A.4 Simulated Radiation Patterns

Calculating the Stokes parameters from some simple nanostructures allows a more direct comparison to experimental results, by incorporating LSPR mode-mixing and structural deviations from the analytical dipole model, and by including the electron beam excitation source. Some simple structures are presented here to demonstrate the calculation of the Stokes parameters using simulation results from the MNPBEM toolbox and help understand the CL polarimetry data presented in Chapter 4.

A.4.1 Nanowire

The first nanostructure is a nanowire with a length of 35 nm and a diameter of approximately 5 nm. The procedure outlined in Section A.3.3 was followed to simulate the Stokes parameters as a function of electron beam location (Figure A.12(a,b)) and the AR Stokes parameters at a given excitation location (Figure A.12(c)). Rotating the nanowire with respect to the mirror is equivalent to rotating the mirror with respect to the nanowire. The projections of the mirror/slit mask at two orientations are shown on the AR plots in (c), where the colour of the mirror/slit outline corresponds to the matching orientation in the left column. The areas within the mirror/slit mask are integrated for each electron beam location to produce the spatially-resolved maps shown in (a,b). The energy chosen corresponds to the peak of the dipolar mode of this nanowire.

The nanowire dipolar mode is strongly excited when the electron beam is located at one end of the nanowire (Figure A.12: Location A). The AR patterns of the S_0, S_1, and S_2 parameters bear a strong resemblance to the AR patterns of an analytical electric dipole oriented along the x axis (Figure A.5(a)). The S_3 parameter, however, indicates that the nanowire response deviates from the ideal electric dipole case and there may be a small contribution from another electric dipole oriented along the z-axis (the electron beam propagation direction) with a small phase shift (*e.g.*, compare to Figure A.11(b)), which is not unexpected from CL experiments [167, 186].

The radiation is dominantly linearly polarized along the longitudinal axis of the nanowire (Figure A.12(a,b)); the contributions from $(45, 135)^\circ$ linearly polarized light and circularly polarized light are very small. The S_2 and S_3 parameters are strongest when the electron beam is not exciting the nanowire on its symmetry axis, but there the overall emission intensity is also lower.

The S_2 parameter is almost perfectly symmetrical when the beam is on a symmetry axis, but moving the electron beam to a symmetry-breaking location causes a slight distortion in the S_2 angular emission (indicated by the orange dashed lines in

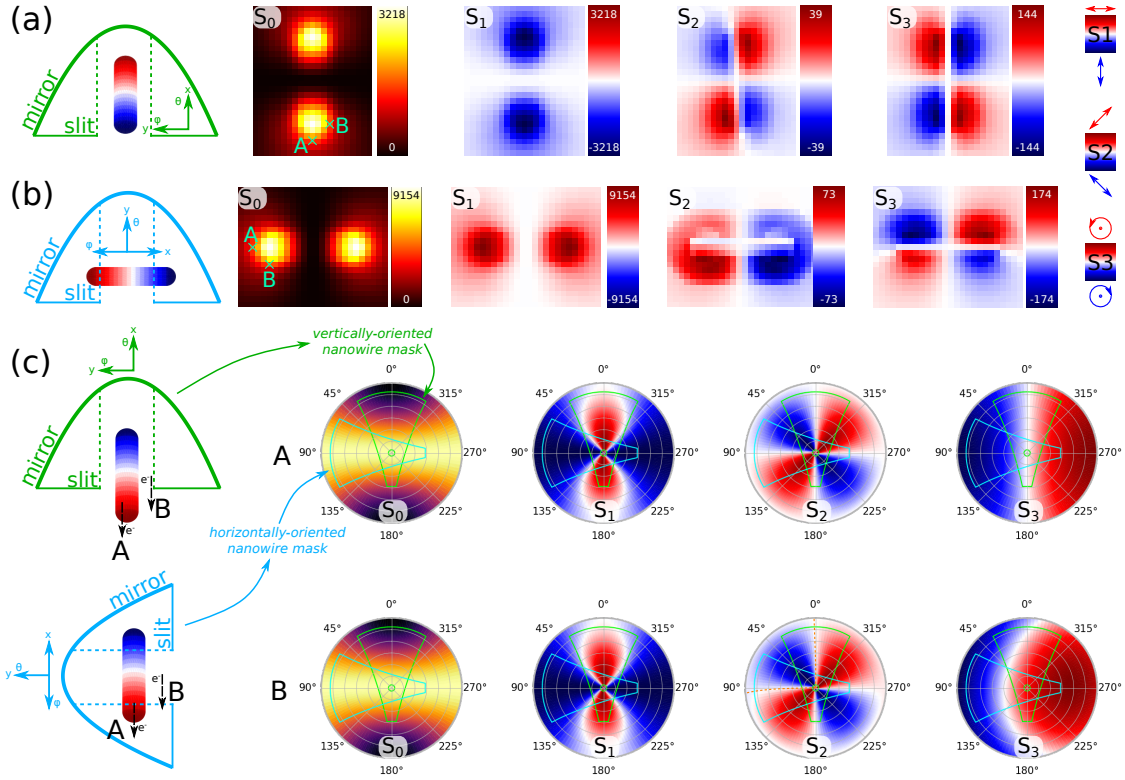

Figure A.12: Stokes parameters of the dipolar mode of a simulated nanowire. (a,b) Spatially resolved Stokes parameters (Cartesian coordinates) from the emission of a nanowire oriented (a) vertically and (b) horizontally with respect to the mirror (orientation indicated in the left column); (c) AR Stokes parameters (spherical coordinates) for the dipolar emission from a nanowire at two locations, A and B, as indicated in the left column. The outlines for the two orientations of the mirror/slit mask used for (a) and (b) are shown on the AR plots in green and blue.

Figure A.12(c): S_2), which causes a non-zero net S_2 after integration over the mirror. The rotation of the coordinate systems with the mirror rotation and with mapping the spherical coordinates onto the 2D image (x, y) coordinate system causes the change in sign in S_2 between the angular plots and the spatially-resolved plots. The polarization represented by the spatially-resolved images is consistent with the references in the right-hand column; the polarization conventions for the AR plots are consistent with those represented in Figure A.3 and A.4(b).

The angular distribution of the S_3 parameter is also symmetrical when the electron beam excitation is on the nanowire longitudinal axis, but has a much larger change towards either LHC or RHC when the electron beam is off-axis (Figure A.12(c): Location B), depending on the beam location. The off-axis electron beam breaks the symmetry of excitation and causes larger circular components in the emitted radiation, revealing an interesting dependence of the polarization state on the location of the electron beam.

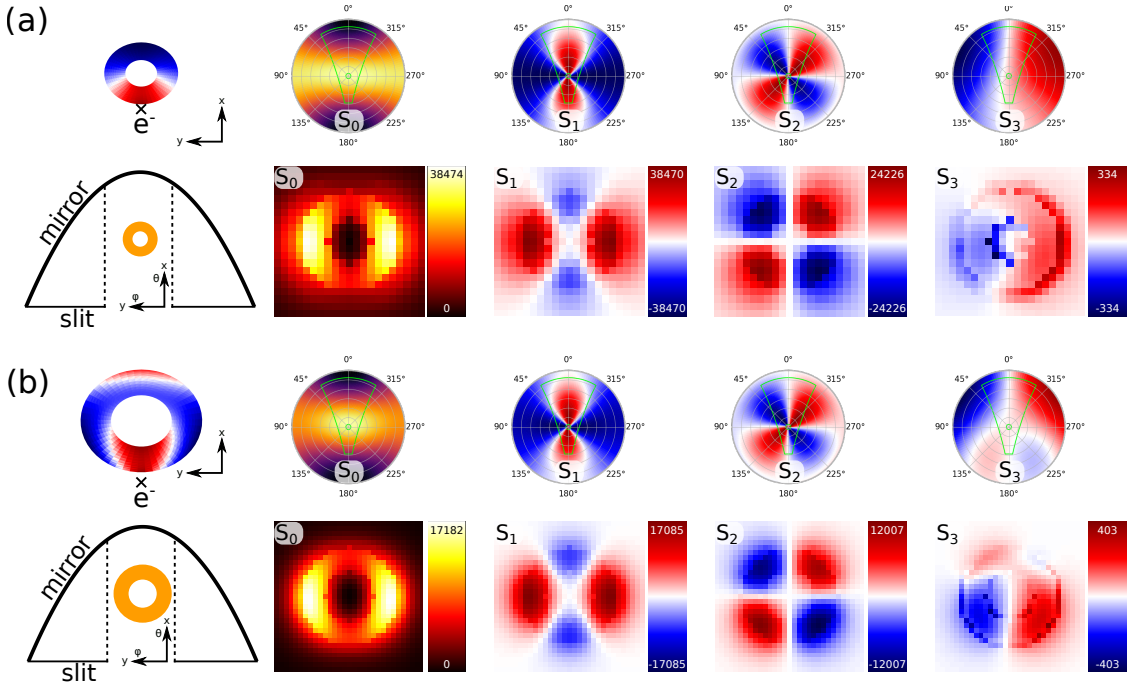

Figure A.13: Stokes parameters of the (a) dipolar and (b) quadrupolar modes of simulated torii. The top row of both (a) and (b) shows the induced surface charges and electron beam excitation location, and the AR Stokes parameters (spherical coordinates) for that location (outlines on the AR plots shows the mirror/slit collection range); the bottom row shows the mirror and slit configuration (left) and spatially-resolved Stokes parameters (Cartesian coordinates) as the simulated electron beam is scanned over the torus.

A.4.2 Dipole and Quadrupole Modes of a Torus

Similar to the nanowire, but with C_∞ in-plane rotational symmetry, the torus presents a nanostructure in which a dipole mode can be excited from any location around the torus circumference. The Stokes parameters for the emission from the dipolar mode of a torus with a diameter of 50 nm and a poloidal radius of 10 nm are shown in Figure A.13(a). The Stokes parameters of the emission from the quadrupolar mode of a larger torus, with a diameter of 150 nm and a poloidal radius of 25 nm, are shown in Figure A.13(b). Because of the rotational symmetry of the torus, only one mirror orientation is used for the spatially-resolved plots: rotating the mirror produces identical plots.

The strongest emission of a linear dipole is perpendicular to the dipole axis, so the S_0 parameter (CL intensity) is highest when the dipole across the torus is excited in the y direction (Figure A.13(a)). As a consequence of this, the horizontally polarized emission is also stronger than the vertically polarized emission in the S_1 map. The vertically polarized radiation is emitted when a vertical dipole is excited, but this radiation is primarily emitted horizontally and is not collected by the mirror/slit combination. The S_2 is strongest when the dipole mode is excited at a 45° angle to the

mirror, and the linear polarization direction maps directly to the dipole orientation. Interestingly, the S_3 parameter is not spatially symmetrical; it is not known why this is the case, but it could be a function of numerical error in the subtraction. The AR S_3 parameter when the electron beam is at the bottom of the torus is very symmetrical, and small deviations to one side or the other, caused by asymmetries in the mirror mesh or the torus mesh, could swing the integration to favour one S_3 sign over the other. The other AR Stokes parameters match very well with those of a linear in-plane electric dipole (Figure A.5(a,b)).

The AR Stokes parameters of the quadrupolar mode (Figure A.13(b)) are very similar to those for the dipole, except for S_3. S_3 develops an extra pair of anti-nodes at high ϕ angles. The S_0 parameter is slightly more focused towards the vertical emission direction and there are small changes to the shape of the features in the S_1 and S_2 AR plots. Spatially, the quadrupolar mode seems to be more tightly confined to the structure, but except for S_3, the maps are very similar to those for the dipolar mode on a smaller torus. Both the AR and spatially-resolved S_3 plots have an extra pair of anti-nodes in the pattern compared to the dipolar mode. The AR plot shows the anti-nodes at high ϕ angles when the electron beam is at $\phi = 180°$; when the electron beam is at $\phi = 0°$, these smaller anti-nodes will be directed towards the mirror, resulting in the difference in the spatially-resolved plot compared to the dipole mode.

A.5 Summary

This appendix has detailed the polarization properties of light as relevant to the work presented in the main body of the thesis (primarily Chapter 4). The polarization properties can be fully described using the Stokes parameters. More information on the polarization properties of light can be found in the references cited and, in the context of a CL experiment, in the theses of Dr. Coenen [195] and Dr. Brenny [187]. The AR Stokes parameters are shown for ideal electric and magnetic point dipoles, and combinations of these basic dipole moments using various orientation and phase relationships. These radiation patterns are shown as a demonstration case to exhibit the appearance of the Stokes parameters as a function of angle and to help interpret the experimental and simulated results.

Some simulations of basic nanostructures, a nanowire and a torus, were shown to demonstrate the radiation patterns. These patterns differ from the ideal dipole case because of LSPR mode-mixing, structural parameters, and the asymmetry induced by the localized electron beam excitation, but often a strong resemblance to the ideal dipole patterns can be identified. AR plots demonstrate how the emission changes with the electron beam excitation position and how the dominant Stokes parameters are determined for a given pixel in a spatially-resolved image, after integrating over the mirror. The spatially-resolved images are the equivalent of wavelength-filtered Stokes parameters calculated from experimental spectrum images.

Appendix B

Electron Microscopy Hardware

In this appendix, the microscope hardware used to acquire EELS and CL datasets is described more completely than in Chapter 2. The information given is not necessary to understand the content of the thesis, but helps to clarify some of the parameters used in the experimental conditions. The appendix begins with a description of the FEI Titan instrument used for STEM-EELS acquisitions. Perhaps of particular interest in this section is the description of the operation of the electron monochromator. Following this section is a brief description of the SEM system, though repetition of information from Chapter 2 or of similar concepts from the STEM-EELS section has been avoided where possible. Further information, in addition to the description and references given in Section B.1.2, on the FEI monochromator can be found in [361,362] and a comparison of different monochromators is given by Kimoto [363].

B.1 STEM-EELS

The instrument used for STEM-EELS acquisitions is an FEI Titan 80-300 microscope. This tool is capable of operating with beam energies between 80 and 300 keV and is equipped with a monochromator, image corrector, and Gatan Tridiem spectrometer. Briefly, electrons are emitted from a field emission gun, dispersed according to their energy by the monochromator; accelerated to their full energy; focused onto the sample by the condenser system; then, after passing through the sample, they are scattered onto the annular dark-field detector and EELS spectrometer.

B.1.1 Field Emission Gun

The electron gun is the source of the electron beam that is used to probe the sample. Electron guns range from tungsten or LaB_6 thermionic emitters to field-emission tungsten tips. The microscope used in this research was equipped with a Schottky field emission gun (SFEG) before it was exchanged for an XFEG partway through the experiments presented in this thesis.

SFEGs are tungsten crystals shaped into a finely pointed tip and coated with a thin layer of zirconia. An electric potential is applied between the tip (cathode) and the extraction anode, creating a very high electric field at the sharpest point of the tungsten tip [364]. The high field effectively lowers the local work function at the tip, making it easier for electrons to tunnel out of the tip [364]. The zirconia coating also lowers the gun work function, improving the emission characteristics and stability of the tip [141]. To maintain good emission characteristics, the surface of the tip must be kept clean. This is either done by keeping the tip in ultra-high vacuum at ambient temperatures (a cold FEG: CFEG) and periodically heating up the tip (flashing) to remove surface contaminants, or by holding the tip at approximately 1800 K to prevent contaminant build-up (SFEG) and to keep the zirconia layer replenished from a reservoir of molten zirconium [141]. The SFEG does not require such a high vacuum as the CFEG, nor does it require flashing to burn off contaminants, but it has a lower brightness, larger source size, and worse energy spread than the CFEG [141]. The SFEG requires a vacuum around 10^{-6} Pa and has a high brightness and good coherence [364].

The XFEG is a field-emission gun, sold by FEI (now Thermo Fisher Scientific), operating in Schottky mode. The XFEG is a tungsten single crystal with a thin zirconia layer and is kept at equally high temperatures as the SFEG, but it has a much higher brightness by approximately an order of magnitude [365].

The energy resolution of EELS is normally limited by the energy spread of the incident beam on the specimen [143]. The energy spread of the emission process from the SFEG or XFEG is approximately 0.7 eV [364,366]. Instabilities in the high tension supply can cause further broadening of the energy resolution (approximately 0.2 eV), as can the spectrometer resolution and point spread function [366]. The energy spread in the beam may also increase from collision broadening when the beam is focused at the gun cross-over or from the Boersch effect in the region just after the gun where the current density is highest [143]. The Boersch effect describes the effect of Coulomb interactions of electrons in close proximity to each other: following electrons are retarded and advanced electrons are accelerated by Coulomb interactions, increasing the energy spread in the beam [143]. To achieve the high energy resolution required for LSPR studies down to the IR region, monochromation of the incident electron beam is desired.

B.1.2 Monochromator

Immediately after the gun is the gun lens (GL): a three-electrode electrostatic lens (extraction anode, gun lens electrode, and monochromator) which controls the emission from the filament and channels it into the monochromator [367]. The monochromator is the third electrode of this lens and is placed before the accelerator [366], so that electrons travelling through the monochromator do so at low energy [368]. The gun and monochromator are held at high voltage relative to ground, introducing difficulties in

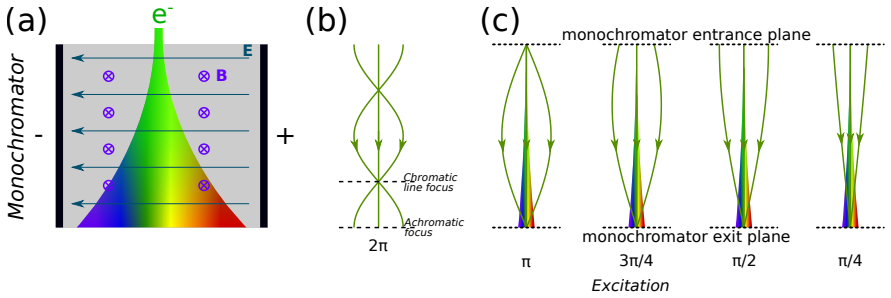

Figure B.1: Dispersion action of the monochromator. (a) Electric and magnetic fields are applied to disperse the electron beam according to energy at the exit plane of the monochromator; (b) a monochromator excitation of 2π returns off-axis beams to their original axis; (c) as the monochromator excitation is varied, the gun lens is used to change the convergence of the beam entering the monochromator to maintain a chromatic line focus at the exit plane.

maintaining the stability of the electrical supplies and currents [143].

Adding the monochromator into the column increases the path length at which electrons are at low potential, increasing the impact of the Boersch effect on the energy resolution and the effect that transverse Coulomb interactions between beam electrons have on increasing the apparent source size [368]. Particularly with a high brightness source such as the SFEG or XFEG, these factors limit the monochromator resolution, and the usable beam current in the monochromator is limited to approximately 30 nA (before the reductions in beam current inside the condenser system) [366, 368].

In the Titan microscope, the monochromator is a Wien filter. The Wien filter is an electromagnetic (EM) filter which uses an electric field and a magnetic field, both of which are perpendicular to each other and to the electron beam [143,366,367], such that the electric and magnetic forces are applied to beam electrons in opposition to each other [143]. The Wien filter is a relatively simple monochromator and allows the beam to continue travelling on a straight trajectory without bending [369, 370].

The electric and magnetic fields of the monochromator are balanced in opposing directions such that electrons at the selected average velocity travelling on the optic axis remain undeflected, while other electrons are deflected according to their energy difference and distance from the optic axis (Figure B.1(a)) [143, 367]. An electron with higher velocity than desired experiences a higher magnetic field and is deflected towards the negative electrostatic electrode, which reduces its kinetic energy before deflecting it back to the optic axis with a reduced velocity [367]. Similarly, an electron with a lower velocity on the optic axis will experience a dominant electric field and be deflected towards the positive electrode until its velocity is increased and the magnetic force dominates and returns it towards the optic axis [367].

Electrons entering the monochromator off-axis are deflected towards the centre and onwards to the opposite electrode, then return to their original axis; the fraction of this cycle that is completed depends on the monochromator excitation [367]. At an excitation value of $2\pi \approx 6.28$, an off-axis electron has returned to its original

axis and there is an achromatic focus (Figure B.1(b)) [143]. The velocity component perpendicular to the EM forces is not affected [143]. The maximum possible excitation on the Titan microscope is 2.2 [367]. After π radians of a cycle, the monochromator produces a chromatic line focus, offset by $\pi/2$ from the achromatic focus [143].

Increasing the excitation in the monochromator increases the strength of the deflection fields and bends the electrons more strongly, resulting in a higher dispersion at the monochromator exit plane [367]; the magnification of the source onto the exit plane is also decreased when the excitation goes up, providing a smaller source image and better resolution at higher excitation, up to a limit (excitation ≈ 1.8) where aberrations from the filter begin to impair the resolution [370]. Regardless of the excitation used, it is desirable to create an image of the source at the exit plane, but with different excitations, the electrons undergo different amounts of deflection. The GL is used in concert with the monochromator excitation to keep a dispersed image of the source focused at the exit plane by modifying the convergence of electrons entering the monochromator as the excitation is changed (Figure B.1(c)) [366,367]. The strength of the GL is decreased as the excitation increases in order to maintain the focus at the exit plane, which also results in a reduction of the GL aberrations when the monochromator is excited [367,370]. The strongest aberration in the GL is coma from misalignment of the tip with the GL and monochromator entrance aperture [366].

Use of a single Wien filter results in a rainbow illumination on the sample: the beam becomes a line oriented in the dispersion direction, with a spectrum of energies down the line [369]. High energy resolution with the Wien filter is obtained by using a slit or aperture placed in the monochromator exit plane or a conjugate plane to cut this rainbow of electron energies [366, 367]. The electric and magnetic fields of the single Wien filter provide focusing of the source image in the dispersive direction, producing a broad blurred source image in the non-dispersive direction. Adding an electric quadrupole system to the filter makes it a double-focusing Wien filter with equal focusing power in the dispersive and non-dispersive directions, a state which is much more amenable to using the image of the source for imaging a sample [367].

For many applications, a high current is desired to obtain a good signal-to-noise ratio (SNR); the FEI monochromator is optimized to maximize the current passing through the filter by using a short filter with flexible excitation and potential settings [370]. However, when the monochromator is set up to allow the maximum current to go through, aberrations in the FEG, GL, and the filter limit the obtainable resolution. Therefore two modes of operation are defined in the monochromator: accelerating mode, and decelerating mode [366]. The key differences in these modes are the relative potentials at which the monochromator and GL are held. At a low monochromator potential, the dispersion is higher, reducing the stochastic image blurring, but the Boersch effect is increased because the electrons travel slower and spend more time in the filter [368]. Accelerating mode provides a higher resolution at the expense of reduced current; decelerating mode provides a lot of current, but lower resolution [366].

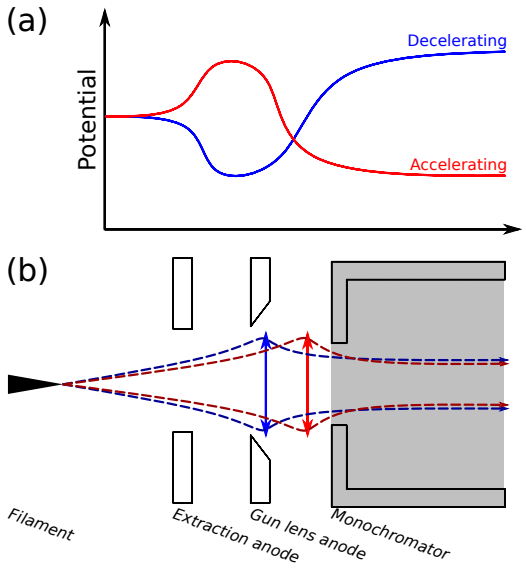

Figure B.2: Schematic of accelerating and decelerating modes of the FEI monochromator. (a) Sketch of the relative potentials applied at each part of the gun lens in relation to the schematic in (b); (b) components of the FEI gun lens. Red and blue arrows show where the lensing action of accelerating and decelerating modes takes place, respectively. Inspired by [367].

Accelerating Mode

In accelerating mode, the Wien filter is held at a lower potential than the GL, which is at a higher potential than the extraction anode (Figure B.2: red) [367]. Electrons travel faster through the GL and the lensing action of the GL is closer to the monochromator entrance aperture, so the lens collects a smaller portion of the emission cone from the FEG [366, 367]. The smaller acceptance angle means that contributions from aberrations of the GL and Wien filter are reduced, and the lower current reduces the Coulomb interactions and Boersch effect within the GL and monochromator, so higher energy resolution can be obtained [366, 367]. With the monochromator at lower potential, electrons travel more slowly through the filter, so the dispersing action is greater [366, 367]. However, more time spent in the filter increases the sensitivity of the beam to instabilities in the filter fields, making alignments difficult to reproduce [367].

The filter operating in accelerating mode has a theoretical energy resolution of 0.016 eV with 4 nA of beam current [366]. The accelerating mode of operation is only available with the SFEG and is disabled in microscopes with XFEGs.

Decelerating Mode

In decelerating mode, the GL electrode is at lower potential than the extraction anode and the monochromator is at higher potential relative to both (Figure B.2: blue) [367]. The lensing action of the GL is closer to the GL electrode and the tip, capturing a

larger part of the emission cone from the tip with a high acceptance angle [366, 367]. The proximity to the tip also means that the object distance for the GL is half of that for the accelerating GL, resulting in a 2× magnification of the source at the exit plane of the monochromator relative to the accelerating GL [366].

Although the coefficients of spherical and chromatic aberrations of the GL are smaller in decelerating mode, the high acceptance angles mean that these aberrations and parasitic coma associated with tip misalignment have a greater effect on the resolution [366, 367]. The GL aberrations are higher than those of accelerating mode, but as the excitation of the monochromator is increased, the strength of the GL is reduced, thereby reducing the effect of the GL aberrations [366].

A higher beam current passing through the filter also means that Coulomb interactions are increased, further impairing the achievable resolution, increasing the effective source size, and making the Boersch effect more prominent [366, 367]. Decelerating mode is therefore best suited to applications in which a high beam current is desired and the best resolution is not needed [366]. Decelerating mode has a theoretical energy resolution of 0.02 eV with 10 nA of filter current [366]. The higher brightness of the XFEG means that the beam diameter can be reduced relative to the SFEG, while maintaining the same current, which reduces the acceptance angle and effect of the GL aberrations [367].

B.1.3 Condenser System

After passing through the monochromator, the electron beam is accelerated to its full kinetic energy, 80 keV for the work shown in this thesis, by the accelerator. The accelerator works as a weak lens to pass the image of the exit plane of the monochromator to the plane of the first condenser lens aperture [367]. Following the accelerator, the condenser system is used to form a demagnified image of the source on the specimen [141].

There are three condenser lenses in the Titan system: 'C1', 'C2', and 'C3', as well as a mini-condenser lens and the upper objective lens (Figure B.3(a)) [371]. The plane of the C1 aperture is a conjugate plane of the monochromator's exit plane, so inside the C1 aperture strip, there are a variety of slits used to cut the energy distribution of the dispersed source when the monochromator is turned on [367]. In this thesis, the C2 aperture is sometimes used to cut the energy distribution of the beam, instead of a slit in the C1 aperture plane.

The C1 and C2 lenses are used together to set the spot size of the microscope, which affects the beam current and the demagnification of the source [141, 371, 372]. Increasing the spot number increases the strength of C1, spreading the beam more over the C2 aperture and reducing the amount of current which goes through C2 when C2 is the limiting aperture [371]. A higher spot number therefore decreases the current hitting the sample and increases the demagnification of the source, allowing smaller probes and higher resolution imaging [371]. A series of monochromator spot

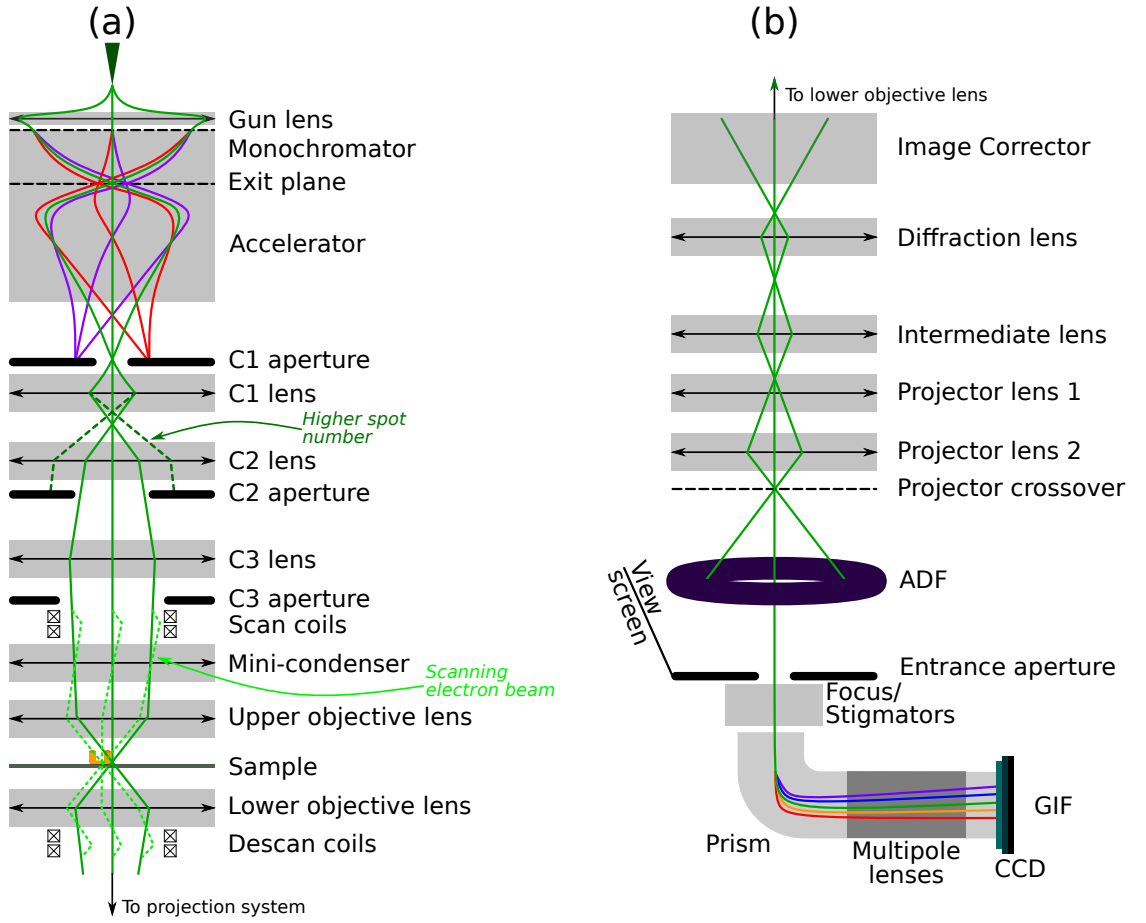

Figure B.3: Schematic of the Titan column. (a) Upper part of the column, showing the energy dispersion inside the monochromator, energy selection using the C1 aperture, spreading of the electron beam by the spot size over the C2 aperture, and the use of the upper objective lens to focus the beam, including also the scan and descan coils for STEM scanning; (b) projection system forming a beam cross-over before the ADF detector and EELS spectrometer. Inspired by [367, 372].

numbers is also available on the Titan because use of the monochromator reduces the achievable demagnification of the source. The monochromator spot numbers use C1 at its maximum strength and C2 and C3 in concert to help further demagnify the source, making C3 the beam-limiting aperture [367, 371].

The C2 and C3 lenses are used to set the convergence angle in probe (STEM) mode, or the illuminated area in TEM mode. In normal spot numbers, increasing the strength of C2 increases the acceptance angle of the C2 aperture and the diameter of the beam entering C3, which changes the convergence angle of the probe hitting the sample and may vary the current slightly [371, 372]. C3 makes the beam roughly parallel before it enters the probe-forming upper objective lens [371]. In normal operation modes in STEM the C2 lens is only weakly excited and there is a virtual source image between C2 and C3; this reduces the aberrations from the condenser

system in the probe, but limits the accessible range of convergence angles [372].

The minicondenser lens does not operate in nanoprobe mode, the mode most commonly used for STEM imaging, but is primarily used in microprobe mode to make larger parallel beams in TEM [371, 372].

The upper objective lens is the probe-forming lens; it takes the roughly-parallel illumination from C3 and focuses it into a STEM probe [141, 371]. The spatial resolution of the STEM image is determined by the size of the probe on the specimen, which is determined by the demagnification of the source in the condenser system and contributions from aberrations of the objective lens [141]. Scanning of the electron beam is achieved using deflection coils above the objective lens, to which an AC signal is applied according to the scan parameters [141, 373].

B.1.4 Projection System

After the sample, the lower objective lens transfers the image to the projection system, which consists of the diffraction lens, the intermediate lens, and two projector lenses, 'P1' and 'P2' (Figure B.3(b)) [372]. These four lenses in the projection system keep the image or diffraction pattern in focus, provide the correct magnification and rotation of the image or diffraction pattern, and place a cross-over in the differential pumping aperture between the column and the projection chamber or spectrometer [372]. In the Titan used for this thesis, there is also an image corrector, which corrects aberrations in TEM mode, but in STEM primarily passes the beam onwards down the column.

Beam shift from the scan coils above the specimen can cause movement of the cross-over after the projection chamber, which is seen as an apparent shift in energy of the spectrum, since it is this cross-over which the spectrometer images [372]. Therefore it is necessary to undo the effect of the beam shift from the scan coils using the image deflection coils below the sample, in order to return the beam to the optic axis [372, 373]. The descan coils are below the lower objective lens and keep the diffraction pattern stationary while the beam is scanning. Descan coil misalignment causes the object point of the spectrometer to move, resulting in movement of the spectrum across the spectrometer camera or the addition of aberrations towards the sides of large field-of-view SIs as the object point moves off the spectrometer axis [138].

B.1.5 Annular Dark-Field Detector

As the electron beam is scanned over the sample, the STEM image is formed by integrating the intensity of electrons which are scattered to high enough angles to hit an annular dark-field (ADF) detector [141]. The scattering angles which are detected depends on the camera length setting. The camera length determines the collection angles of annular detectors and the spectrometer, and the magnification of the diffraction pattern onto the viewing screen or camera.

The ADF detector is an annulus composed of scintillator material coupled to a

light pipe and photo-multiplier tube; it measures the total electron signal scattered to angles between the inner and outer detector radius (10-50 mrad for ADF, 50-150 mrad for high-angle ADF (HAADF) [147]), allowing unscattered electrons or electrons scattered to angles lower than the inner radius of the detector to continue propagating through the column, potentially to be collected by an EELS spectrometer [141].

B.1.6 Spectrometer

The transmitted electron beam passes through the centre of the ADF and is collected by the EELS spectrometer. The object of the spectrometer lenses is the demagnified image of the probe that is present in the cross-over after the projection system; the spectrometer turns this object into a line spectrum dispersed according to energy, and images this spectrum onto the EELS camera or onto a mechanical slit for energy-filtered imaging [141, 143]. The EELS spectrum recorded on the detector is a convolution of the spectrum with the image of this object point [143]. This image must be kept small to keep good energy resolution in the spectrometer and reduce off-axis aberrations [143, 374].

In STEM mode, the collection angle of the spectrometer is determined by the combination of the camera length and the size of the spectrometer entrance aperture (SEA) used [374]. A small aperture limits the collection angle and reduces the effect of lens aberrations inside the spectrometer [141]. The Gatan Imaging Filter (GIF Tridiem [375, 376]) on the Titan is a magnetic prism spectrometer combined with an energy-filtering imaging system [374]. The electrons that make it into the SEA enter a magnetic sector prism with a 90° bend [141, 143], throughout which a magnetic field is applied perpendicular to the electron beam path and the electrons travel through a circular arc with a radius of curvature according to their kinetic energy [138, 141, 143]. The magnetic prism gives a linear energy dispersion over a wide range of energies [143] and focuses electrons entering at different angles to form a line spectrum in the dispersion plane [141, 143].

After the magnetic prism, the GIF has a mechanical energy-selecting slit to select part of the spectrum and transmit only electrons which have lost a certain amount of energy, either reforming an energy-filtered image or integrating the transmitted beam to acquire a serial spectrum by sweeping through energy ranges [141, 143]. The GIF possesses several multipole lenses after the slit for correcting aberrations and distortions introduced by the magnetic prism, magnifying the dispersion or reforming an energy-filtered image and projecting it into a charge-coupled device (CCD) array [141, 143]. Magnification of the line spectrum which comes out of the magnetic prism is necessary to achieve the high dispersion required for low-loss EELS studies.

Each spectrum in a spectrum image is collected on a 2D detector after the GIF. After dispersion and projection from the prism, the electron beam hits a thin scintillator [143, 168]. The scintillator emits light when it is hit by an electron, converting electron signal to photon signal; the light is collected by either fibre optics or a system

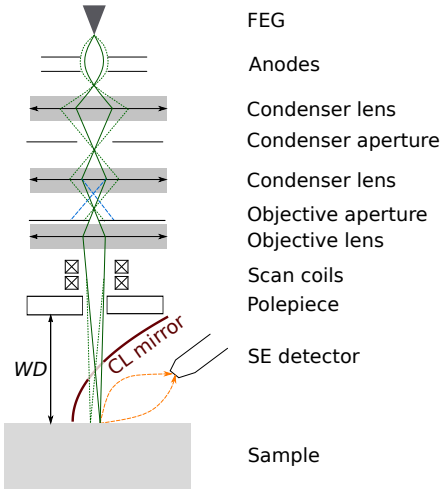

Figure B.4: Schematic of an SEM column with a CL mirror. Green lines show the electron beam path down the column, blue indicates the spreading of the beam over the objective aperture when the spot size is changed. Orange lines indicate SE emission from the sample. The CL mirror imposes a minimum working distance (WD). Repeated from Figure 2.13. Inspired by [154].

of lenses and projected onto a Peltier-cooled CCD array [143,168]. Photons impacting the CCD excite electron-hole pairs, which accumulate over the duration of the acquisition time, after which they are fed to a read-out circuit row-by-row and the signal is counted and displayed on the acquisition computer as an EELS spectrum [143, 168].

B.2 SEM

The SEM is a relatively simple instrument compared to the complexity of the Titan STEM. Similarly to the STEM column, an SEM possesses an electron gun, condenser system, and objective lens. The gun may be a thermionic gun or a FEG, with an anode to extract and accelerate electrons using voltages up to 30 kV on standard instruments. Electrons are emitted from the filament (cathode) and accelerated to the anode, forming a cross-over near the anode. One or two condenser lenses follow the anode to demagnify the source image and set the spot size [137]. There are two pairs of deflection coils (scan coils) to scan the beam across x and y positions in the sample plane and an objective aperture and objective lens, which focuses the beam onto the sample surface [137]. After the objective lens polepiece, the electron beam traverses free space before hitting the sample [137]. The working distance (WD) of the SEM is a variable parameter which defines the focal distance of the objective lens. A schematic of the SEM column is shown in Figure B.4.

A FEG-SEM has a higher brightness, smaller probe, and higher spatial resolution than an SEM with a thermionic tip. Down to 1 nm spatial resolution can be obtained in high resolution SEMs [137]. The spot size and objective aperture size are used to

set the beam current on the instrument and both affect the diameter of the probe impacting the sample. A higher spot size decreases the amount of probe current and allows smaller probe diameters [137]. Each SEM usually has an optimal WD for good spatial resolution, but the addition of a CL mirror necessitates a long WD to account for the mirror size. With a parabolic mirror in the SEM chamber, the WD is fixed such that the sample sits at the focal point of the mirror paraboloid. The long WD and high probe currents used for CL imaging of LSPR modes degrade the spatial resolution of the SEM image. Further descriptions of the CL system optics used in this thesis are given in Chapter 2, Section 2.8.4. Without the mirror, an SEM is a flexible instrument with variable working distance and the possibility to go to very high fields of view with a high depth of focus [137].

Appendix C

FDTD Calculations of Sierpinski Fractal Structures

The following figures (Figure C.1 - C.19) show the simulated electric and magnetic field vectors at the indicated peak energy for horizontally and vertically polarized light. The fields were calculated at a small distance above the silver surface in vacuum; all three field components are presented in the figures ($\varepsilon_x, \varepsilon_y$ as streamlines, ε_z as background colour). For all plots, the polarization direction of the excitation light is given by the green arrow.

The electric and magnetic fields are presented for the two lowest energy optical peaks (both peaks are pairs of degenerate modes) of a triangular aperture in a continuous film (spectra (ix) in Figure 3.7(c)) in Figure C.1 and C.2. The electric and magnetic fields for the two lowest energy peaks of a solid G0 triangle (spectra (i) in Figure 3.7(c)) are presented in Figure C.3 and C.4.

The following plots show the electric field vectors for the two lowest energy peaks (see spectra (ii) in Figure 3.7(c)) of a 285 nm G1 fractal with a small central aperture (73 nm) (Figure C.5, C.6); a 285 nm G1 fractal (see spectra (iv) in Figure 3.7(c)) with a large aperture (120 nm, with 10 nm conductive channels) (Figure C.7, C.8); and a 285 nm G1 fractal with no conductive coupling (see spectra (vi) in Figure 3.7(c)) in Figure C.9, C.10.

Figure C.11 presents calculated electric fields for the two lowest energy peaks of a set of iG2 apertures in a solid silver film (spectrum (iv) in Figure 3.13(a)). The electric fields for all identifiable peaks in the G2 fractal response (see spectrum (iii) in Figure 3.13 or (v) in Figure 3.16) are presented in Figure C.12-C.19 in order of decreasing energy.

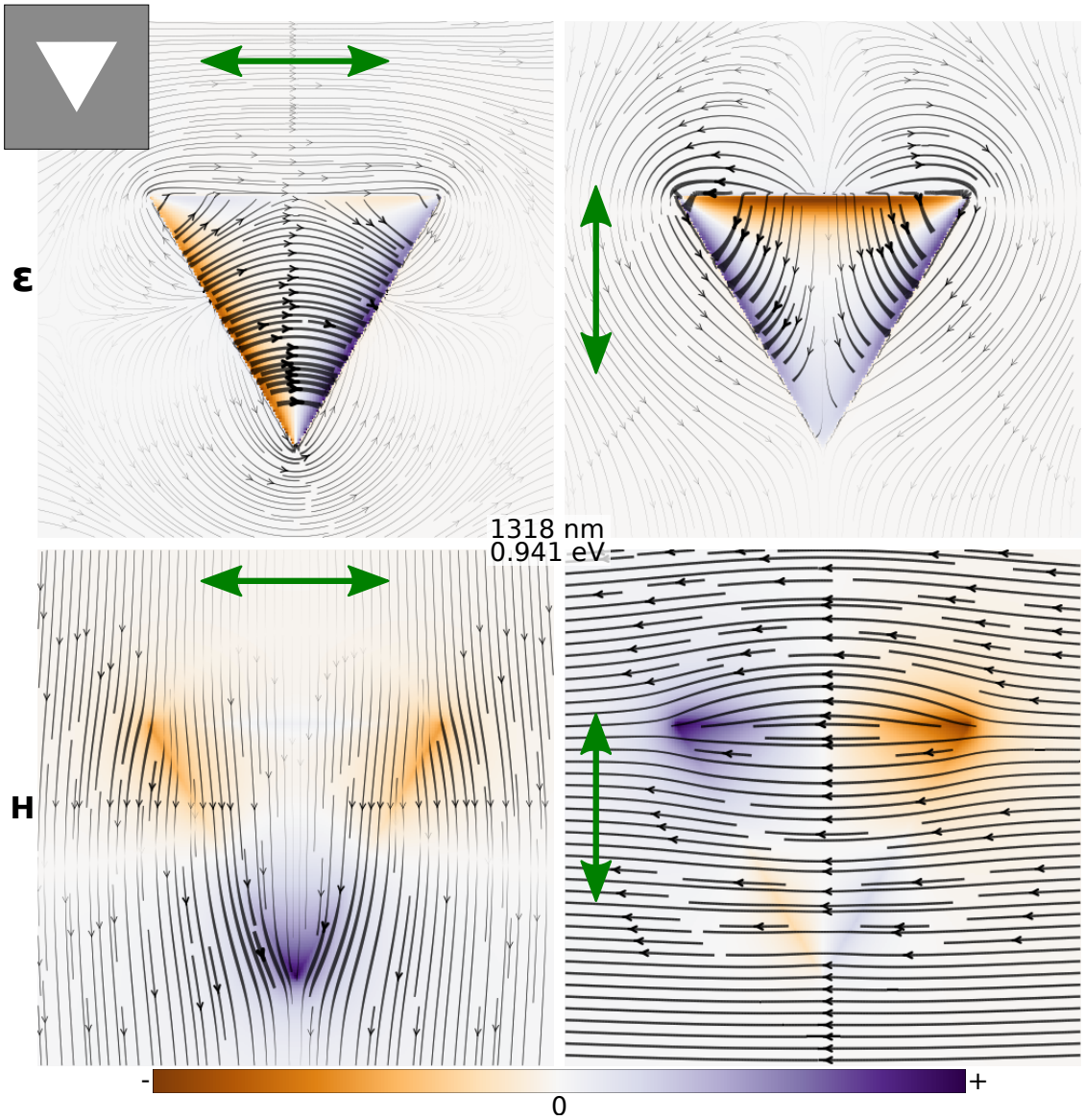

Figure C.1: Simulated electric and magnetic fields for iG0 in a continuous metal film, at 0.941 eV (1318 nm).

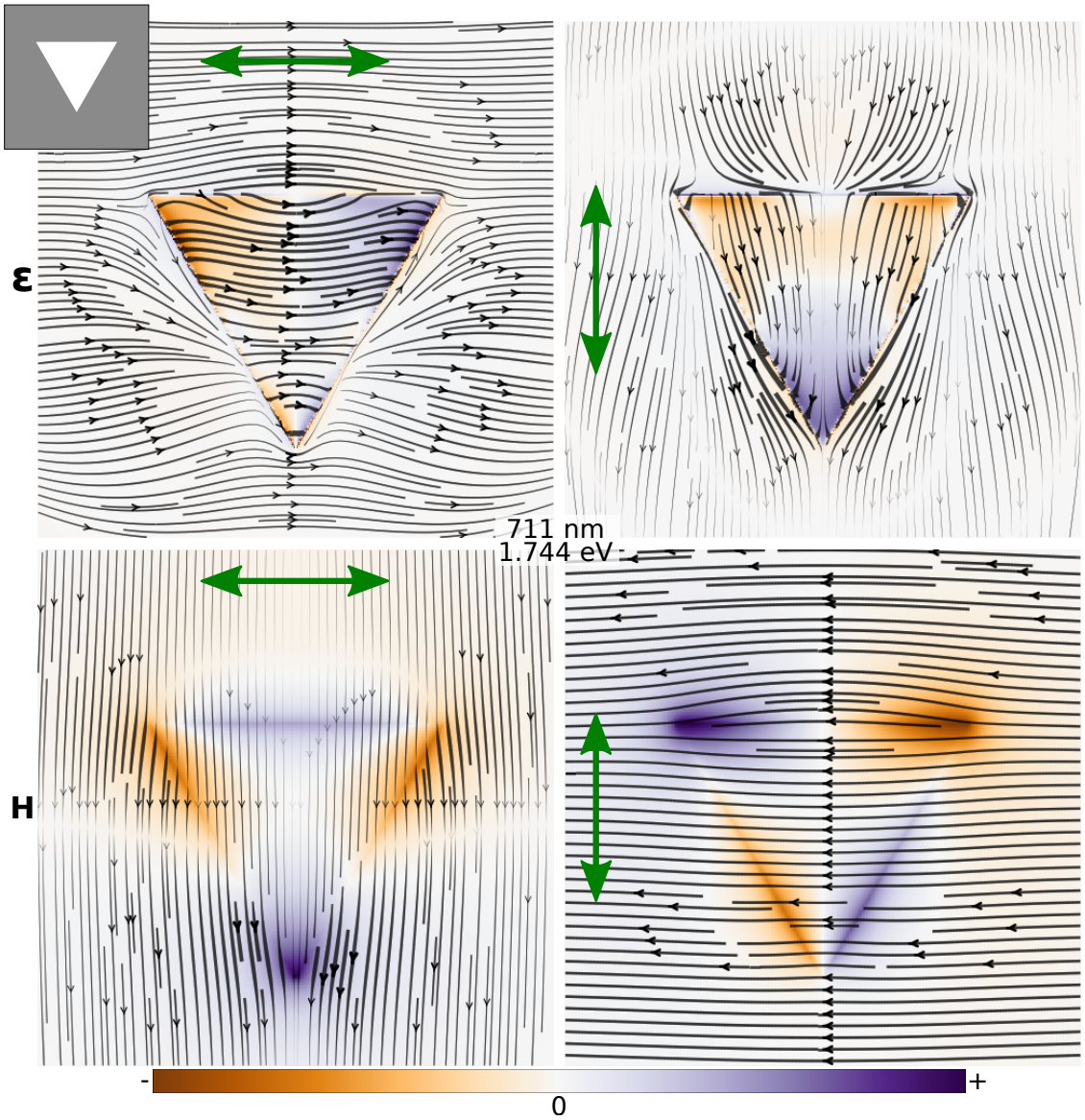

Figure C.2: Simulated electric and magnetic fields for iG0 in a continuous metal film, at 1.744 eV (711 nm).

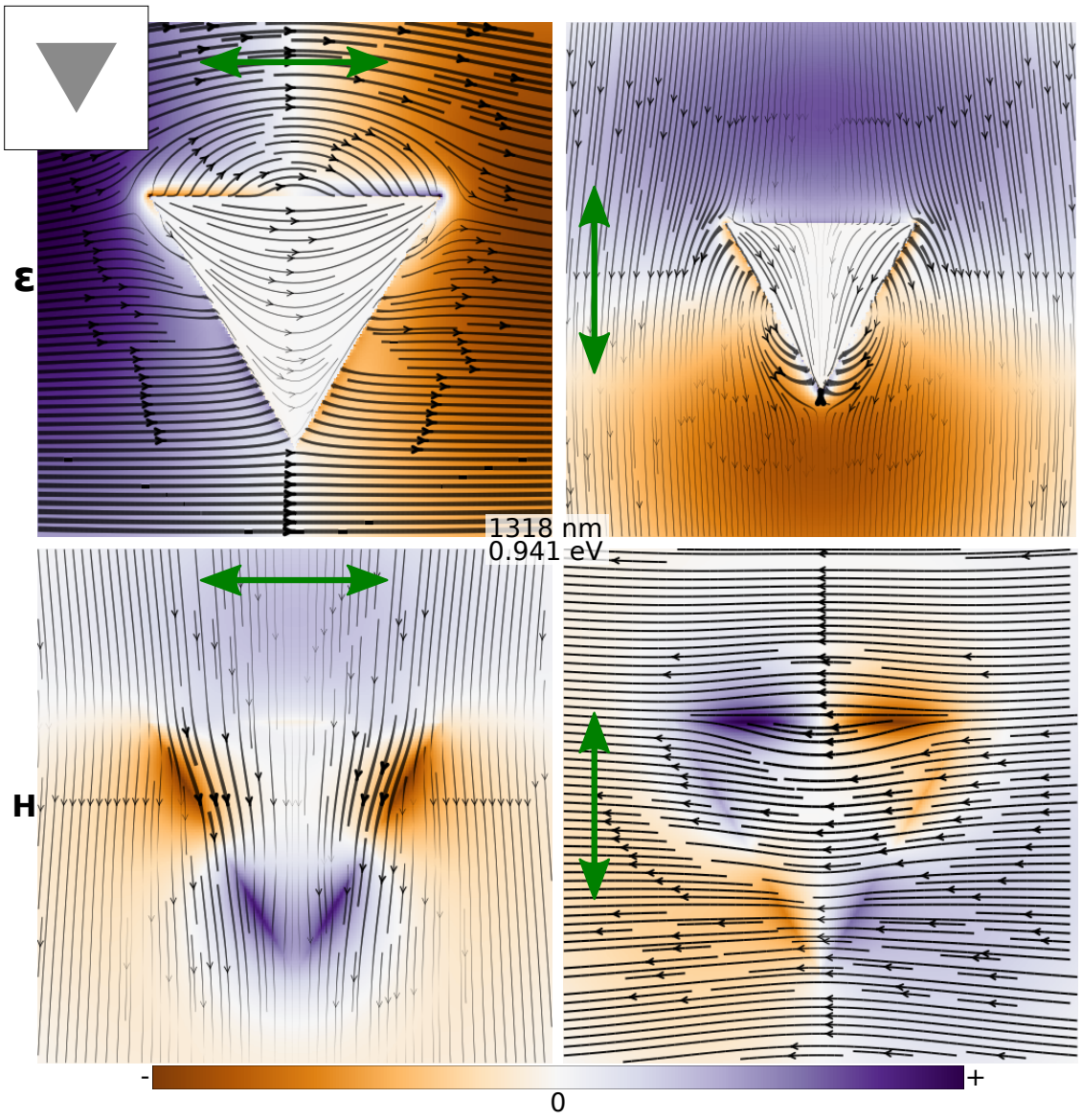

Figure C.3: Simulated electric and magnetic fields for G0, at 0.941 eV (1318 nm).

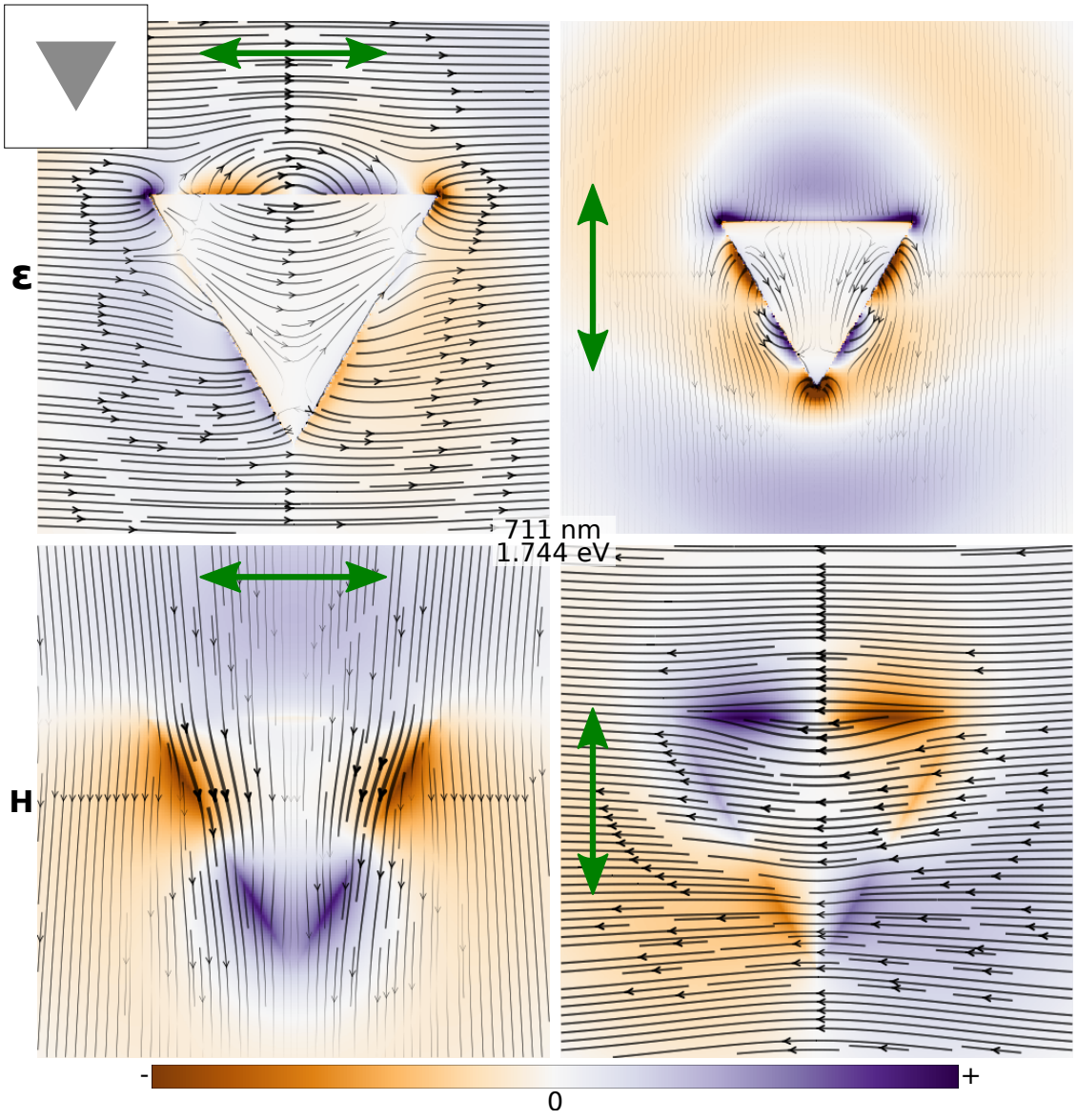

Figure C.4: Simulated electric and magnetic fields for G0, at 1.744 eV (711 nm).

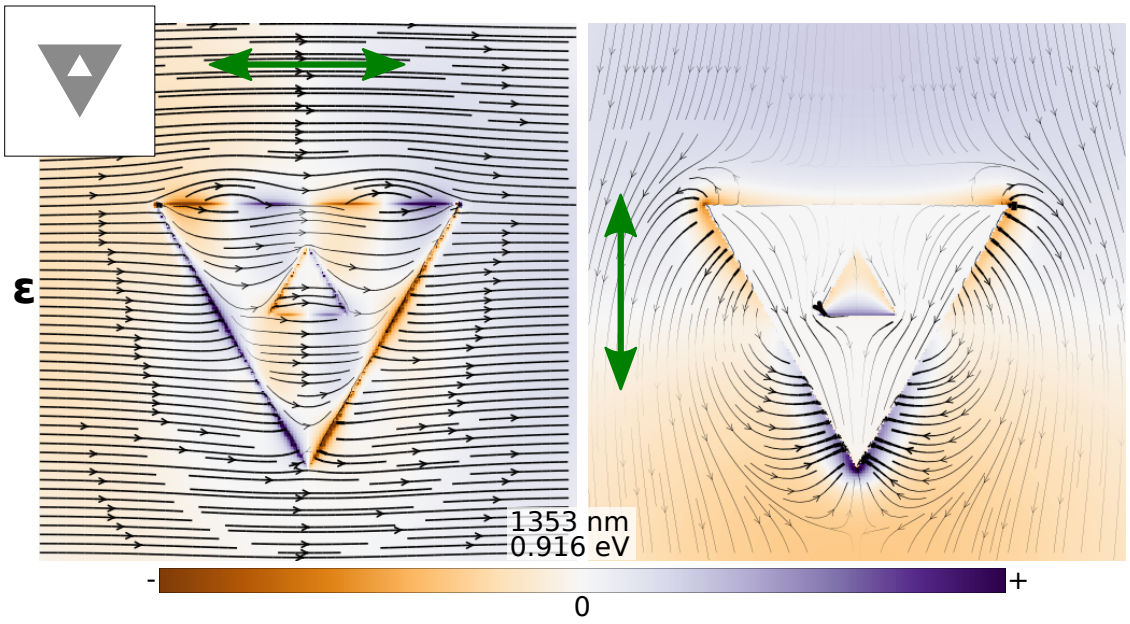

Figure C.5: Simulated electric fields for G1 with a small aperture, at 0.916 eV (1353 nm).

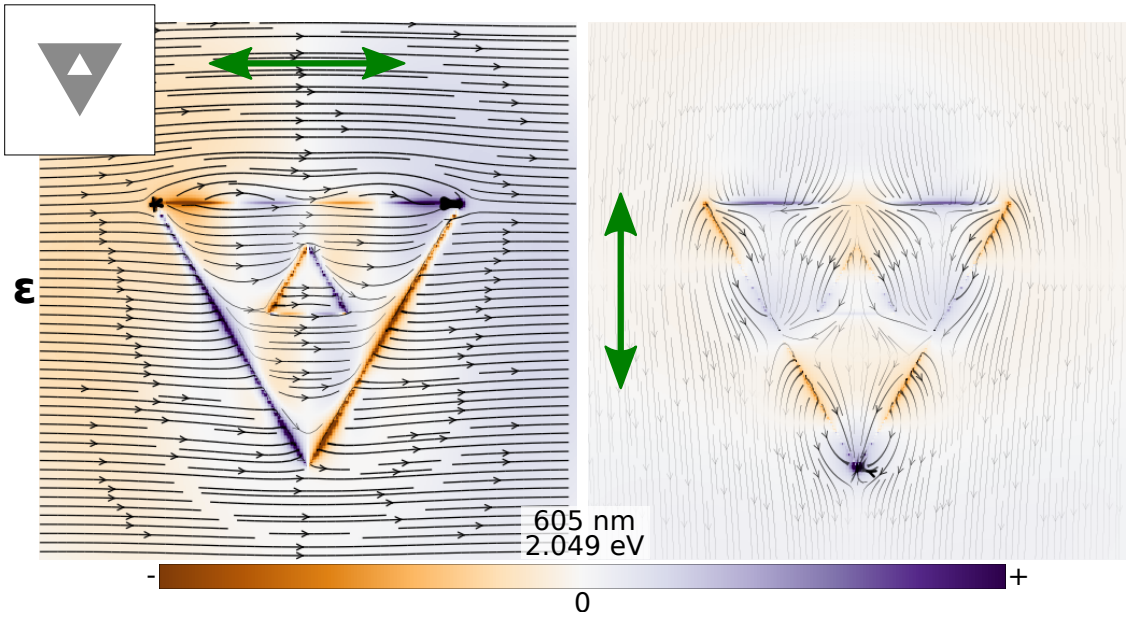

Figure C.6: Simulated electric fields for G1 with a small aperture, at 2.049 eV (605 nm).

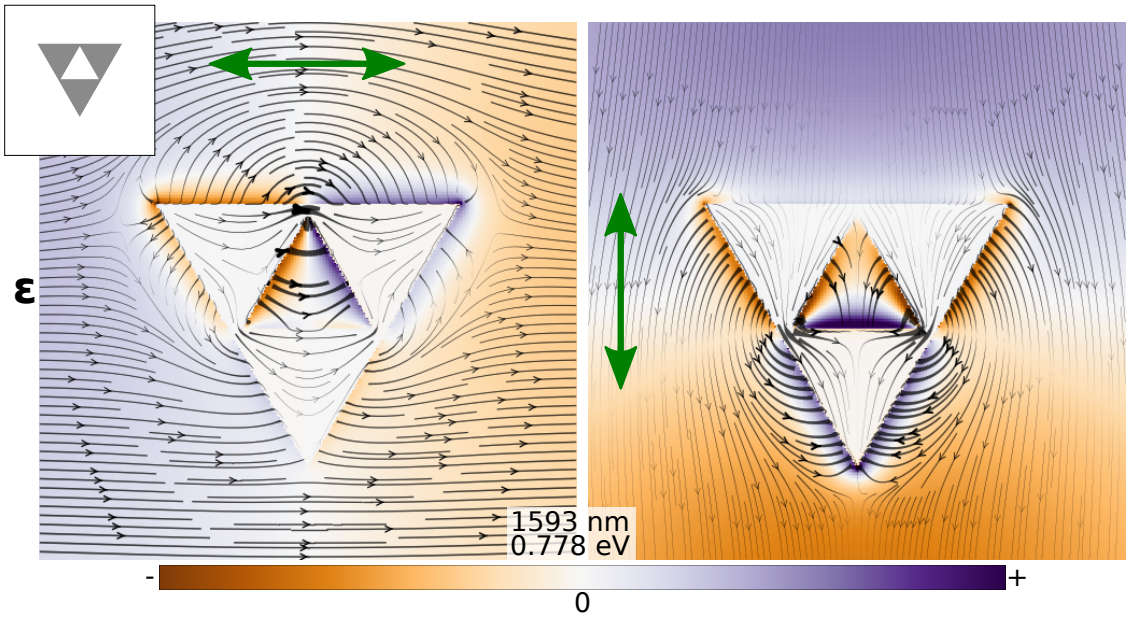

Figure C.7: Simulated electric fields for G1 with a large aperture, at 0.778 eV (1593 nm).

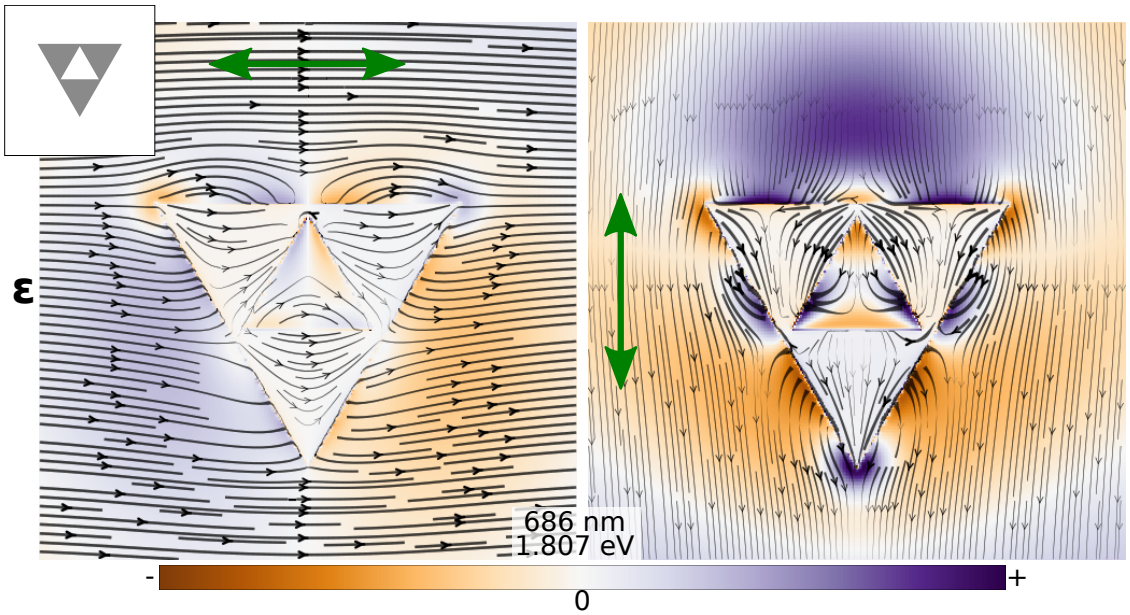

Figure C.8: Simulated electric fields for G1 with a large aperture, at 1.807 eV (686 nm).

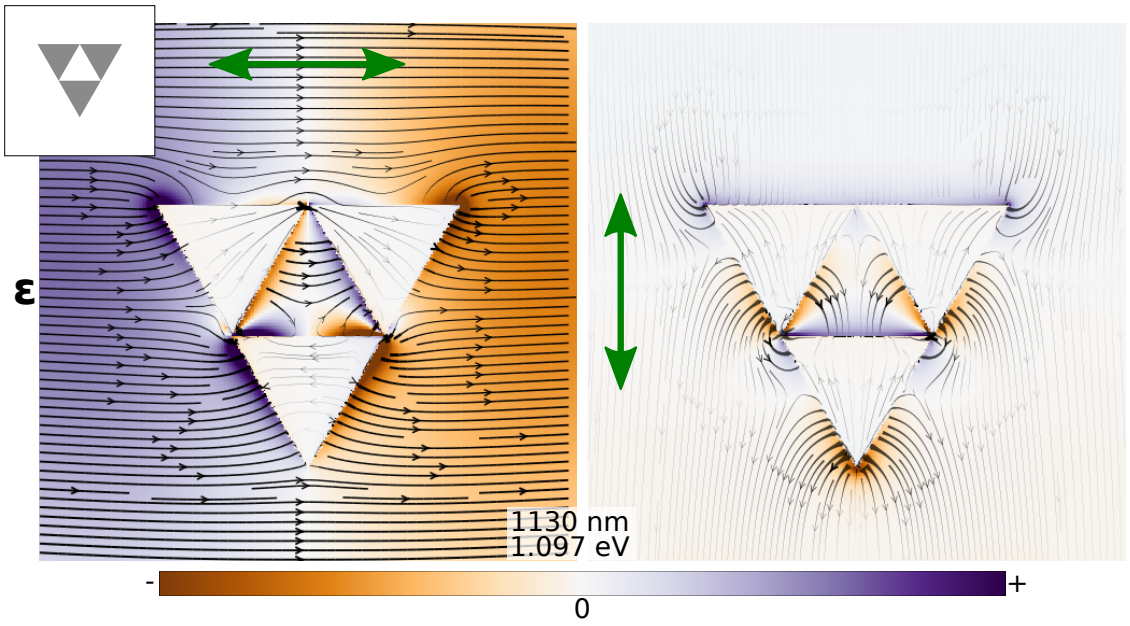

Figure C.9: Simulated electric fields for G1 with a 'perfect' aperture (no conductive coupling), at 1.097 eV (1130 nm).

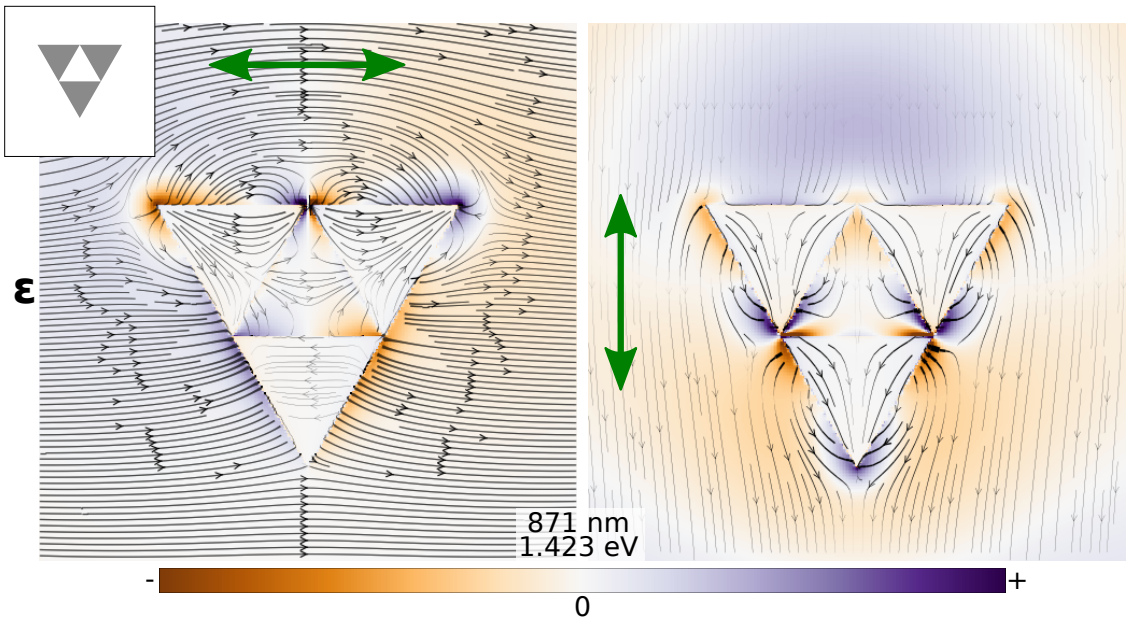

Figure C.10: Simulated electric fields for G1 with a 'perfect' aperture (no conductive coupling), at 1.423 eV (871 nm).

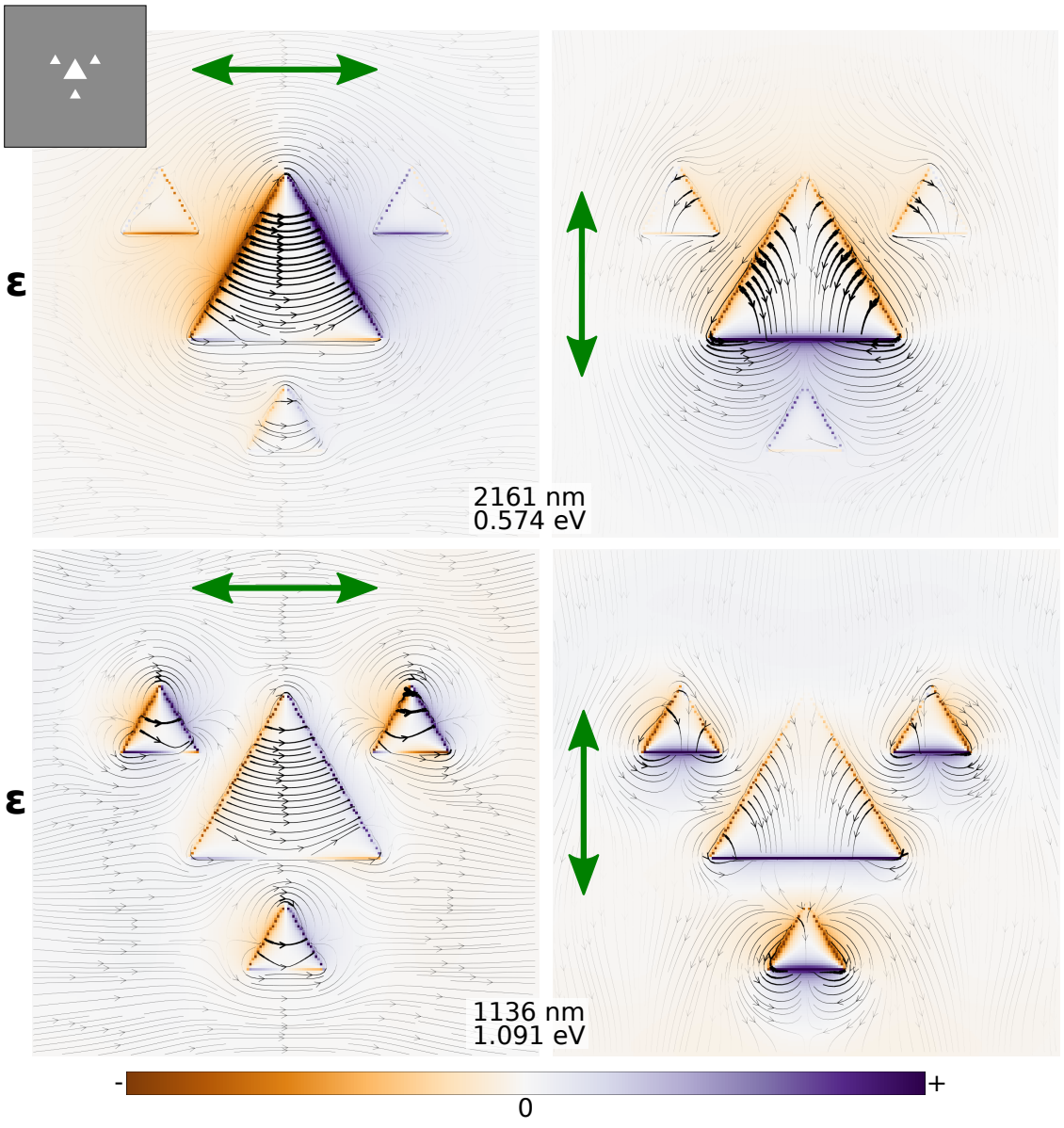

Figure C.11: Simulated electric fields for iG2 apertures in a continuous film, at 0.574 eV (2161 nm) and at 1.091 eV (1136 nm).

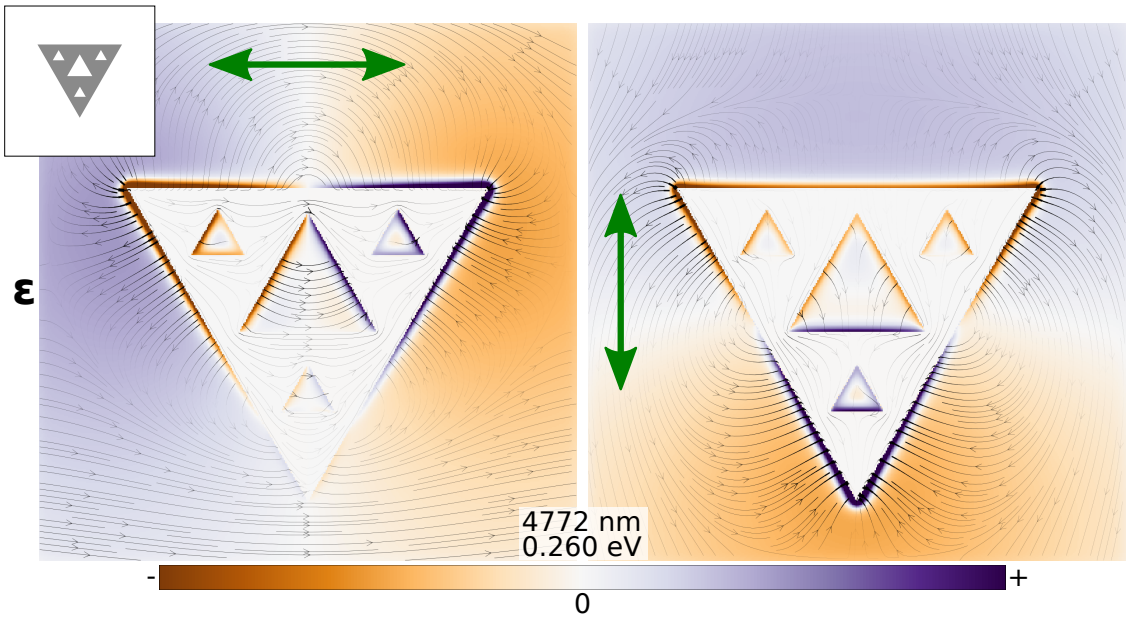

Figure C.12: Simulated electric fields for G2 fractal, at 0.260 eV (4772 nm).

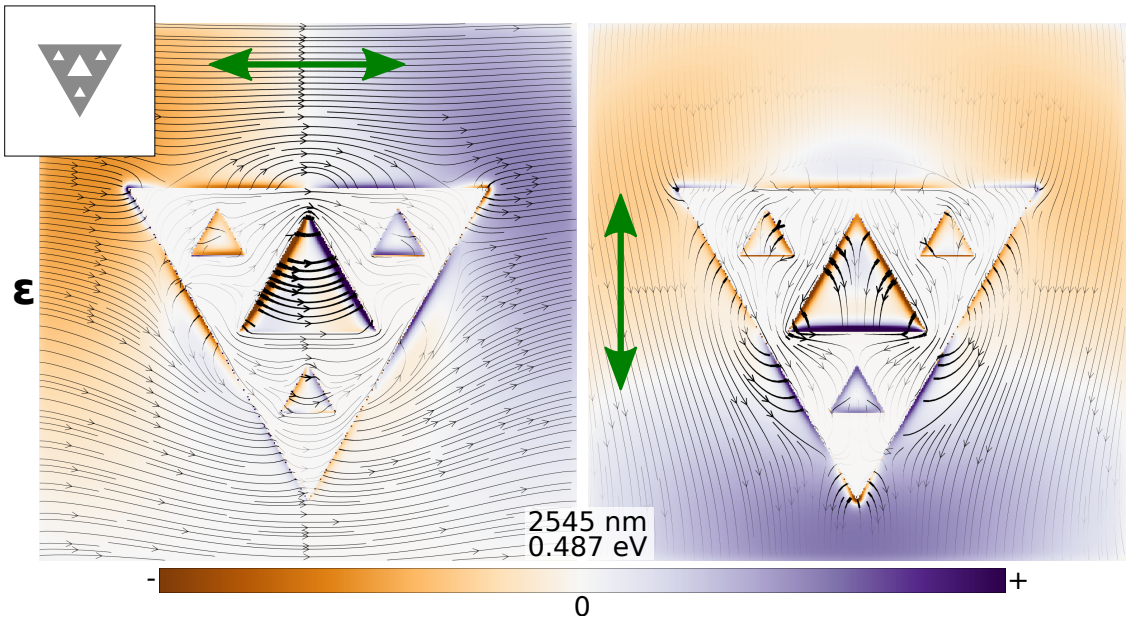

Figure C.13: Simulated electric fields for G2 fractal, at 0.487 eV (2545 nm).

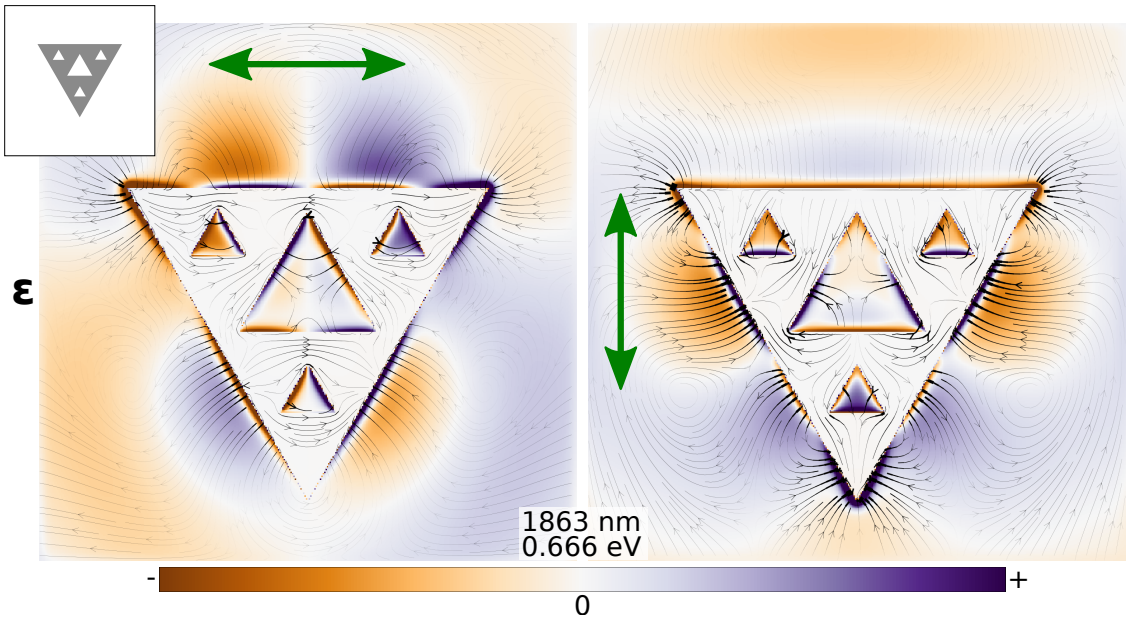

Figure C.14: Simulated electric fields for G2 fractal, at 0.666 eV (1863 nm).

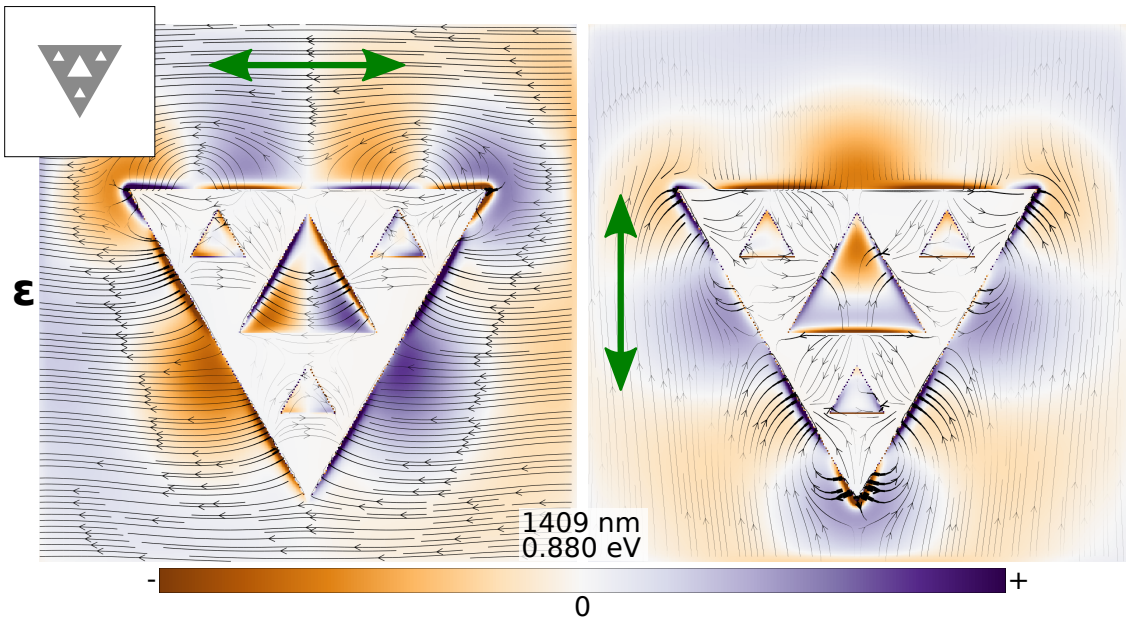

Figure C.15: Simulated electric fields for G2 fractal, at 0.880 eV (1409 nm).

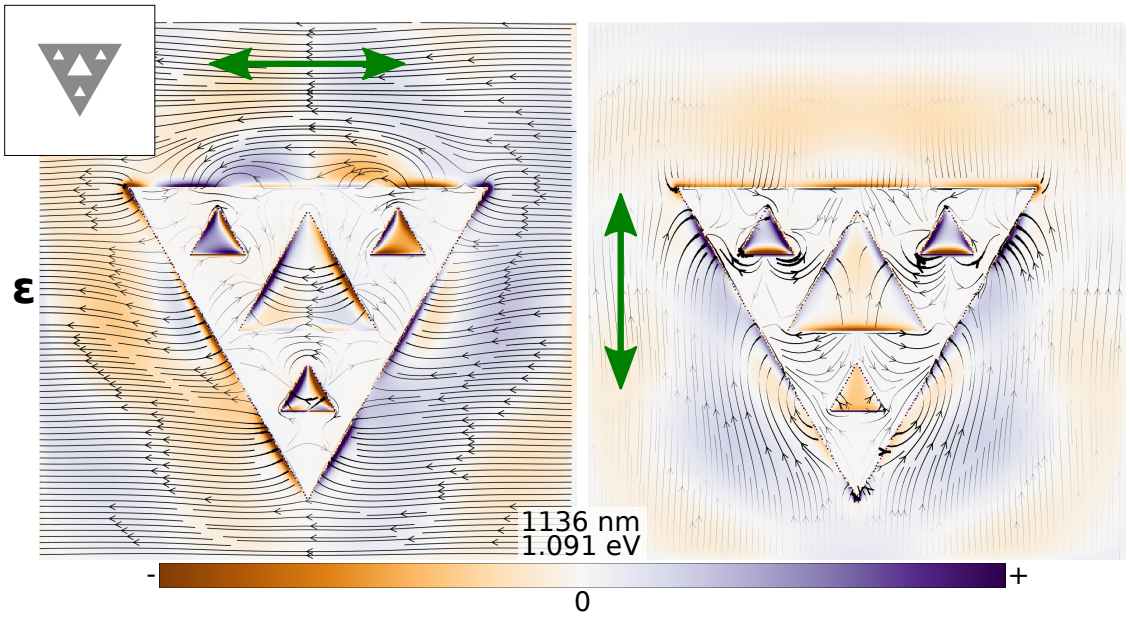

Figure C.16: Simulated electric fields for G2 fractal, at 1.091 eV (1136 nm).

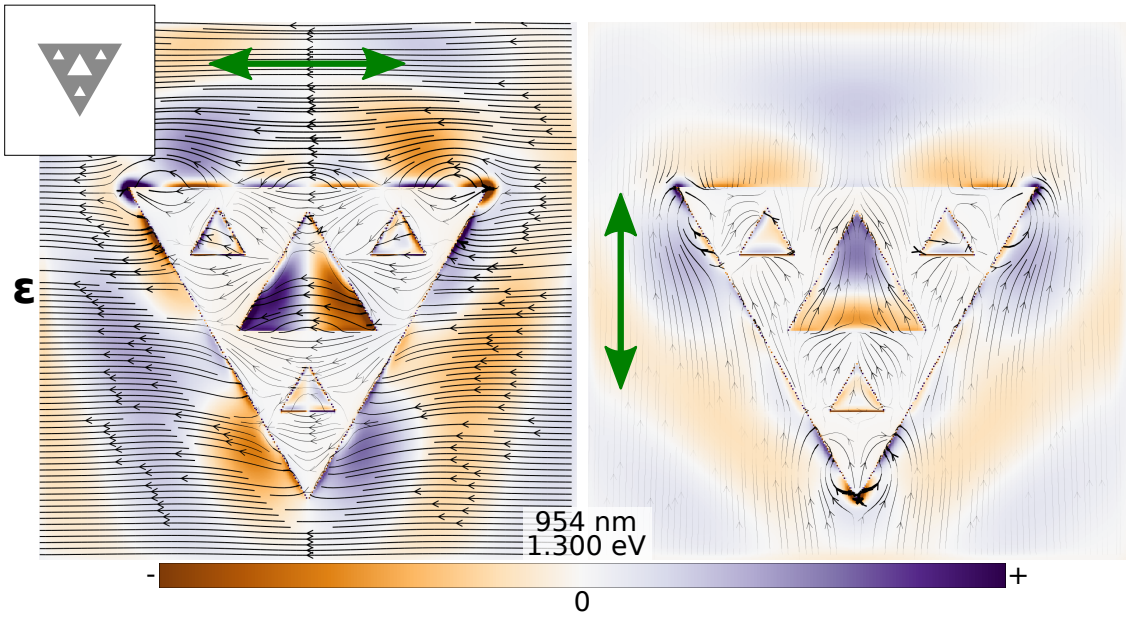

Figure C.17: Simulated electric fields for G2 fractal, at 1.300 eV (954 nm).

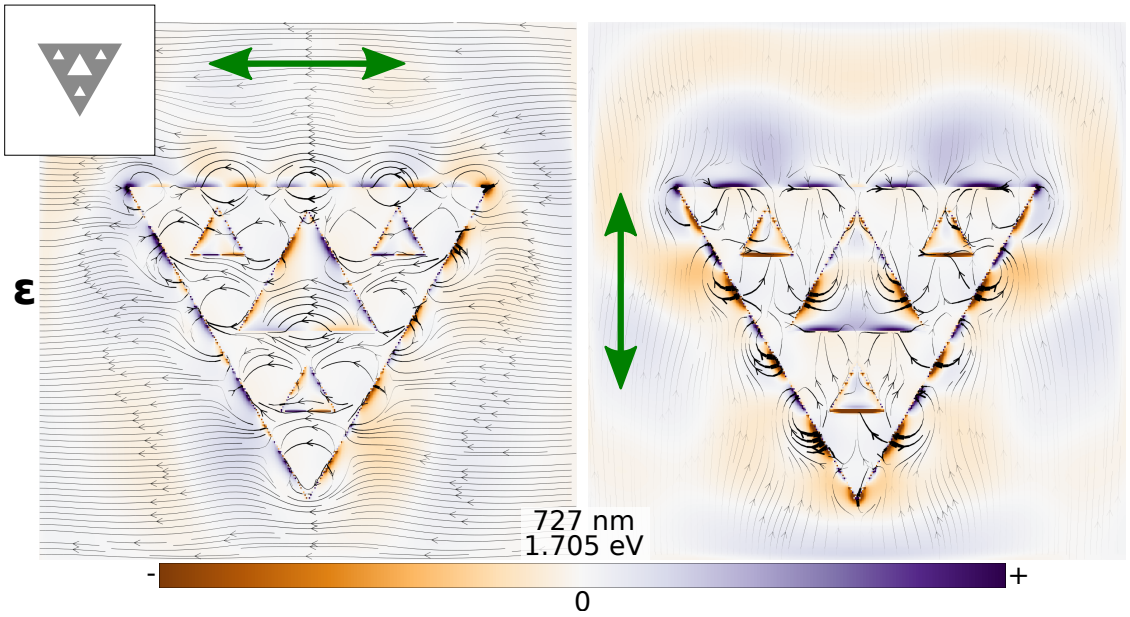

Figure C.18: Simulated electric fields for G2 fractal, at 1.705 eV (727 nm).

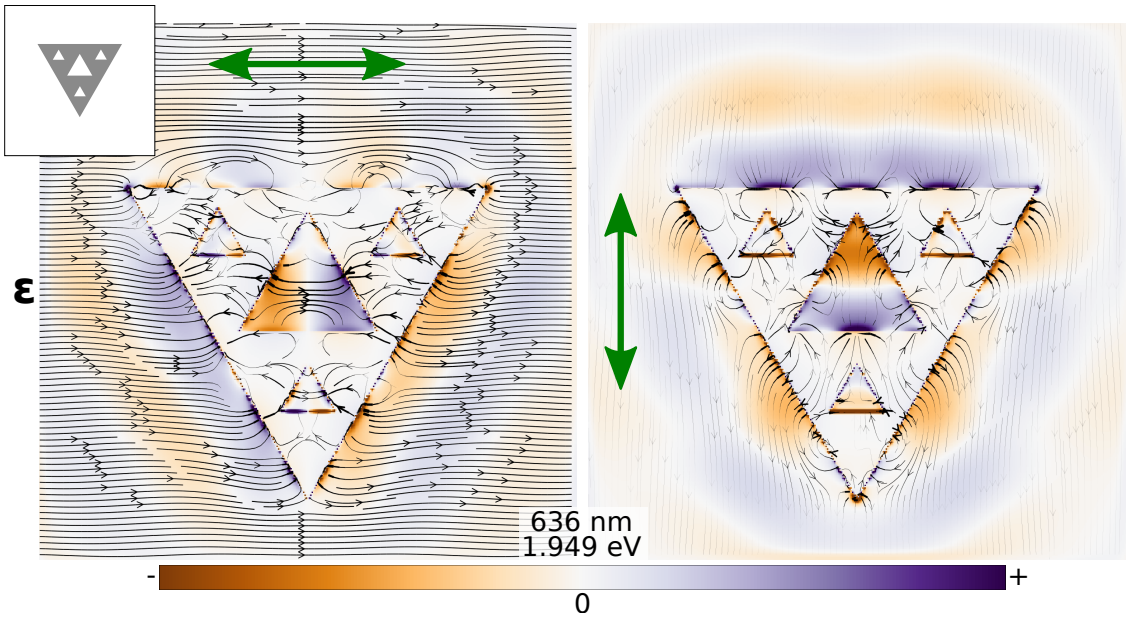

Figure C.19: Simulated electric fields for G2 fractal, at 1.949 eV (636 nm).

Appendix D

Copyright Permissions

This appendix contains copies of the copyright permissions obtained for portions of the content in this thesis, as indicated in the relevant sections of the main text.

IEEE Requesting permission to reuse content from an IEEE publication

The UCLA bi-polar planar-near-field antenna-measurement and diagnostics range

Author: Y. Rahmat-Samii

Publication: IEEE Antennas and Propagation Magazine

Publisher: IEEE

Date: Dec. 1995

Thesis / Dissertation Reuse

The IEEE does not require individuals working on a thesis to obtain a formal reuse license, however, you may print out this statement to be used as a permission grant:

Requirements to be followed when using any portion (e.g., figure, graph, table, or textual material) of an IEEE copyrighted paper in a thesis:

1) In the case of textual material (e.g., using short quotes or referring to the work within these papers) users must give full credit to the original source (author, paper, publication) followed by the IEEE copyright line © 2011 IEEE.
2) In the case of illustrations or tabular material, we require that the copyright line © [Year of original publication] IEEE appear prominently with each reprinted figure and/or table.
3) If a substantial portion of the original paper is to be used, and if you are not the senior author, also obtain the senior author's approval.

Requirements to be followed when using an entire IEEE copyrighted paper in a thesis:

1) The following IEEE copyright/ credit notice should be placed prominently in the references: © [year of original publication] IEEE. Reprinted, with permission, from [author names, paper title, IEEE publication title, and month/year of publication]
2) Only the accepted version of an IEEE copyrighted paper can be used when posting the paper or your thesis on-line.
3) In placing the thesis on the author's university website, please display the following message in a prominent place on the website: In reference to IEEE copyrighted material which is used with permission in this thesis, the IEEE does not endorse any of [university/educational entity's name goes here]'s products or services. Internal or personal use of this material is permitted. If interested in reprinting/republishing IEEE copyrighted material for advertising or promotional purposes or for creating new collective works for resale or redistribution, please go to http://www.ieee.org/publications_standards/publications/rights/rights_link.html to learn how to obtain a License from RightsLink.

If applicable, University Microfilms and/or ProQuest Library, or the Archives of Canada may supply single copies of the dissertation.

BACK CLOSE

Carving Plasmon Modes in Silver Sierpiński Fractals

Author: Isobel C. Bicket, Edson P. Bellido, Danielle M. McRae, et al
Publication: ACS Photonics
Publisher: American Chemical Society
Date: Nov 1, 2019

PERMISSION/LICENSE IS GRANTED FOR YOUR ORDER AT NO CHARGE

This type of permission/license, instead of the standard Terms & Conditions, is sent to you because no fee is being charged for your order. Please note the following:

- Permission is granted for your request in both print and electronic formats, and translations.
- If figures and/or tables were requested, they may be adapted or used in part.
- Please print this page for your records and send a copy of it to your publisher/graduate school.
- Appropriate credit for the requested material should be given as follows: "Reprinted (adapted) with permission from (COMPLETE REFERENCE CITATION). Copyright (YEAR) American Chemical Society." Insert appropriate information in place of the capitalized words.
- One-time permission is granted only for the use specified in your request. No additional uses are granted (such as derivative works or other editions). For any other uses, please submit a new request.

BACK CLOSE WINDOW

Hierarchical Plasmon Resonances in Fractal Structures

Author: Isobel Claire Bicket, Edson Pazur Bellido, Danielle M. McRae, et al
Publication: ACS Photonics
Publisher: American Chemical Society
Date: Apr 1, 2020

PERMISSION/LICENSE IS GRANTED FOR YOUR ORDER AT NO CHARGE

This type of permission/license, instead of the standard Terms & Conditions, is sent to you because no fee is being charged for your order. Please note the following:

- Permission is granted for your request in both print and electronic formats, and translations.
- If figures and/or tables were requested, they may be adapted or used in part.
- Please print this page for your records and send a copy of it to your publisher/graduate school.
- Appropriate credit for the requested material should be given as follows: "Reprinted (adapted) with permission from (COMPLETE REFERENCE CITATION). Copyright (YEAR) American Chemical Society." Insert appropriate information in place of the capitalized words.
- One-time permission is granted only for the use specified in your request. No additional uses are granted (such as derivative works or other editions). For any other uses, please submit a new request.

BACK CLOSE WINDOW

OXFORD UNIVERSITY PRESS LICENSE
TERMS AND CONDITIONS

Feb 11, 2020

This Agreement between Ms. Isobel Bicket ("You") and Oxford University Press ("Oxford University Press") consists of your license details and the terms and conditions provided by Oxford University Press and Copyright Clearance Center.

License Number	4766010509269
License date	Feb 11, 2020
Licensed content publisher	Oxford University Press
Licensed content publication	Microscopy
Licensed content title	Correlative electron energy loss spectroscopy and cathodoluminescence spectroscopy on three-dimensional plasmonic split ring resonators
Licensed content author	Bicket, Isobel C; Bellido, Edson P
Licensed content date	Mar 23, 2018
Type of Use	Thesis/Dissertation

Institution name	
Title of your work	Electron Spectromicroscopy of Multipole Moments in Plasmonic Nanostructures
Publisher of your work	McMaster University
Expected publication date	May 2020
Permissions cost	0.00 CAD
Value added tax	0.00 CAD
Total	0.00 CAD
Title	Electron Spectromicroscopy of Multipole Moments in Plasmonic Nanostructures
Institution name	McMaster University
Expected presentation date	May 2020
Portions	Methods, Results, and Discussion sections, along with Figures 1-6
Requestor Location	Ms. Isobel Bicket 306-1712 Main St W Hamilton, ON L8S1G7 Canada

Attn: Ms. Isobel Bicket

Publisher Tax ID GB125506730

Total 0.00 CAD

Terms and Conditions

STANDARD TERMS AND CONDITIONS FOR REPRODUCTION OF MATERIAL FROM AN OXFORD UNIVERSITY PRESS JOURNAL

1. Use of the material is restricted to the type of use specified in your order details.

2. This permission covers the use of the material in the English language in the following territory: world. If you have requested additional permission to translate this material, the terms and conditions of this reuse will be set out in clause 12.

3. This permission is limited to the particular use authorized in (1) above and does not allow you to sanction its use elsewhere in any other format other than specified above, nor does it apply to quotations, images, artistic works etc that have been reproduced from other sources which may be part of the material to be used.

4. No alteration, omission or addition is made to the material without our written consent. Permission must be re-cleared with Oxford University Press if/when you decide to reprint.

5. The following credit line appears wherever the material is used: author, title, journal, year, volume, issue number, pagination, by permission of Oxford University Press or the sponsoring society if the journal is a society journal. Where a journal is being published on behalf of a learned society, the details of that society must be included in the credit line.

6. For the reproduction of a full article from an Oxford University Press journal for whatever purpose, the corresponding author of the material concerned should be informed of the proposed use. Contact details for the corresponding authors of all Oxford University Press journal contact

can be found alongside either the abstract or full text of the article concerned, accessible from www.oxfordjournals.org Should there be a problem clearing these rights, please contact journals.permissions@oup.com

7. If the credit line or acknowledgement in our publication indicates that any of the figures, images or photos was reproduced, drawn or modified from an earlier source it will be necessary for you to clear this permission with the original publisher as well. If this permission has not been obtained, please note that this material cannot be included in your publication/photocopies.

8. While you may exercise the rights licensed immediately upon issuance of the license at the end of the licensing process for the transaction, provided that you have disclosed complete and accurate details of your proposed use, no license is finally effective unless and until full payment is received from you (either by Oxford University Press or by Copyright Clearance Center (CCC)) as provided in CCC's Billing and Payment terms and conditions. If full payment is not received on a timely basis, then any license preliminarily granted shall be deemed automatically revoked and shall be void as if never granted. Further, in the event that you breach any of these terms and conditions or any of CCC's Billing and Payment terms and conditions, the license is automatically revoked and shall be void as if never granted. Use of materials as described in a revoked license, as well as any use of the materials beyond the scope of an unrevoked license, may constitute copyright infringement and Oxford University Press reserves the right to take any and all action to protect its copyright in the materials.

9. This license is personal to you and may not be sublicensed, assigned or transferred by you to any other person without Oxford University Press’s written permission.

10. Oxford University Press reserves all rights not specifically granted in the combination of (i) the license details provided by you and accepted in the course of this licensing transaction, (ii) these terms and conditions and (iii) CCC’s Billing and Payment terms and conditions.

11. You hereby indemnify and agree to hold harmless Oxford University Press and CCC, and their respective officers, directors, employs and agents, from and against any and all claims arising out of your use of the licensed material other than as specifically authorized pursuant to this license.

12. Other Terms and Conditions:

v1.4

Questions? customercare@copyright.com or +1-855-239-3415 (toll free in the US) or +1-978-646-2777.

Bibliography

[1] M. S. Zubairy, "A Very Brief History of Light," in *Optics in Our Time* (M. D. Al-Amri, M. El-Gomati, and M. S. Zubairy, eds.), pp. 3–24, Cham: Springer International Publishing, 2016.

[2] R. Rashed, "A Pioneer in Anaclastics: Ibn Sahl on Burning Mirrors and Lenses," *Isis*, vol. 81, no. 3, pp. 464–491, 1990.

[3] C. Singer, "Notes on the Early History of Microscopy," *Proc. R. Soc. Med.*, vol. 7, no. Sect_Hist_Med, pp. 247–279, 1914.

[4] I. C. Bicket, "Milford Sound, New Zealand," 2016. JPG file.

[5] "Burning Mirrors." `https://www.math.nyu.edu/~crorres/Archimedes/Mirrors/Tzetzes.html`. Accessed: 2020-02-04.

[6] I. C. Bicket, "Museo Larco silver headdress, Lima, Peru," 2019. JPG file.

[7] J. C. Maxwell, *A Treatise on Electricity and Magnetism*, vol. 1 of *Oxford Classic Texts in the Physical Sciences*. Oxford, New York: Oxford University Press, Dec. 1998.

[8] H. Hertz, *Electric Waves*. Macmillan and Company, 1893. Translation from New York: Dover Publishing Company, 1962.

[9] NASA, "Electromagnetic Spectrum - Introduction." `https://imagine.gsfc.nasa.gov/science/toolbox/emspectrum1.html`, Mar. 2013. Accessed: 2020-02-04.

[10] D. K. Gramotnev and S. I. Bozhevolnyi, "Plasmonics beyond the diffraction limit," *Nat. Photonics*, vol. 4, no. 2, pp. 83–91, 2010.

[11] N. I. Zheludev, "What diffraction limit?," *Nat. Mater.*, vol. 7, no. 6, pp. 420–422, 2008.

[12] A. F. Koenderink, A. Alù, and A. Polman, "Nanophotonics: Shrinking light-based technology," *Science*, vol. 348, no. 6234, pp. 516–521, 2015.

[13] V. J. Sorger, R. F. Oulton, R.-M. Ma, and X. Zhang, "Toward integrated plasmonic circuits," *MRS Bull.*, vol. 37, no. 08, pp. 728–738, 2012.

[14] G. P. Wiederrecht, "Near-field optical imaging of noble metal nanoparticles," *Eur. Phys. J. Appl. Phys.*, vol. 28, no. 01, pp. 3–18, 2004.

[15] K. Ueno, T. Oshikiri, Q. Sun, X. Shi, and H. Misawa, "Solid-State Plasmonic Solar Cells," *Chem. Rev.*, vol. 118, no. 6, pp. 2955–2993, 2018.

[16] C. Huck, M. Tzschoppe, R. Semenyshyn, F. Neubrech, and A. Pucci, "Chemical Identification of Single Ultrafine Particles Using Surface-Enhanced Infrared Absorption," *Phys. Rev. Appl.*, vol. 11, no. 1, p. 014036, 2019.

[17] M. Fan, G. F. S. Andrade, and A. G. Brolo, "A review on the fabrication of substrates for surface enhanced Raman spectroscopy and their applications in analytical chemistry," *Anal. Chim. Acta*, vol. 693, no. 12, pp. 7–25, 2011.

[18] J. Z. Zhang and C. Noguez, "Plasmonic Optical Properties and Applications of Metal Nanostructures," *Plasmonics*, vol. 3, no. 4, pp. 127–150, 2008.

[19] H. Xu, E. J. Bjerneld, M. Käll, and L. Börjesson, "Spectroscopy of Single Hemoglobin Molecules by Surface Enhanced Raman Scattering," *Phys. Rev. Lett.*, vol. 83, no. 21, pp. 4357–4360, 1999.

[20] N. I. Zheludev, "The Road Ahead for Metamaterials," *Science*, vol. 328, no. 5978, pp. 582–583, 2010.

[21] Y. Rahmat-Samii, L. I. Williams, and R. G. Yaccarino, "The UCLA Bi-polar Planar-Near-Field Antenna-Measurement and Diagnostics Range," *IEEE Antennas Propag. Mag.*, vol. 37, no. 6, pp. 16–35, 1995.

[22] British Museum, "The Lycurgus Cup." `https://research.britishmuseum.org/research/collection_online/collection_object_details.aspx?objectId=61219&partId=1`. Accessed: 2019-11-26.

[23] I. Freestone, N. Meeks, M. Sax, and C. Higgitt, "The Lycurgus Cup – A Roman nanotechnology," *Gold Bull.*, vol. 40, no. 4, pp. 270–277, 2007.

[24] J. Molera, C. Bayés, P. Roura, D. Crespo, and T. Pradell, "Key Parameters in the Production of Medieval Luster Colors and Shines," *J. Am. Ceram. Soc.*, vol. 90, no. 7, pp. 2245–2254, 2007.

[25] O. Schalm, V. Van der Linden, P. Frederickx, S. Luyten, G. Van der Snickt, J. Caen, D. Schryvers, K. Janssens, E. Cornelis, D. Van Dyck, and M. Schreiner, "Enamels in stained glass windows: Preparation, chemical composition, microstructure and causes of deterioration," *Spectrochimi. Acta Part B*, vol. 64, no. 8, pp. 812–820, 2009.

[26] M. Faraday, "The Bakerian Lecture: Experimental Relations of Gold (and Other Metals) to Light," *Phil. Trans. R. Soc. Lond.*, vol. 147, pp. 145–181, Jan. 1857.

[27] R. W. Wood, "On a remarkable case of uneven distribution of light in a diffraction grating spectrum," *Philos. Mag. Series 6*, vol. 4, no. 21, pp. 396–402, 1902.

[28] L. Rayleigh, "Note on the remarkable case of diffraction spectra described by Prof. Wood," *Philos. Mag. Series 6*, vol. 14, no. 79, pp. 60–65, 1907.

[29] L. Rayleigh, "On the Dynamical Theory of Gratings," *Proc. R. Soc. A*, vol. 79, no. 532, pp. 399–416, 1907.

[30] L. R. Ingersoll, "Some Peculiarities of Polarization and Energy Distribution by Speculum Gratings.," *Phys. Rev.*, vol. 17, no. 4, pp. 493–501, 1921.

[31] R. W. Wood, "Anomalous Diffraction Gratings," *Phys. Rev.*, vol. 48, no. 12, pp. 928–936, 1935.

[32] D. Pines and D. Bohm, "A Collective Description of Electron Interactions: II. Collective *vs* Individual Particle Aspects of the Interactions," *Phys. Rev.*, vol. 85, no. 2, pp. 338–353, 1952.

[33] D. Bohm and D. Pines, "A Collective Description of Electron Interactions. I. Magnetic Interactions," *Phys. Rev.*, vol. 82, no. 5, pp. 625–634, 1951.

[34] H. Watanabe, "Experimental Evidence for the Collective Nature of the Characteristic Energy Loss of Electrons in Solids–Studies on the Dispersion Relation of Plasma Frequency–," *J. Phys. Soc. Jpn.*, vol. 11, no. 2, pp. 112–119, 1956.

[35] R. H. Ritchie, "Plasma Losses by Fast Electrons in Thin Films," *Phys. Rev.*, vol. 106, no. 5, pp. 874–881, 1957.

[36] R. A. Ferrell, "Predicted Radiation of Plasma Oscillations in Metal Films," *Phys. Rev.*, vol. 111, no. 5, pp. 1214–1222, 1958.

[37] C. J. Powell and J. B. Swan, "Origin of the Characteristic Electron Energy Losses in Aluminum," *Phys. Rev.*, vol. 115, no. 4, pp. 869–875, 1959.

[38] E. A. Stern and R. A. Ferrell, "Surface Plasma Oscillations of a Degenerate Electron Gas," *Phys. Rev.*, vol. 120, no. 1, pp. 130–136, 1960.

[39] W. Steinmann, "Experimental Verification of Radiation of Plasma Oscillations in Thin Silver Films," *Phys. Rev. Lett.*, vol. 5, no. 10, pp. 470–472, 1960.

[40] D. Pines, "Collective Energy Losses in Solids," *Rev. Mod. Phys.*, vol. 28, no. 3, pp. 184–198, 1956.

[41] O. L. Krivanek, N. Dellby, J. A. Hachtel, J.-C. Idrobo, M. T. Hotz, B. Plotkin-Swing, N. J. Bacon, A. L. Bleloch, G. J. Corbin, M. V. Hoffman, C. E. Meyer, and T. C. Lovejoy, "Progress in ultrahigh energy resolution EELS," *Ultramicroscopy*, vol. 203, pp. 60–67, Aug. 2019.

[42] M. A. O'Keefe, "Seeing atoms with aberration-corrected sub-Ångström electron microscopy," *Ultramicroscopy*, vol. 108, no. 3, pp. 196–209, 2008.

[43] P. E. Batson, "A new surface plasmon resonance in clusters of small aluminum spheres," *Ultramicroscopy*, vol. 9, no. 3, pp. 277–282, 1982.

[44] D. Rossouw, M. Couillard, J. Vickery, E. Kumacheva, and G. A. Botton, "Multipolar Plasmonic Resonances in Silver Nanowire Antennas Imaged with a Subnanometer Electron Probe," *Nano Lett.*, vol. 11, no. 4, pp. 1499–1504, 2011.

[45] P. Biagioni, J.-S. Huang, and B. Hecht, "Nanoantennas for visible and infrared radiation," *Rep. Prog. Phys.*, vol. 75, no. 2, p. 024402, 2012.

[46] R. T. Hill, "Plasmonic Biosensors," *Wiley Interdiscip. Rev. Nanomed. Nanobiotechnol.*, vol. 7, no. 2, pp. 152–168, 2015.

[47] J. I. Gersten and A. Nitzan, "Photophysics and photochemistry near surfaces and small particles," *Surf. Sci.*, vol. 158, no. 1, pp. 165–189, 1985.

[48] P. K. Aravind, A. Nitzan, and H. Metiu, "The interaction between electromagnetic resonances and its role in spectroscopic studies of molecules adsorbed on colloidal particles or metal spheres," *Surf. Sci.*, vol. 110, no. 1, pp. 189–204, 1981.

[49] J. W. Attridge and I. A. Shanks, "Long range surface plasma resonance immunoassay," Dec. 1995. US Patent No. US5478755A.

[50] M. W. Foster, "Surface plasmon resonance sensor and methods for the utilization thereof," Jan. 1996. US patent No. US5485277A.

[51] K. Kneipp, Y. Wang, H. Kneipp, L. T. Perelman, I. Itzkan, R. R. Dasari, and M. S. Feld, "Single Molecule Detection Using Surface-Enhanced Raman Scattering (SERS)," *Phys. Rev. Lett.*, vol. 78, no. 9, pp. 1667–1670, 1997.

[52] D. Smith, J. Pendry, and M. Wiltshire, "Metamaterials and Negative Refractive Index," *Science*, vol. 305, no. 5685, pp. 788–792, 2004.

[53] N. Kumar and A. Dixit, "Camouflage and Stealth Technology Based on Nanomaterials," in *Nanotechnology for Defence Applications* (N. Kumar and A. Dixit, eds.), pp. 155–203, Cham: Springer International Publishing, 2019.

[54] D. R. Smith, W. J. Padilla, D. C. Vier, S. C. Nemat-Nasser, and S. Schultz, "Composite Medium with Simultaneously Negative Permeability and Permittivity," *Phys. Rev. Lett.*, vol. 84, no. 18, pp. 4184–4187, 2000.

[55] P. Gay-Balmaz and O. J. F. Martin, "Electromagnetic resonances in individual and coupled split-ring resonators," *J. Appl. Phys.*, vol. 92, no. 5, pp. 2929–2936, 2002.

[56] D. Schurig, J. J. Mock, B. J. Justice, S. A. Cummer, J. B. Pendry, A. F. Starr, and D. R. Smith, "Metamaterial Electromagnetic Cloak at Microwave Frequencies," *Science*, vol. 314, no. 5801, pp. 977–980, 2006.

[57] D. Frank, R. Dennard, E. Nowak, P. Solomon, Y. Taur, and H.-S. P. Wong, "Device scaling limits of Si MOSFETs and their application dependencies," *Proc. IEEE*, vol. 89, no. 3, pp. 259–288, 2001.

[58] Y.-W. Huang, W. T. Chen, P. C. Wu, V. A. Fedotov, N. I. Zheludev, and D. P. Tsai, "Toroidal Lasing Spaser," *Sci. Rep.*, vol. 3, Feb. 2013.

[59] Canadian Centre for Electron Microscopy, "FEI Titan 80-300 LB," 2016. JPEG file. Retrieved from `https://ccem.mcmaster.ca/tem/`.

[60] F. Wooten, "Absorption and Dispersion," in *Optical Properties of Solids*, pp. 42–84, New York; London: Academic Press, 1972.

[61] F. Wooten, "Maxwell's Equations and the Dielectric Function," in *Optical Properties of Solids*, pp. 15–41, New York; London: Academic Press, 1972.

[62] R. Egerton, "Physics of Electron Scattering," in *Electron Energy-Loss Spectroscopy in the Electron Microscope*, pp. 111–229, Boston, MA: Springer US, 3rd ed., 2011.

[63] J. Strong, "Effect of Evaporated Films on Energy Distribution in Grating Spectra," *Phys. Rev.*, vol. 49, no. 4, pp. 291–296, 1936.

[64] U. Fano, "The Theory of Anomalous Diffraction Gratings and of Quasi-Stationary Waves on Metallic Surfaces (Sommerfeld's Waves)," *J. Opt. Soc. Am.*, vol. 31, no. 3, pp. 213–222, 1941.

[65] A. Hessel and A. A. Oliner, "A New Theory of Wood's Anomalies on Optical Gratings," *Appl. Opt.*, vol. 4, no. 10, p. 1275, 1965.

[66] H. Fröhlich and H. Pelzer, "Plasma Oscillations and Energy Loss of Charged Particles in Solids," *Proc. Phys. Soc. A*, vol. 68, no. 6, pp. 525–529, 1955.

[67] S. A. Maier, "Electromagnetics of Metals," in *Plasmonics: Fundamentals and Applications* (S. A. Maier, ed.), pp. 5–19, New York, NY: Springer US, 2007.

[68] H. Ehrenreich and H. R. Philipp, "Optical Properties of Ag and Cu," *Phys. Rev.*, vol. 128, no. 4, pp. 1622–1629, 1962.

[69] F. J. García de Abajo, "Optical excitations in electron microscopy," *Rev. Mod. Phys.*, vol. 82, no. 1, pp. 209–275, 2010.

[70] W. X. Tang, H. C. Zhang, H. F. Ma, W. X. Jiang, and T. J. Cui, "Concept, Theory, Design, and Applications of Spoof Surface Plasmon Polaritons at Microwave Frequencies," *Adv. Opt. Mater.*, vol. 7, no. 1, p. 1800421, 2019.

[71] S. J. Orfanidis, "Oblique Incidence," in *Electromagnetic Waves and Antennas*, pp. 261–322, Rutgers University: Self-published, 2016.

[72] S. J. Orfanidis, "Multilayer Film Applications," in *Electromagnetic Waves and Antennas*, pp. 323–381, Rutgers University: Self-published, 2016.

[73] H. T. Miyazaki and Y. Kurokawa, "Squeezing Visible Light Waves into a 3-nm-Thick and 55-nm-Long Plasmon Cavity," *Phys. Rev. Lett.*, vol. 96, no. 9, p. 097401, 2006.

[74] A. Otto, "Excitation of Nonradiative Surface Plasma Waves in Silver by the Method of Frustrated Total Reflection," *Z. Physik*, vol. 216, no. 4, pp. 398–410, 1968.

[75] E. Kretschmann and H. Raether, "Radiative Decay of Non Radiative Surface Plasmons Excited by Light," *Zeitschrift für Naturforschung A*, vol. 23, no. 12, pp. 2135–2136, 2014.

[76] Y.-Y. Teng and E. A. Stern, "Plasma Radiation from Metal Grating Surfaces," *Phys. Rev. Lett.*, vol. 19, no. 9, pp. 511–514, 1967.

[77] M. Eichelbaum, K. Rademann, R. Müller, M. Radtke, H. Riesemeier, and W. Görner, "On the Chemistry of Gold in Silicate Glasses: Studies on a Non-thermally Activated Growth of Gold Nanoparticles," *Angew. Chem., Int. Ed.*, vol. 44, no. 48, pp. 7905–7909, 2005.

[78] N. Yamamoto, K. Araya, and F. J. García de Abajo, "Photon emission from silver particles induced by a high-energy electron beam," *Phys. Rev. B*, vol. 64, no. 20, p. 205419, 2001.

[79] E. P. Bellido, A. Manjavacas, Y. Zhang, Y. Cao, P. Nordlander, and G. A. Botton, "Electron Energy-Loss Spectroscopy of Multipolar Edge and Cavity Modes in Silver Nanosquares," *ACS Photonics*, vol. 3, no. 3, pp. 428–433, 2016.

[80] M. Kociak, O. Stéphan, A. Gloter, L. F. Zagonel, L. H. G. Tizei, M. Tencé, K. March, J. D. Blazit, Z. Mahfoud, A. Losquin, S. Meuret, and C. Colliex,

"Seeing and measuring in colours: Electron microscopy and spectroscopies applied to nano-optics," *C. R. Phys.*, vol. 15, no. 23, pp. 158–175, 2014.

[81] W. Steinmann, "Optical Plasma Resonances in Solids," *Phys. Status Solidi B*, vol. 28, no. 2, pp. 437–462, 1968.

[82] R. B. Pettit, J. Silcox, and R. Vincent, "Measurement of surface-plasmon dispersion in oxidized aluminum films," *Phys. Rev. B*, vol. 11, no. 8, pp. 3116–3123, 1975.

[83] N. Zabala, A. Rivacoba, and P. M. Echenique, "Coupling effects in the excitations by an external electron beam near close particles," *Phys. Rev. B*, vol. 56, no. 12, pp. 7623–7635, 1997.

[84] E. Prodan, C. Radloff, N. J. Halas, and P. Nordlander, "A Hybridization Model for the Plasmon Response of Complex Nanostructures," *Science*, vol. 302, no. 5644, pp. 419–422, 2003.

[85] P. Nordlander, C. Oubre, E. Prodan, K. Li, and M. I. Stockman, "Plasmon Hybridization in Nanoparticle Dimers," *Nano Lett.*, vol. 4, no. 5, pp. 899–903, 2004.

[86] S. J. Orfanidis, "Radiation Fields," in *Electromagnetic Waves and Antennas*, pp. 709–738, Rutgers University: Self-published, 2016.

[87] F. Hao, E. M. Larsson, T. A. Ali, D. S. Sutherland, and P. Nordlander, "Shedding light on dark plasmons in gold nanorings," *Chem. Phys. Lett.*, vol. 458, no. 4-6, pp. 262–266, 2008.

[88] J. P. Kottmann and O. J. F. Martin, "Retardation-induced plasmon resonances in coupled nanoparticles," *Opt. Lett.*, vol. 26, no. 14, pp. 1096–1098, 2001.

[89] F.-P. Schmidt, A. Losquin, F. Hofer, A. Hohenau, J. R. Krenn, and M. Kociak, "How Dark Are Radial Breathing Modes in Plasmonic Nanodisks?," *ACS Photonics*, vol. 5, no. 3, pp. 861–866, 2018.

[90] J. van de Groep, T. Coenen, S. A. Mann, and A. Polman, "Direct imaging of hybridized eigenmodes in coupled silicon nanoparticles," *Optica*, vol. 3, no. 1, pp. 93–99, 2016.

[91] A. L. Koh, K. Bao, I. Khan, W. E. Smith, G. Kothleitner, P. Nordlander, S. A. Maier, and D. W. McComb, "Electron Energy-Loss Spectroscopy (EELS) of Surface Plasmons in Single Silver Nanoparticles and Dimers: Influence of Beam Damage and Mapping of Dark Modes," *ACS Nano*, vol. 3, no. 10, pp. 3015–3022, 2009.

[92] F. Wen, Y. Zhang, S. Gottheim, N. S. King, Y. Zhang, P. Nordlander, and N. J. Halas, "Charge Transfer Plasmons: Optical Frequency Conductances and Tunable Infrared Resonances," *ACS Nano*, vol. 9, no. 6, pp. 6428–6435, 2015.

[93] A. L. Koh, A. I. Fernández-Domínguez, D. W. McComb, S. A. Maier, and J. K. W. Yang, "High-Resolution Mapping of Electron-Beam-Excited Plasmon Modes in Lithographically Defined Gold Nanostructures," *Nano Lett.*, vol. 11, no. 3, pp. 1323–1330, 2011.

[94] S. Cakmakyapan, N. A. Cinel, A. O. Cakmak, and E. Ozbay, "Validation of electromagnetic field enhancement in near-infrared through Sierpinski fractal nanoantennas," *Opt. Express*, vol. 22, no. 16, pp. 19504–19512, 2014.

[95] H. Duan, A. I. Fernández-Domínguez, M. Bosman, S. A. Maier, and J. K. W. Yang, "Nanoplasmonics: Classical down to the Nanometer Scale," *Nano Lett.*, vol. 12, no. 3, pp. 1683–1689, 2012.

[96] N. A. Mortensen, S. Raza, M. Wubs, T. Søndergaard, and S. I. Bozhevolnyi, "A generalized non-local optical response theory for plasmonic nanostructures," *Nat. Commun.*, vol. 5, p. 3809, May 2014.

[97] C. A. Balanis, "Antennas," in *Antenna theory: analysis and design*, pp. 1–26, Hoboken, NJ: John Wiley, 3rd ed., 2005.

[98] L. Novotny and N. van Hulst, "Antennas for light," *Nat. Photonics*, vol. 5, no. 2, pp. 83–90, 2011.

[99] E. Collett, *Field guide to polarization*, vol. FG05 of *SPIE field guides*. Bellingham, Washington USA: SPIE Press, 2005.

[100] J. Kraus, "Antennas since Hertz and Marconi," *IEEE Trans. Antennas Propag.*, vol. 33, no. 2, pp. 131–137, 1985.

[101] D. B. Rutledge, S. E. Schwarz, and A. T. Adams, "Infrared and submillimetre antennas," *Infrared Phys.*, vol. 18, no. 5, pp. 713–729, 1978.

[102] J. Wessel, "Surface-enhanced optical microscopy," *J. Opt. Soc. Am. B*, vol. 2, no. 9, pp. 1538–1541, 1985.

[103] C. A. Balanis, "Fundamental Parameters of Antennas," in *Antenna theory: analysis and design*, pp. 27–132, Hoboken, NJ: John Wiley, 3rd ed., 2005.

[104] "IEEE Standard for Definitions of Terms for Antennas," *IEEE Std 145-2013 (Revision of IEEE Std 145-1993)*, pp. 1–50, Mar. 2014.

[105] Dubovik, V. M. and Cheshkov, A. A., "Multipole Expansion in Classical and Quantum Field Theory and Radiation," *Sov. J. Particles Nucl.*, vol. 5, no. 3, pp. 318–337, 1975.

[106] V.M. Dubovik, L.A. Tosunyan, and V.V. Tugushev, "Axial toroidal moments in electrodynamics and solid-state physics," *Sov. Phys. JETP*, vol. 63, no. 2, pp. 344–351, 1986.

[107] T. Kaelberer, V. A. Fedotov, N. Papasimakis, D. P. Tsai, and N. I. Zheludev, "Toroidal Dipolar Response in a Metamaterial," *Science*, vol. 330, pp. 1510–1512, Dec. 2010.

[108] V. M. Dubovik and V. V. Tugushev, "Toroid moments in electrodynamics and solid-state physics," *Phys. Rep.*, vol. 187, no. 4, pp. 145–202, 1990.

[109] G. N. Afanasiev and V. M. Dubovik, "Some remarkable charge-current configurations," *Phys. Part. Nucl.*, vol. 29, no. 4, pp. 366–391, 1998.

[110] P. B. Johnson and R. W. Christy, "Optical Constants of the Noble Metals," *Phys. Rev. B*, vol. 6, no. 12, pp. 4370–4379, 1972.

[111] N. E. Christensen and B. O. Seraphin, "Relativistic Band Calculation and the Optical Properties of Gold," *Phys. Rev. B*, vol. 4, no. 10, pp. 3321–3344, 1971.

[112] B. Segall, "Fermi Surface and Energy Bands of Copper," *Phys. Rev.*, vol. 125, no. 1, pp. 109–122, 1962.

[113] E. D. Palik, ed., *Handbook of Optical Constants of Solids*. Burlington, Ontario: Academic Press, 1997.

[114] S. Babar and J. H. Weaver, "Optical constants of Cu, Ag, and Au revisited," *Appl. Opt.*, vol. 54, no. 3, pp. 477–481, 2015.

[115] M.-L. Thèye, "Investigation of the Optical Properties of Au by Means of Thin Semitransparent Films," *Phys. Rev. B*, vol. 2, no. 8, pp. 3060–3078, 1970.

[116] C. J. Murphy, T. K. Sau, A. M. Gole, C. J. Orendorff, J. Gao, L. Gou, S. E. Hunyadi, and T. Li, "Anisotropic Metal Nanoparticles: Synthesis, Assembly, and Optical Applications," *J. Phys. Chem. B*, vol. 109, no. 29, pp. 13857–13870, 2005.

[117] J. C. Hulteen and R. P. V. Duyne, "Nanosphere lithography: A materials general fabrication process for periodic particle array surfaces," *J. Vac. Sci. & Technol., A*, vol. 13, no. 3, pp. 1553–1558, 1995.

[118] J. Henzie, J. Lee, M. H. Lee, W. Hasan, and T. W. Odom, "Nanofabrication of Plasmonic Structures," *Annu. Rev. Phys. Chem.*, vol. 60, no. 1, pp. 147–165, 2009.

[119] E. Yin, A. D. Brodie, F. C. Tsai, G. X. Guo, and N. W. Parker, "Electron optical column for a multicolumn, multibeam direct-write electron beam lithography system," *J. Vac. Sci. Technol., B: Microelectron. Nanometer Struct.– Process., Meas., Phenom.*, vol. 18, no. 6, pp. 3126–3131, 2000.

[120] E. Slot, M. J. Wieland, G. d. Boer, P. Kruit, G. F. ten Berge, A. M. C. Houkes, R. Jager, T. van de Peut, J. J. M. Peijster, S. W. H. K. Steenbrink, T. F. Teepen, A. H. V. van Veen, and B. J. Kampherbeek, "MAPPER: high throughput maskless lithography," in *Emerging Lithographic Technologies XII* (F. M. Schellenberg, ed.), vol. 6921 of *Proceedings of SPIE*, p. 69211P, International Society for Optics and Photonics, Apr. 2008.

[121] A. L. Koh, D. W. McComb, S. A. Maier, H. Y. Low, and J. K. W. Yang, "Sub-10 nm patterning of gold nanostructures on silicon-nitride membranes for plasmon mapping with electron energy-loss spectroscopy," *J. Vac. Sci. Technol. B*, vol. 28, no. 6, pp. C6O45–C6O49, 2010.

[122] E. P. Bellido, D. Rossouw, and G. A. Botton, "Toward 10 meV Electron Energy-Loss Spectroscopy Resolution for Plasmonics," *Micros. Microanal.*, vol. 20, no. 03, pp. 767–778, 2014.

[123] E. P. Bellido, G. D. Bernasconi, D. Rossouw, J. Butet, O. J. F. Martin, and G. A. Botton, "Self-Similarity of Plasmon Edge Modes on Koch Fractal Antennas," *ACS Nano*, vol. 11, no. 11, pp. 11240–11249, 2017.

[124] V. R. Manfrinato, A. Stein, L. Zhang, C.-Y. Nam, K. G. Yager, E. A. Stach, and C. T. Black, "Aberration-Corrected Electron Beam Lithography at the One Nanometer Length Scale," *Nano Lett.*, vol. 17, no. 8, pp. 4562–4567, 2017.

[125] A. N. Broers, "Resolution Limits of PMMA Resist for Exposure with 50 kV Electrons," *J. Electrochem. Soc.*, vol. 128, no. 1, pp. 166–170, 1981.

[126] J. C. Nabity, "Nanometer Pattern Generation System: User's Manual for NPGS v8 and v9," User Manual 7/2005, J. C. Nabity Lithography Systems, Bozeman, MT, USA, 2005.

[127] A. C. F. Hoole, M. E. Welland, and A. N. Broers, "Negative PMMA as a high-resolution resist – the limits and possibilities," *Semicond. Sci. Technol.*, vol. 12, no. 9, p. 1166, 1997.

[128] M. Khoury and D. K. Ferry, "Effect of molecular weight on poly(methyl methacrylate) resolution," *J. Vac. Sci. Technol. B*, vol. 14, no. 1, pp. 75–79, 1996.

[129] V. R. Manfrinato, J. Wen, L. Zhang, Y. Yang, R. G. Hobbs, B. Baker, D. Su, D. Zakharov, N. J. Zaluzec, D. J. Miller, E. A. Stach, and K. K. Berggren, "Determining the Resolution Limits of Electron-Beam Lithography: Direct Measurement of the Point-Spread Function," *Nano Lett.*, vol. 14, no. 8, pp. 4406–4412, 2014.

[130] D. W. Pohl, W. Denk, and M. Lanz, "Optical stethoscopy: Image recording with resolution $\lambda/20$," *Appl. Phys. Lett.*, vol. 44, no. 7, p. 651, 1998.

[131] D. Courjon and C. Bainier, "Near field microscopy and near field optics," *Rep. Prog. Phys.*, vol. 57, no. 10, p. 989, 1994.

[132] B. Hecht, H. Bielefeldt, L. Novotny, Y. Inouye, and D. W. Pohl, "Local Excitation, Scattering, and Interference of Surface Plasmons," *Phys. Rev. Lett.*, vol. 77, no. 9, pp. 1889–1892, 1996.

[133] R. Egerton, "An Introduction to EELS," in *Electron Energy-Loss Spectroscopy in the Electron Microscope*, pp. 1–28, Boston, MA: Springer US, 3rd ed., 2011.

[134] O. L. Krivanek, T. C. Lovejoy, N. Dellby, T. Aoki, R. W. Carpenter, P. Rez, E. Soignard, J. Zhu, P. E. Batson, M. J. Lagos, R. F. Egerton, and P. A. Crozier, "Vibrational spectroscopy in the electron microscope," *Nature*, vol. 514, pp. 209–212, Oct. 2014.

[135] D. B. Williams and C. B. Carter, "Part 2: Diffraction," in *Transmission Electron Microscopy*, pp. 195–368, Boston, MA: Springer US, Jan. 2009.

[136] J. I. Goldstein, D. E. Newbury, D. C. Joy, C. E. Lyman, P. Echlin, E. Lifshin, L. Sawyer, and J. R. Michael, "Electron Beam–Specimen Interactions," in *Scanning Electron Microscopy and X-Ray Microanalysis*, pp. 61–98, New York: Springer, 3rd ed., 2007.

[137] R. Reichelt, "Scanning Electron Microscopy," in *Science of Microscopy* (P. W. Hawkes and J. C. H. Spence, eds.), vol. 1, pp. 133–272, New York: Springer Science+Business Media, LLC, 2008.

[138] G. A. Botton, "Analytical Electron Microscopy," in *Science of Microscopy* (P. W. Hawkes and J. C. H. Spence, eds.), vol. 1, pp. 273–405, New York: Springer Science+Business Media, LLC, 2008.

[139] C. Jeanguillaume and C. Colliex, "Spectrum-image: the next step in eels digital acquisition and processing," *Ultramicroscopy*, vol. 28, pp. 252–257, Apr. 1989.

[140] B. Schaffer, G. Kothleitner, and W. Grogger, "EFTEM spectrum imaging at high-energy resolution," *Ultramicroscopy*, vol. 106, no. 11, pp. 1129–1138, 2006.

[141] P. D. Nellist, "Scanning Transmission Electron Microscopy," in *Science of Microscopy* (P. W. Hawkes and J. C. H. Spence, eds.), vol. 1, pp. 65–132, New York: Springer Science+Business Media, LLC, 2008.

[142] K. Suenaga, M. Tencé, C. Mory, C. Colliex, H. Kato, T. Okazaki, H. Shinohara, K. Hirahara, S. Bandow, and S. Iijima, "Element-Selective Single Atom Imaging," *Science*, vol. 290, no. 5500, pp. 2280–2282, 2000.

[143] R. Egerton, "Energy-Loss Instrumentation," in *Electron Energy-Loss Spectroscopy in the Electron Microscope*, pp. 29–109, Boston, MA: Springer US, 3rd ed., 2011.

[144] J. Nelayah, M. Kociak, O. Stéphan, F. J. García de Abajo, M. Tencé, L. Henrard, D. Taverna, I. Pastoriza-Santos, L. M. Liz-Marzán, and C. Colliex, "Mapping surface plasmons on a single metallic nanoparticle," *Nat. Phys.*, vol. 3, no. 5, pp. 348–353, 2007.

[145] J. A. Alexander, F. J. Scheltens, L. F. Drummy, M. F. Durstock, F. S. Hage, Q. M. Ramasse, and D. W. McComb, "High-resolution monochromated electron energy-loss spectroscopy of organic photovoltaic materials," *Ultramicroscopy*, vol. 180, pp. 125–132, Sept. 2017.

[146] C. Ahn and O. Krivanek, *EELS Atlas: A Reference Guide of Electron Energy Loss Spectra Covering All Stable Elements*. HREM Facility, Center for Solid State Science, Arizona State University: Gatan, 1983.

[147] D. B. Williams and C. B. Carter, "Amplitude Contrast," in *Transmission Electron Microscopy*, pp. 371–388, Boston, MA: Springer US, Jan. 2009.

[148] N. Yamamoto, "Development of high-resolution cathodoluminescence system for STEM and application to plasmonic nanostructures," *Microscopy (Oxf)*, vol. 65, no. 4, pp. 282–295, 2016.

[149] T. Coenen, E. J. R. Vesseur, and A. Polman, "Angle-resolved cathodoluminescence spectroscopy," *Appl. Phys. Lett.*, vol. 99, no. 14, p. 143103, 2011.

[150] C. I. Osorio, T. Coenen, B. J. M. Brenny, A. Polman, and A. F. Koenderink, "Angle-Resolved Cathodoluminescence Imaging Polarimetry," *ACS Photonics*, vol. 3, no. 1, pp. 147–154, 2016.

[151] S. Meuret, L. H. G. Tizei, T. Auzelle, R. Songmuang, B. Daudin, B. Gayral, and M. Kociak, "Lifetime Measurements Well below the Optical Diffraction Limit," *ACS Photonics*, vol. 3, no. 7, pp. 1157–1163, 2016.

[152] S. Meuret, T. Coenen, H. Zeijlemaker, M. Latzel, S. Christiansen, S. Conesa-Boj, and A. Polman, "Photon bunching reveals single-electron cathodoluminescence excitation efficiency in InGaN quantum wells," *Phys. Rev. B*, vol. 96, no. 3, p. 035308, 2017.

[153] T. Coenen, B. J. Brenny, E. J. Vesseur, and A. Polman, "Cathodoluminescence microscopy: Optical imaging and spectroscopy with deep-subwavelength resolution," *MRS Bull.*, vol. 40, no. 04, pp. 359–365, 2015.

[154] J. I. Goldstein, D. E. Newbury, D. C. Joy, C. E. Lyman, P. Echlin, E. Lifshin, L. Sawyer, and J. R. Michael, "The SEM and Its Modes of Operation," in *Scanning Electron Microscopy and X-Ray Microanalysis*, pp. 21–60, New York: Springer, 3rd ed., 2007.

[155] S. J. Smith and E. M. Purcell, "Visible Light from Localized Surface Charges Moving across a Grating," *Phys. Rev.*, vol. 92, no. 4, p. 1069, 1953.

[156] M. K. Krug, M. Reisecker, A. Hohenau, H. Ditlbacher, A. Trügler, U. Hohenester, and J. R. Krenn, "Probing plasmonic breathing modes optically," *Appl. Phys. Lett.*, vol. 105, no. 17, p. 171103, 2014.

[157] R. Gómez-Medina, N. Yamamoto, M. Nakano, and F. J. García de Abajo, "Mapping plasmons in nanoantennas via cathodoluminescence," *New J. Phys.*, vol. 10, no. 10, p. 105009, 2008.

[158] T. Coenen, D. T. Schoen, B. J. M. Brenny, A. Polman, and M. L. Brongersma, "Combined electron energy-loss and cathodoluminescence spectroscopy on individual and composite plasmonic nanostructures," *Phys. Rev. B*, vol. 93, no. 19, p. 195429, 2016.

[159] A. Losquin, L. F. Zagonel, V. Myroshnychenko, B. Rodríguez-González, M. Tencé, L. Scarabelli, J. Förstner, L. M. Liz-Marzán, F. J. García de Abajo, O. Stéphan, and M. Kociak, "Unveiling Nanometer Scale Extinction and Scattering Phenomena through Combined Electron Energy Loss Spectroscopy and Cathodoluminescence Measurements," *Nano Lett.*, vol. 15, no. 2, pp. 1229–1237, 2015.

[160] M. Horák, V. Křápek, M. Hrtoň, A. Konečná, F. Ligmajer, M. Stöger-Pollach, T. Šamořil, A. Paták, Z. Édes, O. Metelka, J. Babocký, and T. Šikola, "Limits of Babinet's principle for solid and hollow plasmonic antennas," *Sci. Rep.*, vol. 9, no. 1, p. 4004, 2019.

[161] N. Kawasaki, S. Meuret, R. Weil, H. Lourenço-Martins, O. Stéphan, and M. Kociak, "Extinction and Scattering Properties of High-Order Surface Plasmon Modes in Silver Nanoparticles Probed by Combined Spatially Resolved Electron

Energy Loss Spectroscopy and Cathodoluminescence," *ACS Photonics*, vol. 3, no. 9, pp. 1654–1661, 2016.

[162] M. J. Lagos and P. E. Batson, "Mapping EELS Vibrational Modes in MgO Nanocubes," *Microsc. Microanal.*, vol. 22, pp. 954–955, July 2016.

[163] O. L. Krivanek, T. C. Lovejoy, M. F. Murfitt, G. Skone, P. E. Batson, and N. Dellby, "Towards sub-10 meV energy resolution STEM-EELS," *J. Phys. Conf. Ser.*, vol. 522, p. 012023, June 2014.

[164] U. Hohenester, H. Ditlbacher, and J. R. Krenn, "Electron-Energy-Loss Spectra of Plasmonic Nanoparticles," *Phys. Rev. Lett.*, vol. 103, no. 10, p. 106801, 2009.

[165] A. Losquin and M. Kociak, "Link between Cathodoluminescence and Electron Energy Loss Spectroscopy and the Radiative and Full Electromagnetic Local Density of States," *ACS Photonics*, vol. 2, no. 11, pp. 1619–1627, 2015.

[166] G. Guzzinati, A. Béché, H. Lourenço-Martins, J. Martin, M. Kociak, and J. Verbeeck, "Probing the symmetry of the potential of localized surface plasmon resonances with phase-shaped electron beams," *Nat. Commun.*, vol. 8, no. 1, pp. 1–8, 2017.

[167] T. Coenen, F. Bernal Arango, A. Femius Koenderink, and A. Polman, "Directional emission from a single plasmonic scatterer," *Nat. Commun.*, vol. 5, p. 3250, Feb. 2014.

[168] J. M. Zuo, "Electron Detection Characteristics of a Slow-Scan CCD Camera, Imaging Plates and Film, and Electron Image Restoration," *Microsc. Res. Tech.*, vol. 49, no. 3, pp. 245–68, 2000.

[169] A. Gloter, A. Douiri, M. Tencé, and C. Colliex, "Improving energy resolution of EELS spectra: an alternative to the monochromator solution," *Ultramicroscopy*, vol. 96, no. 34, pp. 385–400, 2003.

[170] W. H. Richardson, "Bayesian-Based Iterative Method of Image Restoration," *J. Opt. Soc. Am.*, vol. 62, no. 1, p. 55, 1972.

[171] L. B. Lucy, "Optimum strategies for inverse problems in statistical astronomy," *Astron. Astrophys.*, vol. 289, pp. 983–994, Sept. 1994.

[172] L. B. Lucy, "An iterative technique for the rectification of observed distributions," *The Astron. J.*, vol. 79, no. 6, pp. 745–754, 1974.

[173] J. Parsons, C. P. Burrows, J. R. Sambles, and W. L. Barnes, "A comparison of techniques used to simulate the scattering of electromagnetic radiation by metallic nanostructures," *J. Mod. Optic.*, vol. 57, no. 5, pp. 356–365, 2010.

[174] K. S. Yee, "Numerical solution of initial boundary value problems involving maxwell's equations in isotropic media," *IEEE Trans. Antennas Propag.*, vol. 14, no. 3, pp. 302–307, 1966.

[175] E. K. Miller, "Time-domain modeling in electromagnetics," *J. Electromagnet. Wave Appl.*, vol. 8, no. 9-10, pp. 1125–1172, 1994.

[176] N. C. Lindquist, P. Nagpal, K. M. McPeak, D. J. Norris, and S.-H. Oh, "Engineering metallic nanostructures for plasmonics and nanophotonics," *Rep. Prog. Phys.*, vol. 75, no. 3, p. 036501, 2012.

[177] F. J. García de Abajo and A. Howie, "Retarded field calculation of electron energy loss in inhomogeneous dielectrics," *Phys. Rev. B*, vol. 65, no. 11, p. 115418, 2002.

[178] U. Hohenester and A. Trügler, "MNPBEM A Matlab toolbox for the simulation of plasmonic nanoparticles," *Computer Physics Communications*, vol. 183, no. 2, pp. 370–381, 2012.

[179] U. Hohenester, "Simulating electron energy loss spectroscopy with the MNPBEM toolbox," *Comput. Phys. Commun.*, vol. 185, no. 3, pp. 1177–1187, 2014.

[180] F. J. García de Abajo and A. Howie, "Relativistic Electron Energy Loss and Electron-Induced Photon Emission in Inhomogeneous Dielectrics," *Phys. Rev. Lett.*, vol. 80, no. 23, pp. 5180–5183, 1998.

[181] Y. Todokoro, "Double-layer resist films for submicrometer electron-beam lithography," *IEEE Trans. Electron Devices*, vol. 27, no. 8, pp. 1443–1448, 1980.

[182] T. G. Habteyes, S. Dhuey, E. Wood, D. Gargas, S. Cabrini, P. J. Schuck, A. P. Alivisatos, and S. R. Leone, "Metallic Adhesion Layer Induced Plasmon Damping and Molecular Linker as a Nondamping Alternative," *ACS Nano*, vol. 6, no. 6, pp. 5702–5709, 2012.

[183] I. C. Bicket, "SpectrumImageAnalysisPy: 3d Spectrum Image analysis for electron energy loss spectroscopy and cathodoluminescence." `https://github.com/icbicket/SpectrumImageAnalysisPy`, 2019. original date: 2016-09-10. DOI: 10.5281/zenodo.807762.

[184] Astropy Collaboration, T. P. Robitaille, E. J. Tollerud, P. Greenfield, M. Droettboom, E. Bray, T. Aldcroft, M. Davis, A. Ginsburg, A. M. Price-Whelan, W. E. Kerzendorf, A. Conley, N. Crighton, K. Barbary, D. Muna, H. Ferguson, F. Grollier, M. M. Parikh, P. H. Nair, H. M. Unther, C. Deil, J. Woillez, S. Conseil, R. Kramer, J. E. H. Turner, L. Singer, R. Fox, B. A. Weaver, V. Zabalza,

Z. I. Edwards, K. Azalee Bostroem, D. J. Burke, A. R. Casey, S. M. Crawford, N. Dencheva, J. Ely, T. Jenness, K. Labrie, P. L. Lim, F. Pierfederici, A. Pontzen, A. Ptak, B. Refsdal, M. Servillat, and O. Streicher, "Astropy: A community Python package for astronomy," *Astron. and Astrophys.*, vol. 558, p. A33, Oct. 2013.

[185] T. Coenen and A. Polman, "Polarization-sensitive cathodoluminescence Fourier microscopy," *Opt. Express*, vol. 20, no. 17, p. 18679, 2012.

[186] T. Coenen, E. J. R. Vesseur, A. Polman, and A. F. Koenderink, "Directional Emission from Plasmonic Yagi-Uda Antennas Probed by Angle-Resolved Cathodoluminescence Spectroscopy," *Nano Lett.*, vol. 11, no. 9, pp. 3779–3784, 2011.

[187] B. J. M. Brenny, *Probing Light Emission at the Nanoscale with Cathodoluminescence*. Ph.D. Thesis, University of Amsterdam, Amsterdam, Netherlands, June 2016.

[188] I. C. Bicket, E. P. Bellido, D. M. McRae, F. Lagugné-Labarthet, and G. A. Botton, "Carving Plasmon Modes in Silver Sierpiński Fractals," *ACS Photonics*, vol. 6, no. 11, pp. 2974–2984, 2019.

[189] K. Luke, Y. Okawachi, M. R. E. Lamont, A. L. Gaeta, and M. Lipson, "Broadband mid-infrared frequency comb generation in a Si_3N_4 microresonator," *Opt. Lett.*, vol. 40, no. 21, pp. 4823–4826, 2015.

[190] Blender Online Community, "Blender - a 3d modelling and rendering package v. 2.79b." `https://www.blender.org/`.

[191] A. H. Aitkenhead, "READ_stl." `https://www.mathworks.com/matlabcentral/fileexchange/27390-mesh-voxelisation`, 2010.

[192] I. C. Bicket, "CLFields." `https://github.com/icbicket/CLFields`, Apr. 2020. DOI: 10.5281/zenodo.3739564.

[193] E. P. Bellido, *Characterization of Surface Plasmon Resonances in Metallic Planar Nanostructures by Electron Energy Loss Spectroscopy*. Ph.D. Thesis, McMaster University, Hamilton, ON, Canada, July 2017.

[194] D. Rossouw, *Electron Energy Loss Spectroscopy of Metallic Nanostructures and Carbon Nanotubes*. Ph.D. thesis, McMaster University, Hamilton, ON, Canada, Apr. 2014.

[195] T. Coenen, *Angle-Resolved Cathodoluminescence Nanoscopy*. Ph.D. Thesis, University of Amsterdam, Amsterdam, Netherlands, May 2014.

[196] M. G. Blaber, A.-I. Henry, J. M. Bingham, G. C. Schatz, and R. P. Van Duyne, "LSPR Imaging of Silver Triangular Nanoprisms: Correlating Scattering with Structure Using Electrodynamics for Plasmon Lifetime Analysis," *J. Phys. Chem. C*, vol. 116, no. 1, pp. 393–403, 2012.

[197] K. L. Shuford, M. A. Ratner, and G. C. Schatz, "Multipolar excitation in triangular nanoprisms," *J. Chem. Phys.*, vol. 123, no. 11, p. 114713, 2005.

[198] G. Q. Wallace, M. Tabatabaei, R. Hou, M. J. Coady, P. R. Norton, T. S. Simpson, S. M. Rosendahl, A. Merlen, and F. Lagugn-Labarthet, "Superimposed Arrays of Nanoprisms for Multispectral Molecular Plasmonics," *ACS Photonics*, vol. 3, pp. 1723–1732, Sept. 2016.

[199] I. C. Bicket, E. P. Bellido, D. M. McRae, F. Lagugné-Labarthet, and G. A. Botton, "Hierarchical Plasmon Resonances in Fractal Structures," *ACS Photonics*, Apr. 2020. (forthcoming) doi:10.1021/acsphotonics.0c00110.

[200] B. B. Mandelbrot, *The Fractal Geometry of Nature*. Henry Holt and Company, 1983.

[201] C. Bovill, *Fractal Geometry in Architecture and Design*. Boston, MA: Birkhäuser Boston, 1996.

[202] Y. Fisher, *Fractal Image Compression: Theory and Application*. Springer Science & Business Media, Dec. 2012.

[203] E. Giacomazzi, C. Bruno, and B. Favini, "Fractal modelling of turbulent mixing," *Combust. Theory Modell.*, vol. 3, no. 4, pp. 637–655, 1999.

[204] E. Perfect and B. D. Kay, "Applications of fractals in soil and tillage research: a review," *Soil Tillage Res.*, vol. 36, no. 1, pp. 1–20, 1995.

[205] A. Heck and J. M. Perdang, eds., *Applying Fractals in Astronomy*. Springer Science & Business Media, Sept. 2008.

[206] C. Puente, J. Romeu, R. Pous, X. Garcia, and F. Benitez, "Fractal multiband antenna based on the Sierpinski gasket," *Electron. Lett.*, vol. 32, no. 1, pp. 1–2, 1996.

[207] C. Puente-Baliarda and R. Pous, "Fractal Design of Multiband and Low Side-Lobe Arrays," *IEEE Transactions on Antennas and Propagation*, vol. 44, no. 5, pp. 730–, 1996.

[208] H. V. Koch, "Sur une courbe continue sans tangente obtenue par une construction géométrique élémentaire," *Arkiv för Matematik, Astronomi och Fysik*, vol. 1, pp. 681–704, 1904.

[209] W. Sierpinski, "Sur une courbe dont tout point est un point de ramification," *C. R. Acad. Sci.*, vol. 160, pp. 302–305, 1915.

[210] J. P. Gianvittorio and Y. Rahmat-Samii, "Fractal Antennas: A Novel Antenna Miniaturization Technique, and Applications," *IEEE Antennas and Propag. Mag.*, vol. 44, no. 1, pp. 20–36, 2002.

[211] E. Aslan, E. Aslan, R. Wang, M. K. Hong, S. Erramilli, M. Turkmen, O. G. Saracoglu, and L. Dal Negro, "Multispectral Cesaro-Type Fractal Plasmonic Nanoantennas," *ACS Photonics*, vol. 3, no. 11, pp. 2102–2111, 2016.

[212] S. Gottheim, H. Zhang, A. O. Govorov, and N. J. Halas, "Fractal Nanoparticle Plasmonics: The Cayley Tree," *ACS Nano*, vol. 9, no. 3, pp. 3284–3292, 2015.

[213] C. Puente-Baliarda, J. Romeu, R. Pous, and A. Cardama, "On the behavior of the Sierpinski multiband fractal antenna," *IEEE Trans. Antennas Propag.*, vol. 46, no. 4, pp. 517–524, 1998.

[214] M. Waqas, Z. Ahmed, and M. B. Ihsan, "Multiband Sierpinski fractal antenna," in *2009 IEEE 13th International Multitopic Conference*, (Islamabad), pp. 1–6, Dec. 2009.

[215] J. Anguera, C. Puente, C. Borja, R. Montero, and J. Soler, "Small and high-directivity bow-tie patch antenna based on the Sierpinski fractal," *Microw. Opt. Techn. Let.*, vol. 31, no. 3, pp. 239–241, 2001.

[216] S. Sederberg and A. Y. Elezzabi, "Sierpiski fractal plasmonic antenna: a fractal abstraction of the plasmonic bowtie antenna," *Opt. Express*, vol. 19, no. 11, pp. 10456–10461, 2011.

[217] L. Seitl, F. Laible, S. Dickreuter, D. A. Gollmer, D. P. Kern, and M. Fleischer, "Miniaturized fractal optical nanoantennas defined by focused helium ion beam milling," *Nanotechnology*, vol. 31, no. 7, p. 075301, 2019.

[218] A. S. Marathay and J. F. McCalmont, "Diffraction," in *Handbook of Optics* (M. Bass, V. N. Mahajan, C. M. DeCusatis, J. M. Enoch, V. Lakshminarayanan, G. Li, C. MacDonald, and E. van Stryland, eds.), vol. 1, pp. 3.1–3.38, New York (N.Y.); Chicago (Ill.); San Francisco (Calif.): McGraw-Hill, 3rd ed., 2010. OCLC: 690417710.

[219] H. G. Booker, "Slot aerials and their relation to complementary wire aerials (Babinet's principle)," *J. Inst. Electr. Eng. Part IIIA*, vol. 93, no. 4, pp. 620–626, 1946.

[220] M. Hentschel, T. Weiss, S. Bagheri, and H. Giessen, "Babinet to the Half: Coupling of Solid and Inverse Plasmonic Structures," *Nano Lett.*, vol. 13, no. 9, pp. 4428–4433, 2013.

[221] D. Rossouw and G. A. Botton, "Resonant optical excitations in complementary plasmonic nanostructures," *Opt. Express*, vol. 20, no. 7, pp. 6968–6973, 2012.

[222] F. Falcone, T. Lopetegi, M. A. G. Laso, J. D. Baena, J. Bonache, M. Beruete, R. Marqués, F. Martín, and M. Sorolla, "Babinet Principle Applied to the Design of Metasurfaces and Metamaterials," *Phys. Rev. Lett.*, vol. 93, no. 19, p. 197401, 2004.

[223] T. Zentgraf, T. P. Meyrath, A. Seidel, S. Kaiser, H. Giessen, C. Rockstuhl, and F. Lederer, "Babinet's principle for optical frequency metamaterials and nanoantennas," *Phys. Rev. B*, vol. 76, no. 3, p. 033407, 2007.

[224] N. Engheta, A. Salandrino, and A. Alù, "Circuit Elements at Optical Frequencies: Nanoinductors, Nanocapacitors, and Nanoresistors," *Phys. Rev. Lett.*, vol. 95, no. 9, p. 095504, 2005.

[225] N. Engheta, "Circuits with Light at Nanoscales: Optical Nanocircuits Inspired by Metamaterials," *Science*, vol. 317, no. 5845, pp. 1698–1702, 2007.

[226] A. Alù and N. Engheta, "Tuning the scattering response of optical nanoantennas with nanocircuit loads," *Nat. Photonics*, vol. 2, no. 5, pp. 307–310, 2008.

[227] V. J. Keast, C. J. Walhout, T. Pedersen, N. Shahcheraghi, M. B. Cortie, and D. R. G. Mitchell, "Higher Order Plasmonic Modes Excited in Ag Triangular Nanoplates by an Electron Beam," *Plasmonics*, vol. 11, no. 4, pp. 1081–1086, 2016.

[228] A. Campos, A. Arbouet, J. Martin, D. Gérard, J. Proust, J. Plain, and M. Kociak, "Plasmonic Breathing and Edge Modes in Aluminum Nanotriangles," *ACS Photonics*, vol. 4, no. 5, pp. 1257–1263, 2017.

[229] K. L. Shuford, S. K. Gray, M. A. Ratner, and G. C. Schatz, "Substrate effects on surface plasmons in single nanoholes," *Chem. Phys. Lett.*, vol. 435, no. 1, pp. 123–126, 2007.

[230] D. Rodrigo, A. Tittl, A. John-Herpin, O. Limaj, and H. Altug, "Self-Similar Multiresonant Nanoantenna Arrays for Sensing from Near- to Mid-Infrared," *ACS Photonics*, vol. 5, pp. 4903–4911, Dec. 2018.

[231] C. Alexander, I. Giblin, and D. Newton, "Symmetry groups of fractals," *The Mathematical Intelligencer*, vol. 14, pp. 32–38, Mar. 1992.

[232] N. Harris, M. D. Arnold, M. G. Blaber, and M. J. Ford, "Plasmonic Resonances of Closely Coupled Gold Nanosphere Chains," *J. Phys. Chem. C*, vol. 113, pp. 2784–2791, Feb. 2009.

[233] K. Li, M. I. Stockman, and D. J. Bergman, "Self-Similar Chain of Metal Nanospheres as an Efficient Nanolens," *Phys. Rev. Lett.*, vol. 91, p. 227402, Nov. 2003.

[234] G. Q. Wallace and F. Lagugné-Labarthet, "Advancements in fractal plasmonics: structures, optical properties, and applications," *Analyst*, vol. 144, no. 1, pp. 13–30, 2019.

[235] I. C. Bicket, E. P. Bellido, S. Meuret, A. Polman, and G. A. Botton, "Correlative electron energy loss spectroscopy and cathodoluminescence spectroscopy on three-dimensional plasmonic split ring resonators," *Microscopy (Oxf)*, vol. 67, no. suppl_1, pp. i40–i51, 2018.

[236] V. G. Veselago, "The Electrodynamics of Substances with Simultaneously Negative Values of ϵ and μ," *Sov. Phys. Usp.*, vol. 10, no. 4, pp. 509–514, 1968.

[237] J. B. Pendry, A. J. Holden, W. J. Stewart, and I. Youngs, "Extremely Low Frequency Plasmons in Metallic Mesostructures," *Phys. Rev. Lett.*, vol. 76, no. 25, pp. 4773–4776, 1996.

[238] J. B. Pendry, A. J. Holden, D. J. Robbins, and W. J. Stewart, "Low frequency plasmons in thin-wire structures," *J. Phys.: Condens. Matter*, vol. 10, no. 22, pp. 4785–4809, 1998.

[239] J. B. Pendry, A. J. Holden, D. J. Robbins, and W. J. Stewart, "Magnetism from conductors and enhanced nonlinear phenomena," *IEEE Trans. Microwave Theory Tech.*, vol. 47, no. 11, pp. 2075–2084, 1999.

[240] C. Ding, L. Jiang, C. Sun, L. Wu, D. Xu, G. Zhang, and J. Yao, "Stable terahertz toroidal dipolar resonance in a planar metamaterial," *Phys. Status Solidi B*, vol. 252, no. 6, pp. 1388–1393, 2015.

[241] N. Katsarakis, G. Konstantinidis, A. Kostopoulos, R. S. Penciu, T. F. Gundogdu, M. Kafesaki, E. N. Economou, T. Koschny, and C. M. Soukoulis, "Magnetic response of split-ring resonators in the far-infrared frequency regime," *Opt. Lett.*, vol. 30, no. 11, pp. 1348–1350, 2005.

[242] F. von Cube, J. Niegemann, S. Irsen, D. C. Bell, and S. Linden, "Angular-resolved electron energy loss spectroscopy on a split-ring resonator," *Phys. Rev. B*, vol. 89, no. 11, 2014.

[243] I. M. Hancu, A. G. Curto, M. Castro-López, M. Kuttge, and N. F. van Hulst, "Multipolar Interference for Directed Light Emission," *Nano Lett.*, vol. 14, no. 1, pp. 166–171, 2014.

[244] G. Boudarham, N. Feth, V. Myroshnychenko, S. Linden, J. García de Abajo, M. Wegener, and M. Kociak, "Spectral Imaging of Individual Split-Ring Resonators," *Phys. Rev. Lett.*, vol. 105, no. 25, 2010.

[245] S. Linden, C. Enkrich, M. Wegener, J. Zhou, T. Koschny, and C. M. Soukoulis, "Magnetic Response of Metamaterials at 100 Terahertz," *Science*, vol. 306, no. 5700, pp. 1351–1353, 2004.

[246] C. Enkrich, M. Wegener, S. Linden, S. Burger, L. Zschiedrich, F. Schmidt, J. F. Zhou, T. Koschny, and C. Soukoulis, "Magnetic Metamaterials at Telecommunication and Visible Frequencies," *Phys. Rev. Lett.*, vol. 95, no. 20, p. 203901, 2005.

[247] S. Mühlig, C. Menzel, C. Rockstuhl, and F. Lederer, "Multipole analysis of meta-atoms," *Metamaterials*, vol. 5, no. 2, pp. 64–73, 2011.

[248] P. C. Wu, W.-L. Hsu, W. T. Chen, Y.-W. Huang, C. Y. Liao, A. Q. Liu, N. I. Zheludev, G. Sun, and D. P. Tsai, "Plasmon coupling in vertical split-ring resonator metamolecules," *Sci. Rep.*, vol. 5, p. 9726, June 2015.

[249] W. T. Chen, C. J. Chen, P. C. Wu, S. Sun, L. Zhou, G.-Y. Guo, C. T. Hsiao, K.-Y. Yang, N. I. Zheludev, and D. P. Tsai, "Optical magnetic response in three-dimensional metamaterial of upright plasmonic meta-molecules," *Opt. Express*, vol. 19, no. 13, pp. 12837–12842, 2011.

[250] S. Han, L. Cong, H. Lin, B. Xiao, H. Yang, and R. Singh, "Tunable electromagnetically induced transparency in coupled three-dimensional split-ring-resonator metamaterials," *Sci. Rep.*, vol. 6, Feb. 2016.

[251] C. C. Chen, C. T. Hsiao, S. Sun, K.-Y. Yang, P. C. Wu, W. T. Chen, Y. H. Tang, Y.-F. Chau, E. Plum, G.-Y. Guo, N. I. Zheludev, and D. P. Tsai, "Fabrication of three dimensional split ring resonators by stress-driven assembly method," *Opt. Express*, vol. 20, no. 9, pp. 9415–9420, 2012.

[252] C. Y. Liao, M. K. Chen, Y.-W. Huang, W. T. Chen, P. C. Wu, W.-Y. Tsai, H. T. Lin, Y.-T. Huang, T.-Y. Chen, J.-W. Chen, V. Savinov, N. I. Zheludev, and D. P. Tsai, "Optical toroidal response in three-dimensional plasmonic metamaterial," in *Plasmonics: Metallic Nanostructures and Their Optical Properties XIII* (A. D. Boardman and D. P. Tsai, eds.), vol. 9547 of *Proceedings of SPIE*, p. 954724, SPIE, 2015.

[253] E. Ringe, J. M. McMahon, K. Sohn, C. Cobley, Y. Xia, J. Huang, G. C. Schatz, L. D. Marks, and R. P. Van Duyne, "Unraveling the Effects of Size, Composition, and Substrate on the Localized Surface Plasmon Resonance Frequencies of Gold and Silver Nanocubes: A Systematic Single-Particle Approach," *J. Phys. Chem. C*, vol. 114, no. 29, pp. 12511–12516, 2010.

[254] C.-Y. Tsai, J.-W. Lin, C.-Y. Wu, P.-T. Lin, T.-W. Lu, and P.-T. Lee, "Plasmonic Coupling in Gold Nanoring Dimers: Observation of Coupled Bonding Mode," *Nano Lett.*, vol. 12, no. 3, pp. 1648–1654, 2012.

[255] C. Rockstuhl, F. Lederer, C. Etrich, T. Zentgraf, J. Kuhl, and H. Giessen, "On the reinterpretation of resonances in split-ring-resonators at normal incidence," *Opt. Express*, vol. 14, no. 19, pp. 8827–8836, 2006.

[256] L. S. Slaughter, Y. Wu, B. A. Willingham, P. Nordlander, and S. Link, "Effects of Symmetry Breaking and Conductive Contact on the Plasmon Coupling in Gold Nanorod Dimers," *ACS Nano*, vol. 4, no. 8, pp. 4657–4666, 2010.

[257] J. Zuloaga and P. Nordlander, "On the Energy Shift between Near-Field and Far-Field Peak Intensities in Localized Plasmon Systems," *Nano Lett.*, vol. 11, no. 3, pp. 1280–1283, 2011.

[258] T. Matsukata, N. Matthaiakakis, T.-a. Yano, M. Hada, T. Tanaka, N. Yamamoto, and T. Sannomiya, "Selection and Visualization of Degenerate Magnetic and Electric Multipoles up to Radial Higher Orders by Cathodoluminescence," *ACS Photonics*, vol. 6, no. 9, pp. 2320–2326, 2019.

[259] A. García-Etxarri and J. A. Dionne, "Surface-enhanced circular dichroism spectroscopy mediated by nonchiral nanoantennas," *Phys. Rev. B*, vol. 87, no. 23, p. 235409, 2013.

[260] T. Liu, L. V. Besteiro, T. Liedl, M. A. Correa-Duarte, Z. Wang, and A. O. Govorov, "Chiral Plasmonic Nanocrystals for Generation of Hot Electrons: Toward Polarization-Sensitive Photochemistry," *Nano Lett.*, vol. 19, pp. 1395–1407, Feb. 2019.

[261] S. Zhang, C. Gu, and H. Xu, "Single Nanoparticle Couplers for Plasmonic Waveguides," *Small*, vol. 10, no. 21, pp. 4264–4269, 2014.

[262] R. F. Egerton, "Limits to the spatial, energy and momentum resolution of electron energy-loss spectroscopy," *Ultramicroscopy*, vol. 107, no. 8, pp. 575–586, 2007.

[263] D. Rossouw and G. Botton, "Plasmonic Response of Bent Silver Nanowires for Nanophotonic Subwavelength Waveguiding," *Phys. Rev. Lett.*, vol. 110, no. 6, 2013.

[264] J. A. Dionne, L. A. Sweatlock, H. A. Atwater, and A. Polman, "Planar metal plasmon waveguides: frequency-dependent dispersion, propagation, localization, and loss beyond the free electron model," *Phys. Rev. B*, vol. 72, no. 7, p. 075405, 2005.

[265] F. J. García de Abajo and M. Kociak, "Probing the Photonic Local Density of States with Electron Energy Loss Spectroscopy," *Phys. Rev. Lett.*, vol. 100, no. 10, p. 106804, 2008.

[266] Y. B. Zel'dovich, "Electromagnetic interaction with parity violation," *Sov. Phys. JETP*, vol. 6, pp. 1184–1186, Dec. 1957.

[267] G. N. Afanasiev and Y. P. Stepanovsky, "The electromagnetic field of elementary time-dependent toroidal sources," *J. Phys. A: Math. Gen.*, vol. 28, no. 16, pp. 4565–4580, 1995.

[268] Y. Aharonov and D. Bohm, "Significance of Electromagnetic Potentials in the Quantum Theory," *Phys. Rev.*, vol. 115, no. 3, pp. 485–491, 1959.

[269] A. E. Miroshnichenko, A. B. Evlyukhin, Y. F. Yu, R. M. Bakker, A. Chipouline, A. I. Kuznetsov, B. Luk'yanchuk, B. N. Chichkov, and Y. S. Kivshar, "Nonradiating anapole modes in dielectric nanoparticles," *Nat Commun*, vol. 6, p. 8069, Aug. 2015.

[270] A. D. Boardman, K. Marinov, N. Zheludev, and V. A. Fedotov, "Dispersion properties of nonradiating configurations: Finite-difference time-domain modeling," *Phys. Rev. E*, vol. 72, no. 3, p. 036603, 2005.

[271] G. N. Afanasiev, "Simplest sources of electromagnetic fields as a tool for testing the reciprocity-like theorems," *J. Phys. D: Appl. Phys.*, vol. 34, no. 4, pp. 539–559, 2001.

[272] C. Ederer and N. A. Spaldin, "Towards a microscopic theory of toroidal moments in bulk periodic crystals," *Phys. Rev. B*, vol. 76, no. 21, p. 214404, 2007.

[273] N. A. Spaldin, M. Fiebig, and M. Mostovoy, "The toroidal moment in condensed-matter physics and its relation to the magnetoelectric effect," *J. Phys.: Condens. Matter*, vol. 20, no. 43, p. 434203, 2008.

[274] E. E. Radescu and G. Vaman, "Exact calculation of the angular momentum loss, recoil force, and radiation intensity for an arbitrary source in terms of electric, magnetic, and toroid multipoles," *Phys. Rev. E*, vol. 65, no. 4, p. 046609, 2002.

[275] M. Fiebig, "Revival of the magnetoelectric effect," *J. Phys. D: Appl. Phys.*, vol. 38, no. 8, pp. R123–R152, 2005.

[276] V. Dubovik, M. Martsenuyk, and N. Martsenuyk, "Reversal of magnetization of aggregates of magnetic particles by a vorticity field and use of toroidness for recording information," *J. Magn. Magn. Mater.*, vol. 145, no. 1, pp. 211–230, 1995.

[277] D. W. Watson, S. D. Jenkins, J. Ruostekoski, V. A. Fedotov, and N. I. Zheludev, "Toroidal dipole excitations in metamolecules formed by interacting plasmonic nanorods," *Phys. Rev. B*, vol. 93, no. 12, p. 125420, 2016.

[278] Z.-G. Dong, P. Ni, J. Zhu, X. Yin, and X. Zhang, "Toroidal dipole response in a multifold double-ring metamaterial," *Opt. Express*, vol. 20, no. 12, pp. 13065–13070, 2012.

[279] A. A. Basharin, M. Kafesaki, E. N. Economou, C. M. Soukoulis, V. A. Fedotov, V. Savinov, and N. I. Zheludev, "Dielectric Metamaterials with Toroidal Dipolar Response," *Phys. Rev. X*, vol. 5, no. 1, p. 011036, 2015.

[280] J. B. Pendry, L. Martín-Moreno, and F. J. Garcia-Vidal, "Mimicking Surface Plasmons with Structured Surfaces," *Science*, vol. 305, no. 5685, pp. 847–848, 2004.

[281] S.-H. Kim, S. S. Oh, K.-J. Kim, J.-E. Kim, H. Y. Park, O. Hess, and C.-S. Kee, "Subwavelength localization and toroidal dipole moment of spoof surface plasmon polaritons," *Phys. Rev. B*, vol. 91, no. 3, p. 035116, 2015.

[282] Q. W. Ye, L. Y. Guo, M. H. Li, Y. Liu, B. X. Xiao, and H. L. Yang, "The magnetic toroidal dipole in steric metamaterial for permittivity sensor application," *Phys. Scr.*, vol. 88, no. 5, p. 055002, 2013.

[283] V. Savinov, V. A. Fedotov, and N. I. Zheludev, "Toroidal dipolar excitation and macroscopic electromagnetic properties of metamaterials," *Phys. Rev. B*, vol. 89, no. 20, p. 205112, 2014.

[284] V. A. Fedotov, A. V. Rogacheva, V. Savinov, D. P. Tsai, and N. I. Zheludev, "Resonant Transparency and Non-Trivial Non-Radiating Excitations in Toroidal Metamaterials," *Sci. Rep.*, vol. 3, Oct. 2013.

[285] K. Marinov, A. D. Boardman, V. A. Fedotov, and N. Zheludev, "Toroidal metamaterial," *New J. Phys.*, vol. 9, no. 9, p. 324, 2007.

[286] N. Papasimakis, V. A. Fedotov, K. Marinov, and N. I. Zheludev, "Gyrotropy of a Metamolecule: Wire on a Torus," *Phys. Rev. Lett.*, vol. 103, no. 9, 2009.

[287] T. A. Raybould, V. A. Fedotov, N. Papasimakis, I. Kuprov, I. J. Youngs, W. T. Chen, D. P. Tsai, and N. I. Zheludev, "Toroidal circular dichroism," *Phys. Rev. B*, vol. 94, no. 3, p. 035119, 2016.

[288] L. Y. Guo, M. H. Li, Q. W. Ye, B. X. Xiao, and H. L. Yang, "Electric toroidal dipole response in split-ring resonator metamaterials," *Eur. Phys. J. B*, vol. 85, no. 6, p. 208, 2012.

[289] A. Mary, A. Dereux, and T. L. Ferrell, "Localized surface plasmons on a torus in the nonretarded approximation," *Phys. Rev. B*, vol. 72, no. 15, p. 155426, 2005.

[290] Z.-G. Dong, J. Zhu, J. Rho, J.-Q. Li, C. Lu, X. Yin, and X. Zhang, "Optical toroidal dipolar response by an asymmetric double-bar metamaterial," *Appl. Phys. Lett.*, vol. 101, no. 14, p. 144105, 2012.

[291] Z.-G. Dong, J. Zhu, X. Yin, J. Li, C. Lu, and X. Zhang, "All-optical Hall effect by the dynamic toroidal moment in a cavity-based metamaterial," *Phys. Rev. B*, vol. 87, no. 24, p. 245429, 2013.

[292] Y. Bao, X. Zhu, and Z. Fang, "Plasmonic Toroidal Dipolar Response under Radially Polarized Excitation," *Sci. Rep.*, vol. 5, p. 11793, June 2015.

[293] L. Ge, L. Liu, S. Dai, J. Chai, Q. Song, H. Xiang, and D. Han, "Unidirectional scattering induced by the toroidal dipolar excitation in the system of plasmonic nanoparticles," *Opt. Express*, vol. 25, no. 10, pp. 10853–10862, 2017.

[294] H. Xiang, L. Ge, L. Liu, T. Jiang, Z. Q. Zhang, C. T. Chan, and D. Han, "A minimal discrete model for toroidal moments and its experimental realization," *Phys. Rev. B*, vol. 95, no. 4, p. 045403, 2017.

[295] P. C. Wu, W. T. Chen, Y.-W. Huang, W.-L. Hsu, C. Y. Liao, V. A. Fedotov, V. Savinov, N. I. Zheludev, and D. P. Tsai, "Three-dimensional metamaterials: from split ring resonator to toroidal metamolecule," in *Plasmonics: Metallic Nanostructures and Their Optical Properties XII* (A. D. Boardman, ed.), vol. 9163, (San Diego, CA, United States), pp. 63 – 66, SPIE, 2014.

[296] N. Talebi, B. Ögüt, W. Sigle, R. Vogelgesang, and P. A. van Aken, "On the symmetry and topology of plasmonic eigenmodes in heptamer and hexamer nanocavities," *Appl. Phys. A*, vol. 116, no. 3, pp. 947–954, 2014.

[297] B. Ögüt, N. Talebi, R. Vogelgesang, W. Sigle, and P. A. van Aken, "Toroidal Plasmonic Eigenmodes in Oligomer Nanocavities for the Visible," *Nano Lett.*, vol. 12, no. 10, pp. 5239–5244, 2012.

[298] S. Guo, N. Talebi, A. Campos, M. Kociak, and P. A. van Aken, "Radiation of Dynamic Toroidal Moments," *ACS Photonics*, vol. 6, no. 2, pp. 467–474, 2019.

[299] Y.-W. Huang, W. T. Chen, P. C. Wu, V. Fedotov, V. Savinov, Y. Z. Ho, Y.-F. Chau, N. I. Zheludev, and D. P. Tsai, "Design of plasmonic toroidal metamaterials at optical frequencies," *Opt. Express*, vol. 20, no. 2, pp. 1760–1768, 2012.

[300] M.-W. Chu, V. Myroshnychenko, C. H. Chen, J.-P. Deng, C.-Y. Mou, and F. J. García de Abajo, "Probing Bright and Dark Surface-Plasmon Modes in Individual and Coupled Noble Metal Nanoparticles Using an Electron Beam," *Nano Lett.*, vol. 9, no. 1, pp. 399–404, 2009.

[301] G. Haberfehlner, F.-P. Schmidt, G. Schaffernak, A. Hörl, A. Trügler, A. Hohenau, F. Hofer, J. R. Krenn, U. Hohenester, and G. Kothleitner, "3D Imaging of Gap Plasmons in Vertically Coupled Nanoparticles by EELS Tomography," *Nano Lett.*, vol. 17, no. 11, pp. 6773–6777, 2017.

[302] C. Sönnichsen, T. Franzl, T. Wilk, G. von Plessen, J. Feldmann, O. Wilson, and P. Mulvaney, "Drastic Reduction of Plasmon Damping in Gold Nanorods," *Phys. Rev. Lett.*, vol. 88, no. 7, p. 077402, 2002.

[303] B. Foerster, A. Joplin, K. Kaefer, S. Celiksoy, S. Link, and C. Sönnichsen, "Chemical Interface Damping Depends on Electrons Reaching the Surface," *ACS Nano*, vol. 11, no. 3, pp. 2886–2893, 2017.

[304] M. Bosman, E. Ye, S. F. Tan, C. A. Nijhuis, J. K. W. Yang, R. Marty, A. Mlayah, A. Arbouet, C. Girard, and M.-Y. Han, "Surface Plasmon Damping Quantified with an Electron Nanoprobe," *Sci. Rep.*, vol. 3, Feb. 2013.

[305] J. Verbeeck, H. Tian, and P. Schattschneider, "Production and application of electron vortex beams," *Nature*, vol. 467, no. 7313, pp. 301–304, 2010.

[306] M. Uchida and A. Tonomura, "Generation of electron beams carrying orbital angular momentum," *Nature*, vol. 464, no. 7289, pp. 737–739, 2010.

[307] P. Grahn, A. Shevchenko, and M. Kaivola, "Electromagnetic multipole theory for optical nanomaterials," *New J. Phys.*, vol. 14, p. 093033, Sept. 2012.

[308] A. Góngora T. and E. Ley-Koo, "Complete electromagnetic multipole expansion including toroidal moments," *Rev. Mex. de Fís. E*, vol. 52, no. 2, pp. 188–197, 2006.

[309] R. J. LeVeque, I. M. Mitchell, and V. Stodden, "Reproducible Research for Scientific Computing: Tools and Strategies for Changing the Culture," *Comput. Sci. Eng.*, vol. 14, no. 4, pp. 13–17, 2012.

[310] L. Hatton, "The Chimera of Software Quality," *Computer*, vol. 40, no. 8, pp. 104–103, 2007.

[311] L. Hatton and A. Roberts, "How accurate is scientific software?," *IEEE Trans. Soft. Eng.*, vol. 20, no. 10, pp. 785–797, 1994.

[312] D. Kelly, "Industrial Scientific Software – A Set of Interviews on Software Development," in *Proceedings of the 2013 Conference of the Center for Advanced Studies on Collaborative Research*, CASCON '13, (Riverton, NJ, USA), pp. 299–310, IBM Corp., 2013.

[313] J. Segal, "Some Problems of Professional End User Developers," in *IEEE Symposium on Visual Languages and Human-Centric Computing (VL/HCC 2007)* (P. Cox and J. Hosking, eds.), (Los Alamitos, Ca, USA), pp. 111–118, IEEE Computer Society/Conference Publishing Services, Sept. 2007.

[314] G. V. Wilson, "Where's the Real Bottleneck in Scientific Computing?," *American Scientist*, vol. 94, no. 1, pp. 5–6, 2006.

[315] Z. Merali, "Computational science: ...Error," *Nature*, vol. 467, pp. 775–777, Oct. 2010.

[316] J. E. Hannay, C. MacLeod, J. Singer, H. P. Langtangen, D. Pfahl, and G. Wilson, "How Do Scientists Develop and Use Scientific Software?," in *Proceedings of the 2009 ICSE Workshop on Software Engineering for Computational Science and Engineering*, SECSE '09, (Vancouver, BC, Canada), pp. 1–8, IEEE Computer Society, 2009.

[317] J. Segal, "Models of scientific software development," in *SECSE 08, First International Workshop on Software Engineering in Computational Science and Engineering*, (Leipzig, Germany), May 2008.

[318] D. Hook and D. Kelly, "Testing for trustworthiness in scientific software," in *2009 ICSE Workshop on Software Engineering for Computational Science and Engineering*, pp. 59–64, May 2009.

[319] U. Kanewala and J. M. Bieman, "Techniques for Testing Scientific Programs Without an Oracle," in *Proceedings of the 5th International Workshop on Software Engineering for Computational Science and Engineering*, SE-CSE '13, (San Francisco, CA, USA), pp. 48–57, IEEE Press, 2013.

[320] K. Kreyman and D. L. Parnas, "On Documenting the Requirements for Computer Programs Based on Models of Physical Phenomena," SQRL Report 1, Software Quality Research Laboratory, McMaster University, McMaster University, Hamilton, ON, Canada, Jan. 2002.

[321] G. Wilson, D. A. Aruliah, C. T. Brown, N. P. C. Hong, M. Davis, R. T. Guy, S. H. D. Haddock, K. D. Huff, I. M. Mitchell, M. D. Plumbley, B. Waugh, E. P. White, and P. Wilson, "Best Practices for Scientific Computing," *PLOS Biology*, vol. 12, no. 1, p. e1001745, 2014.

[322] P. F. Dubois, "Designing Scientific Components," *Comput. Sci. Eng.*, vol. 4, no. 5, pp. 84–90, 2002.

[323] R. E. Pattis, "Textbook errors in binary searching," in *Proceedings of the Nineteenth SIGCSE Technical Symposium on Computer Science Education*, SIGCSE '88, (New York, NY, USA), pp. 190–194, Association for Computing Machinery, Feb. 1988.

[324] J. Segal, "When Software Engineers Met Research Scientists: A Case Study," *Empir. Software Eng.*, vol. 10, no. 4, pp. 517–536, 2005.

[325] D. F. Kelly, "A Software Chasm: Software Engineering and Scientific Computing," *IEEE Software*, vol. 24, no. 6, pp. 120–119, 2007.

[326] D. Spinellis, "Version control systems," *IEEE Software*, vol. 22, no. 5, pp. 108–109, 2005.

[327] Python Software Foundation, "26.4. unittest – Unit testing framework – Python 3.6.10 documentation." `https://docs.python.org/3.6/library/unittest.html`.

[328] pytest, "Full pytest documentation." `https://docs.pytest.org/en/latest/contents.html`.

[329] D. L. Parnas, "Precise Documentation: The Key to Better Software," in *The Future of Software Engineering* (S. Nanz, ed.), pp. 125–148, Berlin, Heidelberg: Springer, 2011.

[330] D. L. Parnas and P. C. Clements, "A rational design process: How and why to fake it," *IEEE Trans. Software Eng.*, vol. SE-12, no. 2, pp. 251–257, 1986.

[331] S. Smith, "Systematic Development of Requirements Documentation for General Purpose Scientific Computing Software," in *14th IEEE International Requirements Engineering Conference (RE'06)*, pp. 209–218, IEEE Computer Society, Sept. 2006.

[332] S. Smith, L. Lai, and R. Khedri, "Requirements Analysis for Engineering Computation: A Systematic Approach for Improving Reliability," *Reliable Comput.*, vol. 13, no. 1, pp. 83–107, 2007.

[333] W. S. Smith and N. Koothoor, "A Document-Driven Method for Certifying Scientific Computing Software for Use in Nuclear Safety Analysis," *Nucl. Eng. Technol.*, vol. 48, no. 2, pp. 404–418, 2016.

[334] D. L. Parnas, "On the Criteria to Be Used in Decomposing Systems into Modules," *Commun. ACM*, vol. 15, no. 12, pp. 1053–1058, 1972.

[335] T. E. Oliphant, "Python for Scientific Computing," *Comput. Sci. Eng.*, vol. 9, no. 3, pp. 10–20, 2007.

[336] K. J. Millman and M. Aivazis, "Python for Scientists and Engineers," *Comput. Sci. Eng.*, vol. 13, no. 2, pp. 9–12, 2011.

[337] J. D. Hunter, "Matplotlib: A 2D Graphics Environment," *Comput. Sci. Eng.*, vol. 9, no. 3, pp. 90–95, 2007.

[338] T. E. Oliphant, *Guide to NumPy*. USA: Trelgol Publishing, 2006.

[339] S. van der Walt, S. C. Colbert, and G. Varoquaux, "The NumPy Array: A Structure for Efficient Numerical Computation," *Comput. Sci. Eng.*, vol. 13, no. 2, pp. 22–30, 2011.

[340] F. Pérez and B. E. Granger, "IPython: A System for Interactive Scientific Computing," *Comput. Sci. Eng.*, vol. 9, no. 3, pp. 21–29, 2007.

[341] F. de la Peña, E. Prestat, V. T. Fauske, P. Burdet, P. Jokubauskas, M. Nord, T. Ostasevicius, K. E. MacArthur, M. Sarahan, D. N. Johnstone, J. Taillon, J. Lähnemann, V. Migunov, A. Eljarrat, J. Caron, T. Aarholt, S. Mazzucco, M. Walls, T. Slater, F. Winkler, pquinn dls, B. Martineau, G. Donval, R. McLeod, E. R. Hoglund, I. Alxneit, D. Lundeby, T. Henninen, L. F. Zagonel, and A. Garmannslund, "hyperspy/hyperspy: Hyperspy v1.5.2," Sept. 2019.

[342] DELMIC BV, "ODEMIS: Integrated software for microscopy solutions | DELMIC." `http://www.delmic.com/odemis`.

[343] P.-I. Raynal, "Python DM3 Reader v. 1.2." `https://bitbucket.org/piraynal/pydm3reader/src/master/`.

[344] P. Ercius, "ercius/openNCEM." `https://github.com/ercius/openNCEM`, Jan. 2020. original-date: 2016-11-19.

[345] Python Software Foundation, "27.5. timeit – Measure execution time of small code snippets – Python 3.6.10 documentation." `https://docs.python.org/3.6/library/timeit.html`.

[346] G. M. Amdahl, "Validity of the single processor approach to achieving large scale computing capabilities," in *Proceedings of the April 18-20, 1967, Spring Joint Computer Conference*, AFIPS '67 (Spring), (New York, NY, USA), pp. 483–485, Association for Computing Machinery, 1967.

[347] D. Beazley, "Understanding the Python GIL." `https://www.youtube.com/watch?v=Obt-vMVdM8s`, 2010. Presented at PyCon'2010.

[348] G. M. Amdahl, "Computer Architecture and Amdahl's Law," *Computer*, vol. 46, no. 12, pp. 38–46, 2013.

[349] V. Kapetanovic, *Plasmon Excitations in Sn-Doped Indium Oxide Nanostructures using Electron Energy Loss Spectroscopy.* MASc. Thesis, McMaster University, Hamilton, ON, Canada, Dec. 2018.

[350] A. Agrawal, S. H. Cho, O. Zandi, S. Ghosh, R. W. Johns, and D. J. Milliron, "Localized Surface Plasmon Resonance in Semiconductor Nanocrystals," *Chem. Rev.*, vol. 118, no. 6, pp. 3121–3207, 2018.

[351] T. P. Rossi, M. Kuisma, M. J. Puska, R. M. Nieminen, and P. Erhart, "Kohn-Sham Decomposition in Real-Time Time-Dependent Density-Functional Theory: An Efficient Tool for Analyzing Plasmonic Excitations," *J. Chem. Theory Comput.*, vol. 13, no. 10, pp. 4779–4790, 2017.

[352] S. J. Orfanidis, "Uniform Plane Waves," in *Electromagnetic Waves and Antennas*, pp. 37–82, Rutgers University: Self-published, 2016.

[353] J. M. Bennett, "Polarization," in *Handbook of Optics* (M. Bass, V. N. Mahajan, C. M. DeCusatis, J. M. Enoch, V. Lakshminarayanan, G. Li, C. MacDonald, and E. van Stryland, eds.), vol. 1, pp. 12.3–12.31, New York (N.Y.); Chicago (Ill.); San Francisco (Calif.): McGraw-Hill, 3rd ed., 2010. OCLC: 690417710.

[354] R. A. Chipman, "Mueller Matrices," in *Handbook of Optics* (M. Bass, V. N. Mahajan, C. M. DeCusatis, J. M. Enoch, V. Lakshminarayanan, G. Li, C. MacDonald, and E. van Stryland, eds.), vol. 1, pp. 14.1–14.44, New York (N.Y.); Chicago (Ill.); San Francisco (Calif.): McGraw-Hill, 3rd ed., 2010. OCLC: 690417710.

[355] R. A. Chipman, "Polarimetry," in *Handbook of Optics* (M. Bass, V. N. Mahajan, C. M. DeCusatis, J. M. Enoch, V. Lakshminarayanan, G. Li, C. MacDonald, and E. van Stryland, eds.), vol. 1, pp. 15.1–15.46, New York (N.Y.); Chicago (Ill.); San Francisco (Calif.): McGraw-Hill, 3rd ed., 2010. OCLC: 690417710.

[356] H. G. Berry, G. Gabrielse, and A. E. Livingston, "Measurement of the Stokes parameters of light," *Appl. Opt.*, vol. 16, no. 12, pp. 3200–3205, 1977.

[357] E. J. R. Vesseur and A. Polman, "Plasmonic Whispering Gallery Cavities As Optical Nanoantennas," *Nano Lett.*, vol. 11, no. 12, pp. 5524–5530, 2011.

[358] Z. Thollar, C. Wadell, T. Matsukata, N. Yamamoto, and T. Sannomiya, "Three-Dimensional Multipole Rotation in Spherical Silver Nanoparticles Observed by Cathodoluminescence," *ACS Photonics*, vol. 5, no. 7, pp. 2555–2560, 2018.

[359] T. Matsukata, C. Wadell, N. Matthaiakakis, N. Yamamoto, and T. Sannomiya, "Selected Mode Mixing and Interference Visualized within a Single Optical Nanoantenna," *ACS Photonics*, vol. 5, no. 12, pp. 4986–4992, 2018.

[360] M. N. O. Sadiku, "Coordinate Systems and Transformation," in *Elements of Electromagnetics*, pp. 28–52, New York: Oxford University Press, 5th ed., international ed., 2011.

[361] P. C. Tiemeijer, M. Bischoff, B. Freitag, and C. Kisielowski, "Using a monochromator to improve the resolution in TEM to below 0.5 Å. Part I: Creating highly coherent monochromated illumination," *Ultramicroscopy*, vol. 114, pp. 72–81, Mar. 2012.

[362] P. C. Tiemeijer, M. Bischoff, B. Freitag, and C. Kisielowski, "Using a monochromator to improve the resolution in TEM to below 0.5 Å. Part II: Application to focal series reconstruction," *Ultramicroscopy*, vol. 118, pp. 35–43, July 2012.

[363] K. Kimoto, "Practical aspects of monochromators developed for transmission electron microscopy," *Microscopy (Oxf)*, vol. 63, no. 5, pp. 337–344, 2014.

[364] D. B. Williams and C. B. Carter, "Electron Sources," in *Transmission Electron Microscopy: A Textbook for Materials Science*, pp. 73–89, Boston, MA: Springer US, jan 2009.

[365] "Titan on-line help manual – Working with a FEG (XFEG) V1.3," user manual, FEI Electron Optics.

[366] P. C. Tiemeijer, "Operation Modes of a TEM Monochromator," in *Electron Microscopy and Analysis Group Conf. EMAG99*, vol. 161 of *Inst. Phys. Conf. Ser.*, (Sheffield), pp. 191–194, IOP Publishing Ltd, 1999.

[367] P. C. Tiemeijer, "Monochromator manual Titan V1.2 and higher," User manual, FEI Electron Optics, Mar. 2011.

[368] P. C. Tiemeijer, "Measurement of Coulomb interactions in an electron beam monochromator," *Ultramicroscopy*, vol. 78, no. 1, pp. 53–62, 1999.

[369] E. Plies, K. Marianowski, and T. Ohnweiler, "The Wien filter: History, fundamentals and modern applications," *Nucl. Instrum. Methods Phys. Res., Sect. A*, vol. 645, no. 1, pp. 7–11, 2011.

[370] P. C. Tiemeijer, "Monochromator applications, optics and alignment," June 2019. Presented at the 2019 CCEM Summer School on Electron Microscopy.

[371] "Titan Condenser manual V1.0," User manual, FEI Electron Optics.

[372] P. C. Tiemeijer, "Titan optics and alignments," June 2019. Presented at the 2019 CCEM Summer School on Electron Microscopy.

[373] "Titan on-line help manual – Alignments V1.6.4," User manual, FEI Electron Optics.

[374] R. F. Egerton, "Advances in Electron Energy-Loss Spectroscopy," June 2019. Presented at the 2019 CCEM Summer School on Electron Microscopy.

[375] H. A. Brink, M. M. G. Barfels, R. P. Burgner, and B. N. Edwards, "A sub-50 meV spectrometer and energy filter for use in combination with 200 kV monochromated (S)TEMs," *Ultramicroscopy*, vol. 96, no. 34, pp. 367–384, 2003.

[376] G. Kothleitner and F. Hofer, "EELS performance measurements on a new high energy resolution imaging filter," *Micron*, vol. 34, no. 3, pp. 211–218, 2003.